

Synthesis and Characterisation of Zinc Oxide and Sodium Zirconate particles

Faith Timilehin Bamiduro

Submitted in accordance with the requirements for the degree of
Doctor of Philosophy

The University of Leeds
Institute for Materials Research
School of Chemical and Process Engineering

September, 2015

The candidate confirms that the work submitted is his own, except where work which has formed part of jointly-authored publications has been included. The contribution of the candidate and the other authors to this work has been explicitly indicated below. The candidate confirms that appropriate credit has been given within the thesis where reference has been made to the work of others.

Chapter 4 of the thesis contains material from the following jointly authored publication:

Bamiduro, Faith, Ward, Michael B., Brydson, Richard, Milne, Steven J., Hierarchical Growth of ZnO Particles by a Hydrothermal Route, J. Am. Ceram. Soc., 97(5), 2014, 1619 - 1624

All the experimental work presented in the above publication with the exception of transmission electron microscopy, was carried out by the candidate under the supervision of Dr S. J. Milne, Prof R. M. D. Brydson and Dr A. P. Brown (Co-authors and supervisors) who provided significant contributions in terms of advice and corrections during the course of manuscript preparation. Transmission electron microscopy was performed by M.B. Ward (co-author).

This copy has been supplied on the understanding that it is copyright material and that no quotation from the thesis may be published without proper acknowledgement.

The right of Faith Bamiduro to be identified as Author of this work has been asserted by him in accordance with the Copyright, Designs and Patents Act 1988.

© <2015> The University of Leeds and <Faith Timilehin Bamiduro>

Acknowledgements

I would like to extend my profound gratitude to my supervisors Dr Steven J. Milne, Dr Andrew P. Brown and Prof Richard M. D. Brydson, who through the course of my PhD provided invaluable support, advice and were there every time I needed them. I really do want to say a special thank you to my main supervisor Dr Milne who was a model supervisor, friend and mentor. Thank you Steve, Andy and Rik for your constant encouragement, it made the going a lot easier.

I am also indebted to Mr John Harrington, Dr Mike Ward and Mr Stuart Micklethwaite of Leeds Electron Microscopy and Spectroscopy Centre (LEMAS), for all the help I received from them with regards to electron microscopy. Special thanks to Dr Nicole Hondow for her insightful contributions and for being ready to help anytime I approached her.

I would like to thank my past and current office mates and colleagues whom have been through all the ups and downs of PhD studentship with me. I also would like to appreciate members of admin staff of IMR and SCAPE.

My deep gratitude to Dr Victor Ebebuwa and Mr Samson Morakinyo who have been wonderful mentors; words would fail to describe the immense impact your words, advice and support have had on me. I'd love to thank my family in Leeds: DLBC Leeds, in your midst I found love unqualified and fellowship sweet.

I would love to thank my parents Engr and Mrs C.O Bamiduro, my siblings Toyin, Hope and Love for being the best I could ever have wished for.

I would like to acknowledge the EPSRC for funding this research.

Finally, but most importantly, I want to say thank you Lord. I give all glory to You.

Abstract

Presented in this thesis are findings from investigations into the hydrothermal synthesis and growth sequence of (a) zinc oxide (ZnO) particles and (b) synthesis via normal evaporation drying and spray drying of sodium zirconate powders (Na_2ZrO_3) for CO_2 capture applications. Particle characterisation involved the usage mainly of X-ray diffraction analysis, and scanning and transmission electron microscopy to acquire information on changes in particle properties as synthesis conditions were varied.

Zinc oxide particles were grown hydrothermally from suspensions produced by drop-wise mixing of a zinc acetate solution and aqueous sodium hydroxide. The precursor suspensions were heated in an acid digestion vessel at a steady rate ($5\text{ }^\circ\text{C per min}$), to a dwell temperature of 120°C and then held for different dwell times. Analysis of characterisation results revealed that particle growth occurred through a hierarchical process, starting with zinc oxide nanocrystallites which self-assembled into $\leq 20\text{ nm}$ wide particles. Progression of hierarchical growth led to the emergence of hexagonal ZnO microrods through the stacking along the $\langle 0001 \rangle$ direction of hexagonal layers, (each $\sim 50\text{ nm}$ thick), made up of the assembled $\leq 20\text{ nm}$ particles. The process ended with the formation of hexagonal double rods ($\leq 1.8\text{ }\mu\text{m}$ and width $\leq 0.6\text{ }\mu\text{m}$) through multiple mechanisms, including secondary growth of rods off the basal layers of fully developed pre-existing rods, end-to-end attachment of rods, and possibly growth via crystal twinning.

In another series of experiments, the sequential multistage growth process of high aspect ratio zinc oxide rods are presented for hydrothermal treatment of a precursor suspension obtained by titration of a solution of zinc acetate dissolved in distilled water against an ammonium hydroxide solution. In this case, particle growth commenced with the emergence of metastable octahedral wulfingite [$\epsilon\text{-Zn(OH)}_2$] particles which transformed to high aspect ratio hexagonal ZnO microrods with increased reaction times.

Finally, sodium zirconate powders composed of nanoscale primary particles were synthesized via evaporation drying and spray drying of a mixture of sodium acetate and zirconium acetate in nitric acid for applications in CO₂ capture. Loose agglomerates (~10 μm) of irregular shaped particles were obtained from evaporation drying, while < 5 μm porous and hollow granules with nanoparticle sub-structure were obtained from spray drying. Phase composition of calcined powders from both synthesis methods was mainly Na₂ZrO₃ with minor proportions of monoclinic ZrO₂. Analysis of results from subjecting both powders to multiple carbonation (700 °C, 22 % CO₂ atmosphere) and decarbonation (900 °C, 100 % N₂ atmosphere) in thermogravimetric analysis (TGA) cycles showed that the spray dried powder had a superior CO₂ uptake performance, providing ~ 80 % CO₂ uptake efficiency (molar uptake/theoretical molar uptake) compared to ~ 45 % and ~ 15 % for the evaporation dried and commercial powders respectively. The improved performance of the spray dried sample was attributed to the morphology of the particles, as the relatively high porosity of the hollow granules enabled a faster rate of gas-solid reactions relative to the evaporation dried powder.

Table of Contents

Acknowledgements	iii
Abstract	iv
Table of Contents	vi
List of Tables	xii
List of Figures	xiv
List of Symbols and Abbreviations	xxiv
List of Publications / Presentations	xxv
Chapter 1	1
1.1 Background.....	1
1.1.1 Hydrothermal Synthesis of Zinc Oxide.....	1
1.1.2 Sodium Zirconate Sorbents for Post Combustion CO ₂ Capture	2
1.2 Aims and Objectives	4
1.2.1 Aims.....	4
1.2.2 Objectives	4
1.3 Layout of Thesis	5
Chapter 2	6
2.1 Introduction	6
2.1.1 History.....	6
2.1.1.1 Pre 1950: Synthesis and Characterisation Research	7
2.1.1.2 1950 – 1970: Synthesis and Characterisation Research	8
2.1.1.3 1970 – 1990: Synthesis and Characterisation Research	10
2.1.1.4 1990 – date: Synthesis and Characterisation Research	12
2.2 Synthesis of Zinc Oxide	17
2.2.1 The French (Indirect) Route for Production of Zinc Oxide ...	17
2.2.2 The American or Direct Process for Production of Zinc Oxide	19
2.2.3 Solution Based Synthesis of Zinc Oxide	21
2.2.4 Grading Zinc Oxide	21

2.2.5	'Non-Commercial' Synthesis Methods for Zinc Oxide	22
2.2.6	Hydrothermal Synthesis of Zinc Oxide	25
2.2.7	Advantages and Disadvantages of the Hydrothermal Technique	28
2.2.8	Factors that Could Influence Hydrothermal Growth of Zinc Oxide	30
2.3	Properties and Applications of Zinc Oxide	31
2.3.1	Properties	31
2.3.1.1	Physical Properties of Zinc Oxide	31
	<u>Physical properties: Colour</u>	31
	<u>Physical properties: Morphology</u>	32
2.3.1.2	Chemical Properties of Zinc Oxide	36
2.3.1.3	Crystal Structure and Properties of Zinc Oxide	37
2.3.1.4	Mechanical Properties of Zinc Oxide	39
2.3.1.5	Optical Properties of Zinc Oxide	41
2.3.1.6	Electrical/Electronic Properties of Zinc Oxide	44
	<u>Electrical Properties: Defects, n-type and p-type Conductivity in Zinc Oxide</u>	46
2.3.2	Applications of Zinc Oxide	49
2.3.2.1	General / Generic Applications of Zinc Oxide	49
2.3.2.2	Medical / Biological Applications of Zinc Oxide	50
2.3.2.3	Gas Sensing Applications of Zinc Oxide	51
2.3.2.4	Hydrogen Production and Fuel Cell Related Applications of Zinc Oxide	54
2.3.2.5	Photonic / Optoelectronic Applications of Zinc Oxide	55
2.3.2.6	Energy Harvesting / Generation Applications of Zinc Oxide	55
2.3.2.7	Dye Degradation / Photolysis related Applications of Zinc Oxide	57
2.3.2.8	Other Applications of Zinc Oxide	58
Chapter 3		59
3.1	Particle Synthesis	59
3.1.1	Hydrothermal Synthesis of Zinc Oxide Particles	59
3.1.1.1	Stage 1: Preparation	59
	<u>Precursor Preparation: Sodium Hydroxide (NaOH) Route</u>	60

<u>Precursor Preparation: Ammonium Hydroxide (NH₄OH) Route</u>	61
3.1.1.2 Stage 2: Hydrothermal Treatment.....	61
<u>125 mL reactor</u>	61
<u>2000 mL reactor</u>	62
3.1.1.3 Stage 3: Product Recovery, Washing and Storage	63
3.1.2 Synthesis of Sodium Zirconate powders.....	65
3.1.2.1 Stage 1: Precursor Powder Preparation	65
3.2 Analytical Methods for Particle Characterisation.....	68
3.2.1 Powder X-ray Diffraction Analysis (XRD).....	68
3.2.1.1 Principles	68
<u>Miller Indices</u>	71
<u>Phase Identification and Phase Composition</u>	72
3.2.1.2 Specimen / Sample Preparation	74
3.2.1.3 Analytical Procedure and Parameters.....	75
3.2.1.4 Limitations of the X-ray Diffraction Technique	77
3.2.2 Scanning Electron Microscopy (SEM).....	79
3.2.2.1 Principles and Applications	79
3.2.2.2 Limitations of Scanning Electron Microscopy.....	87
3.2.2.3 Sample Preparation	89
3.2.2.4 Analytical Procedure and Parameters.....	90
3.2.3 Transmission Electron Microscopy (TEM)	91
3.2.3.1 Principles and Applications	91
3.2.3.2 Sample Preparation	92
3.2.4 Dynamic Light Scattering (DLS).....	93
3.2.4.1 Principles and Applications	93
3.2.4.2 Limitations of the Dynamic Light Scattering Technique	95
3.2.4.3 Sample Preparation	96
3.2.4.4 Analytical Procedure and Parameters.....	97
3.2.5 Thermogravimetric Analysis (TGA).....	99
3.2.5.1 Principles and Applications	99
3.2.5.2 Sample Preparation	100
3.2.5.3 Analytical Procedure and Parameters.....	100

Chapter 4	102
4.1 Introduction	102
4.1.1 Samples	103
4.2 Effect of Dwell Times on Zinc Oxide	104
4.2.1 Freshly Prepared Precipitate, No Hydrothermal Treatment	104
4.2.2 Half Hour (0.5 h) Hydrothermal Treatment Products	112
4.2.3 One Hour (1 h) Hydrothermal Treatment Products	116
4.2.4 Three Hour (3 h) Hydrothermal Treatment Products	119
4.2.5 Six Hour (6 h) Hydrothermal Treatment Products	121
4.2.6 Twelve Hour (12 h) Hydrothermal Treatment Products	123
4.2.7 Twenty Four Hour (24 h) Hydrothermal Treatment Products	125
4.2.8 Further Characterisation of 12 h Hydrothermal Treatment Products	127
4.2.9 Comparative Analysis of the Effect of Hydrothermal Treatment Durations (Dwell Times) on Growth Process of Zinc Oxide Hexagonal Double Rods	129
4.2.10 Chemistry, Crystal Structure, Synthesis Conditions, Particle Morphology Relationships and Zinc Oxide Double Rod growth Mechanisms	138
4.2.11 Hierarchical Growth Process of Zinc Oxide Hexagonal Double Rod Particles	144
4.3 Investigation via FIB-SEM and TEM, of Particle Formation Process and Interfacial Junctions in Zinc Oxide Hexagonal Double Rods	148
4.3.1 Energy Dispersive Spectroscopy on the TEM (TEM- EDX line scan)	151
4.3.2 Focused Ion Beam Milling	153
4.4 Effect of pH on Particle Growth Process	156
4.4.1 pH 7 Precursor Suspension	156
4.4.2 pH 9 Precursor Suspension	157
4.4.3 pH 11 Precursor Suspension	157
4.4.4 pH 13 Precursor Suspension	157
4.4.5 Comparative Analysis of the Effect of pH on Particle Growth	158
Chapter 5	159
5.1 Introduction	159
5.1.1 Samples	160

5.2	Effect of Hydrothermal Treatment Duration on Particle Characteristics	161
5.2.1	Freshly Prepared Precipitate, No Hydrothermal Treatment	161
5.2.2	One Hour (1 h) Hydrothermal Treatment Products	166
5.2.3	Two Hour (2 h) Hydrothermal Treatment Products	169
5.2.4	Three Hour (3 h) Hydrothermal Treatment Products	172
5.2.5	Six Hour (6 h) Hydrothermal Treatment Products	174
5.2.6	Twelve Hour (12 h) Hydrothermal Treatment Products.....	176
5.2.7	Twenty Four Hour (24 h) Hydrothermal Treatment Products.....	178
5.3	Phase Transition from Zinc Hydroxide (wulfingite) to Zinc Oxide (wurtzite)	180
5.4	Investigating the Role of Ammonia in Buffering the pH of Reaction Medium and Particle Growth.....	189
5.5	Hierarchical Growth of Zinc Oxide Hexagonal Double Rods (Chapter 4) and High Aspect Ratio rods (Chapter 5)	191
Chapter 6	194
6.1	Introduction	194
6.2	Effect of Synthesis Route on Characteristics (Phase Content and Morphology) of Sodium Zirconate Powders	196
6.2.1	Samples.....	196
6.2.2	Precursor Powders	197
6.2.3	Freshly Calcined Powders	199
6.2.4	One Hour (1 h) Carbonation Products	206
6.2.5	Ten (10) Carbonation – Decarbonation Cycle Products.....	210
6.2.6	Thirty (30) Carbonation – Decarbonation Cycle Products..	216
6.2.7	Comparative Analysis of Changes in Phase Content and Particle Morphology	219
6.3	Comparison of CO ₂ Uptake Performance of Evaporation Dried, Spray Dried and Commercial Sodium Zirconate Powders over Multiple TGA Cycles	225
6.3.1	Investigation of Durability of Evaporation Dried and Spray Dried Sodium Zirconate over 50 TGA cycles	228
Chapter 7	230
7.1	Summary of Findings and Conclusions.....	230
7.1.1	Zinc Oxide Hexagonal Double Rods.....	230
7.1.2	Zinc Oxide High Aspect Ratio Hexagonal Rods.....	232

7.1.3 Sodium Zirconate Powders for CO ₂ capture	234
7.2 Recommendations for Future Work	235
7.2.1 Scale up of Hydrothermal Synthesis of Zinc oxide Hexagonal Double Rods	235
7.2.2 ZnO p-n Homojunctions	235
7.2.3 Applications	236
7.2.4 Introduction of Spacers	236
7.2.5 Further TGA Analysis.....	236
References.....	237

List of Tables

Table 2.1: Breakdown of zinc oxide related publications from 1946 till date.	13
Table 2.2: Authors with more than 100 zinc oxide related publications.....	15
Table 2.3: Country ranking in terms of volume of zinc oxide related publications.....	16
Table 2.4: Grades of commercial zinc oxide.....	22
Table 2.5: Methods that have been used in the synthesis of zinc oxide.	23
Table 2.6: Some hybrids of the hydrothermal technique (Suchanek and Riman, 2006; Yoshimura and Byrappa, 2007)	27
Table 2.7: Reported particle morphologies for zinc oxide.	32
Table 2.8: Chemical properties of zinc oxide (Klingshirn, 2007).	36
Table 2.9: Crystallographic properties of zinc oxide (Pearton et al., 2005, Özgür et al., 2005; Abrahams and Bernstein, 1969, ICDD 04-013-6607).	38
Table 2.10: Some mechanical properties of wurtzite ZnO.....	40
Table 2.11: Comparison of properties of n-type / p-type ZnO films before and after annealing at 750 °C (Tüzemen et al., 2001).	46
Table 2.12: Electrical properties of zinc oxide (Ashkenov, et al., 2003; Coleman and Jagadish, 2006; Janotti, and Van de Walle, 2009; Maeda, et al., 2005).	48
Table 3.1 Operating conditions of LabPlant spray dryer.....	67
Table 3.2 Indexing of experimental pattern from synthesis of zinc oxide double rods to ICDD reference pattern 04-013-6607 for wurtzite ZnO.	74
Table 3.3: X-ray diffraction analysis parameters.....	77
Table 3.4: Comparison between electron guns (Hitachi, 2013; Hafner, 2007).....	82
Table 3.5: SEM imaging parameters.....	90
Table 3.6: Dynamic Light Scattering measurement parameters.....	97
Table 4.1: List of samples and selected experiment conditions.....	103
Table 4.2: X-ray diffraction data for LBZA after (Poul et al., 2000).	105
Table 4.3: Indexing of peaks from sample <i>Zn01t0</i> to ICDD reference pattern 04-013-6607 for wurtzite zinc oxide.....	107

Table 4.4: Indexing of d-spacings from TEM-SAED of sheet-like background material in Figure 4.3 to wurtzite ZnO (ICDD reference 04-013-6607).	110
Table 4.5: Indexing of d-spacing from TEM SAED of equiaxed nanoparticles in Figure 4.6 to ZnO (ICDD reference 04-013-6607).....	111
Table 4.6: Comparison of relative peak intensities of X-ray diffraction patterns showing slight variations in peak intensities.....	129
Table 4.7: Description of particle morphologies in different samples as observed through scanning electron microscopy.....	134
Table 4.8: Changes in particle shape and size as a function of precursor pH.	158
Table 5.1: Listing of samples and a selection of experiment conditions.....	160
Table 5.2: Indexing of peaks from sample <i>ZnO2t0</i> to ICDD reference pattern for 04-012-2300 for wulffingite.	164
Table 6.1: List of samples and selected experiment conditions.....	196
Table 6.1: Indexing of peaks from samples <i>NZ01C0</i> (evaporation dried) and <i>NZ02C0</i> (spray dried) to ICDD Na ₂ ZrO ₃ pattern 00-035-0770.....	202
Table 6.3: identification of Phases in samples NZ01c10 and NZ02c10 using ICDD reference patterns for Sodium zirconate (00-035-0770), monoclinic zirconium oxide (01-083-0944), for 04-012-2300 for wulffingite.	214
Table 6.4: Composition of phase content of evaporation dried samples as obtained from XRD analysis.	220
Table 6.5: Composition of spray dried samples from XRD analysis data.	223

List of Figures

Figure 2.1: Publication volumes of zinc oxide research between 1950 and 1970.	9
Figure 2.2: Publication volumes of zinc oxide research: 1970 to 1990.	11
Figure 2.3: Annual number of zinc oxide related publication from the year 1946 till May, 2015	14
Figure 2.4: Flowsheet of the French (Indirect) process (Moezzi et al., 2012).....	18
Figure 2.5: Vapour pressure of water as a function of temperature; obtained from the Dortmund Data Bank (DDB, 2014).....	25
Figure 2.6: Zinc oxide powder from (a) zinc acetate dihydrate and sodium hydroxide (b) zinc acetate dihydrate and ammonium hydroxide (c) commercially source (Aldrich, 99.99% trace metal basis).	31
Figure 2.7: Morphologies of zinc oxide: (a) Nanowires (b) double rods (c) elongated microrods (d) irregular nanoparticles (e) nanolathes (f) spherical nanoparticles (g) hollow rods (i) nanoflakes (see chapter 4 & 5 for details).	35
Figure 2.8: Zinc oxide wurtzite structure showing arrangement of Zn and O atoms (Amin, 2012; Matsui and Tabata, 2010).....	37
Figure 3.1: Hydrothermal reactors (a) 125 mL capacity non-stirred Acid Digestion Vessel [Parr Instruments Model – 4748], (b) 2 L stirred bench top reactor [Parr Instruments Model – 4250]. (c) Comparison of both reaction vessels	63
Figure 3.2: Schematic of the LabPlant spray dryer showing key elements of the equipment (Souza et al., 2008).....	66
Figure 3.3: Picture of the LabPlant SD-05 spray dryer.	67
Figure 3.4: Illustration of diffraction geometry (Jurgens, 2013).	70
Figure 3.5: Illustration of electron energy levels in copper and associated $k\text{-}\alpha$ and $k\text{-}\beta$ emissions (Bearden, 1964).	70
Figure 3.6: Illustration of Miller indices using a cubic crystal system (Ungersboeck, 2007).....	71
Figure 3.7: Indexed X-ray diffraction patterns for single phase wurtzite zinc oxide showing hkl planes.	73
Figure 3.8: Sample preparation for X-ray diffraction analysis (a) off-cut silicon sample holder (b) 5 mm-bore steel sample holder (c) side view of the off-cut silicon sample holder.....	75

Figure 3.9: (a) The Phillips PANanalytical X'Pert diffractometer used (b) close up view of equipment setup and PW3064 sample stage.	76
Figure 3.10: Sample – electron interactions after (Caceres, 2002).	80
Figure 3.11: Thermionic and field emission guns: after (Goodhew, et al., 2007).	81
Figure 3.12: LEO (Zeiss) Gemini 1530 FEG-SEM.	83
Figure 3.13: Hitachi SU8230 UHR Cold-Emission FE-SEM.	83
Figure 3.14: Schematic of an Everhart-Thornley detector (Hafner, 2007).	84
Figure 3.15: Schematics showing operations of the lower upper, top detectors for SE & BSE imaging in the Hitachi SU8230 cold emission FE-SEM (Micklethwaite, 2015).	86
Figure 3.16: Schematic of a typical transmission electron microscope (Gringer, 2015).	91
Figure 3.17: Scattering Intensity, Particle volume distribution and Particle number distribution plots of the same DLS measurement of zinc oxide double rods, showing sensitivity of DLS data to particle size.	95
Figure 3.18: The Malvern Instruments Zetasizer Nanoseries equipment and sample cells for Dynamic Light Scattering particle size measurements.	98
Figure 3.19: The Perkin Elmer STA 8000 and Lauda Alpha RA 8 Chiller unit.	101
Figure 3.20: Multicycle TGA plot of percentage weight changes as a function time showing repetitive weight gain and losses during carbonation –decarbonation process (see Chapter 6 for details).	101
Figure 4.1: (a) X-ray diffraction pattern of layered basic zinc acetate (LBZA) with <i>hkl</i> planes labelled (Poul et al., 2000; Hosono, 2004); (inset) XRD pattern showin peak shifts (Cui et al., 2008).	105
Figure 4.2: X-ray diffraction pattern of <i>Zn01t0</i> , showing peaks indexed to wurtzite zinc oxide (ICDD ref. 04-013-6607) with peaks thought to be LBZA marked with an 'x'.	106
Figure 4.3: SEM image of sample <i>Zn01t0</i> with high magnification inset highlighting equiaxed nanoparticles	108
Figure 4.4: Annotated TEM micrograph of sample <i>Zn01t0</i> showing equiaxed nanoparticles resting on sheet-like zinc oxide; the red box highlight the area from which selected area electron diffraction (SAED) images were taken while the black sub-box was the point selected for energy dispersive X-ray analysis.	109
Figure 4.5: TEM-EDX spectrum of sample <i>Zn01t0</i> (annotated as black sub-ring in Figure 4.3).	109

Figure 4.6: SAED pattern of equiaxed nanoparticles in sample <i>Zn01t0</i>	110
Figure 4.7: TEM-EDX spectrum of equiaxed nanoparticle in sample <i>Zn01t0</i> (Identified by a black box in Figure 4.6).	111
Figure 4.8: Comparison between X-ray diffraction patterns of samples <i>Zn01t0</i> and <i>Zn01t0.5</i> with peaks from LBZA highlighted using an 'X'	112
Figure 4.9: SEM micrographs of sample <i>Zn01t0.5</i> showing rod-like ZnO particles co-existing with large sheets of zinc oxide.	113
Figure 4.10: SEM showing substructure on the basal planes and sides of rods.....	113
Figure 4.11: Histogram showing particle size distribution and aspect ratios in sample <i>Zn01t0.5</i>	114
Figure 4.12: (a) SEM of sample <i>Zn01t0.5</i> , where a particle similar to the one examined in the TEM is highlighted; (b) TEM, insets are HRTEM images showing substructure on ends and sides of the particle.	115
Figure 4.13: (a) SEM and (b) HRTEM images of rod from sample <i>Zn01t0.5</i> showing crystalline nature of substructure on basal planes, (b) lattice imaging, (d) TEM SAED pattern of showing smearing of diffraction spots.....	115
Figure 4.14: X-ray diffraction pattern of sample <i>Zn01t1</i> showing phase composition to be zinc oxide.	116
Figure 4.15: SEM micrographs of sample <i>Zn01t1</i> particles showing double rod morphology (inset) higher magnification to highlight uneven surfaces.....	117
Figure 4.16: SEM and TEM micrographs of <i>Zn01t1</i> particles showing details of nanostructured particle growth.	117
Figure 4.17: Histogram showing distribution of width of particles and aspect ratios in sample <i>Zn01t1</i>	118
Figure 4.18: X-ray diffraction pattern of sample <i>Zn01t3</i>	119
Figure 4.19: SEM micrographs of sample <i>Zn01t3</i>	120
Figure 4.20: Distribution of particle widths and aspect ratios in sample <i>Zn01t3</i>	120
Figure 4.21: X-ray diffraction pattern of sample <i>Zn01t6</i>	121
Figure 4.22: SEM micrographs of sample <i>Zn01t6</i>	122
Figure 4.23: Distribution of particle widths and aspect ratios in sample <i>Zn01t6</i>	122
Figure 4.24: X-ray diffraction pattern of sample <i>Zn01t12</i>	123
Figure 4.25: SEM of sample <i>Zn01t12</i> showing double rods and other particles.	124

Figure 4.26: Distribution of particle width and aspect ratios in sample <i>Zn01t12</i>	124
Figure 4.27: X-ray diffraction pattern of sample <i>Zn01t24</i>	125
Figure 4.28: SEM image of particles from sample <i>Zn01t24</i>	126
Figure 4.29: Distribution of particle width and aspect ratios in sample <i>Zn01t24</i>	126
Figure 4.30: BJH adsorption plot of sample <i>Zn01t12</i>	127
Figure 4.31: FTIR spectrum of sample <i>Zn01t12</i>	128
Figure 4.32: Compilation of X-ray diffraction patterns showing slight changes as a function of hydrothermal treatment time.	131
Figure 4.33: pH profile as a function of hydrothermal treatment duration.	133
Figure 4.34: Collage of SEM images highlighting changes in particle shape and size with respect to hydrothermal treatment time (A) 0 h, (B) 0.5 h, (C) 1 h, (D) 3 h, (E) 6 h, (F) 12 h.....	135
Figure 4.35: Comparison of particle widths as a function of hydrothermal treatment times showing gradual increase in particle widths as hydrothermal treatment duration (dwell times) increased.	136
Figure 4.36: Comparison of aspect ratios of particles as a function of hydrothermal treatment time showing increase in particle anisotropy with increasing hydrothermal treatment times.	137
Figure 4.37: Schematic showing crystal planes in a wurtzite zinc oxide hexagonal rod (Amin, 2012).....	140
Figure 4.38: Illustration of particle growth via crystal twinning leading to emergence of (A) bi-pyramidal shaped (B) dumbbell shaped zinc oxide hexagonal double rods (Wang et al., 1998)....	141
Figure 4.39: Illustration of linkage mechanism leading to formation of zinc oxide hexagonal double rods (Hu et al., 2004).....	142
Figure 4.40: SEM image showing side to side attachment of ZnO rods.....	142
Figure 4.41: (a) TEM micrograph of the interfacial junction of a double rod particle (b) Result of EDXS analysis of area labelled as 'spt1' (c) Results of EDXS analysis of area labelled as 'spt2' (Bitenc et al., 2010).	143
Figure 4.42: Schematic describing key growth stages leading to formation of zinc oxide hexagonal double rods.....	146

Figure 4.43: Schematic describing particle growth stages using SEMs of ZnO particles from zinc acetate and sodium hydroxide. Image in stage 1 shows equiaxed nanoparticles; Image in stage 2 shows striated particle showing evidence of stacking of nanoplates while SEM in stage 3 is a single rod particle and SEMs in Stages 4 5a & 5b show double rod growth via secondary growth and end to end attachment of rods.	146
Figure 4.44: SEM collection illustrating (a) particle deposition on an existing rod-like particle and (b) subsequent stages of recrystallizing to produce (c) a well-defined hexagonal double rod.	147
Figure 4.45: TEM micrograph of a stage 5a double rod (b) TEM of same particle with contrast modified to highlight the absence of hollow cavities and gaps at the interface between the components of the double rod.	148
Figure 4.46: (a) low magnification, (b) high resolution TEM, and (c) lattice imaging showing no discontinuity between component rods and (0002) lattice planes running coherently across the interfacial junction.	149
Figure 4.47: TEM micrograph of a stage 5b double rods showing (a) gaps at interfacial junction (b) disjointed interface between components of the double rod particle.	149
Figure 4.48: (a) low magnification showing disjointed interface (b – c) lattice imaging showing (0002) planes of individual component rods (d) HRTEM of interface and (e) lattice imaging showing (0002) lattice planes at the interfacial junction with gaps.	150
Figure 4.49: (a) STEM micrograph of interfacial junction within stage 5b type of particle (b-c) TEM-SAED patterns from top and bottom sections of double rod particle showing diffraction as a single crystal (d) line indicating the area analysed by TEM- EDX line scan.	151
Figure 4.50: Results of TEM- EDX line scan across the interfacial junction between top and bottom components of a double rod particle showing no sudden rise in silicon signal across the interface relative to zinc, oxygen and copper signal from the specimen grid. Thick black line indicates interfacial junction between component rods.	152
Figure 4.51: SEM of double rod and TEM of the longitudinal cross section.	153
Figure 4.52: TEM showing cavity at interfacial junction inside double rod.	153
Figure 4.53: TEM-SAED diffraction pattern from edge mid portions of the top and bottom component of a double rod particle.	154

Figure 4.54: TEM image showing the presence of a seam at the interfacial junction of component rods.....	154
Figure 4.55: SEM image of sample <i>Zn01t12</i> showing single rod particles with pitted surfaces in coexistence with double rod particles.	155
Figure 4.56: (a) XRD pattern of sample <i>Zn01p7</i> compared with ICDD reference pattern for zinc oxide (b) SEM image of sample <i>Zn01p7</i> showing three different types of particle shapes.	156
Figure 4.57: (a) XRD pattern of sample <i>Zn01p11</i> compared with ICDD reference pattern for zinc oxide (b) SEM image showing nanoflakes.	157
Figure 4.58: (a) XRD of sample <i>Zn01p13</i> compared with ICDD reference pattern for zinc oxide (b) SEM image showing flower-like nanoclusters.....	158
Figure 5.1: X-ray diffraction pattern of sample <i>Zn02t0</i> , showing peaks indexed to wulffingite [ϵ -Zn(OH) ₂] and ICDD (Zn(OH) ₂) reference pattern.....	162
Figure 5.2: (left) SEM image showing octahedral shaped particles (inset) higher resolution image of a single particle (right) a schematic of an octahedral crystal structure showing the {111} planes.	162
Figure 5.3: Histogram of particle size distribution in sample <i>Zn02t0</i> .	163
Figure 5.4: X-ray diffraction pattern of sample <i>Zn02t1</i> and ICDD reference pattern number 04-012-2300 for wulffingite.....	166
Figure 5.5: SEM micrograph of sample <i>Zn02t1</i> showing rod like particles (red arrow) surrounded by multifaceted particles.....	167
Figure 5.6: Histogram showing particle size distribution in sample <i>Zn02t1</i>	167
Figure 5.7: Comparison between X-ray diffraction pattern of sample <i>Zn02t1</i> and ICDD reference pattern 04-013-6607 for zinc oxide...	168
Figure 5.8: XRD pattern of sample <i>Zn02t2</i> compared with ICDD reference for ZnO. Peaks from phases indexed to ZnO and Zn(OH) ₂ are highlighted.....	169
Figure 5.9: SEM showing the co-existence of octahedral shaped multifaceted and hexagonal rod-like particles in sample <i>Zn02t2</i> .	170
Figure 5.10: Histogram showing particle size distribution and distribution of particle aspect ratios in sample <i>Zn02t2</i>	171
Figure 5.11: X-ray diffraction pattern of sample <i>Zn02t3</i> and ICDD reference pattern for zinc oxide.....	172
Figure 5.12: SEM micrograph of sample <i>Zn02t3</i> with arrow highlighting a multifaceted particle.....	173

Figure 5.13: Histogram showing particle size distribution and aspect ratio in sample <i>ZnO2t3</i>	173
Figure 5.14: X-ray diffraction pattern of sample <i>ZnO2t6</i> and ICDD reference pattern 04-013-6607 for zinc oxide.	174
Figure 5.15: SEM micrograph of sample <i>ZnO2t6</i>	175
Figure 5.16: Histogram showing particle size distribution in sample <i>ZnO2t6</i>	175
Figure 5.17: X-ray diffraction pattern of sample <i>ZnO2t12</i> and ICDD reference pattern 04-013-6607 for zinc oxide.	176
Figure 5.18: SEM micrograph of sample <i>ZnO2t12</i> (inset) high magnification SEM and (b) Schematic showing the corresponding <i>hkl</i> planes.	177
Figure 5.19: Histogram showing distribution of particle size and aspect ratios in sample <i>ZnO2t12</i>	177
Figure 5.20: X-ray diffraction pattern of sample <i>ZnO2t24</i>	178
Figure 5.21: SEM micrograph of particles from sample <i>ZnO2t24</i>	179
Figure 5.22: Histogram showing distribution of particle size and aspect ratios in sample <i>ZnO2t24</i>	179
Figure 5.23: Schematic representation of the major particle growth stages for the high aspect ratio hexagonal zinc oxide rods using SEM images.	180
Figure 5.24: A comparison of X-ray diffraction patterns showing graduation phase transition as a function of hydrothermal dwell time.	181
Figure 5.25: A comparison of SEMs showing changes in particle morphology as a function of hydrothermal dwell times.	181
Figure 5.26: Distribution of Zn(II) hydroxo-complexes in equilibrium with crystalline zinc oxide at infinite dilution at 298 K (Zhang and Mohammed, 2001).	185
Figure 5.27: Schematic illustrating hypothetical pathway for formation of zinc oxide from zinc acetate and ammonium hydroxide.	187
Figure 5.28: SEM showing a hexagonal rod-like particle evolving from a Zn(OH) ₂ boulder-like particle, surrounded by both particle types.	188
Figure 5.29: SEM micrographs showing multifaceted or boulder like particles coexisting with a hexagonal rod particle and crystallites.	188
Figure 5.30: pH profile of reactor contents as a function of dwell time.	190

Figure 5.31: Combination of high magnification SEM micrographs illustrating particle growth sequence of zinc oxide hexagonal double rods; (a) particle from sample <i>Zn01t0.5</i> showing deposition of nanoparticles on the basal sections of an existing rod-like particle and (b) subsequent stages of recrystallizing to produce (c) a well-defined hexagonal double rod from sample <i>Zn01t12</i>	193
Figure 5.32: Combination of high magnification SEM micrographs illustrating ZnO particle growth sequence of high aspect ratio hexagonal rods (a) particle from sample <i>Zn02t2</i> showing co-existence of hexagonal rod-like with multifaceted octahedral shaped and boulder-like particles (b) another particle from sample <i>Zn02t2</i> showing stepwise growth of the basal planes (c) particle from sample <i>Zn02t12</i> showing a fully recrystallized rod with well-defined hexagonal basal terminal.	193
Figure 6.1: XRD plot of as prepared precursor powders obtained from evaporation drying (ED) and spray drying (ED) synthesis routes.	197
Figure 6.2: Comparison of XRD patterns of precursor powders from evaporation dried and spray dried routes with ICDD reference patterns for sodium carbonate, sodium zirconate and monoclinic zirconia.	198
Figure 6.3: XRD plot of freshly calcined evaporation dried sample <i>NZ01c0</i> ; peaks from sodium zirconate labelled with corresponding miller indices.	199
Figure 6.4: SEM of freshly calcined evaporation dried sample <i>NZ01c0</i> showing irregular shaped loose aggregates of particles.	200
Figure 6.5: XRD plot of freshly calcined spray dried sample <i>NZ02c0</i> ; peaks from sodium zirconate labelled with corresponding miller indices.	201
Figure 6.6: SEM of freshly calcined spray dried sample <i>NZ02c0</i> showing hollow granules of sodium zirconate with nanostructure.	201
Figure 6.7: Comparison of evaporation dried sample <i>NZ01c0</i> and spray dried sample <i>NZ02c0</i> showing differences in particle morphology.	204
Figure 6.8: Schematic illustration of the formation of ruptured and hollow sodium zirconate precursor particles during spray drying process.	205
Figure 6.9: XRD pattern of evaporation dried (ED) sample <i>NZ01c1</i> after 1 h of carbonation at 700 °C in 22% CO ₂	206
Figure 6.10: SEM of sample <i>NZ01c1</i> after carbonation for 1 h.	207
Figure 6.11: SEM-EDX of sample <i>NZ01c1</i> after 1 h carbonation.	207

Figure 6.12: XRD pattern of spray dried (SD) sample <i>NZ02c1</i> after 1 h of carbonation at 700 °C in 22% CO ₂	208
Figure 6.13: SEM of sample <i>NZ02c1</i> showing rounded agglomerate particles with substructure of nanoparticles and smooth glassy material.....	209
Figure 6.14: SEM-EDX of sample <i>NZ02c1</i> after 1 h carbonation showing distribution of sodium carbonate and zirconia in the sample.	209
Figure 6.15: Results XRD analysis of evaporation dried (sample <i>NZ01c10</i>) after 10 TGA cycles (terminating the process on a carbonation stage).....	211
Figure 6.16: SEM of sample <i>NZ01c10</i> after 10 TGA cycles.	212
Figure 6.18: SEM of sample <i>NZ02c10</i> after carbonation for 10 TGA cycles showing a reduction in average sizes of the agglomerates relative to freshly calcined sample <i>NZ02c0</i>	213
Figure 6.19: XRD pattern of sample <i>NZ01c30</i>	216
Figure 6.20: SEM of sample <i>NZ01c30</i> showing increase in nanoparticle size and porosity of agglomerates.....	217
Figure 6.21: XRD pattern of sample <i>NZ02c30</i> with peaks from phases identified as sodium zirconate, sodium carbonate, monoclinic and tetragonal zirconia labelled respectively.....	218
Figure 6.22: SEM of spray dried sample <i>NZ02c30</i>	218
Figure 6.23: Comparison of XRD patterns of evaporation dried samples showing changes in phase content.	219
Figure 6.24: Crystal polymorphs and phase transition of pure zirconium oxide (Bertin and Roberts, 1999).	221
Figure 6.25: SEM of samples showing changes in substructure of sorbent agglomerate particles (a) freshly calcined sample <i>NZ01c0</i> (b) 1 h carbonation products sample <i>NZ01c1</i> (c) sample <i>NZ01c10</i> obtained after 10 TGA cycles, and (d) <i>NZ01c30</i> obtained after 30 TGA cycles.....	221
Figure 6.26: Comparison of XRD patterns of spray dried samples showing changes in phase content.	223
Figure 6.27: SEM of spray dried samples showing changes in substructure of rounded agglomerates (a) freshly calcined sample <i>NZ02c0</i> (b) 1 h carbonation products sample <i>NZ02c1</i> (c) sample <i>NZ02c10</i> obtained after 10 TGA cycles, and (d) <i>NZ02c30</i> obtained after 30 TGA cycles.....	224
Figure 6.28: Multicycle TGA of evaporation dried sample <i>NZ01c0</i> showing percentage weight gains and losses per cycle.....	225
Figure 6.29: Multicycle TGA of sample <i>NZ02c0</i> showing percentage weight gains and losses per cycle over 20 cycles.....	226

Figure 6.30: Multicycle TGA of sample <i>MELSORB 2390</i>, showing percentage weight gains and losses per cycle for 20 cycles.	226
Figure 6.31: Comparison of percentage CO₂ conversion of samples <i>NZ01c0</i>, <i>NZ02c0</i> and <i>MELSORB 2390</i> over 20 TGA cycles.	228
Figure 6.32: Multicycle TGA of evaporation dried sample <i>NZ02c50</i> and spray dried <i>NZ02c50</i> for 50 cycles.....	229
Figure 6.33: CO₂ capture efficiency over 50 TGA cycles.....	229

List of Symbols and Abbreviations

BET	Brunauer, Emmett and Teller surface area analysis
BSE	Back-scattered electrons
DLS	Dynamic light scattering
EDX	Energy dispersive X-ray analysis
FEG	Field emission gun
FIB-SEM	Focused ion beam coupled with scanning electron microscopy
FTIR	Fourier transform infrared spectroscopy
ICDD	International Centre for Diffraction Data
SAED	Selected area electron diffraction
SE	Secondary electrons
SEM	Scanning electron microscope
STA	Simultaneous thermal analyser equipment
TEM	Transmission electron microscope
TGA	Thermogravimetric analysis
XRD	X-ray diffraction

List of Publications / Presentations

Paper

1. Bamiduro, Faith, Ward, Michael B., Brydson, Richard, Milne, Steven J., Hierarchical Growth of ZnO Particles by a Hydrothermal Route, J. Am. Ceram. Soc., 97(5), 2014, 1619 - 1624
2. Mu Q, David CA, Galceran J, Rey-Castro C, Krzemiński L, Wallace R, Bamiduro F, Milne SJ, Hondow NS, Brydson R, Vizcay-Barrena G, Routledge MN, Jeuken LJ, Brown AP., Systematic investigation of the physicochemical factors that contribute to the toxicity of ZnO nanoparticles, Chem Res Toxicol. 27(4), 2014 Apr 21, 558-67.

Conference Presentation

1. BACG 2014: Annual Conference of the British Association for Crystal Growth, Leeds, 13-15 July 2014
Oral Presentation: Hierarchical Growth of ZnO Hexagonal Microrods by Hydrothermal Processing.
2. 4th Annual Postgraduate Symposium on Nanotechnology, University of Birmingham, 15th of December 2014
Oral Presentation: Hierarchical Growth of Nanostructured ZnO Hexagonal double-rods
3. 1st Northern Postgraduate Chemical Engineering Conference, (NPCEC, 2013), Newcastle University, 8th & 9th August 2013
Poster Presentation: Hierarchical Growth of Nanostructured ZnO Hexagonal double-rods
4. ChemEngDayUK 2014, University of Manchester, 7–8 April 2014.
Poster Presentation: Scalable hydrothermal synthesis of conjoined hexagonal rods of zinc oxide for optoelectronic applications
5. Microscience Microscopy Congress 2014, Manchester, United Kingdom, 30th June - 3rd July 2014
Poster Presentation: Hydrothermal synthesis, FIB-SEM and TEM analysis of nanostructured hexagonal ZnO double rods

6. ChemEngDayUK 2015, Sheffield, United Kingdom, 8–9 April 2015.
Poster Presentation: Hydrothermal Synthesis of Zinc Oxide: Laboratory Scale-up
7. Microscience Microscopy Congress 2015 incorporating Electron Microscopy and Microanalysis Group (EMAG) 2015, Manchester, United Kingdom, 30th June - 3rd July 2015
Poster Presentation: FIB-SEM and TEM analysis of nanostructured hexagonal ZnO double rods prepared by hydrothermal synthesis

Chapter 1

Introduction

1.1 Background

1.1.1 Hydrothermal Synthesis of Zinc Oxide

Zinc oxide can be obtained naturally in the form of the mineral zincite, albeit with elements such as manganese (Mn) and cadmium (Ca) most of the time incorporated as impurities (Klingshirn, 2007). It is also possible for zinc oxide to be extracted from ores that contain oxides or carbonates of zinc such as franklinite and calamine or smithsonite (Moezzi et al., 2012). In addition to being referred to by its mineral name (i.e. zincite), zinc oxide is also known by other names such as: Calamine, Philosopher's wool, and Chinese white (Moezzi et al., 2012; Prakash and Madan, 1987).

The popularity of zinc oxide as a multifunctional semiconductor material stems from its unique optoelectronic properties; a wide band gap of ~ 3.37 eV, UV absorbance and emission capabilities, high exciton binding energy (60 meV). It is also known to have good biocompatibility as well as strong chemical and photo stability (Wang, 2004; Fan and Lu, 2005; Schilling et al., 2010). These characteristics, make it a good candidate for electronic, medical, acoustic, catalytic and sensor applications. ZnO particles are also utilised in the degradation of dye pollutants in waste water treatment, among other conventional uses (Willander et al., 2010).

The synthesis and engineering of zinc oxide particles for various applications is a research area that is still attracting considerable research interest mainly because a significant proportion of the behaviour exhibited by particulate zinc oxide on the micro and nanoscale (such as band gap, photoluminescence, UV interaction) could be influenced by the route and conditions of particle synthesis (Jung et al., 2012). Zinc oxide particles with rod-like or wire-like morphologies have shown promise in a number of applications; such as improved detection

abilities, in gas sensing applications and strong solar energy conversion efficiencies in solar cell applications (Willander et al., 2010).

A sizeable portion of zinc oxide-related research activities are focused on developing simpler, more efficient, less toxic and cheaper synthesis techniques that combine improved yield of high purity products with a greater level of control over product characteristics. Techniques with the foregoing abilities would be of immense benefit to commercial efforts which require relatively large quantities of material to be produced with high level of purity and batch traceability. Hydrothermal synthesis is considered a suitable candidate that reasonably fulfils the aforementioned criteria (Baruah and Dutta, 2009; Suchanek and Riman 2006).

1.1.2 Sodium Zirconate Sorbents for Post Combustion CO₂ Capture

The subject of CO₂ capture, is also one that has received an increased amount of research interest since the turn of the millennium due to greater levels of awareness being created about the link between increasing CO₂ emission rates and rapid increases in global temperatures (global warming); leading to stronger combinations of political and scientific will to cut down heavily on pollution worldwide and reduce the impact of anthropogenic activities on our environment (DEFFRA, 2015; NRC, 2010).

Although there are no fixed global targets for CO₂ reduction, several countries have policy guidelines as to how much reduction in CO₂ emission that could be achieved by the year 2050. For instance, the European Union targets that global temperature rises (global warming) would not be more than 2 °C above levels recorded before the industrial era (~ 280 parts per million) by the year 2050. It has been noted, that for this EU target to be achievable, the amount of CO₂ in the atmosphere would need to drop to within the range of 550 parts per million (ppm) (Adam, 2008). The United Kingdom, aims to reduce greenhouse gas emissions by at least 80% (using the year 1990 as a baseline) by year 2050 (DEFFRA, 2015).

Of the plethora of ways being explored to reduce global CO₂ emissions, there is a general consensus, that achieving any bulk reduction in the amount of CO₂ belched out by our industries would significantly improve our hopes of slowing

down global warming. A key industrial sector that accounts for a huge chunk of CO₂ emission of most industrialised countries, is the power generation sector. It accounts for between 30 – 50 % of CO₂ emissions depending on the country (EPA, 2015). Therefore efforts are on the rise to develop means of minimising the quantity of CO₂ escaping from the exhaust pipes of fossil-fuel fired power plants and other single-point industrial emitters (Anthony et al., 2007).

One route to managing CO₂ emissions from single-point emitters is to develop CO₂ capture and storage modules for post-combustion CO₂ capture using materials that can reversibly physically or chemically bind CO₂ gas molecules. Sodium zirconate (Na₂ZrO₃) is one of such materials. It can combine with CO₂ to yield sodium carbonate (Na₂CO₃) and zirconium oxide (ZrO₂) under favourable conditions; the sodium zirconate can then be regenerated by heating up the products (i.e. sodium carbonate and zirconium oxide) in the process releasing the captured CO₂.

For a CO₂ capture material (sorbent) to be of any use commercially, it needs to fulfil a number of criteria, one of which is that its synthesis process should be environmentally friendly, an energy intensive / environmentally burdensome synthesis process effective cancels out the gains that could be derived from making use of the sorbents in CO₂ capture applications. Another criteria is that the sorbent material itself should have low environmental toxicity and be easily disposable when spent, so we don't create another problem trying to solve one. Furthermore, it is expected that the CO₂ capture material should be able to retain close to its original CO₂ capture capacity over long term repeated or cyclic use, and this is where the challenge usually lies with developing suitable sorbent materials for use in post-combustion capture of CO₂ (MacKenzie et al., 2007; Manovic et al., 2009).

1.2 Aims and Objectives

1.2.1 Aims

The overall aim of research work was to explore the use of environmentally benign and relatively low energy synthesis processes to produce zinc oxide and sodium zirconate particles. The first point of emphasis was on understanding the growth process of zinc oxide particles, and the effect of variation in synthesis conditions on the growth process and product characteristics. Secondly the capabilities of sodium zirconate powders to reversibly capture CO₂ gas were studied with the aim of engineering the powders to produce durable and efficient CO₂ capture sorbents that could be used in large scale commercial processes.

1.2.2 Objectives

- Achieve additive-free growth of zinc oxide particles via the hydrothermal route
- Investigate the growth process of the hydrothermally grown ZnO particles and examine the role of length of hydrothermal treatment and precursor pH in influencing growth characteristics of the ZnO particles
- Synthesise sodium zirconate powders using soft chemical routes (evaporation from solution and spray drying)
- Employ in-house characterisation techniques: X-ray diffraction analysis, scanning and transmission electron microscopy, to acquire information about the properties of the synthesised zinc oxide and sodium zirconate particles.
- Investigate the CO₂ capture performance of the sodium zirconate powders to determine which method of synthesis provided powders with the best CO₂ capture performance.

1.3 Layout of Thesis

This Thesis comprises of a total of seven chapters. In chapter 1 is presented an introduction to the research, an outline of its aims and objectives as well as a documentation of the layout of the thesis.

Chapter 2 contains details of a review of literature on zinc oxide covering its synthesis, properties and reported applications, with focus on hydrothermal synthesis.

Chapter 3 dwells on the materials and methods employed for the hydrothermal synthesis of zinc oxide as well as evaporation and spray drying synthesis processes for production of sodium zirconate powders. An overview of the background science of key analytical techniques employed in the characterisation of both zinc oxide and sodium zirconate is also presented.

Chapter 4 presents and discusses the results of hydrothermal synthesis of zinc oxide hexagonal double rods. Insights into the multiple stages that occur in the course of particle growth are provided with a focus on the effects of hydrothermal dwell times and pH of precursor on the properties of the product zinc oxide particles. In addition to proffering a mechanism to explain the emergence of the double rods, chapter 4 also provides a discussion of investigations into the interfacial junction within the double rod particle using a combination of electron microscopy and focused ion beam milling.

Chapter 5 contains a presentation and discussion of results from hydrothermal synthesis of high aspect ratio hexagonal zinc oxide rods. The occurrence of phase transformation from wulfingite zinc hydroxide to wurtzite zinc oxide leading to the emergence of the high aspect ratio rods is chronicled along with an analysis of the influence of ammonia on the particle growth process.

Chapter 6 presents the details of evaporation and spray drying synthesis of sodium zirconate powders. The influence of synthesis method on particle morphology and microstructure of the sodium zirconate powders is examined. The chapter also provides an analysis of the CO₂ capture credentials of powders obtained from both synthesis routes in comparison to a commercially sourced sample. The effect of extended multicycle TGA runs on CO₂ capture performance was also examined. Finally, a conclusion of findings and recommendations for future work are provided in chapter 7.

Chapter 2

Literature Review: Zinc Oxide

2.1 Introduction

In this chapter, a review of literature surrounding the material zinc oxide, its synthesis and related research is presented. Section 2.1 briefly explores the historical significance of zinc oxide and the history of its synthesis.

In section 2.2, the evolution of zinc oxide synthesis process is examined focussing on the main commercial processes through which the material is currently produced. Furthermore, the section also provides a review of literature surrounding hydrothermal processing of materials and its usage in the synthesis of zinc oxide. A comparison of the hydrothermal method with other synthesis routes is presented in this chapter to set the stage for the discussions in chapters 4 and 5.

The characteristics of zinc oxide which has made it garner a relatively large amount of research interest over the course of the last six decades are highlighted in section 2.3, alongside a summary of literature covering some of the applications based that have been developed, or are in the process of development involving zinc oxide particles.

2.1.1 History

As reported in New Jersey Zinc Company's technical bulletin, zinc oxide's origins are in a way indeterminate, but can be traced all the way back to the production of the copper – zinc alloy 'brass' by the romans during the Middle Ages ([New Jersey Zinc Company, 1940](#)). Later in the medieval times, Alchemists made philosopher's wool or '*lana philosophica*' in Latin by combusting zinc during efforts to purify left-over brass in galvanizer's dross ([Brown, 1957](#); [Rao, 2010](#)). In fact, zinc oxide production has always been associated with the production of the metal zinc itself, and documentation of scientific research related to zinc oxide covers more than a century ([Klingshirn et al., 2010](#)).

2.1.1.1 Pre 1950: Synthesis and Characterisation Research

Zinc oxide since its 'official' discovery has attracted scientific curiosity. The Alchemists in their quest to turn base metals to gold found that they could increase the weight of gold by 'adding a fourth part of cadmia'; cadmia was an alloy of zinc and copper (brass) (Brown, 1957). Cramer around the late 1700s published details of zinc oxide synthesis from metallic zinc, while Courtois discovered its suitability for paints around 1782. It is reported, that the element cadmium was discovered in 1817, by K.S.L. Hermann and J.C.H. Roloff who were investigating the purity of zinc oxide used for medical purposes (Brown, 1957; Cadmium, 2015).

Commercial synthesis of zinc oxide predates the 1900s. The French or indirect process for the production of zinc oxide which has some similarities to the medieval philosopher's wool synthesis process was developed in France by Le Clair around 1840 (IZA, 2015). It was not until a few decades later that the American or direct process was developed. Both processes are still being actively used today to produce zinc oxide in tonnes per annum (New Jersey Zinc Company, 1940; IZA, 2015). By 1926, publications describing multimillion dollar (in 1926 USD) commercial production of zinc oxide from ores mined from the Mascot and Franklin mines in America for usage in the tyre and pigment industries were already in circulation (American Zinc, 1926).

The invention of the electron microscope in 1931 by Max Knoll and Ernst Ruska, provided scientists with greater abilities to explore the realm of submicron particle sizes (Dykstra and Reuss, 2003) and expectedly a lot of attention was being paid to studying the particle shape and size of industrially significant materials of that era, one of which was zinc oxide (Palucka, 2002; Miller Jr., 1941). One of the early mentions of microscopic analysis of zinc oxide was by Fordham (1940) as highlighted by Preston (1941) in Nature, where he referred to Fordham's electron micrographs of zinc oxide nanoneedles (~ 450 nm long, < 45 nm wide). Also, Fuller (1944) reported the observation of crystal twinning in zinc oxide crystals.

In terms of laboratory synthesis, [Laudise and Ballman \(1960\)](#) reported the use of the hydrothermal route for synthesis of zincite (zinc oxide) crystals, while [Kröger \(1940\)](#) reported on photoluminescence in zinc oxide, pointing out that zinc oxide's UV characteristics were similar to zinc sulphide (ZnS) and cadmium sulphide (CdS).

2.1.1.2 1950 – 1970: Synthesis and Characterisation Research

By the 1950s, research interest in zinc oxide had gone beyond purification. Efforts were being devoted to acquire a deeper understanding of the behaviour of zinc oxide. Scientists were interested in unravelling the linkage and complexity behind zinc oxide's abilities such as its hiding power (ability to cover stains) when used in paints as well as other optical, physical and chemical abilities that made it indispensable in the paint and the tyre industries at that time ([New Jersey Zinc Company, 1940](#)). There was already an appreciable understanding of some of zinc oxide's properties; interest was in what then was tagged 'frontier properties of zinc oxide'. It is recorded that at the 1955 annual Symposium for Catalysis held in Russia, eight of the twelve papers presented were on zinc oxide, an attestation to the dominance of zinc oxide-related research during that era ([Brown, 1957](#)). Scientists were interested in its photochemical properties, n-type conductivity, photoconductivity, crystal structure, defects and associated phenomena ([Brown, 1957](#); [Heiland et al., 1959](#); [Huston, 1957](#)). A quick review of some of scientific publications dated within this period, shows that [Miller \(1951\)](#) published on the temperature dependence of conductivity in zinc oxide, proposing that interstitial Zn atoms in zinc oxide varied their charges based on temperature of measurement. Further investigations into temperature effects on carrier concentration in zinc oxide crystals, were performed by [Huston \(1957\)](#) involving measurements of Hall coefficient and electrical conductivity at temperatures between 55 - 300 K. Mollow was credited with the discovery of the possibility of incorporating hydrogen into zinc oxide to introduce imperfections into its crystal structure, thereby modifying its optical and semiconductor properties ([Brown, 1957](#); [Heiland et al., 1959](#); [Mollwo, and Schreiber, 1970](#)). Excitonic emissions, and refractive indices of zinc oxide at different temperatures, as well as the temperature dependence of band gap in zinc oxide were the subject of work by

Park and Schieder (1968). while Damen et al., (1966) studied Raman scattering in zinc oxide and reported observing double E₂ vibrations at 101 cm⁻¹ and 437 cm⁻¹; single transverse and a longitudinal A₁ vibrations at 381 cm⁻¹ and 574 cm⁻¹ respectively and finally single transverse and longitudinal E₁ vibrations at 407 cm⁻¹ and 583 cm⁻¹ respectively. Zinc oxide's pyroelectric properties were discussed by Heiland, and Ibach (1966), while Heiland and Kunstmann (1969) published details of the observation of polarity in zinc oxide crystals. Figure 2.1 shows a histogram showing the volume of publications involving zinc oxide recorded during the 1950 - 1970 era. Data presented in the chart was sourced from the Scopus database of peer-reviewed publications.

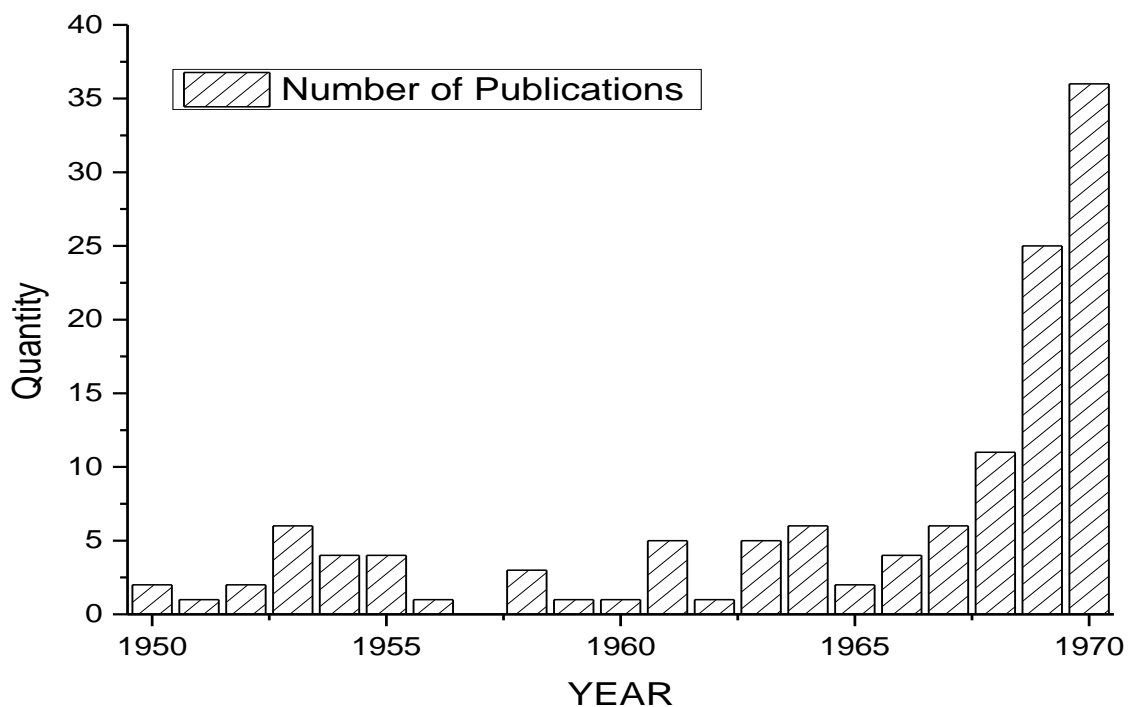


Figure 2.1: Publication volumes of zinc oxide research between 1950 and 1970.

N.B. *the absence of data for the year 1957, does not necessarily mean that no zinc oxide related publications were produced in the year 1957, rather it means that the Scopus database, which was the source of data used in the production of the histogram in Figure 2.1 contained no publication within the year 1957, that was picked up the terms of our search queries.*

2.1.1.3 1970 – 1990: Synthesis and Characterisation Research

Building on knowledge from previous decades, scientific investigations during this period revolved around applications that exploited the semiconductor properties of zinc oxide. In order to achieve this, a number of pre-existing synthesis methods were adapted for the production of high purity zinc oxide suitable for use in the fabrication of devices such as varistors and transducers (Tomura et al., 1972; Larson et al., 1972; Meaney, 2010). However, frustrations with inability to obtain stable and consistent p-type conductivity in zinc oxide dampened momentum along these lines (Willander, et al., 2010).

Some key developments reported during this era included: p-type conductivity in zinc oxide (Fan et al., 2013; Klingshirn, 2010; Willander et al., 2010); methods such as: radio frequency magnetron sputtering (Fahmy and Adler, 1972), vapour transport methods (Fan et al., 2013; Dodson and Savage, 1968; Piekarczyk et al., 1972), hydrolysis (Vogel and Nelson 1986), spray pyrolysis (Nobbs and Gillespie, 1970; Bahadur et al., 1986), hydrothermal synthesis (Croxall et al., 1974), ion beam deposition (Suzuki et al., 1988), were used to synthesise zinc oxide. This development was necessitated by the need for thin films and polycrystalline zinc oxide that covered large areas for use in electronic applications.

On the commercial side of things, this period witnessed a ‘fall from grace’ of zinc oxide as a major component in paints with titanium dioxide coming to the fore as a cheaper and better alternative (faster drying time) for white pigments (De Liedekerke, 2006). However, zinc oxide continued to be actively used in the rubber industry as an activator. Estimated global consumption of zinc oxide in 1990 was around 500,000 tonnes, with the rubber industry accounting for approximately 45 % of that amount (De Liedekerke, 2006; Moezzi et al., 2012).

Publications related to the synthesis and characterisation of zinc oxide during this era included investigations into the introduction of p- type conductivity in zinc oxide by doping with Li- and Cu- and other elements (Klingshirn, 1971; Klingshirn and Mollwo, 1972). There was an increased usage of vapour transport methods to grow epitaxial layers of zinc oxide and doped zinc oxide on sapphire (Schneck and Helbig, 1975; Helbig, 1972). Vogel and Nelson

(1986), described the synthesis of submicron zinc oxide phosphors via hydrolysis of zinc ethoxide mixed with ethanol. The use of a spray technique for obtaining improved adhesion of thin films of zinc oxide on substrates was demonstrated by Nobbs and Gillespie (1970), while Bahadur et al., (1986) reported the synthesis of zinc oxide thin films via spray pyrolysis of zinc nitrate tetrahydrate. Ion beam deposition of thin films of zinc oxide on Corning 7059 glass and the irradiation effects of particle bombardment were reported by Suzuki and co-workers (1988). Chemical vapour transport was used in the synthesis of zinc oxide crystals as described by Piekarczyk et al., (1972), with bromine and chlorine acting as carrier gases. While helium was used as carrier gas in the chemical vapour deposition of zinc oxide films on sapphire by Brady et al., (1973). Investigations into the occurrence of polarity in zinc oxide were discussed by Schulz, and Thiemann (1979) following on observations from Heiland and Kunstmann (1969). While results of investigations into the isoelectric point of zinc oxide in different media was published by Blok and De Bruyn (1970).

On a general note, it was observed that research activities relatively dipped or stagnated during this period in terms of year-on-year growth (Figure 2.2).

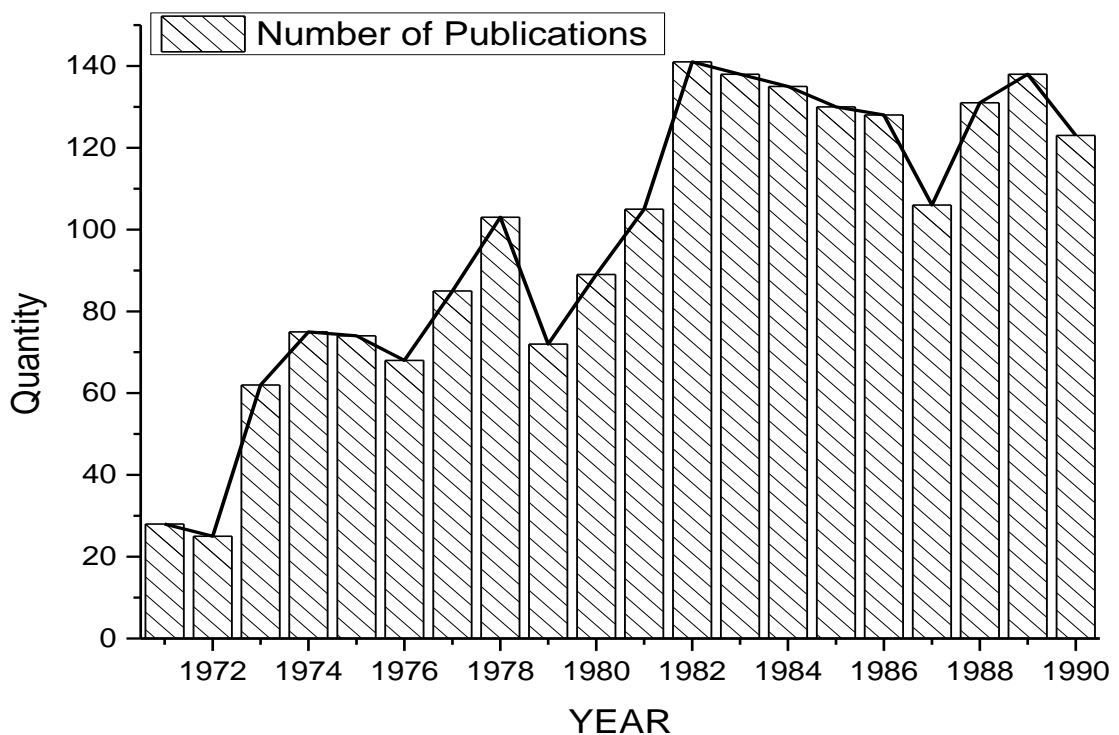


Figure 2.2: Publication volumes of zinc oxide research: 1970 to 1990.

2.1.1.4 1990 – Date: Synthesis and Characterisation Research

The mid 1990s witnessed a resurgence in zinc oxide related research. It is thought that the renaissance was due to successes achieved in commercialising other semiconductor materials with similar characteristics to zinc oxide (Fan, et al., 2013; Özgür, et al., 2005). Focus once again returned to exploiting zinc oxide's excellent optoelectronic properties. In addition to electronic devices, research into zinc oxide's usage in other applications such as gas sensing, lubrication, dye degradation, waste treatment, cancer treatment, and other medical applications began to become more pronounced (Battez, et al., 2008; Chan, et al., 2009; de Lacy Costello, et al., 2008; Liu, et al., 2011; Mitra, et al., 1998; Rasmussen, et al., 2010).

Generally speaking, research since the 1990s has concentrated on micro and nanoparticles of zinc oxide, and efforts have been made to compare the material's behaviour on the nanoscale with bulk behaviour (Kouhnavard, et al., 2014; Wang, 2009; Xu and Wang, 2011). Researchers have also been looking at the fabrication of ZnO-based devices such as: LEDs emitting a wide range of colours, nanogenerators, and solar cells (Willander, et al., 2010; Fan, et al., 2013). In addition, a number of hitherto unmentioned synthesis methods have also been employed in the production of zinc oxide with several publications detailing the effects of synthesis parameters on the characteristics of product materials (Arya, et al., 2012; Ji and Ye, 2008; Wang, 2004).

Another theme common to zinc oxide related research publications within this era was toxicology. Several research efforts were (and are still being) devoted to understanding the toxicity of zinc oxide especially nanoparticles of the materials to plants and animals (Heim, et al., 2015; Schilling, et al., 2010; Yang and Ma, 2014).

The number of publications on zinc oxide during this period mushroomed with the publication of more than 2000 research papers per annum according to Klingshirn et al., (2010); the bulk of research findings referred to in this thesis were conducted during this period, hence there will be no need for a summary review of publications dated to this period.

A search of the Scopus database of peer-reviewed literature for publications with zinc oxide in its title, abstract or keywords from the year 1946 was performed. Results showed a total of 66727 publications have been documented so far. It pertinent to note that the while the search results might not be all-inclusive, it represents a verifiable picture of documentation of zinc oxide related scientific research.

Shown in Table 2.1 is a breakdown of the types of peer-reviewed publications that comprised the 66,727 publications on zinc oxide from the year 1946 as compiled from a search of the Scopus database. While Figure 2.1 is a breakdown of the publication by annual publication volume, from 1946 till date.

Table 2.1: Breakdown of zinc oxide related publications from 1946 till date.

S/N	DOCUMENT TYPE	No. of Publications
1	Article	51,455
2	Conference Paper	12,491
3	Review	1,320
4	Article in Press* (08 May, 2015)	368
5	Letter	159
6	Short Survey	147
7	Note	110
8	Conference Review	56
9	Editorial	42
10	Book Chapter	14
11	Book	7
12	Report	2
13	Erratum	1
14	Undefined	555
	TOTAL	66,727

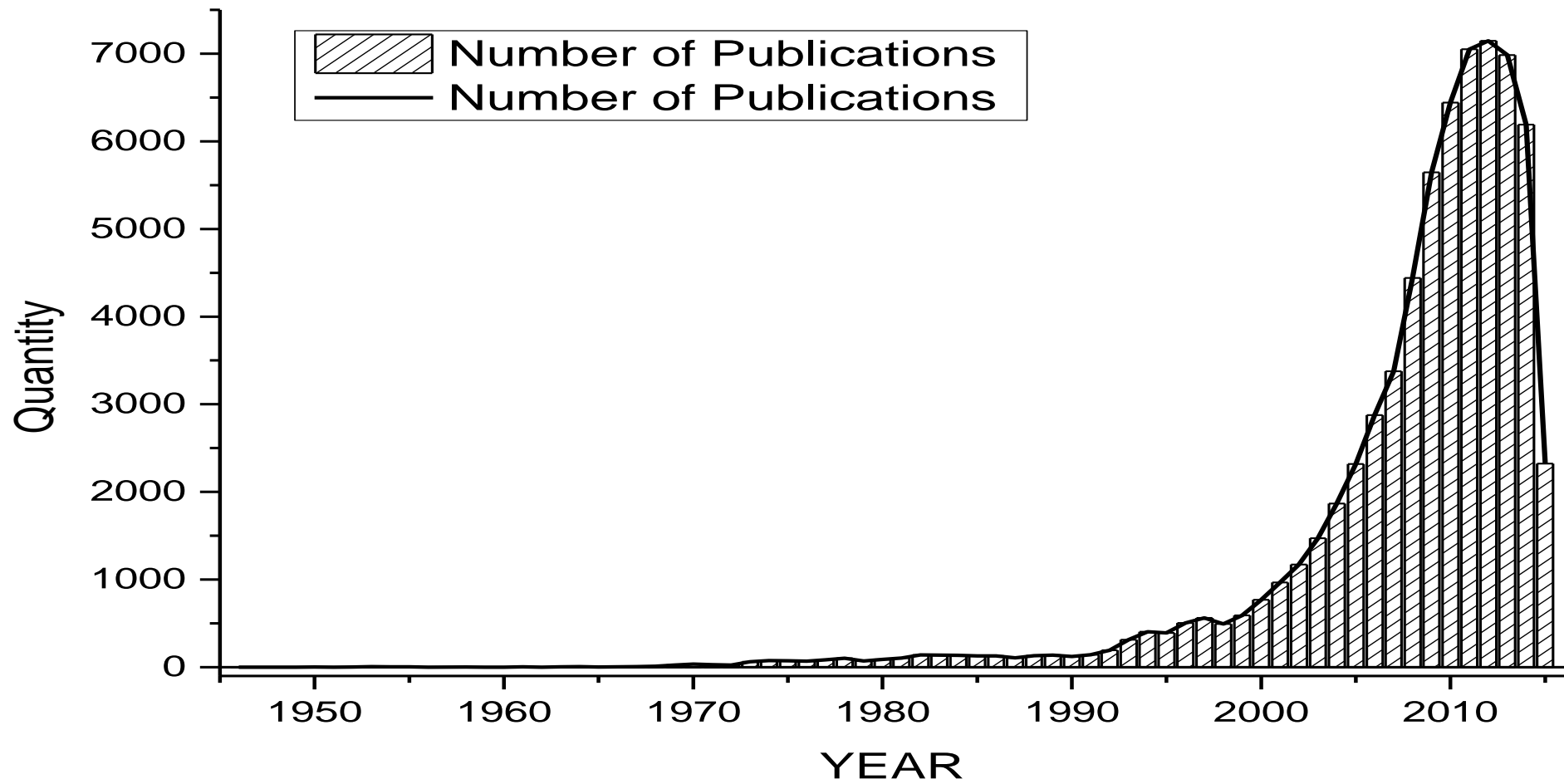


Figure 2.3: Annual number of zinc oxide related publication from the year 1946 till May, 2015

Presented in Table 2.2 is a list of some 'key' authors in the field of zinc oxide related research in terms of volume of publications. Data was obtained from a search of Scopus database of peer-reviewed literature for documents (Table 2.1) with zinc oxide in its title, abstract or keywords. Results have been truncated to show only authors with more than 100 publications.

Table 2.2: Authors with more than 100 zinc oxide related publications.

S/N	AUTHOR	No. of Pub	S/N	AUTHOR	No. of Pub
1	Wang, Z. L.	262	18	He, H.	117
2	Pearton, S. J.	206	19	Fan, X. W.	114
3	Grundmann, M.	192	20	Look, D. C.	113
4	Rusop, M.	179	21	Lu, Y. M.	112
5	Shen, D. Z.	229	22	Yao, T.	111
6	Norton, D. P.	177	23	Fortunato, E.	109
7	Sun, X. W.	161	24	Willander, M.	108
8	Ye, Z.	293	25	Yi, G.C.	107
9	Ren, F.	154	26	Chang, S. J.	107
10	Zhu, L. P.	149	27	Mamat, M. H.	107
11	Liu, Y. C.	144	28	Myoung, J. M.	107
12	Nur, O.	140	29	Nahm, C. W.	106
13	Zhao, D. X.	139	30	Yao, B.	105
14	Zhao, B. H.	136	31	Martins, R.	101
15	Lorenz, M.	135	32	Djurisic, A. B.	101
16	Haneda, H.	127	33	Cho, H.K.	100
17	Kawasaki, M.	119			

Table 2.3: Country ranking in terms of volume of zinc oxide related publications.

COUNTRY	Quantity	COUNTRY	Quantity	COUNTRY	Quantity
China	16609	Mexico	581	Slovenia	177
US	9552	Saudi Arabia	555	Argentina	169
South Korea	6126	Thailand	531	Slovakia	155
Japan	6030	Egypt	501	Hungary	141
India	5314	Netherlands	480	Morocco	134
Germany	3646	Portugal	436	Moldova	110
Taiwan	3441	Romania	435	Serbia	102
France	2284	Greece	382	Puerto Rico	95
UK	2026	Czech Republic	370	Indonesia	87
Spain	1314	Belgium	366	Chile	84
Iran	1212	Ukraine	316	Viet Nam	84
Malaysia	1105	South Africa	306	Colombia	78
Italy	1092	Pakistan	280	Croatia	78
Singapore	1019	Ireland	275	Iraq	72
Australia	1004	Denmark	244	Estonia	64
Russia	936	Algeria	238	Bangladesh	63
Turkey	855	Austria	237	Latvia	62
Canada	820	Norway	234	Jordan	56
Sweden	808	Israel	223	Nigeria	54
Hong Kong	772	Tunisia	222	Belarus	53
Brazil	746	Finland	203	Lithuania	51
Poland	727	Bulgaria	196	Oman	48
Switzerland	616	New Zealand	191	UAE	41

2.2 Synthesis of Zinc Oxide

It's fair to say that commercial synthesis of zinc oxide preceded its laboratory synthesis, considering the Romans started out making brass using zinc oxide albeit unwittingly. In some quarters, zinc oxide is even regarded as the first man made compound ([New Jersey Zinc Company, 1940](#); [Brown, 1957](#); [Habashi, 2001](#)). In modern times however, there are arguably three major routes to producing industrially significant quantities of zinc oxide namely:

- French (Indirect) route
- American (Direct) route
- Solution based routes

The first two are pyrometallurgical and also favourites ([Moezzi et al., 2012](#)).

2.2.1 The French (Indirect) Route for Production of Zinc Oxide

The French route also known as the indirect process for zinc oxide synthesis was the first commercial process designed for the commercial production of zinc oxide. It was developed in France around 1840 by E.J. Leclaire and first patented in the US on 7th May, 1850, by Leclaire and Barruel ([Brown, 1957](#); [Leclaire and Barruel, 1850](#); [Moezzi et al., 2012](#)).

According to the text of Leclaire's 1850 patent, the French process of manufacturing zinc oxide involves loading zinc ingots into a furnace (i.e. zinc metal is the raw material) where it is heated till it melts and vaporises; zinc metal has a melting point of 420 °C and a boiling point of 907 °C. The vaporised metal is then exposed to air which rapidly oxidizes it to form zinc white (zinc oxide). The product particles are then channelled through a cooling chamber before they are trapped and collected in a bag house. The patent goes on to further describe mechanisms for ensuring purity and easy recovery of the zinc oxide products ([Leclaire and Barruel, 1850](#); [Moezzi et al., 2012](#)).

In theory, 2.245 kg of zinc oxide can be produced per kg of zinc metal feedstock, however, in practice the yield is only about 2.20 kg zinc oxide / kg of zinc metal feedstock. Also, the purity of the product zinc oxide is also dependent on the purity of the zinc metal feedstock such that to synthesise pharmaceutical grade zinc oxide via the indirect route, the feedstock has to be

special high grade (99.99 % Zn) zinc metal (Moezzi, et al., 2012). Figure 2.6 is a process flowsheet of the French (indirect) process for making zinc oxide according to Leclaire's patent.

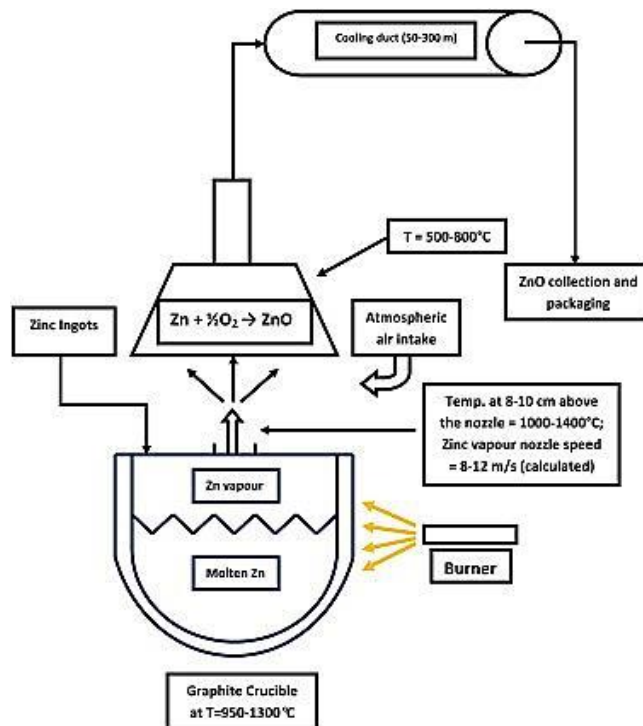


Figure 2.4: Flowsheet of the French (Indirect) process (Moezzi et al., 2012).

There have been several modifications to the process described in Leclaire's patent. For instance, Norzinco GmbH manufactures zinc oxide using a modified French process called the New Jersey method (after New Jersey Zinc Company). The modification involves fractionally distilling the vaporised zinc metal before it is contacted with air to form zinc oxide. This modification allows for very pure zinc oxide to be obtained from relatively impure zinc metal feedstock (Norzinco, 2015). Other process upgrades include the use of conveyor belts to feed in the raw material, feeding the zinc as a liquid as opposed to loading an ingot, the use of gas fired or electrically heated furnaces, (Moezzi et al., 2012).

2.2.2 The American or Direct Process for Production of Zinc Oxide

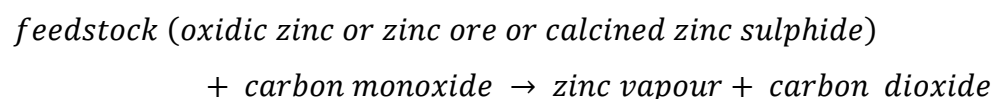
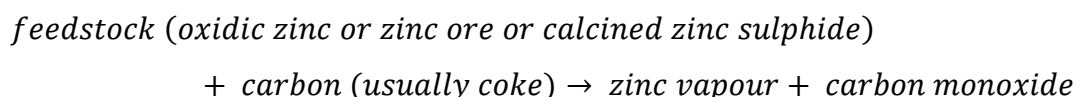
The American synthesis process was developed about a decade after the advent of Leclaire's French process by Wetherill and Jones at the New Jersey Zinc Company, based upon the discovery by Burrows from the adjacent Passaic Chemical Company of white fumes of zinc emanating from a mixture of zinc ore and coal which was he had tossed unto a furnace grate accidentally (Ball, 2012; Brown, 1957; De Liedekerke, 2006; New Jersey Zinc Company, 1940).

This process of manufacture involves reduction-oxidation (redox) reactions. In contrast to the French process which have pure zinc metal as its feedstock, the America process has the flexibility of being able to accommodate a variety of materials as its feedstock such as zinc containing compounds and zinc mineral ores (which could contain multiple elements as impurities), dross, furnace slag, or off-grade zinc oxide (De Liedekerke, 2006; Moezzi et al., 2012).

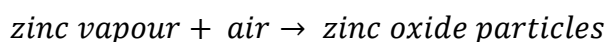
The American or direct synthesis process starts with the carbothermal reduction of the raw material to zinc metal. This is achieved by mixing the feedstock with a graphitic carbon source (normally coke or coal) before heating it up. The generation of CO₂ / CO mixture from the carbon source reduces the feed stock to zinc metal, which then proceeds to melt and vaporise as temperature rises. The zinc vapour produced is then fed into an oxidising chamber where is turned to zinc oxide particles and the particles collected in a fashion similar to the French process (IZA, 2011; Moezzi et al., 2011).

The following general equations summarize the chemistry that typify the American (direct) process (De Liedekerke 2006).

Stage 1: Reduction of Feedstock to Zinc Metal



Stage 2: Re-oxidation of Zinc Vapour to Zinc Oxide



In addition to the generation of zinc vapour, side reactions occur which are vital to maintaining the continuity of the reduction process namely:

- The combustion of the coke to carbon dioxide
- The Boudouard reaction

The combination of both reactions generates the necessary CO/CO₂ atmosphere in the furnace that promotes the production of zinc vapour and inhibits its re-oxidation back to zinc oxide while in the furnace.

Because multiple feedstock usually containing high amounts and a variety of impurities is used in the American process, its products are usually not as pure as those from the French process and as such is usually not suitable for pharmaceutical, cosmetic and research applications, but can be used in paint and rubber applications, furthermore, the relative lack of control over product properties such as surface area, also serve as a disadvantage to the American process. However, the American process has a lower energy demand in comparison to the French process (IZA, 2011; Moezzi et al., 2011).

On a general note the French process (and modifications) is responsible for the bulk of global zinc oxide production accounting for more than 75 % of supply. 10 – 20 % of global supply of zinc oxide is produced using the American process, while solution based routes account for ~2 % of global zinc oxide production (De Liedekerke, 2006).

2.2.3 Solution Based Synthesis of Zinc Oxide

In addition to the foregoing pyrometallurgical methods for producing zinc oxide, a number of hydrometallurgical processes have been also exploited on a commercial scale. The attractiveness of these routes hinges on lower energy requirements, as well as yield of products with a greater surface area than the former. Usually powders obtained via hydrometallurgical routes have specific surface area greater than $20 \text{ m}^2\text{g}^{-1}$ as shown in Table 2.4 (De Liedekerke, 2006; IZA, 2011).

Some of the methods that fall under this category include:

Spray pyrolysis of zinc acetate, zinc formate, zinc carboxylate, zinc nitrate or zinc sulphate. Here, the zinc salt is dissolved and sprayed from an atomizer into a heated chamber where the salt is thermally decomposed into zinc oxide (De Liedekerke, 2006; Moezzi et al., 2011).

Zinc oxide is also produced as a by-product in the synthesis of sodium hydrosulphite which is a key chemical used as a bleaching agent in the textile and paper industry. In this process, zinc hydrosulphite is first synthesised after which it is then reacted with sodium hydroxide or sodium carbonate to yield zinc oxide or basic zinc carbonate. The zinc carbonate can be converted to zinc oxide by further alkali treatment, or via calcination (IZA, 2011; Moezzi et al., 2011).

Ammonium chloride or ammonium carbonate leaching of zinc oxide ore followed by calcination to recover zinc oxide is also another method that has been commercially explored for the synthesis of zinc oxide (De Liedekerke, 2006; IZA, 2011; Moezzi et al., 2011).

2.2.4 Grading Zinc Oxide

Commercially, zinc oxide is graded according to its level of purity and the surface area of the product particles. However, there are a number of variations across the globe; some of the standards employed in grading zinc oxide include: ASTM D79, BS 254, DAB 8, T 31 006 NF, and ISO R 275 (De Liedekerke, 2006). Therefore, the rule of thumb in ascertaining the quality of any commercially sourced zinc oxide powder is to consult its accompanying materials safety and data sheet (MSDS) which should have percentage

composition of impurities e.g. lead, sulphur, and cadmium. Table 2.4 adapted from Moezzi et al., (2012) shows common quality grades of zinc oxide and their specifications.

Table 2.4: Grades of commercial zinc oxide.

S/N	ZnO Grade	Nominal purity [%]	Specific surface area [m ² g ⁻¹]	Production process
1	Gold Seal	99.995	4–7	French Process
2	Pharma Grade	99.8–99.9	3–9	French Process
3	White Seal	99.8	3–5	French Process
4	Green Seal	99.6–99.7	4–10	French Process
5	Red Seal	99.5	3–5	French Process
6	American Grade	98.5–99.5	Max. 3	American Process
7	Active Grade	93–98	Min. 30	Wet process
8	Feed Grade	90–99	–	Various

2.2.5 ‘Non-Commercial’ Synthesis Methods for Zinc Oxide

There are many other methods through which zinc oxide could be manufactured. Some of them include pulse laser deposition (Divoska, 2011), molecular-beam epitaxy (Heo et al., 2002), wet chemical synthesis routes (Chen and Gao, 2006; Gong et al., 2010; Jalal et al., 2010), chemical vapour deposition (d’Abaddie et al., 2010; Huang et al., 200; Park et al., 2002; Yuan and Zhang, 2004), hydrothermal routes (Guo et al., 2010; Nishizawa et al., 1984; Li et al., 1998; Lu and Yeh, 1999; Suchanek and Riman, 2006; Xu et al., 2002), etc. Of the foregoing, solution based routes are highly favoured for particle synthesis (Baruah and Dutta, 2009a; Wang, 2004).

These methods can be classified according to the state involved in the process:

- Vapour –liquid-solid / vapour – solid methods
- Solution-liquid-solid / solution – solid methods
- Solid state reaction methods

In using the term ‘non-commercial’, it is not implied that these methods have no commercial viability or cannot be used to produce zinc oxide on a large scale. The term ‘non-commercial’ is used as a way of indicating that the methods under this classification do not currently enjoy as much industrial patronage as the synthesis routes reviewed in sections 2.3.1 – 2.3.3.

Table 2.5 lists out some of the methods that have been reportedly used in the synthesis of zinc oxide,

Table 2.5: Methods that have been used in the synthesis of zinc oxide.

Synthesis Method	Source Publication
Metal-organic vapour phase epitaxy	Park et al., 2002
Hydrothermal discharging-gas	Li et al., 1999
Cathodically induced sol-gel deposition	Ozturk et al., 2011
Pulsed laser deposition	Divoska et al., 2011
Microwave assisted synthesis	Hamedani et al., 2011; Kajbafvala et al., 2009; Cho et al., 2009
Solvothermal synthesis	Chen et al., 2010; Wang et al., 2011; Yin et al., 2013
Mechanochemical synthesis	Lu et al., 2008; Vojisavljevi et al., 2008; Xu et al., 2002
Ultra sound assisted synthesis	Alammar and Mudring, 2009
RF Sputtering	Fahmy and Adler, 1972
Spray pyrolysis	Nobbs and Gillespie, 1970; Bahadur et al., 1986
Ion beam deposition	Suzuki et al., 1988
Chemical vapour transport (CVT)	Piekarczyk et al., 1972; Dodson and Savage, 1968

Synthesis Method	Source Publication
Electrochemical growth	Illy et al., 2005
Precipitation from solution	Pawar et al., 2011
Sol-gel synthesis	Xu and Wang, 2011 ; Wallace et al., 2013
Chemical bath deposition	Cao and Cai, 2008
Hydrothermal synthesis	Cheng and Samulski, 2004 ; Wang et al., 2007 ; Gao et al., 2004 ; Look, 2007
Sonochemical synthesis	Ghosh et al., 2014
Hydrolysis	McBride et al., 2003
Electrospinning	Zhao et al., 2010
Chemical deposition	Mitra et al., 1998
Room temperature synthesis	Perales-Perez et al., 2004 ; Zhang et al., 2011
Hydrothermal continuous flow	Li et al., 2011
Green Chemistry	Gong et al., 2010
Wet chemical synthesis	Chen and Gao, 2006 ; Wang et al., 2010
Hydrometallurgical synthesis	Liao et al., 2012
Thermal decomposition	Pushpanathan and Kumar, 2010
Template assisted solution growth	Cho and Lee, 2012
Thermal evaporation	Umar and Hahn, 2006
Emulsion	Kołodziejczak-Radzimska and Jesionowski, 2014

2.2.6 Hydrothermal Synthesis of Zinc Oxide

Hydrothermal synthesis is essentially a solution-based crystal growth technique that employs elevated temperatures and pressures to drive crystallisation in a sealed environment (Yoshimura and Byrappa, 2007).

Hydrothermal pressures are usually autogenous. Figure 2.5 shows the vapour pressure of water as a function of temperature and pressure.

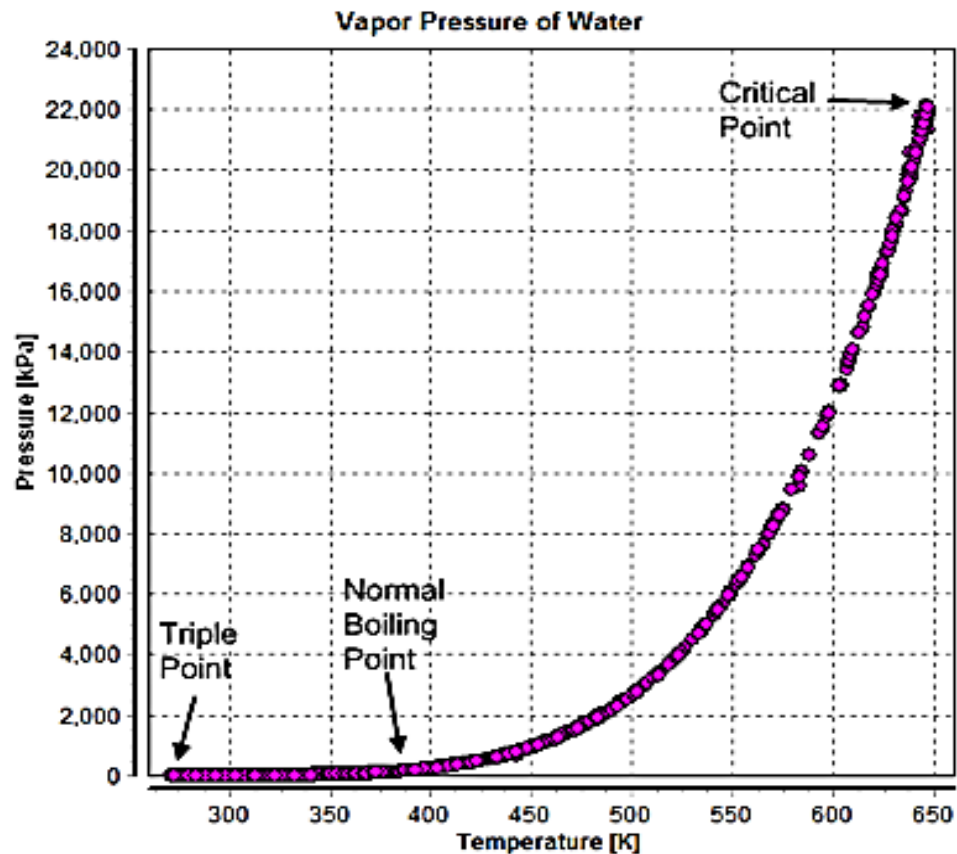


Figure 2.5: Vapour pressure of water as a function of temperature; obtained from the Dortmund Data Bank (DDB, 2014).

Evolution of Hydrothermal Synthesis

The usage of processes that fit into the description of hydrothermal synthesis date back to around 1850 with reports of geologists trying to recreate natural hydrothermal phenomena in the laboratory, having established a link between the hydrothermal conditions that occur underground and the production of many minerals (Morey, 1953; Yoshimura and Byrappa, 2007). The phrase 'hydrothermal' is credited to Sir Roderick Murchinson, and the first reports of

hydrothermal synthesis of a material was by Schafthaul, K.F.E, who described production of quartz crystal from silicic acid using a Papin's digester (Yoshimura and Byrappa, 2007).

Other landmarks in the evolution of hydrothermal synthesis include:

- The use of glass tubes sealed into steel tubes by French mineralogist H. De Senarmont around the 1850s forming a precedent for the modern day autoclave design,
- The hydrothermal synthesis of artificial diamonds by Hannay in 1880,
- The isolation of aluminium from bauxite by K. J. Bayer in 1908 (Yoshimura and Byrappa, 2007).

Early hydrothermal processes involved relatively high temperatures and pressure leading many researchers to limit exploration of its usage to mainly processes requiring supercritical conditions. However, it is now known, that hydrothermal synthesis can be performed at temperatures and pressures lower than 100 °C and 1.5 MPa respectively (Suchanek and Riman, 2006).

Over the years, hydrothermal synthesis equipment have evolved from high temperature, high pressure reactions into relatively low temperatures and pressure reactions (Morey, 1952), and the future of hydrothermal processes appears to be heading towards green chemistry (usage of biomaterials and organic solvents), multi-energy processing technology, design of purpose-built reactors incorporating multi-energy processing and kinetic stimulation of reactions (Guo et al., 2011; Yoshimura and Byrappa, 2007).

Modifications / Hybrids of Hydrothermal Synthesis

Although the word 'hydrothermal' connotes an aqueous environment, hydrothermal synthesis embodies the usage of non-aqueous solvents, and the term 'hydrothermal synthesis' could be used to refer to a range of processes. For instance, the term could be used to refer to pressurised wet chemical synthesis processes where other solvents have been used (also called solvothermal synthesis). Various other modifications or variants of the hydrothermal process exist (Table 2.6). Modifications are usually introduced to alter reaction kinetics, enable usage of specific reagents or for measurement purposes (Suchanek and Riman, 2006).

Table 2.6: Some hybrids of the hydrothermal technique (Suchanek and Riman, 2006; Yoshimura and Byrappa, 2007).

Name	Modification
Solvothermal synthesis	Involves the substitution of water with organic or inorganic solvents (e.g. ethanol)
Microwave-Hydrothermal synthesis	Microwave energy is used with or without the inclusion of direct reactor heating
Hydrothermal-Electrochemical synthesis	Electrochemistry is performed under hydrothermal conditions
Hydrothermal-Sonochemical synthesis	Ultrasonication is used in synthesis process occurring under hydrothermal conditions
Hydrothermal-Photochemical synthesis	hydrothermal synthesis combined with optical radiation
Green chemistry	Usage of relatively low temperatures, biological (or environmentally friendly) materials or substrates and organic solvents
Mechanochemical-Hydrothermal synthesis	Wet milling of reactant is used in conjunction with hydrothermal synthesis
Hydrothermal hot pressing	Hydrothermal conditions is combined with hot pressing

2.2.7 Advantages and Disadvantages of the Hydrothermal Technique

Some of the advantages that hydrothermal synthesis has over other processes include ease of setup and usage, relatively high reproducibility, low energy consumption (as it usually involves relatively low heating temperatures) and ease of scale up (Baruah and Dutta, 2009).

The hydrothermal synthesis method could be easily adapted to synthesise a large variety of products, and it has been reportedly used in the synthesis of other commercially significant materials such as zeolites, quartz, GaPO₄, GaN, langsite and non-oxides such as carbon nanotubes, diamonds and nanocomposites (Dem'yanets et al., 2008; Suchanek and Riman, 2006). This is especially advantageous to industries that need to produce multiple products on a scale that does not require the use of a dedicated production line.

Hydrothermal synthesis of ZnO involves hydrolysis and dehydration reactions that could be influenced by the nature, strength and adsorption characteristics of the ions involved in the process (Baruah and Dutta, 2009; Wang, 2004). This sensitivity results in the possibility of engineering particles with different characteristics by manipulating synthesis parameters (temperature, stirring and heating regimes, pH, concentration of reactants) a wide range of particle morphologies have been reported for zinc oxide (Wang, 2004; Suwanboon et al., 2014; Kumar et al., 2012).

Also, it has been reported that zinc oxide particles produced via hydrothermal route possessed better UV absorption power and purity (Suchanek, 2009).

Hydrothermal synthesis also provides the flexibility of morphology and size tuning (Baruah and Dutta, 2009; Moulahi and Sediri, 2014; Ma et al., 2005; Kuo et al., 2005; Wang, 2004). ZnO crystals of different size ranges have been produced via hydrothermal synthesis. Particle sizes ranging from about 9 nm (Sue, et al., 2004), up to single particle of dimensions 50 mm by 50 mm by 15 mm (Ohshima, et al., 2004), have been reported in literature.

Furthermore, hydrothermal synthesis is quite a robust synthesis route, in that it can be used for both one pot 'batch process type' synthesis where the reactants are charged into the hydrothermal vessel and heated up (Bitenc et al., 2010; Ohshima et al., 2004), as well as flow 'continuous process' type of

synthesis (Sue, et al., 2004). The technique also supports a wide range of growth control additives (Kuo, et al. 2005; Liu, et al., 2011; Moulahi and Sediri, 2013) as well as the use of substrates (Jung, et al., 2012).

The hydrothermal technique can be used to synthesise undoped n-type ZnO particles as well as doped ZnO particles (Fan, et al., 2013; Jung, et al., 2012; Wang, et al., 2007; Zuo, et al., 2011). The procedure has been used in the synthesis of p-doped ZnO nanorods by Duan, et al, (2013). They reported a two-step process involving a seed generation step where zinc salt dissolved in ethanol was spincoated onto a glass substrate, while the second step involve hydrothermal synthesis to generate Ag–N dual-doped p-type ZnO rods which coalesced into a film.

Fang and co-workers have also reported the synthesis of ZnO p-n homojunctions via the hydrothermal technique. They grew p-type ZnO nanorods from zinc acetate dihydrate ($\text{Zn}(\text{Ac})_2 \cdot 2\text{H}_2\text{O}$) and ammonium dihydrogen phosphate ($\text{NH}_4\text{H}_2\text{PO}_4$) on a substrate made of Silicon coated with n-type ZnO film via magnetron sputtering (Fang, et al., 2009).

Other advantages that have been associated with the use of the hydrothermal technique for particle synthesis include:

- Ease of automation of raw material charging, transportation, mixing and recovery of products (mainly because hydrothermal synthesis usually involves the use of solvent and solutions which can be transported in the liquid state)
- Most hydrothermal processes are run on a batch or semi-batch basis with interest in only recovering the final products, the cost of process control and instrumentation is relatively lower

(Dem'yanets, et al. 2008; Suchanek and Riman, 2006; Yoshimura and Byrappa, 2007).

Disadvantages associated with hydrothermal synthesis include; little or no opportunity for direct observation of reaction kinetics because it occurs in a sealed environment (i.e. covered up pressurized reactor). Nanoproducts could also exhibit 1-D functionality (Suchanek and Riman, 2006).

2.2.8 Factors that Could Influence Hydrothermal Growth of Zinc Oxide

The simplicity of hydrothermal synthesis makes it possible to easily pinpoint the major factors that drive the course of particle growth. In the case of zinc oxide synthesis, a survey of literature has indicated that the following parameters could be modified during hydrothermal synthesis to control the properties of ZnO product crystals (Chen and Gao, 2006; Elen, et al., 2009; Li, et al., 1999; Lu and Yeh, 2000; Meulenkamp, 1998; Suchanek and Riman 2006):

- Temperature
- Concentration
- Heating regime
- Substrate
- Growth additives
- Precursor type
- Stirring
- Base species
- Reaction duration
- pH

2.3 Properties and Applications of Zinc Oxide

2.3.1 Properties

Zinc oxide is located in the group II-VI oxide semiconductor materials. It possesses similar properties to oxides of titanium, gallium, cadmium, and indium. Zinc oxide is considered a unique material in that it exhibits multiple semiconducting, piezoelectric, pyroelectric, antibacterial and bio-compatible properties (Wang, 2004).

2.3.1.1 Physical Properties of Zinc Oxide

Physical properties: Colour

Bulk zinc oxide nano- / micro powder is commonly reported to have a milky white pigmentation. However, it has also been noted for a long time, that zinc oxide possessed thermochromic properties in that when it is heated, it could reversibly change colour from milky white to canary yellow at around 300°C (Brown, 1957). This phenomenon is observed to occur due to changes in ZnO's crystal lattice occasioned by heat induced exit of oxygen atoms (Zhang, 1996).

Pure single crystals of zinc oxide are colourless; however, incorporation of impurities and dopants could result in crystals with different colouration and hues (Maeda et al., 2005; Morkoç and Özgür, 2009); for instance, transparent crystals with pale yellow hue were reported by (Ohshima, 2004). Figure 2.6 shows zinc oxide powder obtained from different sources:

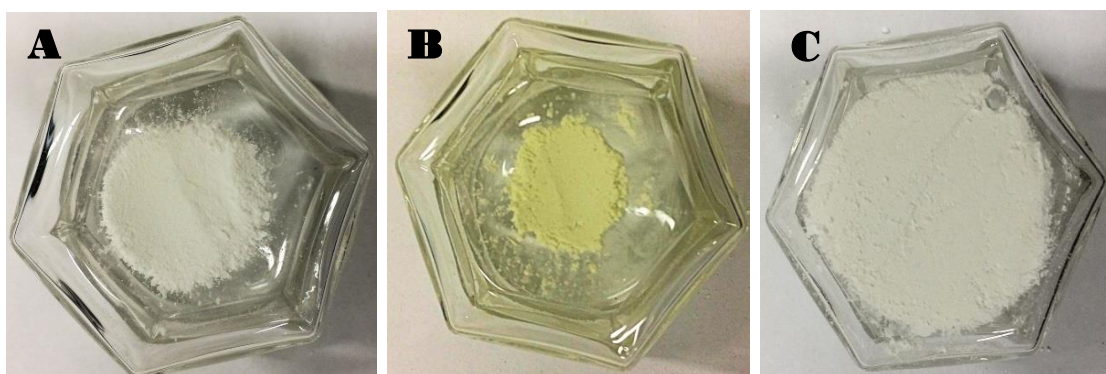


Figure 2.6: Zinc oxide powder from (a) zinc acetate dihydrate and sodium hydroxide (b) zinc acetate dihydrate and ammonium hydroxide (c) commercially source (Aldrich, 99.99% trace metal basis).

Physical properties: Morphology

Zinc oxide has the ability to grow into a variety of particle shapes. This has created the possibility of engineering zinc oxide particles for shape-specific applications e.g. drug delivery, catalysis, solar applications, and sensors (Baruah and Dutta, 2009; Elias, et al., 2010; Kajbafvala, et al., 2010; Kuo, et al., 2005, Wang, 2004; Zhang, et al., 2003). Some of the morphologies that have been reported for zinc oxide are presented in Table 2.7

Table 2.7: Reported particle morphologies for zinc oxide.

Particle Shape	Source Publication
Nanorods	Wang et al., 2011, Sun et al., 2002
Microrods	Kuo et al., 2005; Yan et al., 2008
Nanobelts	He et al., 2009; Hu et al., 2007
Dumbbell-shaped	Liu et al., 2011
Narcis-like	Kajbafvala et al., 2010
Thin films	Öztürk et al., 2011
Nanoshperes	Tay et al., 2007; Xie and Wu, 2010
Nanoflakes	Ghosh et al., 2014; Duan et al., 2006
Nanoneedles	Cho et al., 2009
Nanoplates	Cao and Cai, 2008; Cao et al., 2008; Illy et al., 2005
Nanotubes	Cheng and Chen, 2009; Duan et al., 2006; Seo et al., 2007; Yang et al., 2009; Wang et al., 2007
Mesocrystalline Disks	Yan et al., 2009
Tetrapods	Li et al., 2011
Octahedron	Zheng et al., 2009
Multipods	Wang and Gao, 2004
Microcapsules	Lipowsky et al., 2007

Microspheres	Kuo et al., 2005; Yan et al., 2009
Star-like	McBride et al., 2013
Micro and nanosheets	Kuo et al., 2005; Hosono et al., 2005
Pagoda	Yao et al., 2012
Platelets	Mondal et al., 2013; Mo et al., 2008
Nanowires	Pradel et al., 2013; Sun et al., 2006
Bipyramids	Wang et al., 2011
Nanosprings	Wang, 2004
Flower-like	Zhang et al., 2003; Xie et al., 2009; Li et al., 2011
Double microrods	Bamiduro et al., 2012; Singh et al., 2015;
Spindles	Pawar et al., 2011
Rotor-like	Gao, et al., 2009
Nanowhiskers	Xie et al., 2009
Bipods	Bitenc et al., 2010; Jang et al., 2011
Tetrapods	Dai et al., 2002
Turriform	Zhang et al., 2013
Quantum dots	Liu et al., 2011
Castellated	Zhang et al., 2013
Nanograss	Zhu et al, 2013
Nanorings	Ma et al, 2008
Micro & nano Disks	Peng et al., 2006; Xu et al., 2004
Nanocombs	Wang et al., 2006
Equiaxed	Lu and Zhao, 2010
Star shaped	Li et al., 2011
Nanotips	Wang et al., 2010
Chestnut-like	Wang, et al., 2010b

Furthermore, superstructures such as nanowire arrays, microtubules, nanopropellers and hollow urchin-like structures formed from the assemblage of zinc oxide primary particles have also been reported (Elias, et al., 2010; Kuo et al., 2005; Mo et al., 2008; Ozgur, 2005; Wang, 2004). Solution based synthesis has been identified as one of the preferred routes for the production of materials with multiple morphologies as well as for size and shape tuning of zinc oxide particles (Baruah and Dutta, 2009a; Pearton et al. 2005).

Factors that have been observed to influence the shape of zinc oxide particles during synthesis include: reaction duration, pressure, reactant concentration, method of synthesis, type of solvents, Length of precursor ageing, additives, mixing regime, stirring speed, sequence of reactant addition, substrates, and capping agents (d' Abaddie et al., 2010; Kanade et al., 2006; Ma et al., 2008; Polsongram et al., 2008; Shojaee et al., 2010; Sunwanboon et al., 2013, Xie et al., 2009; Yang and Xiang, 2013).

With respect to the hydrothermal synthesis of zinc oxide; research has shown that particle shape could be dependent on a wide variety of synthesis variables such as: pH (Baruah and Duttah, 2009b; Samaele et al., 2010), type of precursor used (Lin and Jinag, 2011), etc. (Pal et al., 2006). The effect of reaction solvent on particle morphology was investigated by Cheng and Samulski, (2004) using solutions made by dissolving of zinc acetate dihydrate and sodium hydroxide in methanol and ethanol to act as sources of Zn^{2+} ions and OH^- ions respectively. They reported that zinc oxide particle shape was influenced by the type of solvent used.

Zinc oxide appears to have a relatively high sensitivity in terms of shape dependence on synthesis conditions, as there are a plethora of ways through which its particle shape could be influenced during the course of synthesis. Although this might be good news in terms of increased avenues to engineer zinc oxide particle 'to taste', it could introduce challenges with respect product uniformity and batch variation which could impact negatively on the scale up potentials of some synthesis routes for commercial purposes. Figure 2.7 shows examples of different types of particle shapes for zinc oxide obtained in the course of research investigations detailed in this PhD thesis.

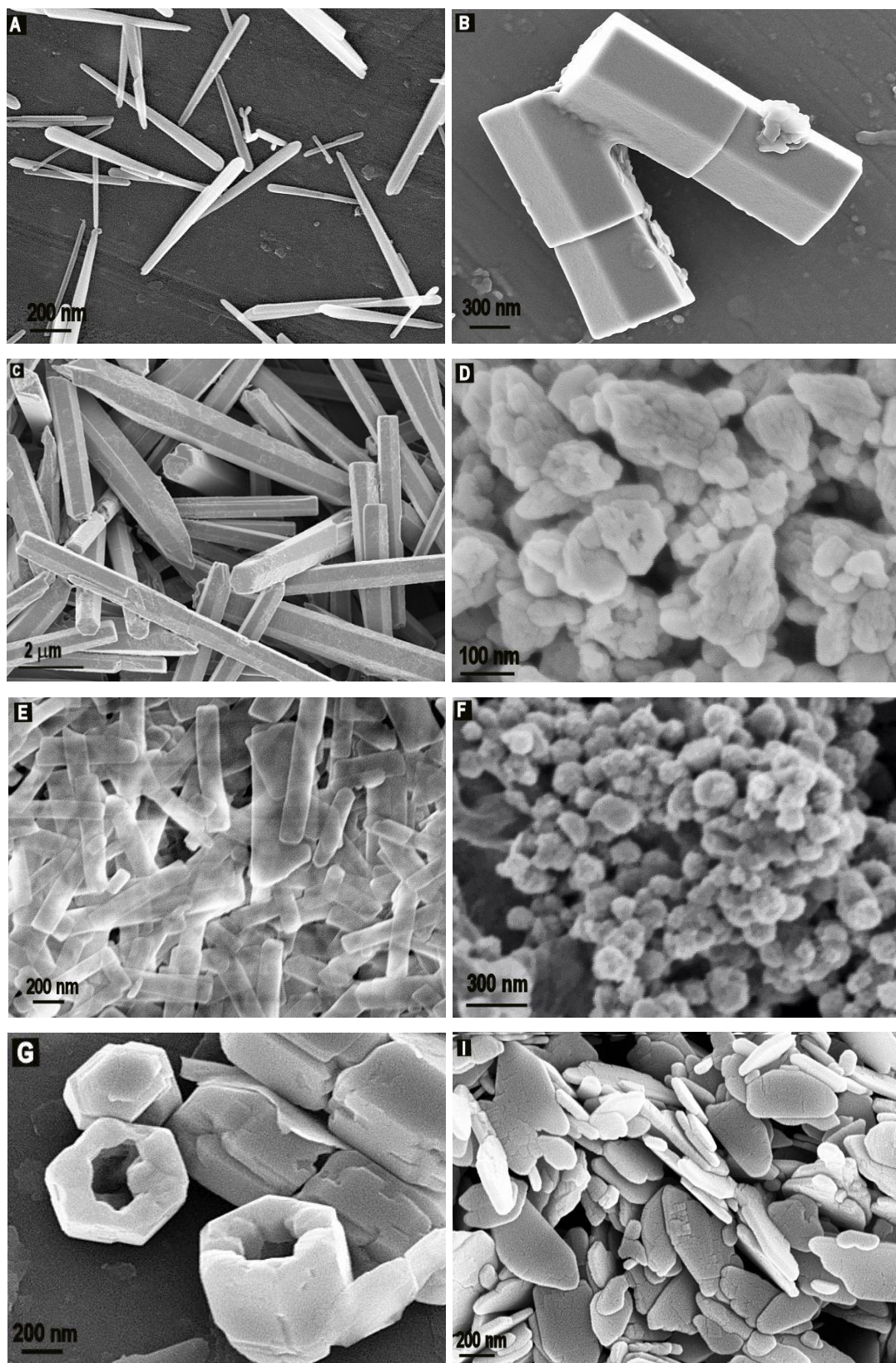


Figure 2.7: Morphologies of zinc oxide: (a) Nanowires (b) double rods (c) elongated microrods (d) irregular nanoparticles (e) nanolathes (f) spherical nanoparticles (g) hollow rods (i) nanoflakes (see chapter 4 & 5 for details).

2.3.1.2 Chemical Properties of Zinc Oxide

Zinc is known to have two oxidation states +1 and + 2, with the latter being the most common; although, there recently have been arguments about the possibility of the existence of a third (+ 3) oxidation state (Scholder et al., 2012, Samantha and Jenas, 2012).

Bulk zinc oxide, is sparingly soluble in water at neutral conditions ($\sim 5 \text{ mg L}^{-1}$). However, nanoparticles of zinc oxide have been shown to have increased solubility in water at neutral pH values, and several factors such as size, crystallinity, and shape could affect its solubility rates (Zhao et al., 2012; Mistra et al., 2012). Solubility values of $7.18\text{--}7.40 \text{ mg L}^{-1}$ were reported for nanoparticles of zinc oxide pure water at pH of 7.3 (Reed et al., 2012), while zinc oxide's solubility at temperatures between $150 \text{ }^\circ\text{C}$ and $350 \text{ }^\circ\text{C}$ have been documented (Bénézech et al., 2002). Table 2.8 outlines other chemical properties at room temperature and pressure (except otherwise indicated).

Table 2.8: Chemical properties of zinc oxide (Klingshirn, 2007).

CHEMICAL PROPERTY	VALUES
Flammability	Not flammable
Mol. Weight [g mol^{-1}]	82.39
Density [g cm^{-3}]	5.605
Melting Point [$^\circ\text{C}$]	1975; Sublimes @ $T > 1200 \text{ }^\circ\text{C}$
Heat Capacity [$\text{J mol}^{-1}\text{K}^{-1}$]	40.3
Enthalpy of Formation [kJ mol^{-1}]	-348
Vapour Pressure (@ $1500 \text{ }^\circ\text{C}$) [mmHg]	12
Entropy [$\text{J mol}^{-1}\text{K}^{-1}$]	43.7
Isoelectric Point	8.7 – 10.5
Thermal Expansion [10^{-6} K^{-1}]	6.5 // a & 3.7 // c
Thermal Conductivity [$\text{W m}^{-1}\text{K}^{-1}$ at 300 K]	30
Transparent Wavelength [μm]	0.4 ~ 0.6

2.3.1.3 Crystal Structure and Properties of Zinc Oxide

Zinc oxide is known generally to crystallize with the hexagonal wurtzite crystal structure at ambient temperatures and pressures. The occurrence of a reversible phase transition from a hexagonal wurtzite crystal structure to a cubic crystal structure at elevated pressures (> 10 GPa) has been reported (Özgür et al., 2005). In another case, the cubic phase was found to remain metastable for considerable periods even when pressure was reduced (Özgür et al., 2005).

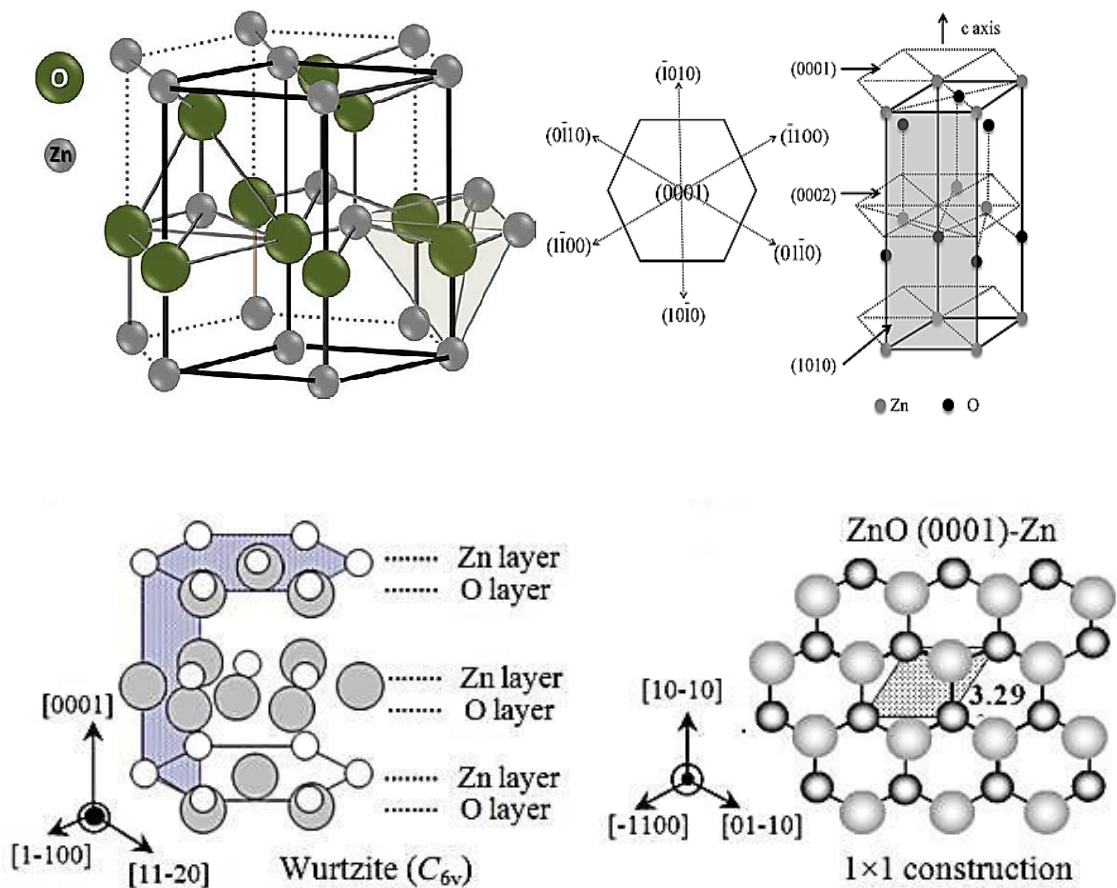


Figure 2.8: Zinc oxide wurtzite structure showing arrangement of Zn and O atoms (Amin, 2012; Matsui and Tabata, 2010).

Planes of wurtzite zinc oxide comprising of tetrahedrally coordinated groups of O^{2-} and Zn^{2+} ions with a unit cell of 4 atoms, which are stacked alternately in the $\langle 0001 \rangle$ direction (Figure 2.6) as a result, the ZnO structure has a polar (0001), surface which could either terminate in a Zn^{2+} rich layer thus making it partially positive or in an O^{2-} rich layer resulting in a partially negative polarity. It

also has non-polar surfaces (1120) and (1010) possessing an equal number of both atoms (Coleman and Jagadish, 2006; Amin, 2012; Matsui and Tabata, 2010). This phenomenon plays a role in zinc oxide possessing piezoelectric properties (Wang, 2004). Nevertheless, zinc oxide is not considered a conventional piezoelectric material because its charge separation is said to be as a result of the combination of both piezoelectricity and free carrier transport (Fu et al., 2007).

Furthermore, although zinc oxide's structure is referred to as hexagonal 'close packed', it has been shown that the constituent atoms only occupy about 44 % of the cell volume whereas the packing efficiency of an ideal hexagonal close packed (hcp) structure is 74%. Thus ZnO's cell has a relatively large amount of space 'left over' and this has been shown to be influential in tailoring zinc oxide's chemical and physical properties (Brown, 1957).

A summary of the crystallographic properties (at ambient conditions) of zinc oxide with wurtzite crystal structure is presented in Table 2.9.

Table 2.9: Crystallographic properties of zinc oxide (Pearson et al., 2005, Özgür et al., 2005; Abrahams and Bernstein, 1969, ICDD 04-013-6607).

CRYSTALLOGRAPHIC PROPERTY	VALUES
Space Group	P63mc
Space Group Number	186
Crystal System	Hexagonal
Number of Atoms per Unit Cell	4
Lattice Constant [Å]	a = 3.245; c = 5.207
Alpha [°]	90.00
Beta [°]	90.00
Gamma [°]	120.00
Cell Volume [10 ⁶ pm ³]	47.62
Refractive Index	n _ω = 2.008 ; n _e = 2.029

2.3.1.4 Mechanical Properties of Zinc Oxide

Zinc oxide has a bulk hardness of $\sim 4.8 \pm 0.2$ GPa and a bulk modulus of around 143 ± 6 GPa (both along the c-axis) and is considered to be a relatively soft material. It has been observed that the mechanical properties of zinc oxide could be influenced by its method of preparation. For instance, in a mechanical examination via spherical nano-indentation and cross-sectional transmission electron microscopy of epitaxial ZnO grown on a- and c-axis sapphire in which Molecular beam epitaxy (MBE) was employed to achieve a-axis directed epitaxial growth, while c-axis (0001) directed epitaxial growth was performed using pulsed laser deposition (PLD); hardness values of 6.6 ± 2.2 GPa for the MBE grown sample, and 5.75 ± 0.8 GPa for the PLD sample were recorded (Coleman et al., 2005). The results showed a significant variation from published values for hardness of bulk zinc oxide (4.8 ± 0.2 GPa); it was suggested that the presence of threading dislocations which are defects usually characteristic of epitaxial growth were responsible for the variation observed in that they inhibited the plane slip mechanism that made bulk zinc oxide relatively soft (Coleman et al., 2005).

From the foregoing analysis, it can be inferred from the differences in hardness values for a-axis and c-axis zinc oxide, that particle morphology (or specifically direction of growth) could influence the mechanical properties of zinc oxide.

In a similar vein, Erde'lyi et al., (2011) performed in-situ bending tests on zinc oxide nanorods (~ 100 nm wide and ~ 2.4 μm long) synthesised through a template assisted electron beam epitaxy (EBE) method. They employed a scanning electron microscope equipped with an atomic force microscope (AFM) tip for the tests, and recorded a bending (flexural) modulus of 36.0 ± 8.3 GPa which was observed to be significantly lower than published values of bulk bending modulus of zinc oxide (~ 140 GPa). The discrepancies were attributed to particle size effects as well as non-uniform cross-sectional area of the nanorods.

Many other researchers have attempted to mechanically characterise micro- and nanoscale zinc oxide with varying results; consequently, there is little

consensus on values for majority of zinc oxide's mechanical properties (Bernardini et al., 1997; Coleman et al., 2005; Desgreniers, 1998; Erde'lyi et al., 2011; Kucheyev et al., 2002; Massidda et al., 1995). Further details on the mechanical properties of zinc oxide (bulk) are presented in Table 2.10; data was sourced from a survey of literature (Bernardini et al., 1997; Coleman et al., 2005; Desgreniers, 1998; Erde'lyi et al., 2011^{*}; Kucheyev et al., 2002; Massidda et al., 1995).

Table 2.10: Some mechanical properties of wurtzite ZnO.

MECHANICAL PROPERTY	VALUES
C- axis Bulk Modulus, B [GPa]	143±6
C- axis Bulk Hardness H [GPa]	4.8±0.2
C- axis Epitaxial Young's Modulus, E [GPa]	310±40
C- axis Epitaxial Hardness, H [GPa]	5.75±0.8
C-axis Epitaxial Bending Modulus, B [GPa] (nanorods)	36.0±8.3 [*]
A- axis Bulk Modulus, B [GPa]	163±6
A- axis Bulk Hardness H [GPa]	2.0±0.2
A- axis Epitaxial Young's Modulus, E [GPa]	318±50
A- axis Epitaxial Hardness, H [GPa]	6.6±2.2
Born Effective Charge, Z[*]	2.1
Spontaneous Polarization [C m⁻²]	-0.057
Bulk Young's Modulus E [GPa]	112.2±4.7
Linear Expansion Coefficient [°C⁻¹]	a ₀ : 6.5 x 10 ⁻⁶ c ₀ : 3.0 x 10 ⁻⁶

2.3.1.5 Optical Properties of Zinc Oxide

Zinc oxide particles have been used in applications such as antireflection coatings, transparent electrodes in solar cells, ultraviolet (UV) light emitters, diode lasers, varistors, and piezoelectric devices as a result of its optoelectronic capabilities. Generally, zinc oxide is accepted to possess a direct band gap of about 3.37 eV at room temperature, however, it is common knowledge that the material's properties be it mechanical, optical, or electronic could be significantly dependent on particle shape, size, dimensionality and method of synthesis. Therefore, researchers have been investigating the effects of these factors in conjunction with other synthesis based conditions such as: laser pulse energy, doping, crystallite size, capping agents, and annealing temperature on the optical properties of zinc oxide e.g. UV-vis absorption, room temperature photoluminescence, and field emission (Feng et al., 2007; klingshirn, 2007; Han et al., 2012; Orimi, 2013; Solati et al., 2014). It has been reported that zinc oxide nanoparticles derived from sol-gel routes exhibited visible fluorescence while hydrothermally synthesised nanocrystals of similar size were UV-emitters (Xiong, 2010).

Adequate understanding of the role these factors play in the influencing the behaviour of zinc oxide particles could increase the scope and flexibility of exploiting its unique properties in current electronic and photonic applications, and could open up avenues for new applications in the future.

An analysis of the optical properties of tetrapod-like zinc oxide particles (width 70 - 150 nm, length 2 – 3 μm) at room temperature was performed by Dai et al., (2002) using a UV-Vis spectrophotometer. An ultraviolet (UV) emission peak was observed at ~380 nm which was attributed to near band-edge emission; also, a green emission peak was observed at ~495 nm, and was assigned to deep-level emission from the zinc oxide particles.

Zhao et al. (2012), employed a solution based route to produce water stable and soluble ZnO nanoparticles of approximately 5.2 nm diameter from zinc acetate dihydrate and potassium hydroxide aided by 3-(2-Aminoethylamino) propyldimethoxymethylsilane. The nanoparticles were UV excited at 350 nm and a green photoluminescence was observed around $\lambda = 526$ nm. Debanath

and Karmakar (2013), reported measuring an optical band gap of 3.63 eV while studying the blue shift of band gap in ZnO nanoparticles (~ 8.5 nm sized) which were made from zinc nitrate hexahydrate and ammonium hydroxide via a wet chemical route, that involved the use of polyvinyl pyrrolidone as a capping agent. From UV-vis analysis of a colloidal solution of the product particles at pH = 7.5, they observed a broad peak at $\lambda = 298.8$ nm (4.16 eV) as opposed to $\lambda = \sim 376$ nm (3.3 eV) for bulk zinc oxide. They reported that the observation of blue shift in band gap was due to size (confinement) effects and that optical band gap of the zinc oxide nanoparticles was inversely related to particle size

The importance of emission type in zinc oxide particle becomes evident when one considers some of the potential applications of these particles. For instance, biological labelling applications exploit a combination of zinc oxide's direct band gap of 3.37 eV, its large exciton binding energy (60 meV), (making it one of the brightest emitters among available wide band gap semiconductors) with its biocompatibility (Asok et al., 2012). Despite this unique capability, the occurrence of condition specific emission in zinc oxide particles means that emphasis would need to be on a careful selection of synthesis conditions and product specifications. In the case of biological labelling, the usage of zinc oxide particles having only a blue emission may be considered not desirable as most cells and tissues usually appear bluish under UV irradiation (Zhao et al., 2012).

Finally, a wide variation has been observed in reportage from experimental investigations into the optoelectronic properties of zinc oxide and this may not be unconnected with the observed sensitivity of zinc oxide to a vast amount of test conditions (Andelman et al., 2005; Mishra et al., 2010; Singh et al., 2009; Coleman and Jagadish, 2006).

About 15 nm sized ZnO nanoparticles were synthesised by Rajalakshmi et al., (2012) from zinc acetate dihydrate and methanol through a solution-based procedure without surfactants or growth additives. They reported that the product nanoparticles gave off blue, green and yellow emissions under UV excitation and attributed them to zinc and oxygen vacancies and interstitials.

They also reported that annealing the ZnO nanoparticles resulted in the emission of only blue light.

Wet chemical synthesis was also employed by [Oliva et al., \(2014\)](#) to produce zinc oxide nanorods (125 nm to 165 nm) and quantum dots from zinc acetate dihydrate and methanol using dodecylamine (DCA) and triethanolamine (TEA) surfactants to obtain nanorods and quantum dots respectively. They reported being able to control the amount of defects that simultaneously emitted yellow and blue light by varying the amount of dodecylamine added to the reaction mixture. Their observations of size dependence of zinc oxide's photoluminescence also corroborated [Debanath and Karmakar's \(2013\)](#) postulations.

2.3.1.6 Electrical/Electronic Properties of Zinc Oxide

Zinc oxide is a II-VI compound semiconductor as pointed out earlier, and the material exhibits n-type conductivity due to electrons moving as charge carriers in the conduction band (Morkoç and Özgür, 2009; Hadi et al., 2012; Monakhov et al., 2009; Vojisavljević et al., 2006).

As with other properties of zinc oxide, its electrical properties could also be influenced by material chemistry (Hafad et al., 2011; Look, 2007). For instance, Tang et al., (2013) reported that there was an exponential relationship between electrical resistance and particle length in belt-like zinc oxide micro- and nanoparticles, which was deviant from normally observed behaviour of bulk zinc oxide.

The influence of microstructure, types and concentrations of defects on the electrical properties of sintered pellets of zinc oxide produced from commercial powder milled in a steel vibro-mill for different time scales was investigated by Vojisavljević et al., (2006). It was reported that reduction in particle & grain sizes by comminution, led to an increase in defect concentration. The introduction of new defects was also observed and suspected to have resulted from Fe-doping occasioned by the use of a steel vibro-mill. It was also observed that the resistivity of the pellets was influenced by the milling time with an increase in milling durations resulting in increased resistivity values.

In a similar vein, Fu et al., (2007) investigated the effects of particle size and structure on the piezoelectric properties of zinc oxide using an optical measurement system based on a scanning Michelson laser beam interferometer. They reported that microtubular zinc oxide particles exhibited piezoelectric properties that varied significantly from those of bulk zinc oxide under low frequency electric field conditions mainly due to structurally induced conductivity differences.

The presence of hydrogen as an impurity / dopant within zinc oxide crystal has been noted to significantly alter the optical and electrical properties of zinc oxide (Ohashi, 2014). It has been suggested that the presence of hydrogen impurities aided the exhibition of p-type conductivity in nitrogen doped zinc oxide particles (Lu et al., 2007). There are reports from other research

investigations detailing observations of the effects of various dopants on the electrical properties of bulk, micro and nanoscale zinc oxide (Fujita et al., 2014; Mandal et al., 2014; Sáaedi et al., 2013; Soumahoro et al., 2014; Zhao et al., 2010; Hoffman et al., 2002; Monakhov et al., 2009; Janotti and Van de Walle, 2005).

Hall mobility measurements of mono-crystalline thin films of ZnO prepared by vapour phase based synthesis route on an Al₂O₃ substrate were conducted by (Dimova-Aliakova, 1976) and they reported that the magnitude of Hall mobility was directly proportional to evaporation temperature in that values increased from 30 cm² V⁻¹ s⁻¹ to 100 cm² V⁻¹ s⁻¹ as temperature was raised from 720 °C to 790 °C. On the other hand, hall mobility was found to be inversely related to carrier concentration reducing from 100 cm² V⁻¹ s⁻¹ to 30 cm² V⁻¹ s⁻¹, as carrier concentration increased from 2.2 x 10¹⁷ cm⁻³ to 2.5 x 10¹⁸ cm⁻³.

The effect of charge carrier mobilities on the performance of zinc oxide based solar cells was the subject of Koster and co-worker's (2007) investigations. They produced a heterojunction solar device with a power conversion efficiency of about 2.6 % from zinc oxide nanoparticles and a poly(p-phenylene vinylene) (PPV) derivative. Measurements of hole and electron mobility resulted in values of 5.5 x 10⁻¹⁰ cm² V⁻¹ s⁻¹ and 2.8 x 10⁻⁹ cm² V⁻¹ s⁻¹ respectively. It was observed, that particle morphology significantly impacted on charge-carrier mobility and consequently the performance of the solar cells.

Room temperature ferromagnetism (RTFM) has been reportedly observed in Cu-doped ZnO thin films (Buchholz et al., 2005), as well as in ZnO thin films doped with 5 % of Sc, Ti, V, Fe, Co or Ni, prepared by pulsed laser deposition (Venkatesan, 2004). Ferromagnetism in 20 nm ZnO nanoparticles capped with organic compounds tryoctylphosphine, dodecylamine, and dodecanethiol were studied by Guglieri et al., (2012), using both combined element-specific X-ray absorption spectroscopy (XAS) and X-ray magnetic circular dichroism (XMCD). It was reported that both intrinsic high temperature ferromagnetism (HTFM) and intrinsic room temperature ferromagnetism (RTFM) were observed in the 20 nm capped nanoparticles. Size dependent room temperature ferromagnetism was also reported in undoped ZnO nanoparticles prepared from zinc acetate,

ethanol (absolute), dimethyl sulfoxide (DMSO), and Tetramethylammonium hydroxide (TMAH) through a wet chemical route. The RTFM was thought to have been induced by point defects in the ~ 5 nm nanoparticles (Xu et al., 2012).

Electrical Properties: Defects, n-type and p-type Conductivity in Zinc Oxide

There are a number of intrinsic defects in ZnO with different ionization energies:

- vacancy (V_O),
- Zn vacancy (V_{Zn}),
- antisite Zn (Zn_O).
- Zn interstitials (Zn_i),
- interstitials (O_i) and

Undoped zinc oxide particles usually exhibit a n-type behaviour, which is attributed to defect levels induced by interstitials, oxygen vacancies, or hydrogen within the crystal (Janotti and Van De Walle, 2005). One of the limitations of ZnO n-type conductivity as noted by Shin, et al., (2013) is that it led to a Fermi level located 50 meV below the conduction band edge resulting in an abundance of excess electrons which in turn acted as a screen to limit the piezoelectric potential generated whenever the crystal is mechanical deformed along the c-axis.

Table 2.11 show's a comparison of properties of n-type and p-type ZnO films (Tüzemen et al., 2001).

Table 2.11: Comparison of properties of n-type / p-type ZnO films before and after annealing at 750 °C (Tüzemen et al., 2001).

PROPERTY	n-type ZnO		p-type ZnO	
	Not annealed	annealed	Not annealed	annealed
Electrical Resistivity ($\Omega.cm$)	>104	100	200	30
Mobility ($cm^2 V^{-1} s^{-1}$)	N/A	20	30	130
Carrier concentration (cm^{-3})	N/A	6×10^{15}	5×10^{15}	5×10^{15}

The possibility of producing zinc oxide particles with p-type conductivity has been proven (Feng, 2012; Fan et al., 2013; Joseph et al., 2001; Kim et al., 2003; Look et al., 2002; Minegishi et al., 1997; Ryu et al., 2003; Xiu et al., 2005; Yamamoto, 2002; Ye et al., 2003). However, there remains several challenges surrounding reproducibility and reliability, largely due to the self-compensation effects from intrinsic donor-type defects (V_o and Zn_i). Self-compensation could be described as the ability of a crystal to lower its energy by forming point defects to counter the effects of a dopant (Look et al. 2011). In other words, native donor defects Zn interstitials (Zn_i), and oxygen vacancies (V_o) which have low formation energies are formed in the ZnO crystal lattice in response to the presence of acceptor-type defects. Other researchers have also suggested that hydrogen incorporation by zinc oxide could also be another mechanism through which the self-compensation which inhibits the stability of p-type doping in ZnO occurred (Fan et al., 2013; Janotti and Van De Walle, 2009).

There are resurgent efforts to develop p-type ZnO as a result of successful production of p-type GaN, a material with similar properties to ZnO (Fan et al., 2013; Feng, 2012; Pradel et al. 2013). Yamamoto and co-workers demonstrated the possibilities of generating stable p-type doping in ZnO via doping with a single dopant or co-doping involving acceptor (A) and donor (D) dopant inclusion (Yamamoto, 2002; Yamamoto and Katayama-Yoshida, 2000). Duan et al, (2013) reported a two-step process involving a seed generation step where zinc salt dissolved in ethanol was spin coated onto a glass substrate, while the second step involve hydrothermal synthesis to generate Ag–N dual-doped p-type ZnO rods which coalesced into a film.

Other researchers have also reported synthesis of p-type ZnO through methods such as molecular beam epitaxy, chemical vapour deposition, RF magnetron sputtering, and ion implantation (Fan et al., 2013), some of these methods have also involved the use dopants such as Gallium (Ga), arsenic (As), antimony (Sb), phosphorous (P), nitrogen (N),Lithium (Li), Sodium (Na), Potassium (K), and excited N_2O (Feng, 2012; Joseph et al., 2001; Kim et al., 2003; Look et al., 2002; Minegishi et al., 1997; Ryu et al., 2003; Xiu et al., 2005; Ye et al., 2003).

Table 2.12: Electrical properties of zinc oxide (Ashkenov, et al., 2003; Coleman and Jagadish, 2006; Janotti, and Van de Walle, 2009; Maeda, et al., 2005).

ELECTRICAL PROPERTY	VALUES
Debye Temp [K]	370
Electron and hole effective mass	$m_e = 0.28, m_h = 0.59$
Exciton binding energy, E_b [meV]	60
Electron saturation velocity [cm s ⁻¹]	3.2×10^7
Electron mobility for low n-type conductivity [cm ² V ⁻¹ s ⁻¹]	200
Static dielectric constant	8.656
Electrical conductivity [Ω^{-1} cm ⁻¹]	$\sigma = 10^{-2} e^{-\frac{2 \times 10^{-2}}{KT}} \text{ (T < 25 } ^\circ\text{C)}$ $\sigma = 10^2 e^{-\frac{-7 \times 10^{-2}}{KT}} \text{ (400 < T < 700) } ^\circ\text{C}$
Band gap [eV]	3.3
Pyroelectric constant [Amp ⁻¹ sec ⁻¹ cm ⁻² k ⁻¹]	6.8×10^{10}
Piezoelectric coefficient, D_{33} [pC N ⁻¹]	12
Cohesive Energy, E_{coh} [eV]	2.89
Dielectric constant (thin films)	$E \perp c \quad E \parallel c$
ϵ_0^a	7.46 8.59
ϵ_∞	3.61 3.76

2.3.2 Applications of Zinc Oxide

2.3.2.1 General / Generic Applications of Zinc Oxide

Some of the more familiar uses of zinc oxide occur in the rubber, paints and cosmetics manufacturing industries. The inclusion of zinc oxide in paints appears to be one of the earliest modern era usage of zinc oxide in commercial quantities. Zinc oxide is added to paint to serve a number of purposes, the main one being to serve as a filler in paint formulations. For over 100 years, paints were made using zinc oxide when it was observed that zinc oxide paints were resistant to sulphuric 'darkening' however nowadays, titanium dioxide is used instead (New Jersey Zinc Company, 1940). Zinc oxide also helps to mitigate the weathering effect of UV rays on painted outdoor surfaces by absorbing UV radiation (NavBharat, 2015). Its antimicrobial properties are exploited to produce paints with mould and mildew growth resistant capabilities. Zinc oxide containing paints have also been used in photocatalytic paints to prevent microbial growth (Jašková et al., 2013). Zinc oxide has been added to antifouling paints to enhance the mechanical strength of coats produced from the paint, thereby increasing the service life of the coats. Also, zinc oxide could act as a formulation stabilizer in the paints while it is still on the shelf by reacting with some of the acidic components in the formulation that may unbalance the stability of the paint mixture (Diebold et al., 2003; ippic, 2012).

Furthermore, zinc oxide's biocompatibility and amphoteric abilities are exploited in the food industry where it is included in lacquer coatings for work surfaces. Here, zinc oxide acts to prevent discolouration of the surfaces due to attack from iron or tin sulphides as well as corrosion from food acids (Shankar et al., 2015). Zinc oxide – aluminium amalgam (ZnO:Al) has been employed in window coatings because the amalgam combines transparency in visible light region with reflectivity in the infrared region. Zinc oxide primers are also used in the paint industry to protect metallic surfaces by sacrificially reacting with salt water in boats, it also serves as buffer phase between metallic surfaces and organic paints preventing reaction between both that could degrade the paints. (Moezzi et al., 2012; Pugazhenty, 1991).

Zinc oxide is a key material in the rubber industry, the majority of bulk zinc oxide powder produced worldwide is consumed by the rubber industry where it is used to activate rubber vulcanisation processes, it is also employed as a preservative and fungistat (fungi growth inhibitor) to prevent the degradation of harvested latex while in storage. Zinc oxide is also added during the production of some tyres, to improve the heat reinforcement and stability of the tyres (Moezzi et al., 2012; Pugazhenty, 1991).

Zinc oxide has been employed in cosmetic applications such as skin lotions, ointments and sunscreens. Cosmetic applications of zinc oxide mainly exploit its ability to absorb UV radiation (Moezzi et al., 2012). A great deal of research effort have been devoted to understanding the structure, composition, toxicology and safety in relation to the usage of zinc oxide in the cosmetic industry (Lewicka et al., 2011; Monteiro-Riviere et al., 2011). Guedens et al., (2013), reported on the synthesis of zinc oxide-based sunscreen for education based laboratory experiments.

2.3.2.2 Medical / Biological Applications of Zinc Oxide

Zinc oxide has been used for medicinal purposes for centuries. As early as the medieval period, there was already an established understanding of the therapeutic and medicinal abilities of zinc oxide (pompholyx or philosopher's wool then) (Brown, 1957). A popular zinc oxide containing medical product is calamine lotion used to treat a number of skin-related conditions, here zinc oxide serves as a mild astringent (body tissue binder), anti-itching component and antiseptic (NavBharat, 2015). Zinc oxide creams for antimicrobial purposes are also in existence (Rahman et al., 2015). Zinc oxide has been actively used in the development of bandages and wound dressing materials (Yadollahi et al., 2015; Kumar, et al., 2012). Nanofibers of zinc oxide were also reportedly combined with poly vinyl alcohol (PVA) and sodium alginate to produce dressings for wounds (Shalumon et al., 2011).

In addition to the foregoing, zinc oxide–polyurethane composites have also been developed for tissue engineering (Amna et al., 2013). Zhao, et al. (2012) employed a solution based route to produce water stable and soluble ZnO nanoparticles with green photoluminescence showing that they could be used

in bio-labelling. In a complimentary investigation, [Zhou et al., \(2006\)](#) studied the biodegradability and biocompatibility of zinc oxide nanoparticles by observing their stability and dissolution in biofluids. They observed that the zinc oxide nanowires dissolved in acidic deionised water, basic ammonia and alkaline sodium hydroxide solutions which is characteristic of its amphoteric nature. Observations of the stability of the nanoparticles in blood serum showed that they degraded into mineral ions only after a few hours.

Other medical and biological applications of zinc oxide include drug delivery, bio-imaging and cancer treatment ([Rasmussen et al., 2010](#); [Urban et al., 2011](#); [Wang, 2004](#); [Zhang et al., 2011](#)). Nanoprobes made from gadolinium doped zinc oxide quantum dots have been reportedly developed for use in magnetic resonance imaging (MRI) scans where they could potentially enhance current MRI imaging methods by providing fluorescence imaging capabilities in combination with magnetic resonance imaging ([Liu et al., 2011](#)).

2.3.2.3 Gas Sensing Applications of Zinc Oxide

Many researchers have been able to fabricate sensors for various gases and other purposes based on ZnO nanoparticles ([Kang et al., 2005](#); [Lupan et al., 2008](#); [Shouli et al., 2011](#); [Wang et al., 2006](#)). For instance, Branched ZnO nanorods were used to fabricate room temperature hydrogen gas nanosensors ([Lupan et al., 2007](#)). The sensors reportedly detected hydrogen (150 ppm concentration) with a sensitivity ranging from 0.6 – 2 % and were also functional with other gases (O₂, CH₄, CO and LPG). [Qurashi et al., \(2011\)](#) also studied the hydrogen gas sensing properties of ZnO nanorods (diameter 100 – 120 nm; lengths ~ 1 µm). They observed that the sensitivity of the ZnO-based sensors was dependent on working temperatures and they obtained optimal sensitivity at 200 °C corroborating [Mitra and co-worker's \(1998\)](#) findings with (0.5 – 5 µm) zinc oxide films.

[Lim et al., \(2010\)](#) coated zinc oxide nanorods onto the surface of fabric and then used it to design a textile hydrogen sensor. Their findings also showed that the sensing capabilities of the ZnO-based fabric gas sensor could be improved by incorporation of platinum coating.

Sensors based on zinc oxide nanoparticles which were activated with a UV-LED of peak wavelength 400 nm and incident light intensity 2.2 mW cm^{-2} were fabricated by [de Lacy Costello et al., \(2008\)](#). The UV activated sensors were then tested on methane, ethane, propane, butane, ethanol, pentane, hexane, toluene, acetone and acetaldehyde. They observed that the sensors were capable of detecting acetone and acetaldehyde at concentrations of about 1 part per billion (ppb). It was noted that the sensitivity of the gas sensors increased with decreasing particle size. Zinc oxide nanorods (diameter 100 – 150 nm; length 1 – 2 μm) were produced via a microwave assisted hydrothermal method and used to fabricate sensors to detect carbon monoxide (CO), ethanol and acetaldehyde. It was concluded that 200 °C was the best working temperature for ZnO- based ethanol sensors ([Rai et al., 2012](#)).

Zinc oxide nanorods produced from zinc acetate dihydrate, potassium hydroxide and methanol using a solvothermal procedure, were used as ethanol gas sensors at a working temperature of 400 °C by [Chen et al., \(2011\)](#). They reported that the sensor could detect ethanol gas at concentrations as low as 5 ppm. It was also observed that sensitivity increased with increasing gas concentrations up to 300 ppm and that response and recovery times of the ZnO nanorod-based sensors were less than 10 s and 30 s, respectively. Similarly, ZnO-based alcohol sensors developed by [Yin et al., \(2013\)](#), showed that using ethanol as solvent produced smaller particle sizes which had better gas sensing abilities when tested on 100 ppm alcohol vapour concentration.

[Zhang et al., \(2013\)](#), explored the ethanol gas sensing abilities of hierarchical castellated and turriform shaped ZnO particles synthesised via an ultrasonic assisted hydrothermal route. They reported that the set of particles which they called turriform shaped particle posted a better gas sensing performance than their castellated counterparts; picking up gas at concentrations as low as 0.5 ppm. They also observed that the gas sensitivity of the ZnO-based sensors increased with temperature up to an optimal value of 425 °C. The foregoing results could be indicative of the influence that particle morphology could have on the gas sensing abilities of zinc oxide.

Using nitrogen dioxide (NO₂) as the test gas, Öztürk, and co-workers (2011) also showed that performance of ZnO-based sensors was significantly dependent on the morphology of the particles. They compared the sensitivity of three different particle morphologies: thin films (30 nm diameter grains), nanowires (avg. 65 nm X 10 µm) and nanorods (avg. 30 nm X 500 nm) to NO₂ gas over concentration range of 100 ppb to 10 ppm at a working temperature of 200 °C. Their experimental findings showed that at 1 ppm NO₂ concentration, zinc oxide nanorods had a response time (t_m) of 24 s, thin films t_m of 30 s, while nanowires had t_m of 84 s.

Zinc oxide nanorods (width 40 – 80 nm; length < 1 µm), produced by hydrothermal treatment of zinc oxide powder in the presence of cetyltrimethylammonium (CTAB) were used to fabricate gas sensors to test for hydrogen sulphide (2 ppm), methanol (50 ppm), liquefied petroleum gas (LPG; 500 ppm), gasoline (50 ppm), carbon monoxide (500 ppm), alcohol (50 ppm) and ammonia (50 ppm) under the heating voltage of 5 V. It was observed that the ZnO-based sensors had a high sensitivity for alcohol, followed by gasoline, methanol then ammonia among the 50 ppm concentration gases. It was noted that the ZnO-based sensors were durable over several cycles of testing (Jiaqiang et al., 2005).

Baruwati et al., (2006) performed a test similar to that of Jiaqiang and co-workers, using ~ 17 nm zinc oxide nanoparticles. They arrived at a similar conclusion, that zinc oxide particles had better sensitivity towards ethanol than LPG. They also observed that doping the particles with palladium (Pd) helped reduce the working temperature by more than 100 °C.

Other instances of the usage of zinc oxide particles in sensor applications include the fabrication of ultra violet radiation activated oxygen sensors using zinc oxide nanobelts which were found to be effective up to a gas concentration of 16.6 ppm by He et al., (2009). It was also observed that the addition of plasma-polymerized acrylonitrile (PP-AN) to the ZnO nanobelts, resulted in a device with improved oxygen-sensing abilities.

In a departure from gas sensing, but following similar processes, Kumar et al., (2013) reported the fabrication of enzymatic glucosensors using ZnO

nanoparticles dip coated onto a silicon wafer to create a thin film. Wang et al., (2006) also reported of the fabrication of glucosensors from nanocombs of zinc oxide grown via vapour phase transport. Also, Wei et al., (2006) reported the production of glucosensors from glucose oxidase (GO_x) immobilized on hydrothermally prepared ZnO nanorod array. In addition to glucose biosensing, zinc oxide has also been used in the fabrication of cholesterol sensors (Batra et al., 2012; Singh et al., 2007; Solanki et al., 2009).

2.3.2.4 Hydrogen Production and Fuel Cell Related Applications of Zinc Oxide

Zinc oxide can be used as an electrode material and a cathodic material as well as a fuel element (solar powered high temperature dissociation of ZnO to Zn) in fuel cells (NavBharat, 2015; Haueter et al., 1999). ZnO particles have also found application in the field of hydrogen generation for energy related purposes (Grimes et al., 2008; Steinfeld, 2005). Zinc oxide nanoparticles synthesised via room temperature precipitation and a reverse micelle method was employed in the photo-catalytic generation of hydrogen from an alkaline Na₂S aqueous solution. It was observed that particle size was a significant determinant of the quantity of hydrogen generated with smaller particle sizes leading to larger volumes of hydrogen generation (Perales-Perez et al., 2004).

Zinc oxide produced from thermal decomposition of zinc oxalate and impregnated with palladium, was used to study the generation of hydrogen through partial oxidation of a methanol stream over a range of temperatures (Cubeiro and Fierrob, 1998). However, in similar experiments, Iwasa et al., (1995) observed that the formation of palladium-zinc alloy by reducing the Pd-ZnO mixture at elevated temperatures prior to methanol conversion, improved the performance of the zinc-oxide based catalytic reformation of methanol.

Steinfeld (2002), described a process in which hydrogen could be generated by splitting water using solar energy. The process occurred over two cycles; in the first cycle zinc oxide is reduced to elemental zinc at very high temperatures (2300 K) before the reduced metal then scavenges oxygen from steam at a much lower temperature (700 K) to regenerate zinc oxide along with the production of hydrogen.

In other fuel cell applications, zinc oxide was used as a support catalyst for gold and platinum to selectively oxidise carbon monoxide in a hydrogen rich stream into carbon dioxide. Findings reported showed that Au:ZnO composition and calcination temperatures significantly influenced the activity and durability of the catalysts (Zhang et al., 2003).

2.3.2.5 Photonic / Optoelectronic Applications of Zinc Oxide

Alloying of zinc oxide for electronic applications include: indium gallium zinc oxide (IGZO) for display technologies and thin-film transistor arrays (Nomura et al, 2004, Sharp, 2013); zinc magnesium oxide (ZnMgO) and zinc cadmium oxide (ZnCdO) for optoelectronic devices (Vispute, 2005; Sadofev, 2008). It is reported that Apple Inc. employs IGZO-based display technology developed by Sharp Electronics Corporation for its Ipad devices. The technology has been touted by Sharp Electronics Corporation as its most advanced energy-efficient panel technology (Sharp, 2013; WSJ Europe, 2013).

2.3.2.6 Energy Harvesting / Generation Applications of Zinc Oxide

In 1866, Georges Leclanché invented the Leclanché cell which made use of a zinc anode. Modern modifications of this cell (zinc-carbon dry cells, zinc-silver oxide batteries) make use of zinc oxide (NavBharat, 2015). Aluminum, (Al), indium (In) and gallium (Ga) doped zinc oxide yields a transparent, highly conducting oxide (TCO) which could serve as a viable alternative material to tin-doped indium oxide (ITO) as a transparent electronic conductor for solar cell applications (Granqvist, 2007; Goris et al., 2009). Ni-doped ZnO nanoparticles and thin films have been studied for use in dye-sensitized solar cells (DSSC) by Thakur et al., (2013); while Lin et al., (2011) prepared nanosheets of ZnO which were then used to fabricate dye-sensitized solar cells.

Nanoparticles of zinc oxide grown on glass substrates coated with both indium tin oxide (ITO) and poly(3,4-ethylenedioxythiophene) polystyrene sulfonate (PEDOT:PSS) were used in the production of solar cells whose power conversion was about 2.5 % efficient (Beek et al., 2004).

Recently, there have been efforts aimed at constructing zinc oxide based self-powering nano devices by exploiting the material's piezoelectric properties and sensing abilities (Qin et al., 2008; Wang, 2007; Yang et al., 2009).

Song et al., (2006) demonstrated the use of a zinc oxide nanowire device to convert mechanical energy to electrical energy as a result of its piezoelectric. It was explained that when such a device experiences mechanical deformation, a strain field occurs in the bent nanowire leading to the occurrence of charge separation across the zinc oxide nanowire, which culminates in the generation of electrical current due to the rectifying characteristic of the Schottky barrier formed between the metal and semiconductor particle (Wang and Song, 2006; Yang et al., 2009). It was noted, that with this ability, zinc oxide based devices could be used to harvest electrical energy from body movements, vibrating devices e.g. acoustics and fluid flow, for powering or charging devices such as implants, and batteries. Nanowire arrays of zinc oxide were used to construct a self-powered nanosystem consisting of multi-layered direct current and alternating current (AC/DC) nanogenerator integrated with a nanosensor. In fabricating the DC nanogenerator, nanotip shaped zinc oxide particles were combined with ZnO nanowires, the resultant device required ultrasonic excitation to generate current. For the AC nanogenerator, only zinc oxide nanowires were employed and current was generated by the application of a uniaxial load on the top electrode. It was observed that connecting a number of zinc oxide based AC nanogenerators in series resulted in an improved voltage output (Xu and Wang, 2011).

Lin et al., (2010) reportedly fabricated wire-shaped electrodes by combining CdSe nanoparticles and ZnO nanowires to form CdSe-sensitized ZnO nanowire arrays which were observed to have a lower dependence on the angle of incident light, and so provided better photo-generation abilities, which could be used in the photochemical generation of hydrogen.

Shin, et al., (2013), explored the enhancement of piezoelectric performance in ZnO nanogenerators through the combination of p-type CuO and n-type ZnO thin films resulting in the fabrication of a CuO–ZnO p-n heterojunction. It was observed that voltage output from the CuO-ZnO nanogenerator was seven times higher than that from a ZnO only nanogenerator. Also their findings showed approximately a ten times increase in current density.

In other investigations, [Choi et al., \(2010\)](#) studied the power generating properties of zinc oxide nanorods (width 30 – 60 nm, length 300 – 500 nm) hydrothermally synthesised on a flexible polyethersulfone (PES) substrate using an I-AFM for experimental analysis and ANSYS for theoretical finite element simulation studies. Their findings showed that the power generation abilities of the device was a result of the combination of the metal-semiconductor (Au–ZnO) interface property and piezoelectric abilities of the zinc oxide nanorods.

2.3.2.7 Dye Degradation / Photolysis related Applications of Zinc Oxide

There are increasing reports of the usage of zinc oxide in the textile industry, although the use of zinc oxide nanoparticles in the degradation of dyes is a relatively widely explored field of research. ZnO particles have been employed in phenol degradation ([Morales-Flores et al., 2011](#)) both undoped and Se-doped ZnO were used in the degradation of trypan blue dye ([Dutta et al., 2013](#)). Photocatalytic degradation of Alizarin Red S dye, within 90 minutes under UV conditions was reported by ([Kansal et al., 2013](#)). A coupled zinc oxide- zirconia system (ZnO – ZrO₂) was employed in the degradation of 2, 4-dichlorophenol ([Sherley et al., 2013](#)). While the use of ZnO nanoparticles to degrade Methylene Blue (MB) and Methyl Orange (MO) dyes was reported by ([Kittur et al., 2011](#)).

Asides from dyes, zinc oxide particles have reportedly found usage in the area of waste treatment, where they could be used to photochemically decompose organics present in the waste water in both aerobic and anaerobic waste degradation processes ([Chan et al., 2009](#); [Chaúque et al., 2014](#)).

[Shukla et al., \(2010\)](#), reported on the usage of commercially sourced zinc oxide particles as catalyst for UV activated degradation of phenolic waste water contaminants. They observed that the combination of zinc oxide and peroxymonosulphate (PMS) under ultraviolet irradiation produced the best contaminant removal results. Studies have shown that the presence of zinc oxide nanoparticles in domestic waste water streams could negatively impact on the ability to remove nitrogen and phosphorous contamination in the affected streams ([Puay et al., 2014](#); [Zheng et al., 2011](#)).

2.3.2.8 Other Applications of Zinc Oxide

In other reported applications for particulate zinc oxide, ZnO particles have been coated onto fabric surfaces to provide UV protection, and antibacterial protection. [Perelshtein et al., \(2012\)](#) investigated the enhancement of antibacterial activity and stability of ZnO particles coated onto cotton fabrics.

Zinc oxide has also been found to be resistant to radiation damage and thus find use in products that could suffer potential exposure to radiation such as space applications ([Fan et al., 2013](#)).

Mixtures of Zirconia (ZrO₂) and ZnO nanoparticles have been trialled as anti-wear additives in oil lubricants ([Battez et al., 2008](#)). [Heris et al., \(2015\)](#) also reported on the use of zinc oxide nanoparticles in lubricants. [Liu and Zhang \(2011\)](#) explored the use of hierarchical ZnO towers in the production of biodiesel.

Zinc oxide also finds usage in the agricultural sector, where it is used as a mouldstat or fungistat to prevent the growth of mould and fungi. It is also added to animal feed as a growth supplement ([NavBharat, 2015](#); [Pugazhenty, 1991](#)).

Chapter 3

Materials and Methods

The chapter provides a description of synthesis of zinc oxide via a hydrothermal route and synthesis of sodium zirconate via solution based routes.

Also included in this chapter, are brief descriptions of key principles behind the primary analytical techniques (X-ray diffraction analysis and scanning electron microscopy) that were used for particle characterisation, along with the analytical protocols involved and a summary of sample/specimen preparation for each of these procedures.

3.1 Particle Synthesis

3.1.1 Hydrothermal Synthesis of Zinc Oxide Particles

Hydrothermal synthesis was employed for the zinc oxide related experimental work presented here. The route was selected after careful consideration of other options based on their advantages and disadvantages (section 2.2.7).

The synthesis process involved the usage of zinc acetate dihydrate (Sigma-Aldrich, ≥ 99.0 % purity), as source of zinc ions (Zn^{2+}). While ammonium hydroxide (Sigma-Aldrich, 28.0 – 30.0 % NH_3 basis), and sodium (natrium) hydroxide (Fischer Scientific, 2 mol dm^{-3}) as sources of hydroxyl ions (OH^-). All reagents were used as supplied with no further purification step taken prior to usage.

3.1.1.1 Stage 1: Preparation

A description of the procedure for precursor preparation is split into two sections based on the type of base species involved.

Precursor Preparation: Sodium Hydroxide (NaOH) Route

Under this route a ZnO precursor suspension was prepared from the combination of zinc acetate and sodium hydroxide.

To prepare zinc acetate solution, approximately 7.5 g of the zinc acetate dihydrate salt was weighed out on an electronic scale (OHAUS Explorer®, New Jersey, USA) and dissolved in 100 mL of distilled water obtained in-house from a Milli-Q Millipore water purification system. The resultant solution had a concentration of about 0.03 molL^{-3} of zinc acetate and a pH value of approximately 6.5. Then 10 mL of a 2 molL^{-3} sodium hydroxide solution was measured out and mixed with 100 mL of distilled water to obtain a $\sim 0.18 \text{ molL}^{-3}$ sodium hydroxide solution.

Both solutions were independently stirred for circa 15 minutes on a Carousel™ stirring hotplate (Radleys, Essex, UK) before the alkaline solution was added drop-wise to the zinc salt solution under continuous stirring. The viscosity of the resulting milky white suspension depended on stirring rate and duration of stirring, varying from milk-like consistency with vigorous stirring to thick yoghurt-like consistency when stirred slowly.

A handheld pH meter (HI-991001N, Hannah Instruments, Bedfordshire, UK) and a bench top pH meter (HI-111-02, Hannah Instruments, Bedfordshire, UK) fitted with both a double junction Ag/AgCl pH probe (HI 1331B) and a temperature probe (HI 7669 / 2 W) were used in the course of experimental work. For both pH meters, a three point calibration method was always used when calibrating the pH meters. The method involved the use of three pH buffers: an acid pH buffer (pH = 4.01), a neutral pH buffer (pH = 7.01) and an alkaline pH buffer (pH = 10.01); all pH buffers were sourced from Hannah Instruments, Bedfordshire, UK. The pH calibration started with dipping the pH probe in the neutral pH buffer and switching the meter into calibration mode. After the buffer was recognised by the meter and confirmed, the probe was then transferred to the next buffer as indicated by the display in the screen of the pH meter which was usually pH = 4.01 buffer, the calibration process was rounded off by dipping the pH probe in the alkaline (pH = 10.01) buffer and waiting for the pH meter to recognise it and reconfigure itself accordingly.

In varying the pH of the precursor mixture, more of fresh 2 molL^{-3} sodium hydroxide stock solution or sodium hydroxide pellets (Sigma-Aldrich, $\geq 97.0 \%$ purity) were added to the precursor suspension under constant stirring until the targeted pH was achieved. Precursor mixtures with pH values of approximately 7.0, 9.0, 11.0 and 13.0 were prepared during the course of experimental investigations.

Precursor Preparation: Ammonium Hydroxide (NH_4OH) Route

Precursor preparation via the ammonium hydroxide route largely followed the same steps as described above for the sodium hydroxide route except for the substitution of sodium hydroxide with ammonium hydroxide. Ammonium hydroxide was sourced from Sigma Aldrich, and supplied in the form of a 890 gL^{-1} aqueous solution (28.0 – 30.0 % NH_3 basis), and was used as supplied.

To begin, 23.5 mL of the stock NH_4OH solution was measured out and mixed with 100 mL of distilled (MilliQ) water to obtain a final solution with a concentration of 4.67 molL^{-3} of hydroxyl ions (OH^-) which was then stirred for about 15 minutes before drop-wise addition to the zinc salt solution to generate a white precursor suspension.

In this case however, the viscosity and opacity of the resultant precursor mixture was largely unchanged with respect to rate of stirring and length of post addition stirring.

3.1.1.2 Stage 2: Hydrothermal Treatment

Hydrothermal treatment of the precursors obtained above was conducted in two types of hydrothermal treatment reactors; a 125 mL capacity Teflon lined non-stirred acid digestion vessel (model 4748, Parr Instruments, Illinois, USA) and a 2 L unlined Hastelloy c-276 bench top reactor (model 4524, Parr Instruments, Illinois, USA).

125 mL reactor

In a standard experimental procedure, 100 mL of precursor solution was transferred into the Teflon cup of the vessel and inserted into its steel jacket after which it was sealed using an O-ring seal mechanism with top end screws.

The ensemble was then placed inside a Carbolite chamber furnace (CWF 1200, Carbolite®, Hope Valley, UK) and the furnace programmed as follows (for a standard hydrothermal treatment run):

- Heating regime: 5 °C per min up to 120 °C
- Dwell/hold regime: 12 h (720 min) at 120 °C
- Cooling regime: 5 °C per min down to 20 °C

Duration of heating and dwell temperatures were varied as part of the experimental investigations. Temperatures were varied between 100 °C and 150 °C, while durations were varied between 30 min and 1440 min

2000 mL reactor

The standard procedure for hydrothermal treatment of a precursor suspension started with the transfer of precursor into the Hastelloy vessel of the reactor. The vessel was then sealed using its split O-ring seal, after which the jacket tube furnace was fitted around the reactor. Standard operating conditions for this equipment were:

- Step 1: heat to 120 °C in 24 min
- Step 2: heat from 120 °C to 120 °C (hold temperature) for 360 min
- Step 3: cool vessel from 120 °C to 20 °C in 24 min
- Step 4: hold temperature at 20 °C indefinitely

Modifications to this general procedure included:

- The usage of a stirrer;
- Volume of precursor in the reactor charge;
- Hydrothermal treatment durations and temperature.

Stirring rates were varied between 0 rpm and 300 rpm.

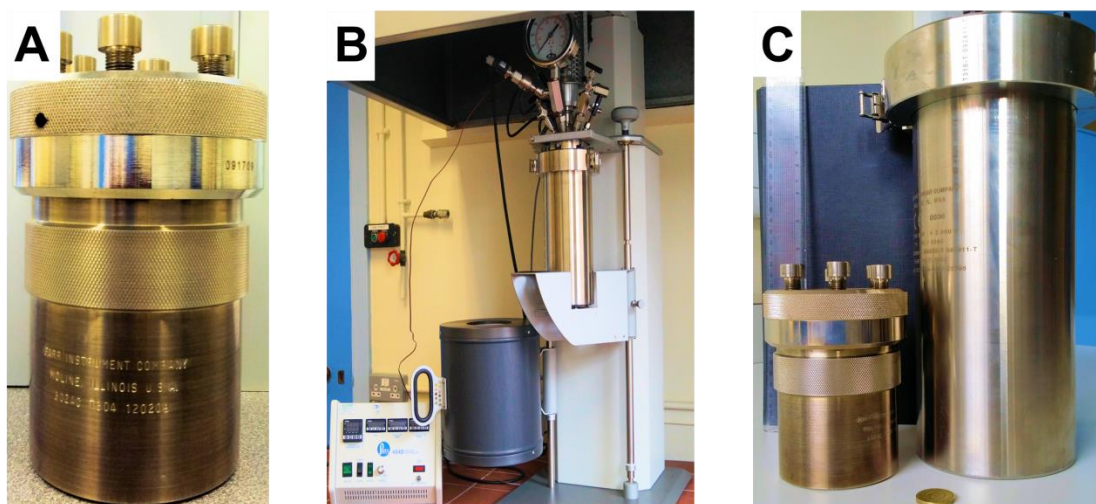


Figure 3.1: Hydrothermal reactors (a) 125 mL capacity non-stirred Acid Digestion Vessel [Parr Instruments Model – 4748], (b) 2 L stirred bench top reactor [Parr Instruments Model – 4250]. (c) Comparison of both reaction vessels

3.1.1.3 Stage 3: Product Recovery, Washing and Storage

After cessation of hydrothermal treatment, the product particles were recovered through a combination of decantation, centrifugation and ultrasonication.

At the end of hydrothermal treatment, when the 125 mL hydrothermal reactor was used, the Teflon cup was removed from its jacket and opened. pH readings were taken before the liquid portion of the container was decanted into a beaker, leaving behind the precipitates settled at the base of the Teflon cup. Distilled water was then squirted into the Teflon cup to dislodge the particles before they were transferred into polypropylene centrifuge tubes for washing.

In the case of the 2000 mL hydrothermal reactor, the post-reaction contents of the vessel were poured into large beakers and left to stand for a few minutes to allow for sedimentation of particles to the bottom of the beaker. pH readings were then taken and the clear liquid portion at the top decanted off into another beaker. The bottom section which contained the solids was then transferred into polypropylene centrifuge tubes for washing.

In both cases, the tubes were placed in a centrifuge (Centurion 2000 series, Chichester, UK) and spun at 6000 rpm for 5 min to separate the particles from other reaction by-products. After centrifugation, the top liquid (supernatant) was decanted off and discarded. The tubes were refilled with Milli-Q purified water before they were placed in an ultrasonic bath for about 5 min to redisperse the particles. After sonication, the tubes were taken back into the centrifuge. The centrifugation-decantation-sonication- centrifugation cycle using purified water was repeated up to a maximum of 4 cycles depending on the solids loading of the centrifuge tubes after which a further 2 cycles were then performed with methanol (Fischer Biotech, Biotech grade $\geq 99.9\%$) employed instead of water to replace the discarded supernatant. The substitution of water for methanol at the end of washing procedure was done for a number of reasons namely:

- To reduce the time taken to dry the suspension into a powder.
- To reduce particle aggregation during drying (since methanol has a lower surface tension than water).
- To facilitate faster sample preparation (via drop casting) for electron microscopy.

After washing, the tubes were emptied into a petri dish and dried overnight in a Sanyo Gallenkamp (Fistreem) laboratory oven (Loughborough, UK) set at 70 °C. Usually, a couple of centrifuge tubes containing the product particles dispersed in methanol were retained to provide samples for electron microscopy and dynamic light scattering analyses.

3.1.2 Synthesis of Sodium Zirconate powders

Sodium zirconate powders (NZO) were prepared through two solution based routes. The first involved preparation of precursor powder by mixing and evaporation of reagents followed by a calcination step. In the second route, a spray drier was used to enhance the quality of dried precursor (increased surface area) before calcination to produce the NZO powder.

Synthesis through both routes involved the usage of sodium acetate (ACS reagent, $\geq 99.0\%$ purity) and zirconium (IV) acetate in dilute nitric acid (Aldrich, 1.279 g mL^{-1}). No purification processes were performed on the reagents prior to usage.

3.1.2.1 Stage 1: Precursor Powder Preparation

Evaporation drying

About 4.1 g (50 mmol) of sodium acetate were dissolved in 300 mL of distilled water obtained in-house from a Milli-Q Millipore water purification system to which 6.5 mL (~25 mmol) of the zirconium acetate in nitric acid solution was added. The resultant solution was then stirred continuously on a heated Carousel™ stirring hotplate (Radleys, Essex, UK) till the solution was evaporated to dryness leaving behind a precipitate.

The resultant precipitate was calcined by placing inside an alumina crucible and transferring into a Carbolite chamber furnace (CWF 1200, Carbolite®, Hope Valley, UK). The furnace was programmed as follows:

- Heating regime: $5\text{ }^{\circ}\text{C}$ per min up to $900\text{ }^{\circ}\text{C}$
- Dwell/hold regime: 2 h (120 min) at $900\text{ }^{\circ}\text{C}$
- Cooling regime: $5\text{ }^{\circ}\text{C}$ per min down to $20\text{ }^{\circ}\text{C}$

After calcination, the product powders were stored under vacuum.

Spray drying

Solution preparation procedure via this route was similar to that for evaporation drying route. However, the prepared solution was spray dried into a fine powder on a LabPlant SD-05 bench-top spray dryer (Lab-Plant, UK). Figure 3.2 shows a schematic of the spray dryer with key parts labelled, while Figure 3.3 is a picture of the LabPlant SD-05 bench-top spray dryer used.

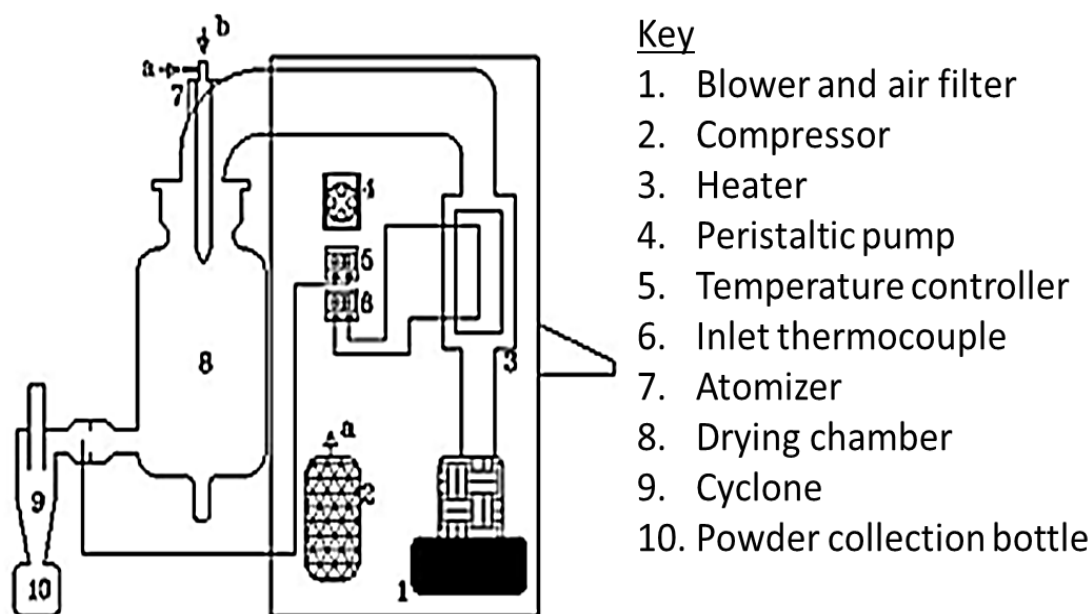


Figure 3.2: Schematic of the LabPlant spray dryer showing key elements of the equipment (Souza et al., 2008).

A concurrent flow regime was used during spray drying. The drying chamber had a diameter of 215 mm and a height of 500 mm (Figure 3.2) The main components of the system were the extract feed system, composed of a peristaltic pump, a two-fluid atomizer (inlet orifice diameter of 0.5 mm) and an air compressor; a feed system for the drying gas, composed of a blower and an air filter; and a temperature control system for the drying gas. The dried product was collected in a Lapple cyclone with a diameter of 0.085 m (cut diameter of 3.9 μm). Table 3.1 contains details of other operation conditions for the LabPlant spray drier:

Table 3.1 Operating conditions of LabPlant spray dryer.

S/N	Conditions	Value
1	Inlet temperature [°C]	200
2	Aspirating air flow [m ³ h ⁻¹]	40
3	Peristaltic pump speed [mL h ⁻¹]	600
4	Compressor pressure [bar]	1.8



Figure 3.3: Picture of the LabPlant SD-05 spray dryer.

3.2 Analytical Methods for Particle Characterisation

Information relating to changes in the material characteristics of the particles such as: morphology, size, structure, composition, dispersion, length of milling, etc. with respect to synthesis conditions and variables were obtained through the following analytical methods:

- Powder X-ray diffraction (XRD) analysis
- Scanning electron microscopy (SEM)
- Transmission electron microscopy (TEM)
- Dynamic light scattering (DLS) analysis
- Thermal gravimetric analysis (TGA)

In addition to the foregoing, some characterisation experiments were also conducted on a 'one-off' basis such analysis included:

- Brunauer–Emmett–Teller (BET) analysis

3.2.1 Powder X-ray Diffraction Analysis (XRD)

3.2.1.1 Principles

X-rays are electromagnetic radiation having a wavelength of about 1 angstrom (Å) (i.e. 10^{-10} m). Powder X-ray diffraction is a widely used and key characterisation technique in the field of material science (Hammond, 2009).

Characteristic X-rays are emitted when a metal source (copper in this case) is bombarded by accelerated electrons emitted from a heated metal filament, resulting in $K\alpha$ and $K\beta$ emissions from the excited copper metal. The $K\alpha$ and $K\beta$ emissions are due to the transitions of electrons from the 2p orbitals of the L shell to the K shell in Cu as shown in Figure 3.5 (Bearden, 1964). These multiple emissions are then monochromatized by a graphite crystal such that characteristic Cu, $K\alpha$ X-ray with wavelength $\lambda = 1.541874$ Å is what ends up incident on the sample. X-rays are normally generated by X-ray tubes, but can be also produced by synchrotron radiation which has shorter wavelength and higher flux relative to conventional X-rays, providing better structural information of the sample (Jeziarski, 2015). The X-ray diffraction analysis

technique works based on the principle, that atoms within a crystalline structure, exist in a three dimensional lattice which could scatter incident X-rays with the occurrence of constructive interference at certain angles to yield a diffraction peak. A series of these diffraction peaks from the particles may form what is called a diffraction pattern. Specific information on the crystallographic properties of the material under investigation can then be obtained from the powder diffraction pattern (Speakman, 2010; Jurgen, 2013).

The origins of X-ray diffraction can be traced to the independent efforts of Laue, Friedrich and Knipping in Munich in 1912 and that of Sir W. H. Bragg and his son Sir W. L. Bragg in Leeds and Cambridge around 1913 (Hammond, 2009). The latter who received the Nobel Prize in physics in 1915 for their work, developed a relationship to illustrate that crystal planes could scatter incident X-ray beams. This relationship is called the Bragg equation. Figure 3.4 is a schematic representation of the Bragg diffraction (equation); in the schematic, incoming monochromatic X-ray beams interact with a crystalline solid and are scattered from lattice planes separated by the distance 'd'. When the scattered waves interfere constructively, they remain in phase as the path length of each wave is equal to an integer multiple of the wavelength 'λ'. The path difference between two waves undergoing constructive interference is given by the relationship $2d\sin\theta$, where 'θ' is the scattering angle (also called the Bragg angle) (Hammond, 2009; Speakman, 2010). Mathematically Bragg's equation is represented as:

$$n\lambda = 2d\sin\theta \qquad \text{Equation 3.1}$$

Where:

'd' is the lattice interplanar spacing of the crystal, and

'n' is an integer

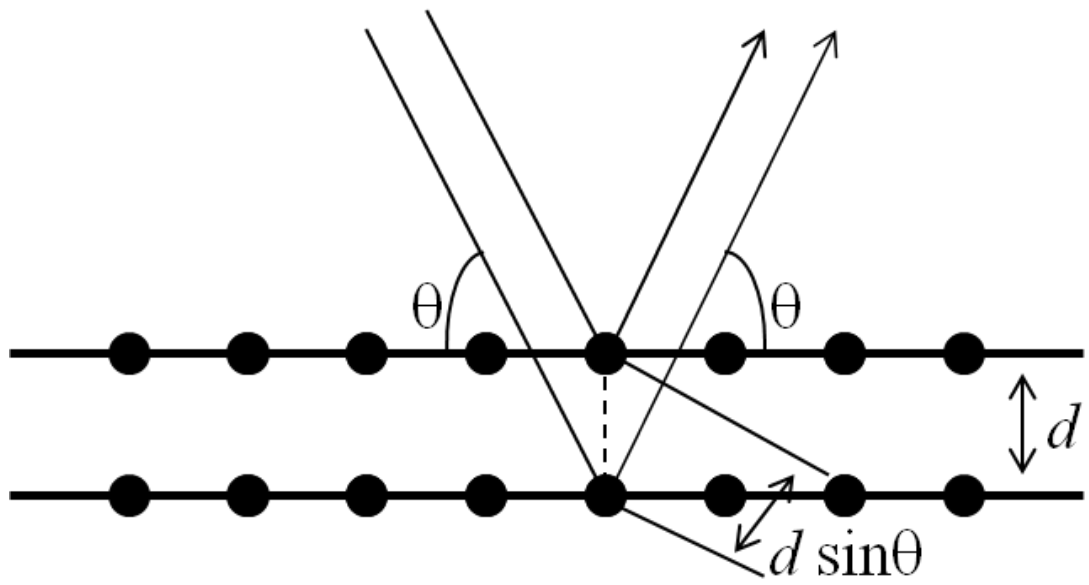


Figure 3.4: Illustration of diffraction geometry (Jurgens, 2013).

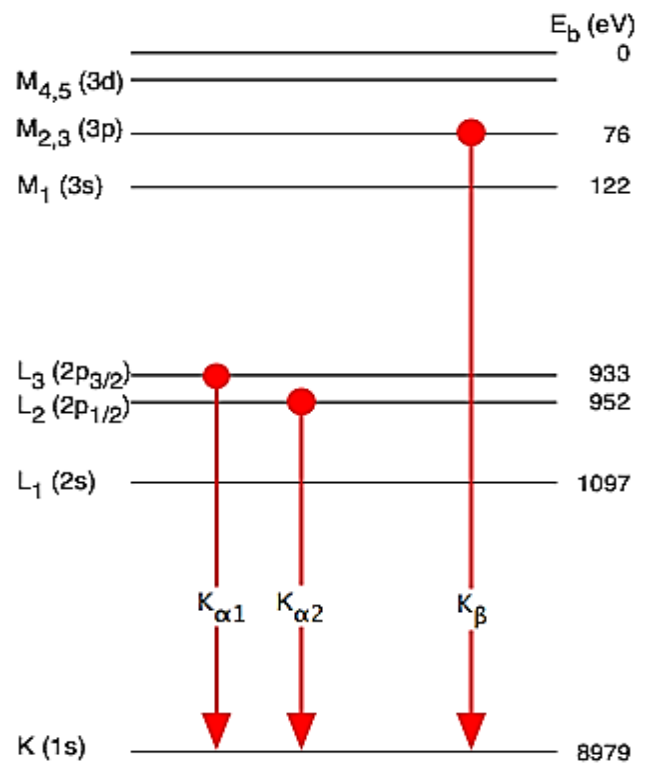


Figure 3.5: Illustration of electron energy levels in copper and associated K α and K β emissions (Bearden, 1964).

Miller Indices

Miller indices are a way of describing directions and planes in a crystal developed by W.H Miller. The Miller index notation uses a system of three integers hkl to describe lattice vectors (Hammond, 2009).

In the cubic crystal system, the integers hkl inside curved brackets i.e. (hkl) is used to identify a plane (or a series of parallel planes) and the Miller indices of a plane are the same as those of the direction perpendicular to the plane (Figure 3.6). A Miller index of 0 means that the plane is parallel to the respective axis. Negative indices are indicated with a bar written over the number.

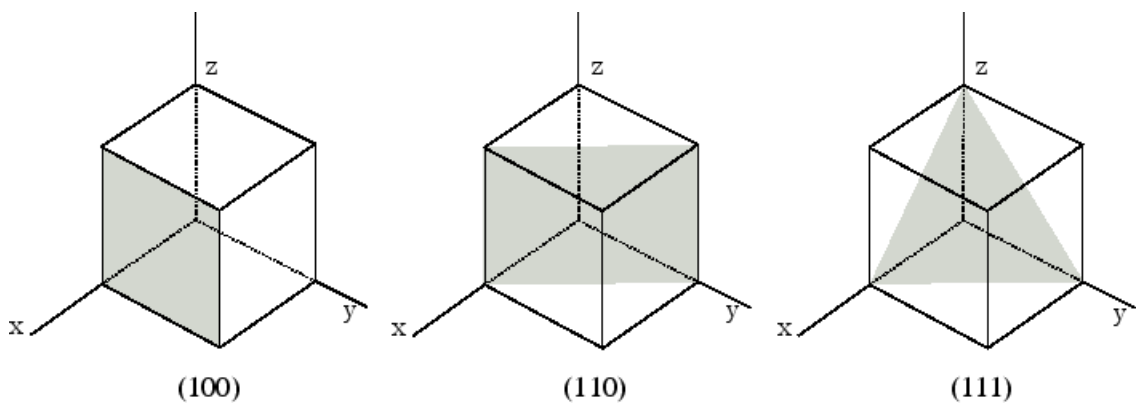


Figure 3.6: Illustration of Miller indices using a cubic crystal system (Ungersboeck, 2007).

Other Miller index notations include:

A combination of hkl integers inside a square bracket i.e. $[hkl]$ to denote vector direction based on lattice vectors e.g. $[100]$, $[010]$ and $[001]$ means the along the a-axis, b-axis and c-axis respectively (Fretwell et al., 2007).

A combination of hkl integers inside a parenthesis i.e. $\{hkl\}$ denotes the set of all planes that are equivalent to the family of planes represented by (hkl) by the symmetry of the lattice. For example, $\{111\}$ comprises of the set of planes (111) , $(\bar{1}\bar{1}1)$, $(1\bar{1}\bar{1})$ $(11\bar{1})$.

A combination of hkl integers inside angular brackets i.e. $\langle hkl \rangle$ denotes the set of directions that are equivalent to direction $[hkl]$. For example $\langle 111 \rangle$ comprises of the lattice directions $[111]$, $[\bar{1}\bar{1}1]$, $[1\bar{1}\bar{1}]$, and $[11\bar{1}]$

For the hexagonal crystal system, the use of Miller indices, results in a situation where crystallographically equivalent planes have indices which appear dissimilar. A modification of the Miller indices called the Miller Bravais indexing system can be used to remedy this (Fretwell et al., 2007; Hammond, 2009). The Miller-Bravais indexing system involves the addition of another integer i to hkl such that the series of planes denoted by (hkl) is now denoted by $(hkil)$ where:

$$i = -(k + l) \qquad \text{Equation 3.2}$$

Phase Identification and Phase Composition

It is possible to distinguish between different phase materials in the same sample by using the three strongest peaks of each phases' characteristic diffraction pattern (tagged d_1 , d_2 and d_3). The diffraction pattern of such a mixture or multiphase compound is a simple sum of the scattering from individual component phases that make up the mixture or compound (Speakman, 2010). Phase identification can be performed by comparing the peak positions (2θ) and corresponding relative intensities of the experimental pattern with a database of known reference peak positions and relative intensities of elements, alloys, organic / inorganic / organo-metallic compounds, and minerals in existence. One of such databases is known as the International Centre for Diffraction Data (ICDD) database; initiated around 1930 by Hanawalt and co-workers at the Dow Chemical Company (Hanawalt and Rinn, 1986); and later expanded by the American Society for Testing and Materials (ASTM) in 1941 before the Joint Committee on Powder Diffraction Standards (JCPDS) got involved in 1969 resulting in the JCPDS database which is now referred to as the ICDD database (Messick, 2011). Other databases from which reference files could be sourced include (Speakman, 2010):

- NIST Structural Database (metals, alloys, intermetallics)
- CCDC Cambridge Structure Database (CSD) (organic materials)

The comparison process is called indexing and a phase or material is identified when a reference file is found with correlating consecutive matches for peak positions and relative intensities. After a match is found, information such as crystal lattice parameters, etc. can then be extracted from the reference

pattern. Table 3.2 shows the indexing process of X-ray diffraction analysis results of a single phase zinc oxide powder using the reference pattern for monophasic wurtzite zinc oxide with the file number 04-013-6607 in the ICDD database: Figure 3.7 is the plot labelled with corresponding hkl planes.

It is possible to automate the phase identification process using software such as HighScore Plus (Spectris, Surrey, UK), which has algorithms that can automatically detect peaks in a diffraction pattern, and then search its inbuilt database according to user query to provide a list of possible matches from which the user can then select a best fit.

Details about a material that could be extracted or derived from data obtained via X-ray diffraction include the following (zur Loye, 2013):

- Lattice parameters
- Phase identity
- Phase purity
- Crystallite size
- Crystal structure
- Percent phase composition

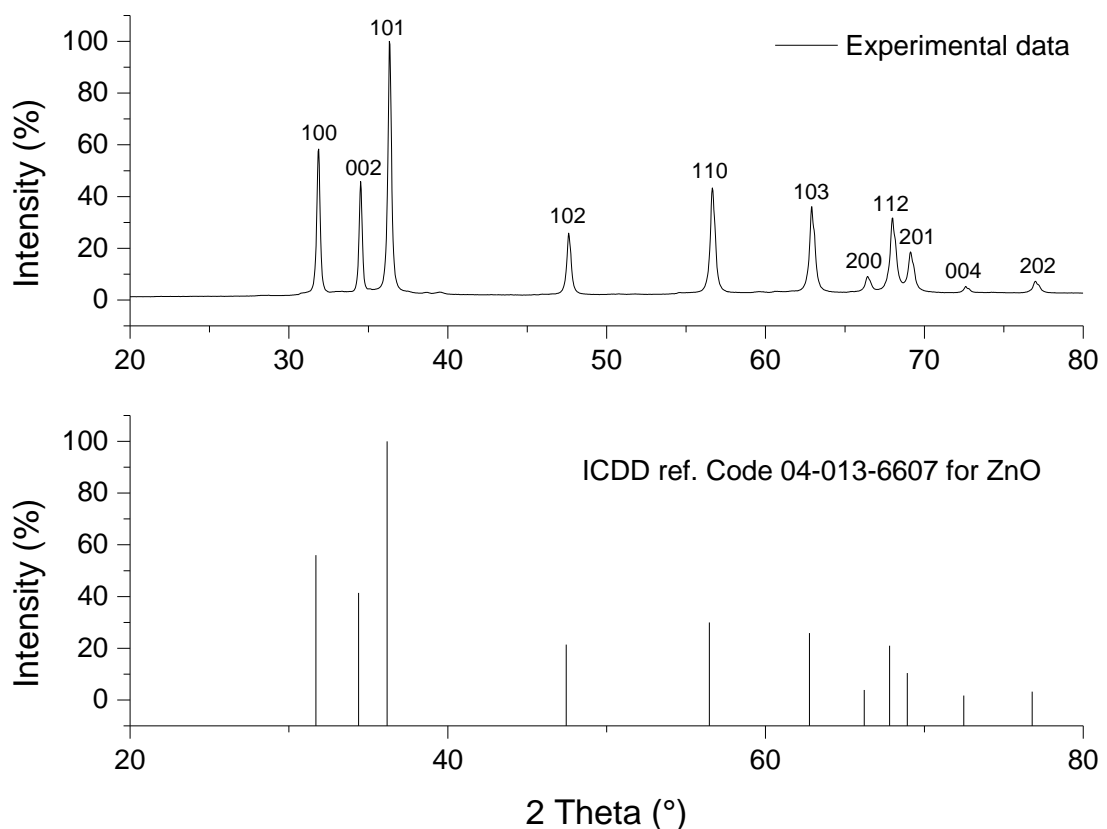


Figure 3.7: Indexed X-ray diffraction patterns for single phase wurtzite zinc oxide showing hkl planes.

Table 3.2 Indexing of experimental pattern from synthesis of zinc oxide double rods to ICDD reference pattern 04-013-6607 for wurtzite ZnO.

Experimental Data			ICDD ZnO reference 04-013-6607						
2θ	d [Å]	I [%]	2θ	d [Å]	I [%]	h	k	i	l
31.70	3.822	53.6	31.77	3.814	55.4	1	0	-1	0
34.35	3.611	53.4	34.43	3.603	41.5	0	0	0	2
36.18	3.483	100.0	36.26	3.476	100	1	0	-1	1
47.46	1.916	25.9	47.55	1.911	21.9	1	0	-1	2
56.50	1.629	39.2	56.60	1.625	31.2	1	1	-2	0
63.77	1.480	35.9	63.88	1.477	27.8	1	0	-1	3
66.27	1.410	5.8	66.39	1.407	4.2	2	0	-2	0
67.84	1.381	29.3	67.96	1.378	23.7	1	1	-2	2
68.98	1.361	15.2	69.10	1.358	11	2	0	-2	1
73.47	1.304	3.5	73.58	1.301	1.8	0	0	0	4
76.84	1.241	4.4	76.98	1.238	3.5	2	0	-2	2
81.30	1.183	3.3	81.41	1.181	1.8	1	0	-1	4
89.47	1.095	8.7	89.63	1.093	7	2	0	-2	3

3.2.1.2 Specimen / Sample Preparation

Sample preparation for XRD analysis of zinc oxide, sodium zirconate and sorbent powders was very similar. Using powders obtained after completion of drying stage, sample holders were selected based on the amount of powder available for analysis. Figure 3.6 shows images of holders used during sample preparation with a pound coin (£ 1) used as a reference point for size comparison. A 10 mm or 20 mm bore diameter steel sample holder was used whenever there was a sizable quantity of powder available (Figure 3.8b), while an off-cut silicone sample holder (Figure 3.8a) was used when the quantity of sample was not sufficient enough to fill the bore of the steel holders. In both

situations, the holders were filled with the powdered sample and the top made flat using a stamping tool or a glass slide. To begin analysis, the sample holder was placed carefully on the spinner stage (Figure 3.9) and locked into position.



Figure 3.8: Sample preparation for X-ray diffraction analysis (a) off-cut silicon sample holder (b) 10 mm-bore steel sample holder (c) side view of the off-cut silicon sample holder

3.2.1.3 Analytical Procedure and Parameters

Powder X-ray diffraction analysis of zinc oxide and sodium zirconate powders was performed on a Phillips PANalytical X'Pert diffractometer (Spectris, Surrey, England).

A spinner stage was used as the preferred sample holder stage. The spinner stage usually was rotated during the course of analysis to improve the level of orientational homogeneity achieved during measurement, thus countering any effects of texturing. Table 3.3 outlines some of the parameters generally used in setting up typical X-ray diffraction scans along with key operational data for

the instrument. The software HighScore Plus also from PANanalytical, was used to analyse the X-ray diffraction results.

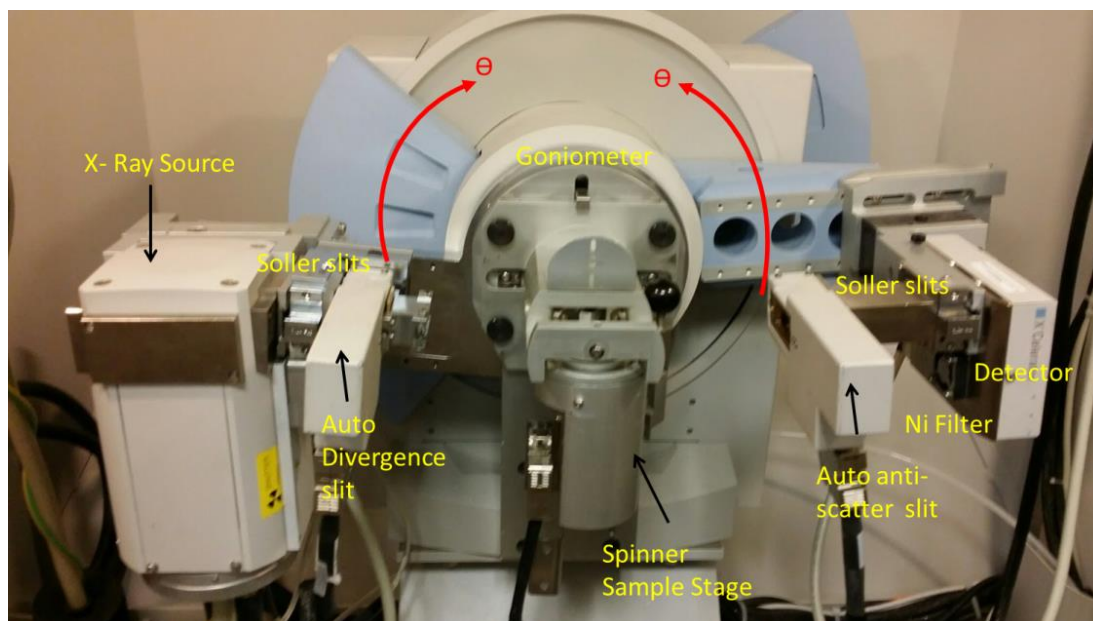


Figure 3.9: (a) The Phillips PANanalytical X'Pert diffractometer used (b) close up view of equipment setup and PW3064 spinner sample stage used.

Table 3.3: X-ray diffraction analysis parameters.

S/N	Parameter	Values
1	K-Alpha1 wavelength [Å]	1.54060
2	K-Alpha2 wavelength [Å]	1.54443
3	K-Beta wavelength [Å]	1.39225
4	K-A2 / K-A1 Intensity Ratio	0.50000
5	Generator Settings	40 mA, 40 kV
6	Irradiated Length [mm]	15.00
7	Specimen Length [mm]	10.00
8	Measurement Temperature [°C]	25.00
9	Anode Material	Cu
10	Scan Axis	Gonio
11	Start Position [°2Th.]	(varied between ~0 and ~20)
12	End Position [°2Th.]	(varied between ~70 and ~85)
13	Step Size [°2Th.]	(varied)
14	Scan Step Time [s]	(dependent on parameters 11 - 13)
15	Sample stage	Spinner PW3064

3.2.1.4 Limitations of the X-ray Diffraction Technique

XRD is a technique that is suitable for well-defined crystals or poorly ordered nanocrystalline material. It is not fit for purpose for the analysis of amorphous substances. Other limitations / errors that relate to XRD analysis include the following:

1. Only a small portion of the crystallites in the sample of materials actually contribute to the diffraction pattern that is produced; this occurs because other crystallites / grains in the sample are not properly oriented to be able to produce observable diffraction. One of the ways to mitigate the impact of

this phenomenon is to rotate the sample during the course of analysis, hence the decision to make use of the Spinner PW3064 stage for experimental work conducted in the course of this PhD. The spinner stage can be rotated as X-ray analysis occurs.

2. Another shortcoming is that just a minute fraction of the X-rays that are scattered by the crystallites in the sample are actually observed by the detector when using a linear detector. This happens because diffraction from multiple random crystallites in the sample form what is called a Debye diffraction cone; however, the X-ray detector scans round the sample in an arc movement therefore a linear diffraction pattern is formed as the detector scans intersects each Debye cone at a single point; producing the appearance of a discrete diffraction peak. The way to mitigate the impact of this phenomenon is to make use of a large area, two-dimensional detector.
3. Furthermore, another phenomenon that could affect the data collected during X-ray diffraction analysis is called preferred orientation or texturing. It has been observed that when crystallites in the sample are not randomly oriented, it results in the attenuation of some Bragg reflections (Grattan-Bellew, 1975). Texturing leads to a systematic error in the observed diffraction peak intensities (Klug and Alexander, 1954). The degree of texturing depends on the amount of crystallites having the preferred orientation relative to the entire bulk of sample under analysis and can significantly alter the appearance of the diffraction pattern (Speakman, 2010). With respect to the experiments conducted in the course of this PhD research, rod-like and flake-like morphologies of zinc oxide were produced via hydrothermal synthesis. These particles have anisotropic dimensions, and tend to settle on their sides and flat faces respectively. Thus, in the event of a large number of the zinc oxide rods settling down on their sides ($\{0110\}$ facets), or of flakes on flat faces ($\langle 0100 \rangle$), there could be the potential for the occurrence of preferred orientation.

3.2.2 Scanning Electron Microscopy (SEM)

3.2.2.1 Principles and Applications

Scanning electron microscopy provides the opportunity to study relatively large sample sizes over a shorter period of time and is well suited for studying particle structure, size, and surface. The scanning electron microscope (SEM) is capable of analysing samples from a few hundred micrometres to nanoparticulate samples. In comparison to the optical microscope, the SEM has higher resolution limits and a much improved (by a factor of ~300) depth-of-focus resolution (Smith and Oatley, 1955; Lenhart, 2005).

In the scanning electron microscope a beam of high energy electrons (up to 40 keV) is produced by an electric gun, after which it is channelled through a system of electromagnetic fields and lenses that focus the electron beam on the sample / specimen placed in a vacuum chamber, the electron beam is then scanned across the sample / specimen by scan coils.

The sample / specimen, interacts with the incident primary electron beam in a number of ways which could involve transmission of the electrons, elastic scattering, and inelastic scattering of the electrons (Figure 3.10). Elastic scattering occurs when the pathway of electrons from the incident beam is deflected by atoms within the specimen with the total kinetic energy of the electron conserved, while inelastic scattering occurs when electrons from the incident beam collide with a nucleus or electron of an atom of the specimen causing it to change direction as well as transfer energy to the specimen (Atteberry, 2009, Henry, 2012; Goodhew, et al., 2007).

Both elastic and inelastic scattering lead to the generation of signals which can be detected and processed to obtain quantitative and qualitative information about the sample (Caceres, 2002). These signals are: secondary electrons (SE), backscattered electrons (BSE), cathodoluminescence (CL), Auger electrons and characteristic X-rays, and they can provide information on:

- Particle size and shape
- Specimen composition
- Topography

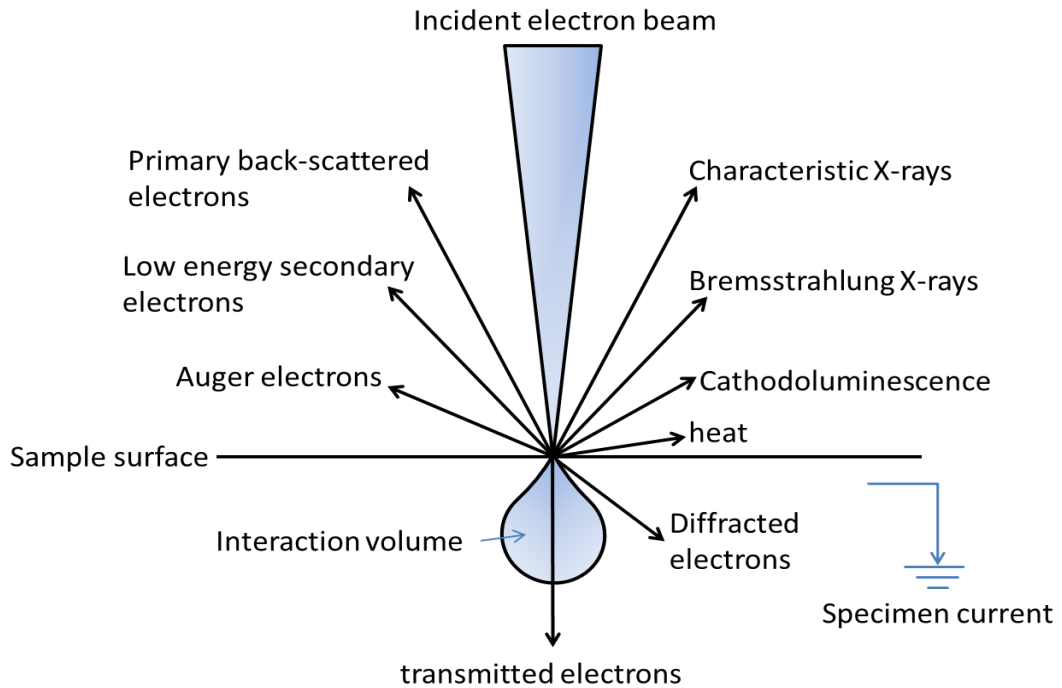


Figure 3.10: Sample – electron interactions after (Caceres, 2002).

Secondary electrons (SE) are electrons ejected from near surface portions of the sample due to the impact of incident electrons from the primary electron beam (inelastic scattering). Secondary electrons have low energies (below 50 eV). Because SE come from close to the surface of the sample, they could provide topographic information, providing a depth of field and 3-D shadowing effects in SE micrographs depending on the number of electrons emitted and their trajectories relative to the position of the detector (Krumeich, 2015).

Backscattered electrons (BSE) result from the deflection of the incident beam by atoms in the sample (elastic scattering), backscattered electrons have higher energies (50 eV up to the SEM accelerating potential) and can be produced over a larger depth range. Because heavy atoms with a high atomic number Z (e.g. Cu, Sn, Zr) produce a stronger scattering relative to lighter atoms, BSE are strongly dependent on the atomic number of the material; thus, compositional information can be deduced from images recorded with back-scattered electrons (BSE) with the heavier atomic number materials appearing brighter; therefore, discrimination of phases based on mean atomic number (Z contrast) can be done when imaging in backscattered (BSE) mode which could help in quick identification of phases in a mixed phase material (Jaimes, 2013).

Types of Electron Guns

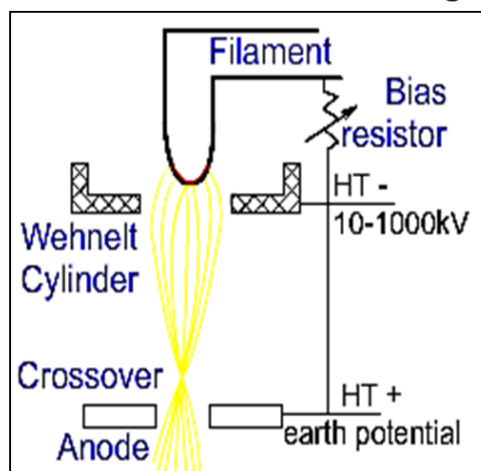
The scanning electron microscope houses an electron gun usually located on the top of the instrument which generates the high energy electron beam that is then focussed by a system of electromagnetic fields and lenses (Atteberry, 2009). There are two major types of electron guns (Figure 3.11):

- Thermionic emission electron gun
- Field emission electron gun

Thermionic electron guns generate electron beams by emitting electrons from a heated filament. Filaments for thermionic emission equipment are usually produced from a high melting point metal with a low work function (the energy required to take an electron from the Fermi level to the vacuum level). Such as tungsten and lanthanum Hexaboride (LaB₆).

A field emission gun generates electrons via the extractive power of a very strong electric field applied to a metal filament. For field emission to occur, the electric field has to be $\geq 10^9 \text{ V m}^{-1}$. Field emission could occur from a cold material when a sufficiently high field, in excess of 10^9 V m^{-1} , is applied; microscopes with this type of electron gun are called cold field emission gun microscopes. A second type of field emission occurs when the filament of a thermionic emitter is coated with another material (e.g. ZrO_x) to enhance its effectiveness of the emitter by reducing its work function. Microscopes with this type of electron gun are called Schottky field emission gun microscopes.

Thermionic emission electron gun



Field emission electron gun

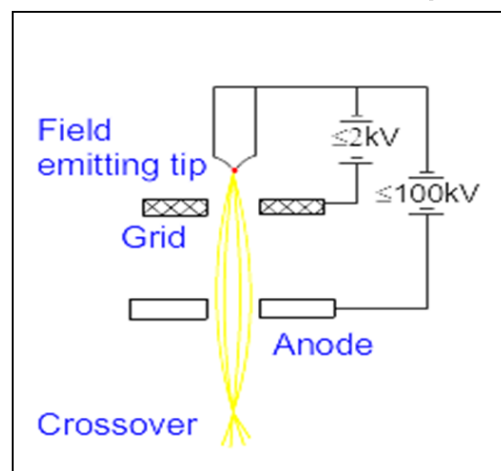


Figure 3.11: Thermionic and field emission guns: after (Goodhew, et al., 2007).

Schottky and cold-field emission are superior to their thermionic counterparts in terms of source size, brightness, and lifetime, however, they have much higher vacuum requirements (Table 3.5).

Cold field emission (CFE) gun microscopes can offer a better signal to noise (S/N) ratio than their thermionic and Schottky field emission counterparts with capabilities of imaging at low acceleration voltages or deceleration voltages. However because they (CFE) rapidly become covered with adsorbate molecules from the vacuum system walls, they need to be cleaned from time to time by “flashing” to high temperature (Hitachi, 2015; Gunasekaran, 2011; Hitachi, 2013; Jaimes, 2013).

Table 3.4: Comparison between electron guns (Hitachi, 2013; Hafner, 2007).

	Field emission		Thermionic emission	
	Cold	Schottky	LaB ₆	Tungsten hairpin
Source size	5 nm	15 – 30 nm	5 - 50 μm	30-100 μm
Energy width [eV]	0.2 – 0.3	0.3 – 1.0	1.5	3.0
Brightness [A cm⁻² sr]	10 ⁸	10 ⁷	10 ⁵	10 ⁵
Cathode Material	Tungsten	Tungsten/ZrO _x	LaB ₆	Tungsten
Working pressure [Pa]	10 ⁻⁸	10 ⁻⁷	10 ⁻⁵	10 ⁻⁴
Cathode Temp [K]	~300	1,700 – 1,800	1,800	2,600
Lifetime (h)	> 1,000	> 1,000	200 – 1,000	40 - 100

N.B.: Majority of the values quoted above could vary slightly, dependent on the make and type of microscope

The LEO (Zeiss) Gemini 1530 microscope used at the beginning of particle characterisation experiment was equipped with a Schottky field-emission gun (Figure 3.12), while the Hitachi SU8230 ultra-high resolution (UHR) microscope used at later stages had a cold field emission electron gun (Figure 3.13).



Figure 3.12: LEO (Zeiss) Gemini 1530 FEG-SEM.

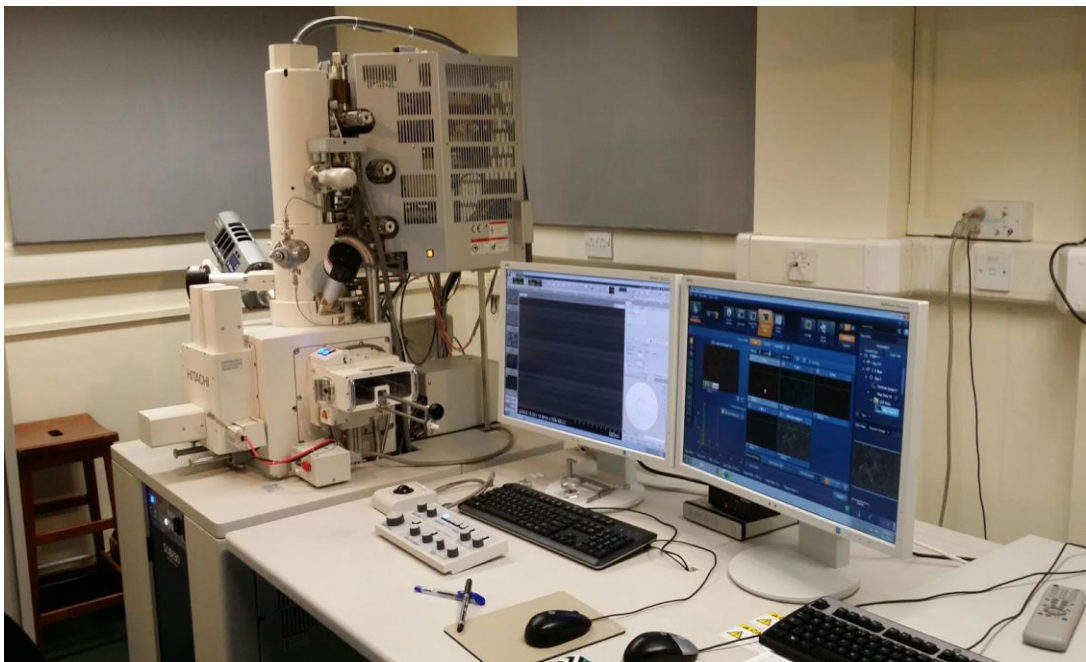


Figure 3.13: Hitachi SU8230 UHR Cold-Emission FE-SEM.

Detectors

Detection of secondary electrons (SE) and backscattered electrons (BSE) can be achieved in most scanning electron microscopes by the use of an Everhart-Thornley detector (ET detector) (Figure 3.14). Named after its designers T. E. Everhart and R. F. M Thornley, the detector consists of a scintillator / photomultiplier construct surrounded by a Faraday cage. When SE strike the scintillator, its electrical energy is converted to a photon. The photon travels down a light pipe, where it enters the photomultiplier tube. In the photomultiplier tube, the photons are changed back to electrical energy, through a series of photon-electron conversions across dynodes. Amplification then occurs to improve the SE signal and achieve high signal to noise ratio (SNR). The signal is further refined in the preamplifier and amplifier before being projected onto the screen of a cathode ray tube (CRT). There is usually a one-to-one correspondence between a point scanned on the sample, and a pixel on the viewing screen (Nessler, 2015; Goodhew et al., 2007; Hafner, 2007; Griffin, 2011). Collection efficiency for the secondary electrons can be enhanced by the application of a small positive bias to the Faraday cage (up to +250 V). The ET detector functions as an inefficient BSE detector as it cannot attract high-energy BSE electrons moving in other directions. To pick up BSE (whose trajectory is in line of sight of the detector), a negative bias (up to – 50 V) can be applied to the Faraday cage as well as removal of scintillator bias (10 – 15 kV), leading to the exclusion of the low energy SE (Hafner, 2007; Griffin, 2011).

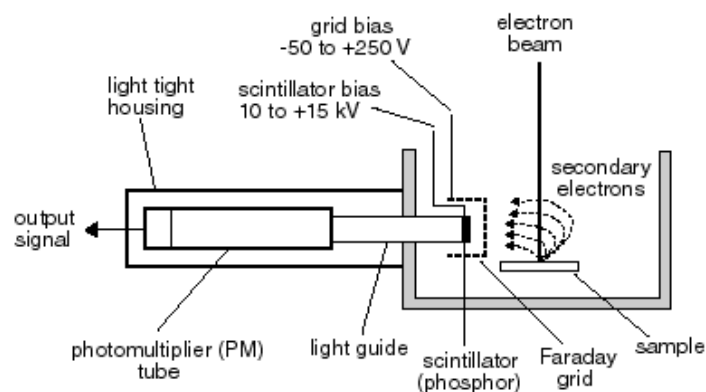


Figure 3.14: Schematic of an Everhart-Thornley detector (Hafner, 2007).

Apart from the ET detector (which is usually side-mounted below the electron column), we have another type of detector called the in-lens ('through the lens') detector because it is located inside the electron column of the microscope on the source side of the pole piece of the final lens and is arranged rotationally symmetric around the optical axis (Griffin, 2011; Brodusch et al., 2014; Hafner, 2007).

The In-lens detector is an improvement over the ET detector in that due to a sophisticated magnetic field at the pole piece, signals can be collected with high efficiency especially at low accelerating voltages and short working distances (Griffin, 2011; Brodusch et al., 2014; Goodhew et al., 2007).

Furthermore, because the ET detector is usually side-mounted below the electron column, it views a sample from one side and so the side of the sample facing away from the detector appears shadowed as SE emitted towards the detector are more likely to be collected than those travelling away from the detector meaning that the position of a sample surface relative to the detector, affects its brightness in the resultant image (shadowing effects). On the other hand, In-lens detectors are positioned higher up (detector views the sample from above), and collection of SE is more symmetrical (Griffin, 2011; Brodusch, et al., 2014; Krumeich, 2015).

In addition to providing information about morphology and surface topography, the in-lens detector can image differences in the work function (e.g., electronic variations) on the sample with high lateral resolution. Most modern day SEMs now come with both an in-lens detector, and an ET detector (Griffin, 2011; Brodusch, et al., 2014; Nessler, 2015).

The LEO Gemini 1530 microscope was equipped with both an in-lens detector and a conventional ET detector, while the Hitachi SU-58 cold SU8230 UHR FESEM was equipped with multiple detectors starting with top, upper (in-lens) detectors and lower (ET) detector for SE & BSE detection (Figure 3.15). The upper detector is capable of SE / BSE signal mixing functions, while the top detector has filter function which can selectivity filter inelastic scattering electrons. It is worthy of note, that the beam deceleration voltage in the Hitachi FESEM, can be optimized to yield a landing voltage of 10 - 2000 V such that

beam sensitive samples, e.g. organic materials, can be observed in their natural state without beam damage or sample deformation; however, this feature was not used in the course of research (Hitachi, 2013). For BSE, the Hitachi FESEM had a yttrium aluminium garnet (YAG) BSE and a photodiode BSE (PD-BSE) detectors (Figure 3.15).

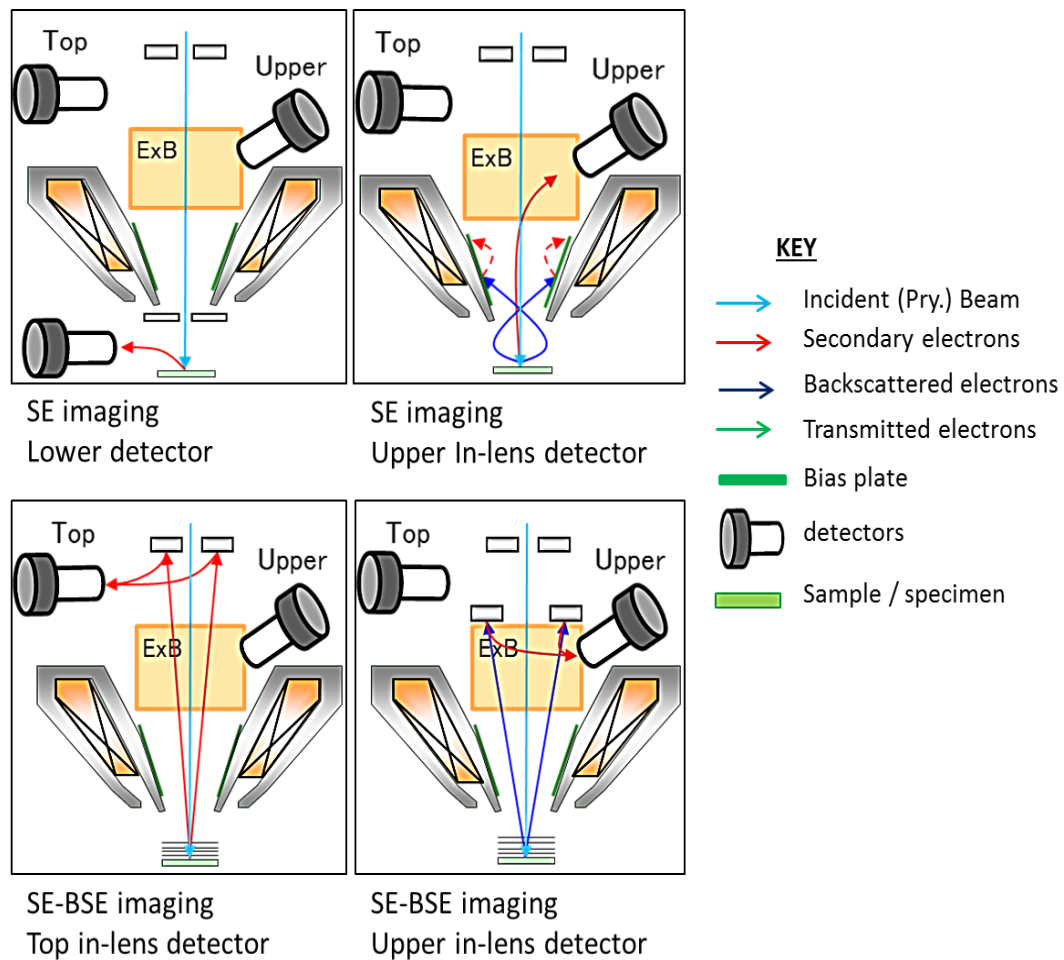


Figure 3.15: Schematics showing operations of the lower upper, top detectors for SE & BSE imaging in the Hitachi SU8230 cold emission FE-SEM (Micklethwaite, 2015).

The Hitachi SU8230 UHR cold FESEM also has a STEM detector for detection of transmitted electrons. The STEM detector is capable of bright field (BF) and dark field (DF) imaging using BF-STEM aperture and DF-STEM holder respectively; however, this feature was not used in the course of research work.

Energy Dispersive X-ray Spectroscopy (EDXS) on the SEM

Energy-dispersive (EDXS) spectrometers provide laterally resolved information about sample composition (Swapp, 2013). When equipped with an EDX detector, one can produce elemental maps of a sample or identify chemical composition of areas on the sample dependent on the interaction volume and resolution (Lenhert, 2005).

Both the Hitachi SU8230 UHR Cold FESEM and the LEO Gemini 1530 FEGSEM had an 80mm X-Max silicon drift (SDD) detector for energy-dispersive X-ray spectroscopy (EDXS). While the Hitachi FESEM also had an electron back scattered diffraction (EBSD) detector.

3.2.2.2 Limitations of Scanning Electron Microscopy

The scanning electron microscope like every other microscope has disadvantages and limitations, and they would be considered relative to similar techniques; the transmission electron microscope as well as optical microscopes.

Colour

Because electrons do not possess intrinsic colour properties, images produced by electron microscopes are normally monochromatic with a single brightness value per pixel and are presented in shades of grey unlike optical microscopes which image using photons of visible light (Caceres, 2002). However it is possible to false colour SEM images to highlight details.

Sample Size

The size of samples / specimen that can be viewed under a scanning electron microscope is usually quite small in comparison to other analytical techniques. Hence care has been taken during sample preparation to ensure that observations on the SEM were not localized and were representative of the bulk of the material.

Sample Preparation and Nature of Samples

With conventional scanning electron microscopes and FEG – SEMs the sample to be analysed needs to be a solid and also be moisture free. Hence it is usually difficult to analyse organic or biological samples on the scanning

electron microscopes. However, there are specialised microscopes like the environmental SEM (ESEM) which have the capability to handle moisture-containing and biological samples. Also, sample preparation procedures, could introduce artefacts which could impact on the quality of the analysis (Swapp, 2013).

Charging

When imaging with most scanning electron microscopes, there is usually the need to make the specimen / sample electrically conductive. This is because the SEM is designed with the sample stage at ground potential in view that that the primary electron beam will be absorbed by the specimen, and its current dissipated through the stage. Charging occurs when there is no / low dissipation of the current, resulting in poor images. Therefore, there should be a conductive path from the point of beam impingement, through the specimen, specimen mount, and finally specimen stage. This can be achieved by coating the sample with a nanolayer of an electrically-conducting material such as gold or platinum. However, it is possible to image non-conducting samples on a FEGSEM when operated at low voltage, and low vacuum (Schweitzer, 2014; Nessler, 2015).

Vacuum

The need to establish vacuum conditions in the scanning electron microscope prior to imaging eliminates the possibility of analysing biological specimens unless they are pre-dehydrated prior to analysis.

EDS Detector

It is usually difficult to identify light element (elements with atomic number lower than that of Sodium) on majority of conventional SEM-EDS systems (Swapp, 2013) However recent advances in EDS technology now make detection light elements including hydrogen possible although the technology is not widely available.

3.2.2.3 Sample Preparation

The presence of moisture in samples usually interferes with the operation of the scanning electron microscope as it degrades the vacuum conditions in the chamber; therefore it is important to ensure samples are dry before loading them into the SEM vacuum chamber (Smith and Oatley, 1955).

Sample preparation procedure was usually dependent on the type specimen to be analysed. Here, samples were either dry powders or particle suspensions.

In the case of particles in methanol / ethanol suspensions, sample preparation involved drop casting onto a cleaned aluminium SEM stub using a pipette, after which the stub was then dried in a hot air specimen dryer. The final stage of sample preparation involves loading the SEM stubs into a Hitachi ZONESEM desktop sample cleaner which removed organic film coatings from the surface of particles to be imaged using non-destructive dual-wavelength UV radiation. The cleaning process improves the quality of imaging, as the hydrocarbon deposits could create problems with focusing (Ogura, 2015).

For dry powders, sticky carbon films were placed on the surface of the aluminium stubs after which the powders were then deposited. Excess powder was blown off the surface off the stubs using compressed air canisters. Since there was no need for a drying step, the stubs were placed into the ozone plasma cleaner where they were cleaned for about 10 minutes.

3.2.2.4 Analytical Procedure and Parameters

Scanning electron microscopic imaging of zinc oxide, and sodium zirconate powders was performed on a LEO (Zeiss) Gemini 1530 FEG-SEM with an Oxford Instruments Aztec Energy EDS system using an 80mm X-Max silicon drift detector and a Hitachi SU8230 UHR Cold-Emission FESEM. Table 3.6 shows value ranges of some of the adjustable parameters during a typical imaging session

Table 3.5: SEM imaging parameters.

S/N	Parameter	Values
1	Accelerating Voltage [kV]	3.0 - 8.0 (imaging)
2	Magnification	varied
3	Working Distance [μm]	3.9 – 3.7; 8.0 (EDS mode)
4	Emission Current [nA]	18800 - 22300 (imaging)
5	Lens Mode	Normal
6	Image format	Tiff
7	Detectors	In-lens, Everhart-Thornley, 80mm X-Max silicon drift detectors (SDD)
8	Sample coating	Platinum
7	Coating height	3 – 5 nm

3.2.3 Transmission Electron Microscopy (TEM)

3.2.3.1 Principles and Applications

The transmission electron microscope operates on a similar principle as the scanning electron microscope, however, it images using transmitted electrons (TE) as opposed to secondary electrons (SE) or backscattered electrons (BSE) used by the SEM (Figure 3.10). Transmitted electrons are electrons that are transmitted through the specimen after an incident beam of electrons have interacted with the specimen being analysed (Caceres, 2002).

The setup of a transmission electron microscope is also similar to that of a scanning electron microscope in that a series of electromagnetic lenses are used to manipulate a beam of high energy electrons emitted from an electron gun (3.2.2.1) onto a specimen located in the specimen chamber. Images and other information are then extracted from the resultant beam- specimen interactions (Goodhew, et al., 2000).

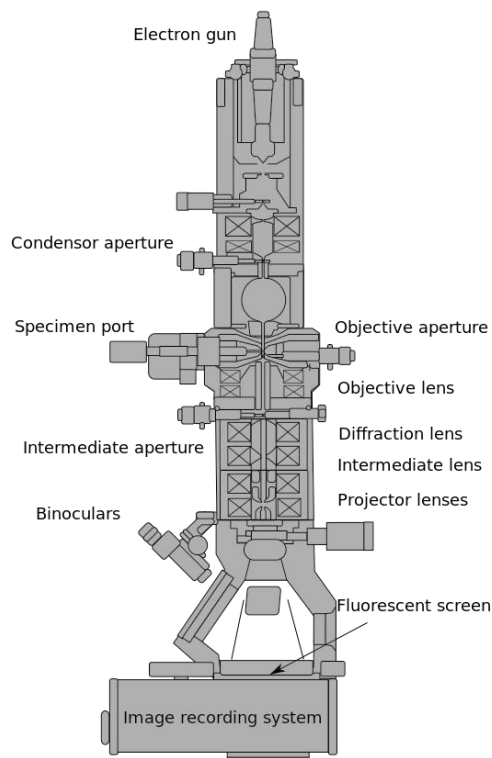


Figure 3.16: Schematic of a typical transmission electron microscope (Gringer, 2015).

Some of the information that could be obtained via transmission electron microscopy include:

- Sample size and shape
- Detailed micro and nanostructure
- Chemical composition, (via TEM-EDX)
- Crystallographic information (lattice imaging, TEM SAED)
- Electronic structure

Limitations:

One of the limitations of transmission electron microscopy (TEM) with respect scanning electron microscopy is that the amount of samples (or sampling area) that can be analysed on the TEM is much smaller. TEM grids are much smaller than SEM sample stubs usually no bigger than a few millimetres.

Also, samples to be analysed on the TEM need to be electron transparent, (i.e. they need to be able to allow electrons to be transmitted through it). This sometimes means special procedures (such as milling or etching) need to be undertaken to make a very thin sample (a few hundred nanometres) before a sample can be analysed on the TEM.

Further details on the principles and operations of the transmission electron microscope can be found in textbooks such as “transmission Electron Microscopy – Basics” by D.B. Williams and C.B. Carter or “Transmission Electron Microscopy: Physics of Image Formation and Microanalysis” by Ludwig Reimer.

3.2.3.2 Sample Preparation

Sample preparation for TEM analysis involved drop casting particles from a methanol / ethanol based suspension onto a holey carbon film- copper grid (Agar Scientific, Essex UK). The TEM grid was allowed to dry before it was loaded into the TEM specimen holder.

TEM analysis was performed using A FEI Tecnai F20 field emission gun TEM operated at 200 kV and equipped with a Gatan Orius SC600A charge coupled device (CCD) camera

3.2.4 Dynamic Light Scattering (DLS)

3.2.4.1 Principles and Applications

Dynamic light scattering is a versatile technique for studying a wide range of fine particle suspension phenomena such as: Brownian motion, turbulence, colloidal stability, using photon correlation spectroscopy. It is based on the understanding, that when a monochromatic beam of light is focused on a colloid / suspension, the incident light beam is scattered by the colloid / suspension, and that the scattering is due to the particles dispersed in the liquid medium.

A 'colloid' or 'colloidal suspension' is described as a dispersion in a liquid medium (solvent or solution) of particles with approximate dimensions of one side of the particle being less than 1 μm , and the particles are assumed not to be soluble in the medium (Goldburg, 1999; Sartor, 2003).

The dynamics of particle motion are observed by measuring the speed at which the particles diffuse due to Brownian motion. Based on the knowledge of the viscosity of the fluid and the refractive indices of both the fluid and particles, it is then possible to calculate the size distribution of the particles involved, as well as providing a description of the particle's motion in the medium by measuring the diffusion coefficient of the particle and using a digital autocorrelation device (Malvern, 2015a; Sartor, 2003).

Intensity of scatter, volume and particle number distribution plots derived from DLS measurements are based on a number of assumptions and theories. The first is that the technique measures the diffusion of particles moving under Brownian motion, and that the probability density function (P), could be represented by the formula (Sartor, 2003):

$$P(r, t | 0,0) = (4\pi Dt)^{3/4} e^{(-r^2/4Dt)} \quad \text{Equation 3.3}$$

Where

'D' is the diffusion constant;

'r' the particle radius and

't' is time

Another key assumption made in DLS analysis is that the particles being observed are spherical in nature hence the term 'hydrodynamic diameter' is used to reflect the reality that particles measured are usually not perfect spheres (Goldburg, 1999; Sartor, 2003).

To obtain a size distribution from the density function, the Stokes-Einstein relationship was employed.

$$d(H) = \frac{K_B T}{3\pi\eta D} \quad \text{Equation 3.4}$$

Where:

' $d(H)$ ' is the hydrodynamic diameter,

' D ' is the particle translational diffusion coefficient, (which depends not only on the size of the particle "core", but also on surface structure, concentration and type of ions in the medium)

' k_B ' is the Boltzmann's constant,

' T ' is absolute temperature, and

' η ' is viscosity (Malvern, 2015b).

DLS combined with the correlation method of data analysis is often referred to as photon correlation spectroscopy; another alias for DLS is Quasi-Elastic Light Scattering (Malvern, 2015a; Sartor, 2003).

Other theories, used to extract size distribution information from light scattered by particles include: Lord Rayleigh's and Gustav Mie's Scattering theories (Malvern, 2015b; Hahn, 2009)

The Rayleigh approximation stipulates that:

$$I \propto d^6 \quad \text{Equation 3.5}$$

And also that

$$I \propto \frac{1}{\lambda^4} \quad \text{Equation 3.6}$$

' I ' is the intensity of light scattered; ' d ' the particle diameter and ' λ ' is the laser wavelength.

3.2.4.2 Limitations of the Dynamic Light Scattering Technique

Most of the limitations that surround the usage, accuracy and reliability of the DLS technique are due to its heavy reliance on theoretical approximations and simplifications. Also, the size, shape and manner of movement of these suspended particles, influence the degree of scattering that they produce.

Agglomeration Sensitivity

Because the intensity of scattered light is proportional to the sixth power of particle diameter, DLS Measurements are very sensitive to the presence of agglomerates and large particles. Although this imbues it with the ability for early detection of flocculation in suspensions, when analysing a sample with high polydispersity, there could potentially be erroneous volume and particle number distribution measurements, since the values for these plots are derived from intensity distribution measurements. The intensity of light scattered by the larger particles or agglomerates would be stronger than that of the smaller particles, leading to the larger particles dominating the signals picked up by the detector. This observation can be better described by examining a typical measurement from a relatively polydisperse sample as shown in Figure 3.17

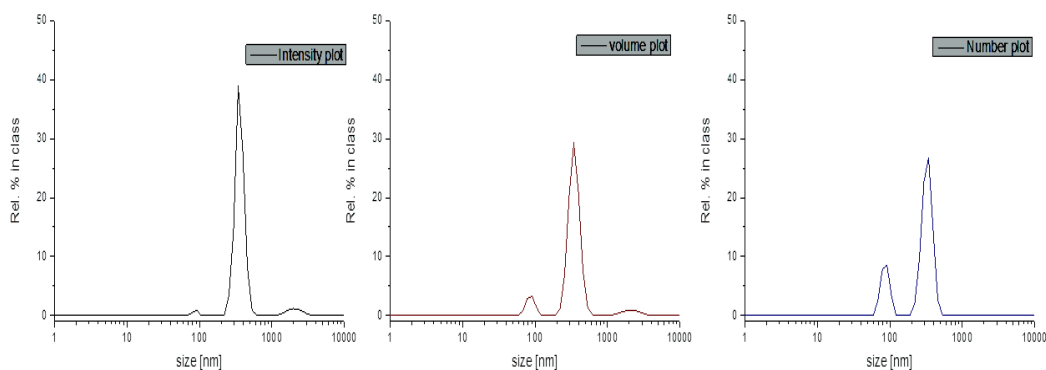


Figure 3.17: Scattering Intensity, Particle volume distribution and Particle number distribution plots of the same DLS measurement of zinc oxide double rods, showing sensitivity of DLS data to particle size.

Multiple Scattering:

When a monochromatic light beam (laser) is focused on a relatively concentrated sample and is scattered, the resultant scattered source illumination does not travel through the entire sample, rather there is the occurrence of secondary scattering, i.e. after a particle has scattered light, other particles further down the path of the scattered light 're-scatter' the light leading to erroneous data capture by a detector placed on the other side of the sampling vessel. This effect is called multiple scattering. One way of overcoming this challenge is to measure back scattered light rather than 'transmitted light' by placing the detector at an angle but on the same side as the laser source. Another way to also reduce the effect of this occurrence, is also to dilute the sample (Malvern, 2015b). When conducting DLS analysis, care was taken to ensure that the concentration of colloidal or particle suspensions analysed were within acceptable ranges for the equipment ($\leq 1.0 \text{ mg mL}^{-1}$).

Reproducibility of Results

It is usually difficult to obtain similar results for repeated measurement runs except in a very stable colloidal suspension or monodispersed sample. Flocculation and time lags between first and last measurement usually lead to a variation in values reported by the equipment. Hence the longer the duration of a measurement, the higher the chances of the results being unrepresentative and divergent especially in unstable samples. Particle size measurements from DLS can be compared with values obtained from microscopic analysis (ISO, 2008).

3.2.4.3 Sample Preparation

Suspensions of zinc oxide with varying concentrations were prepared for DLS analysis using a number of dispersion media:

- Purified water (MilliQ Millipore)
- Methanol (Fischer Biotech, Biotech grade $\geq 99.9 \%$)

In preparing water based ZnO suspensions, concentration calculations were based on 'wet weight', i.e. weight of freshly prepared particles which had not

been dried in the oven and thus the resultant suspensions had approximate concentration values. A stock suspension was prepared by weighing out a known quantity of the wet solid and suspending in 100 mL of MilliQ water. DLS samples were then prepared from the stock suspension. The suspension was ultrasonicated for 30 mins in a 1 L VWR Ultrasonic bath (VWR International, Chicago US) filled with water and operated at 45 kHz with a maximum output power of 120 W. This was done to ensure the ZnO particles were well dispersed in the medium. A micropipette was then used to extract appropriate volumes for target concentration and the volume made up to 10 mL. Typical sample concentrations ranged from $0.01\mu\text{g mL}^{-1}$ to 1.0 mg mL^{-1} .

3.2.4.4 Analytical Procedure and Parameters

Dynamic Light Scattering analysis was done on a Malvern Instruments Zetasizer nanoseries. Table 3.7 contains details of instrument operating conditions and analytical parameters.

Table 3.6: Dynamic Light Scattering measurement parameters.

S/N	Parameter	Values
1	Temperature [°C]	25 ,
2	Sample holder	12mm Square Polystyrene Cuvettes (particle size analysis) Disposable folded capillary cell (Zeta potential)
3	Sample concentration	Varied
4	Refractive index	dependent on medium used and material
5	Viscosity	dependent on medium used
6	Laser type	He-Ne laser wavelength = 633 [nm]
7	Power [mW]	4 (max)



Figure 3.18: The Malvern Instruments Zetasizer Nanoseries equipment and sample cells for Dynamic Light Scattering particle size measurements.

3.2.5 Thermogravimetric Analysis (TGA)

3.2.5.1 Principles and Applications

Thermogravimetric analysis (TGA) is a member of the group of thermal analysis methods where the properties of a material are measured as a function of time or temperature in a highly controlled environment involving programmed heating (and cooling) steps (Haines, 1995). Other thermal analysis methods include:

Differential thermal analysis (DTA) which in addition to weight changes also measures the temperature difference between the sample and a reference

Differential scanning calorimetry (DSC) performs analysis of the heat flow into the sample in comparison to that of a reference. DSC can also monitor the energy released or absorbed via chemical reactions during the heating process.

A TGA kit consists of a sample pan placed in a furnace on a precision balance. During TGA analysis, the temperature of the sample is raised at a gradual and constant rate while the weight of the sample is measured simultaneously. Mass loss is observed during TGA if a thermal event involving loss of a volatile component occurs. Also, chemical reactions such as combustion involve mass losses can be observed; however, a physical change (e.g. melting) does not result in a mass loss. Most TGA equipment, usually incorporate a visualisation terminal (usually a computer) which displays a plot of the sample weight (or change in weight) against temperature or time to illustrate thermal transitions in the material (Perkin Elmer, 2010; PhotoMetrics, 2012).

Results of measurements on the TGA could be affected by:

- The environment under which analysis is made such as: pressure, type of gases (e.g. nitrogen, argon, air)
- The size, morphology and homogeneity of the sample
- Changes in physical properties of the sample during measurement that could affect the analytical process (e.g. rate of heat transfer)
- Type of crucible used
- Calibration of the TGA equipment (Bottom, 2008).

3.2.5.2 Sample Preparation

There was no need for any special sample preparation procedures for the sodium zirconate powders other than that the powders were stored under vacuum prior to analysis. And in many cases where the post-TGA sample was collected for further analysis (XRD, SEM & TEM), the post-TGA sample was also stored under vacuum conditions.

3.2.5.3 Analytical Procedure and Parameters

TGA analysis was conducted on a Perkin Elmer, simultaneous thermal analyser model STA 8000 (Perkin Elmer Inc., Massachusetts USA) coupled with a LAUDA Alpha RA 8 cooling system (LAUDA-Brinkmann, LP, New Jersey USA) as shown in Figure 3.19. The equipment is capable of simultaneous thermogravimetric analysis using both a DTA mode (ΔT) and DSC (mW) mode (Perkin Elmer, 2010).

During a typical TGA run, the sodium zirconate powder sample was loaded into the sample pan sealed and the temperature allowed to equilibrate before the initial weight measurement was taken. The sample was then fully dehydrated and decarbonated by preheating it in the TGA to 900 °C in a nitrogen atmosphere, after which it was then subjected to multiple carbonation-decarbonation cycles (Figure 3.20). Below are details of a typical carbonation-decarbonation cycle:

- Carbonation in a 22% CO₂ – 78 % N₂ atmosphere at 700 °C over a dwell time of 5 or 10 min
- Heating at 20 °C per min to 900 °C in pure N₂ without any hold period, for decarbonation to occur
- Cooling to 700 °C and switch of gases from pure nitrogen to 22 % CO₂-N₂ mix ready for the next carbonation step.



Figure 3.19: The Perkin Elmer STA 8000 and LAUDA Alpha RA 8 Chiller unit.

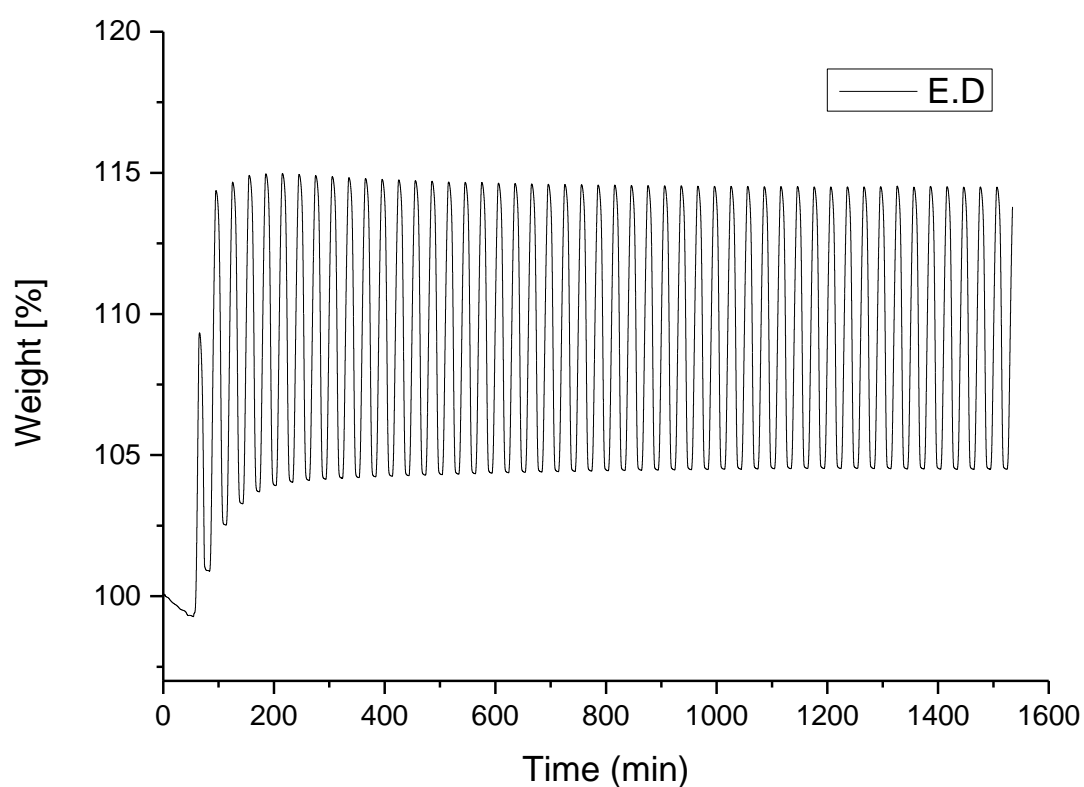


Figure 3.20: Multicycle TGA plot of percentage weight changes as a function time showing repetitive weight gain and losses (see Chapter 6 for details).

Chapter 4

Results and Discussion I

Synthesis and Characterisation of Zinc Oxide Hexagonal Double Rods from Zinc Acetate and Sodium Hydroxide

4.1 Introduction

This chapter provides details of a hierarchical growth process describing the formation of ZnO microrods by hydrothermal treatment of a suspension formed from reaction of zinc acetate and sodium hydroxide, in the absence of any growth control additive.

Characterisation of hydrothermal products mainly involved investigation of phase identity and composition using X-ray diffraction analysis, and examination of particle shape and size using scanning and transmission electron microscopy.

The use of focused ion beam milling (FIB-SEM) and electron microscopy to reveal internal nanostructural growth details of hydrothermally prepared hexagonal faceted ZnO double rods is also presented in this chapter (Section 4.3).

Investigations were conducted to understand the influence of some key hydrothermal synthesis variables on the characteristics of the product particles. Section 4.2.9 discusses the effect of progressive variation of hydrothermal dwell times on particle shape and sizes, while section 4.4.5 examines the influence the pH of the reaction medium could have had on particle growth and characteristics.

4.1.1 Samples

Samples were prepared based on different hydrothermal dwell times and using precursor suspension adjusted to varying pH values to study particle evolution and the influence of changes in hydrothermal treatment time and pH of precursor suspension on particle size and morphology. Table 4.1 provides a listing of the samples prepared and selected synthesis conditions.

Table 4.1: List of samples and selected experiment conditions.

Sample Code	Approx. Precursor pH	Temperature [°C]	Reactant Volume [mL]	Hydrothermal dwell time [h]
<i>Zn01t0</i>	9.0	120	100	0
<i>Zn01t0.5</i>	9.0	120	100	0.5
<i>Zn01t1</i>	9.0	120	100	1
<i>Zn01t2</i>	9.0	120	100	2
<i>Zn01t3</i>	9.0	120	100	3
<i>Zn01t6</i>	9.0	120	100	6
<i>Zn01t12</i>	9.0	120	100	12
<i>Zn01t124</i>	9.0	120	100	24
<i>Zn03p7</i>	7.0	120	100	12
<i>Zn03p11</i>	11.0	120	100	12
<i>Zn03p13</i>	14.0	120	100	12

4.2 Effect of Dwell Times on Zinc Oxide

4.2.1 Freshly Prepared Precipitate, No Hydrothermal Treatment

Investigations commenced with the cloudy white precursor suspension that was generated from mixing NaOH and zinc acetate and labelled sample *Zn01t0*.

Results from powder X-ray diffraction analysis of sample *Zn01t0* (Figure 4.2) showed the presence of crystalline particles in the sample. The main peaks in the resultant powder diffraction pattern were indexed to wurtzite zinc oxide according to ICDD reference file number 04-013-6607 (Figure 4.2). However, there were other peaks which did not have a match in the ICDD reference file. Further comparison of the experimental pattern against ICDD reference patterns for zinc hydroxide (No. 04-016-3076), sodium zinc oxide (No. 00-052-0080), zinc acetate (No. 00-052-0080), zinc acetate dihydrate (No. 00-033-1464) and sodium acetate hydrate (No. 00-028-1030), showed no significant matches. It is thought that these peaks were likely due to layered basic zinc acetate (LBZA) (Morioka, et al., 1999; Ku et al., 2008; Tarat, et al., 2014; Tang, et al., 2012; Hosono, et al., 2004; Poshkus, 1983).

Commonly reported X-ray diffraction data for layered basic zinc acetate (LBZA) show three diffraction peaks between $0^\circ 2\theta$ and $20^\circ 2\theta$; which are due to reflections from the (001), (002), and (003) planes of the material; the (001) peak which occurs $\sim 6.7^\circ 2\theta$ is the characteristic main peak for LBZA (Figure 4.1). In addition, LBZA's diffraction pattern is also known to contain peaks occurring around 33° and 59° which have been identified as diffraction from the (100) and (110) planes of the material respectively (Hosono, et al., 2004; Morioka et al., 1999; Poul et al., 2000; Tarat et al., 2012; Cui et al., 2008).

The occurrence of peak shifts in the X-ray diffraction pattern of LBZA ($\text{Zn}_5(\text{OH})_8(\text{CH}_3\text{COO})_2 \cdot 2\text{H}_2\text{O}$) resulting in a slight displacement of peaks relative to commonly observed values of 2θ peak positions have been reported (Hosono, et al., 2004). This means it could be possible to record slightly different peak positions for pure phase LBZA dependent on synthesis conditions (Figure 4.1b).

LBZA unit cell has the following parameters: $a = 3.138 \text{ \AA}$; $c = 14.75 \text{ \AA}$. Table 4.2 presents details X-ray diffraction data for Layered basic zinc acetate (LBZA)

as reported by [Poul et al., \(2000\)](#); while Figure 4.1 shows two patterns of LBZA obtained from literature annotated to show the corresponding hkl planes.

Table 4.2: X-ray diffraction data for LBZA after ([Poul et al., 2000](#)).

d_{obs} [Å]	d_{calc} [Å]	I [%]	h	k	i	l
14.68	14.75	100	0	0	0	1
7.36	7.38	5	0	0	0	2
4.91	4.92	4	0	0	0	3
-	-	-	0	0	0	4
2.717	2.718	24	1	0	-1	0
1.569	1.569	13	1	1	-2	0
1.359	1.359	3	2	0	-2	0

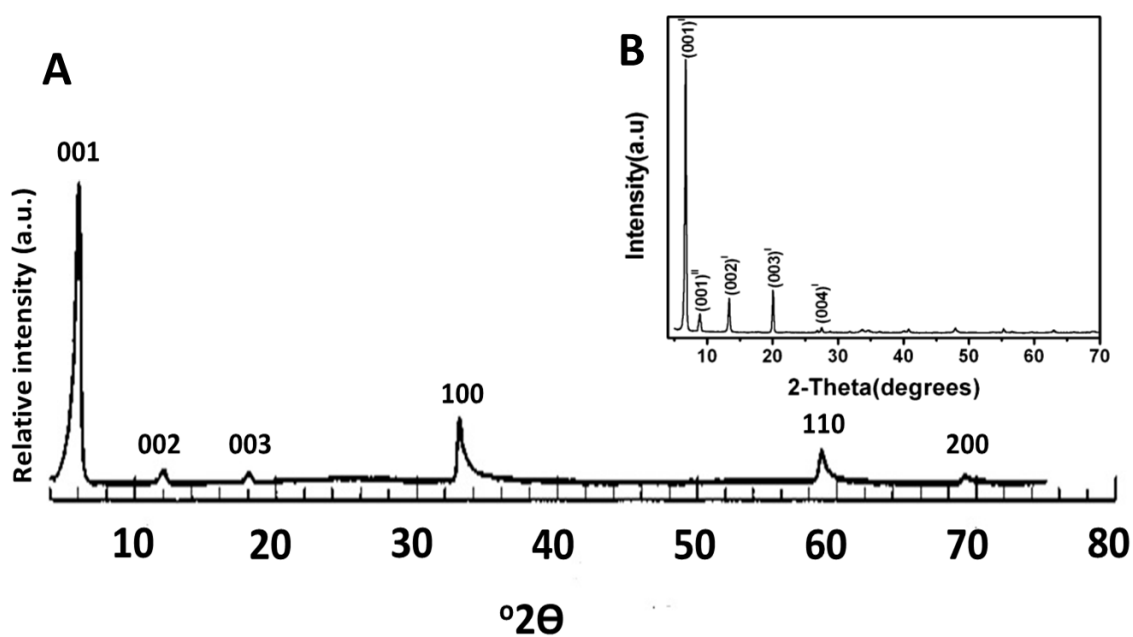


Figure 4.1: (a) X-ray diffraction pattern of layered basic zinc acetate (LBZA) with hkl planes labelled ([Poul et al., 2000](#); [Hosono, 2004](#)); (inset) XRD pattern showing peak shifts ([Cui et al., 2008](#)).

Figure 4.2 is the experimental X-ray diffraction pattern for 0 h sample (*Zn01t0*) indicating multiphasic content. Peaks identified as wurtzite zinc oxide have been labelled with their corresponding hkl planes, while peaks identified as layered basic acetate have been marked with an 'x'. Table 4.3 shows a comparison between the experimental pattern for sample *Zn01t0* and ICDD reference pattern 04-013-6607 for zinc oxide to show how the zinc oxide peaks were identified.

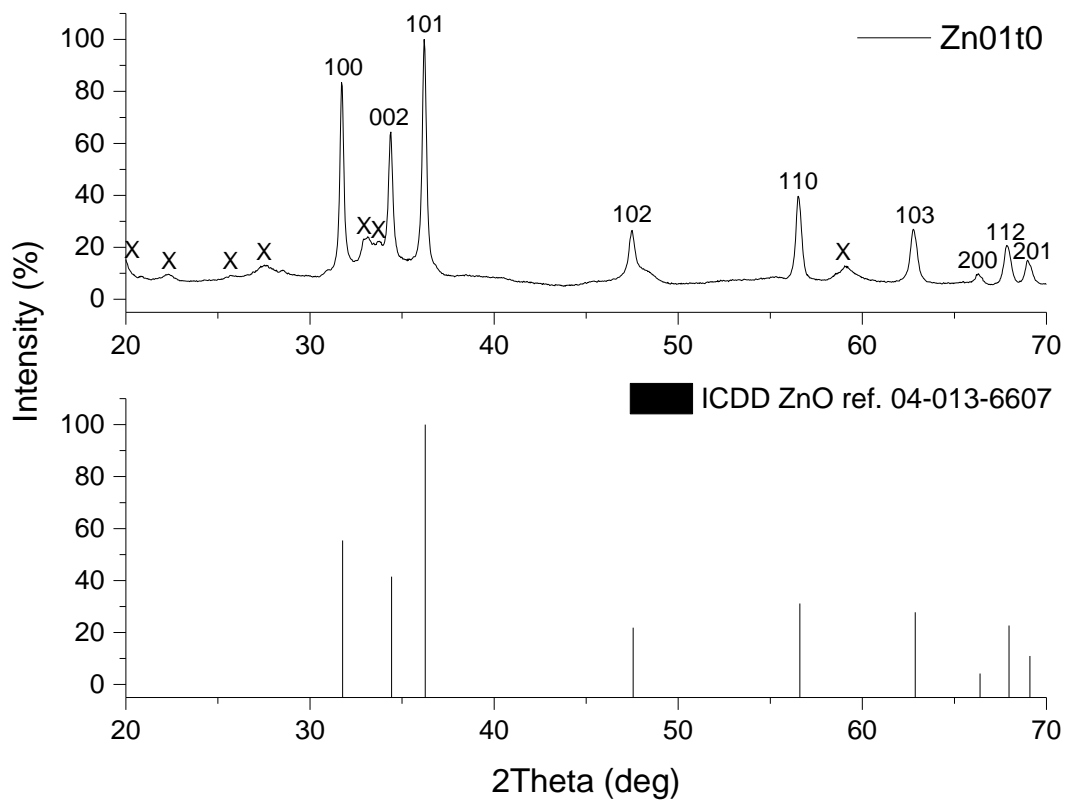


Figure 4.2: X-ray diffraction pattern of *Zn01t0*, showing peaks indexed to wurtzite zinc oxide (ICDD ref. 04-013-6607) with peaks thought to be LBZA marked with an 'x'.

Table 4.3: Indexing of peaks from sample *Zn01t0* to ICDD reference pattern 04-013-6607 for wurtzite zinc oxide.

Sample <i>Zn01t0</i>			ICDD ZnO ref. 04-013-6607						
2θ	d [Å]	I [%]	2θ	d [Å]	I [%]	<i>h</i>	<i>k</i>	<i>l</i>	<i>l</i>
22.3	4.994	2							
25.7	4.466	2							
27.5	4.242	5							
28.6	4.125	3							
31.7	2.820	83	31.8	2.814	57	1	0	-1	0
32.9	2.722	16							
34.8	2.652	15							
34.4	2.608	61	34.4	2.603	42	0	0	0	2
36.2	2.481	100	36.3	2.476	100	1	0	-1	1
40.4	2.232	1							
45.3	2.002	2							
47.5	1.915	23	47.5	1.911	21	1	0	-1	2
48.5	1.878	5							
55.3	1.662	1							
56.5	1.629	36	56.6	1.624	30	1	1	-2	0
59.1	1.563	6							
62.7	1.481	22	62.9	1.477	26	1	0	-1	3
66.2	1.411	4	66.4	1.407	4	2	0	-2	0
67.8	1.382	16	68.0	1.378	21	1	1	-2	2
69.0	1.362	10	69.1	1.358	10	2	0	-2	1

Scanning electron microscopy (SEM) analysis of sample *Zn01t0* (Figure 4.3) showed that the as-prepared precipitate sample was made up of large sheet-like films coexisting with ~ 50 nm diameter equiaxed crystallites.

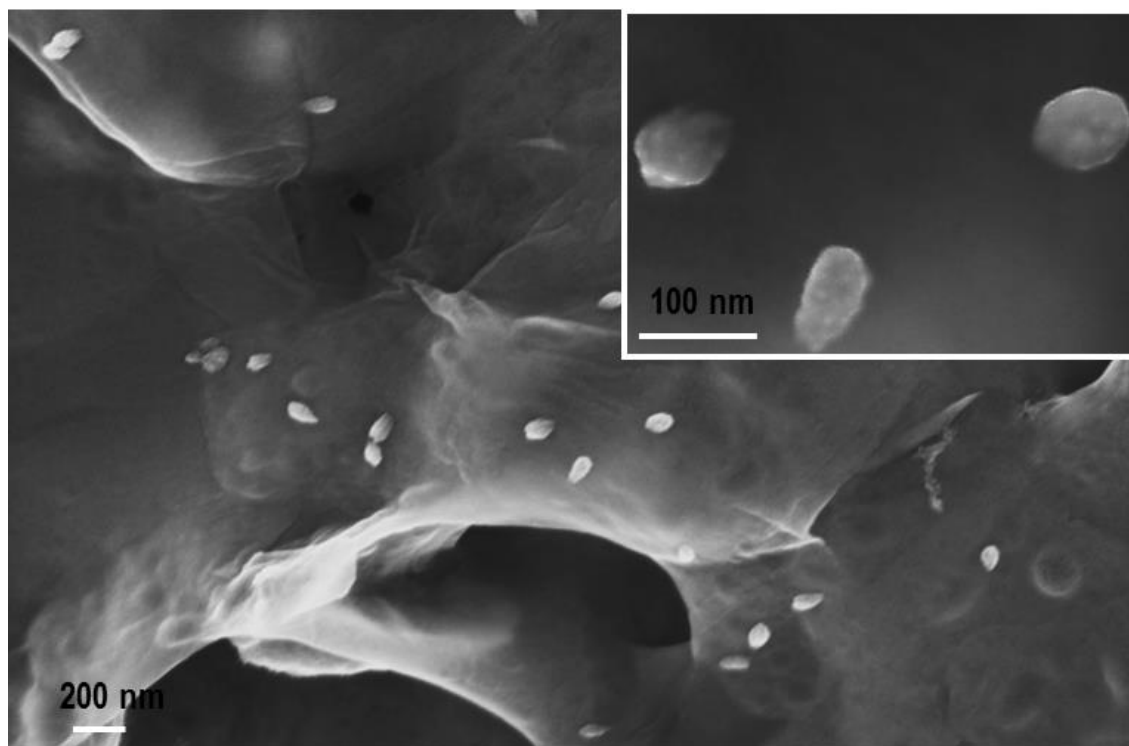


Figure 4.3: SEM image of sample *Zn01t0* with high magnification inset highlighting equiaxed nanoparticles

Further investigation of particle structure in the transmission electron microscope (TEM) revealed that the sheet-like particles were polycrystalline in nature (Figure 4.4) while the equiaxed crystallites were found to be single crystals (Figure 4.6). SAED analysis of the sheet or flake-like material produced a concentric ring pattern indicating the presence of randomly oriented multiple crystals hence polycrystalline. By measuring the diameters of the concentric rings, it was possible to decipher the d-spacings of the material. Table 4.4 shows the indexing of the d-spacings to wurtzite zinc oxide (ICDD reference pattern number 04-013-6607). A spectrum obtained from TEM-EDX (Figure 4.5) confirmed findings from SAED, that the sheet-like background particles were zinc oxide by showing that the particles contained only elements Zn and O. The presence of Copper (Cu) in the spectrum was an artefact due to the TEM copper grid.

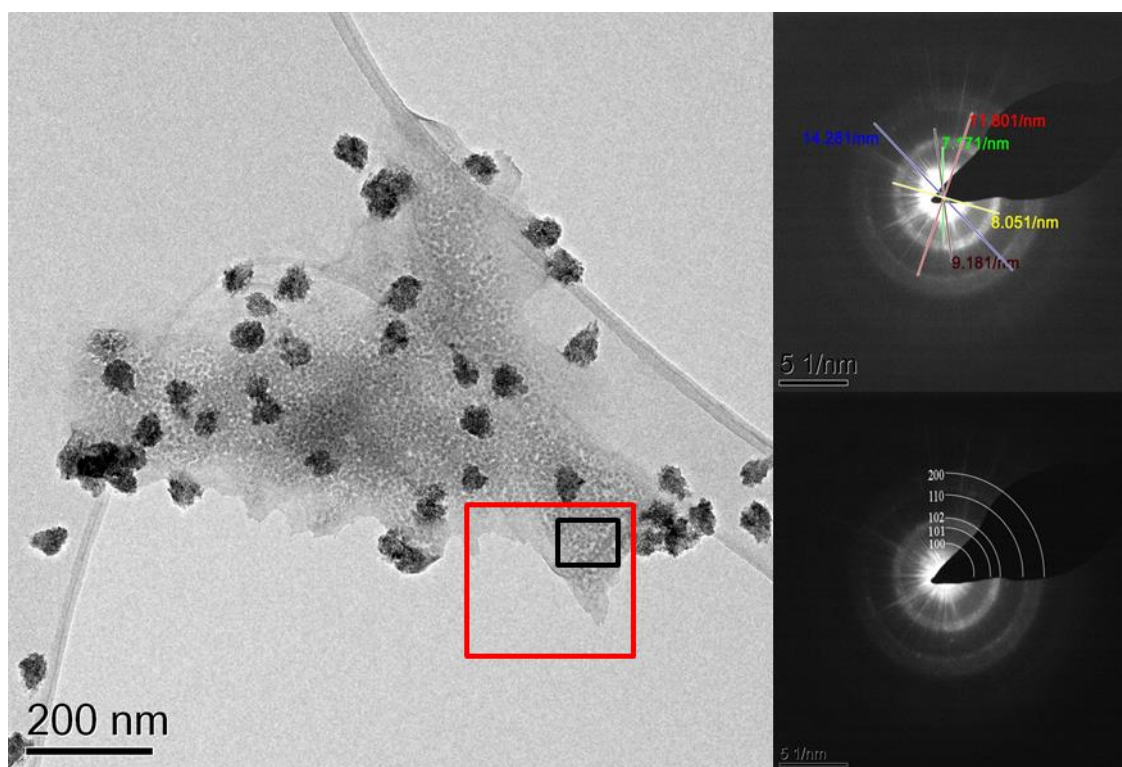


Figure 4.4: Annotated TEM micrograph of sample *Zn01t0* showing equiaxed nanoparticles coexisting with sheet-like zinc oxide; the red box highlight the area from which selected area electron diffraction (SAED) images were taken while the black sub-box was the point selected for energy dispersive X-ray analysis.

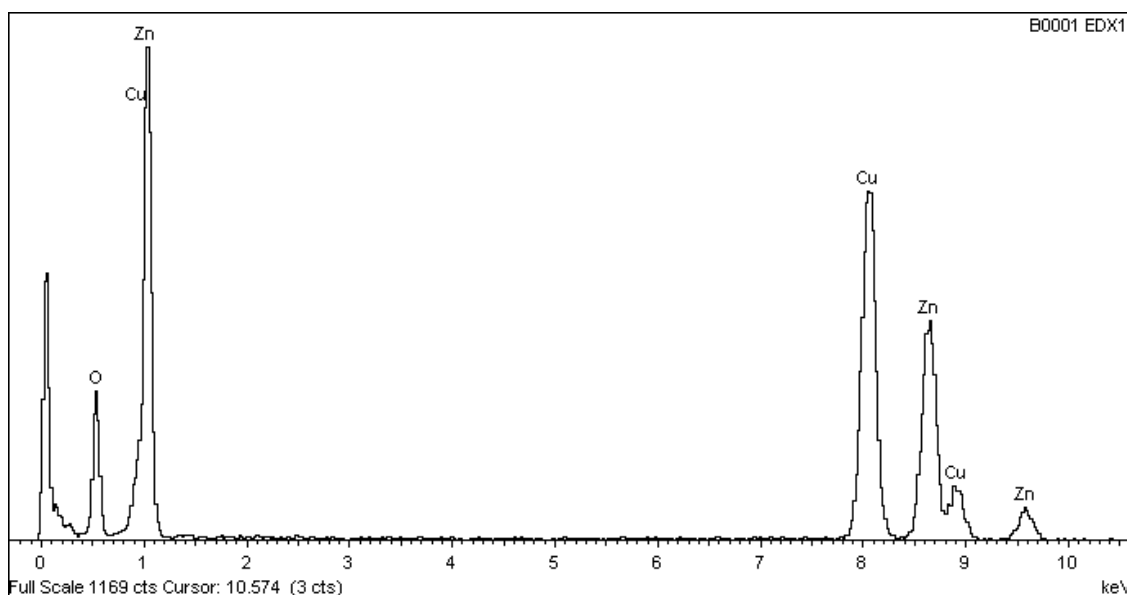


Figure 4.5: TEM-EDX spectrum of sample *Zn01t0* (annotated as black sub-ring in Figure 4.3). *N.B. Cu & C signal are artefacts from TEM grid*

Table 4.4: Indexing of d-spacings from TEM-SAED of sheet-like background material in Figure 4.3 to wurtzite ZnO (ICDD reference 04-013-6607).

Measured Diameter [nm^{-1}]	Calculated d-spacing [\AA]	ICDD ZnO reference d-spacing [\AA]	<i>h k l</i>
7.17	2.79	2.81	10-10*
8.05	2.48	2.48	10-11*
9.18	2.18	1.91	10-12
11.80	1.69	1.63	11-20
14.28	1.40	1.41	20-20

In a similar vein, SAED analysis of the equiaxed nanoparticles produced a pattern with bright spots (Figure 4.6). The presence of the spots indicated diffraction from single crystals. TEM-EDX also confirmed that the equiaxed nanoparticles were zinc oxide (Figure 4.7). The distance between opposite spots was measured, d-spacings calculated and indexed (Table 4.5).

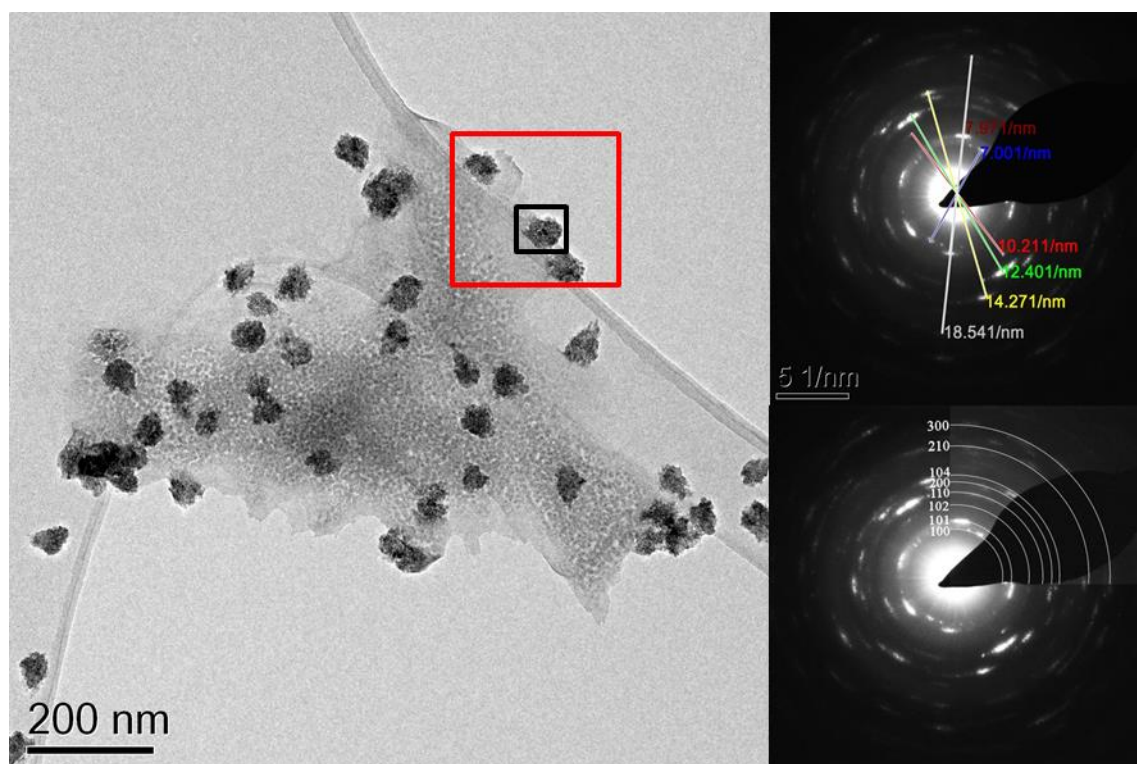


Figure 4.6: SAED pattern of equiaxed nanoparticles in sample *Zn01t0*.

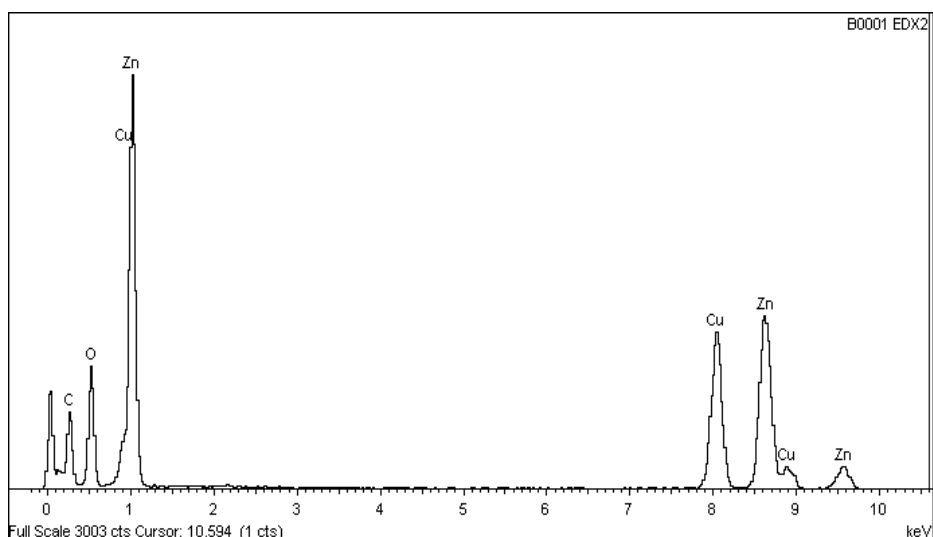


Figure 4.7: TEM-EDX spectrum of equiaxed nanoparticle in sample *Zn01t0* (Identified by a black box in Figure 4.6)

Table 4.5: Indexing of d-spacing from TEM SAED of equiaxed nanoparticles in Figure 4.6 to ZnO (ICDD reference 04-013-6607).

Measured Diameter [nm ⁻¹]	Calculated d-spacing [Å]	ICDD ZnO reference d-spacing [Å]	<i>h k l</i>
7.00	2.86	2.81	10-10*
7.97	2.51	2.48	10-11*
10.21	1.96	1.91	10-12
12.40	1.61	1.63	11-20
14.27	1.40	1.41	20-20
18.54	1.08	1.06	21-30

N.B.: * As highlighted in Tables 4.4 and 4.5, the reflections from the 002 planes have not been labelled. Because the intensity of diffraction from the 002 planes are relatively lower than those of the 100 and 101 planes, the diffraction spots from the 002s were not clearly visible in the SAED patterns. It would require a close scrutiny of the space in-between the spots and ring patterns from the high intensity 100 and 101 reflections to be able to identify the 002 reflections. As a result, they have not been labelled.

4.2.2 Half Hour (0.5 h) Hydrothermal Treatment Products

Hydrothermal runs were conducted for 0.5 h to investigate immediate progression of particle growth.

X-ray diffraction analysis of powder obtained after drying out sample *Zn01t0.5* (Figure 4.8) indicated that its composition was essentially wurtzite zinc oxide as indexed by ICDD reference file 04-013-6607 (Figure 4.8). It was observed, that there were fewer peaks from layered basic zinc acetate (Figure 4.1) in this diffraction pattern in comparison to the diffraction pattern of sample *Zn01t0* (Figure 4.2). Figure 4.7 shows a comparison of X-ray diffraction patterns for both samples.

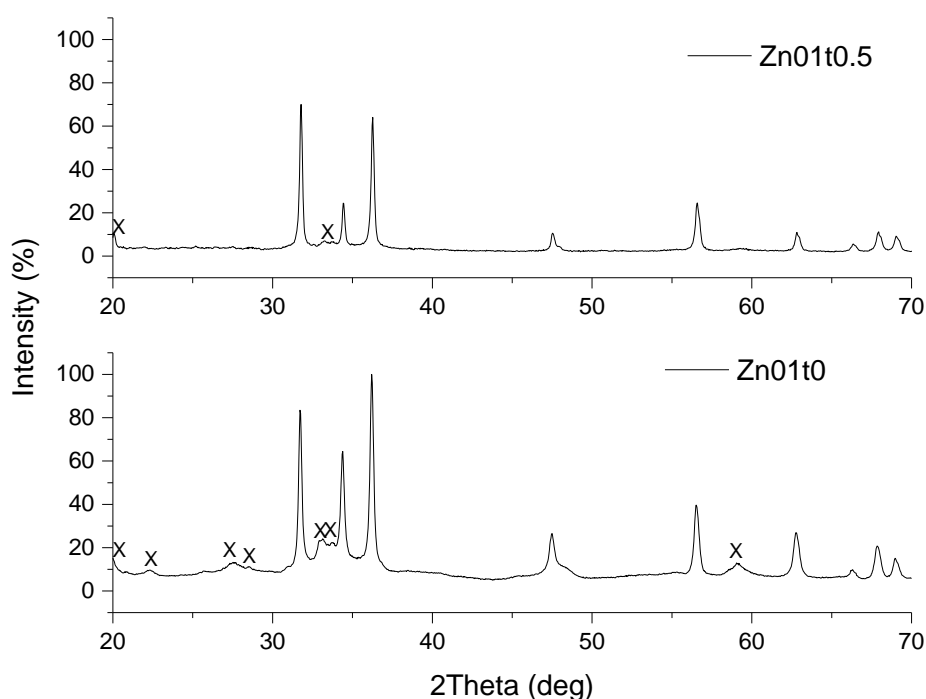


Figure 4.8: Comparison between X-ray diffraction patterns of samples *Zn01t0* and *Zn01t0.5* with peaks from LBZA highlighted using an 'X'.

An examination of sample *Zn01t0.5* on the SEM (Figure 4.9) revealed that there was still a majority presence of the sheet-like zinc oxide material that was first observed in sample *Zn01t0* (Figure 4.3). However in addition, the emergence of particles with distinct hexagonal rod-like morphology was observed. These rod-like particles had an abundance of between 10 - 20 %, and dimensions varied widely with widths of between 50 nm to ~ 1 μ m, while lengths varied from 100 nm to over 2 μ m (Figure 4.11). Furthermore, the

presence of nanoscale substructure on sides and basal faces on these rod-like particles were observed (Figure 4.9).

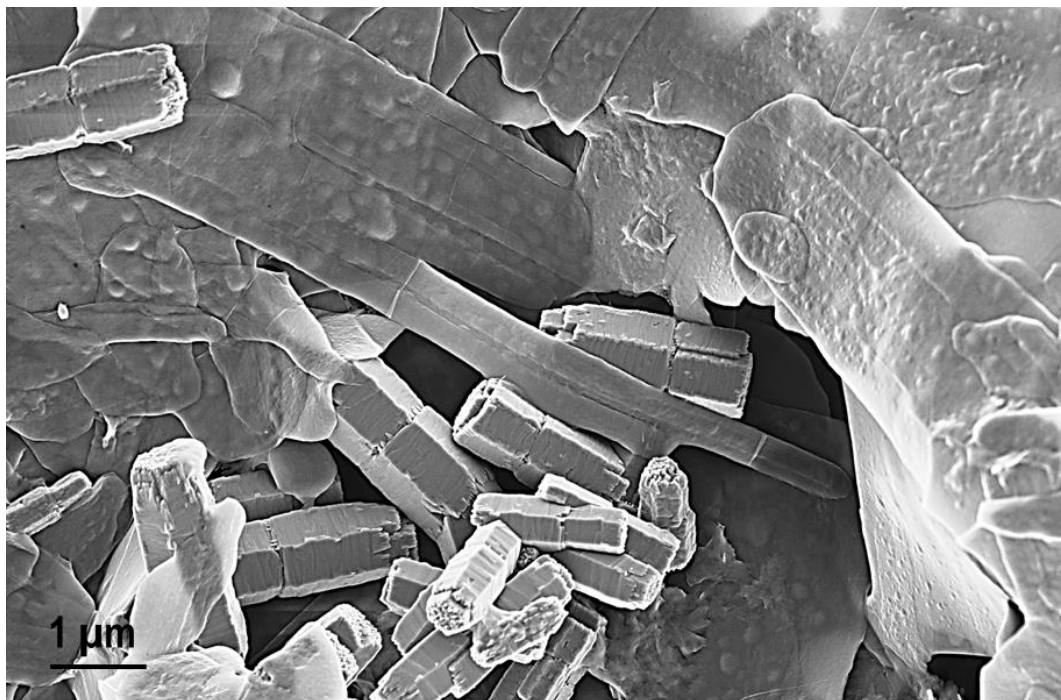


Figure 4.9: SEM micrographs of sample $Zn_{0.1}t_{0.5}$ showing rod-like ZnO particles co-existing with large sheets of zinc oxide.

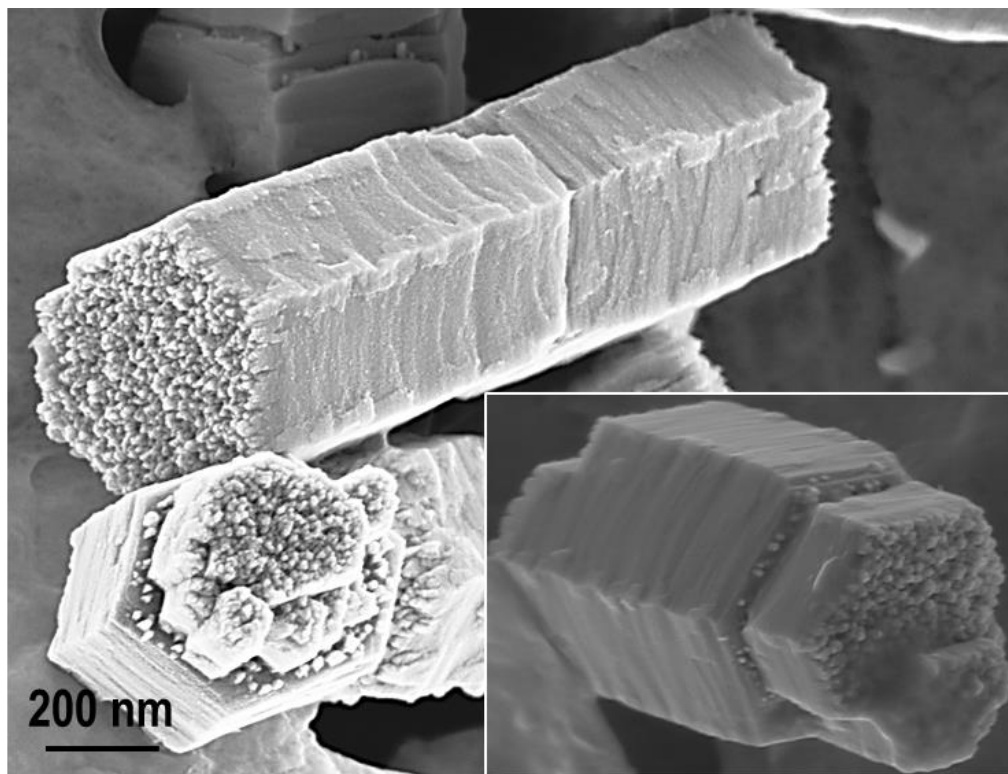


Figure 4.10: SEM showing substructure on the basal planes and sides of rods.

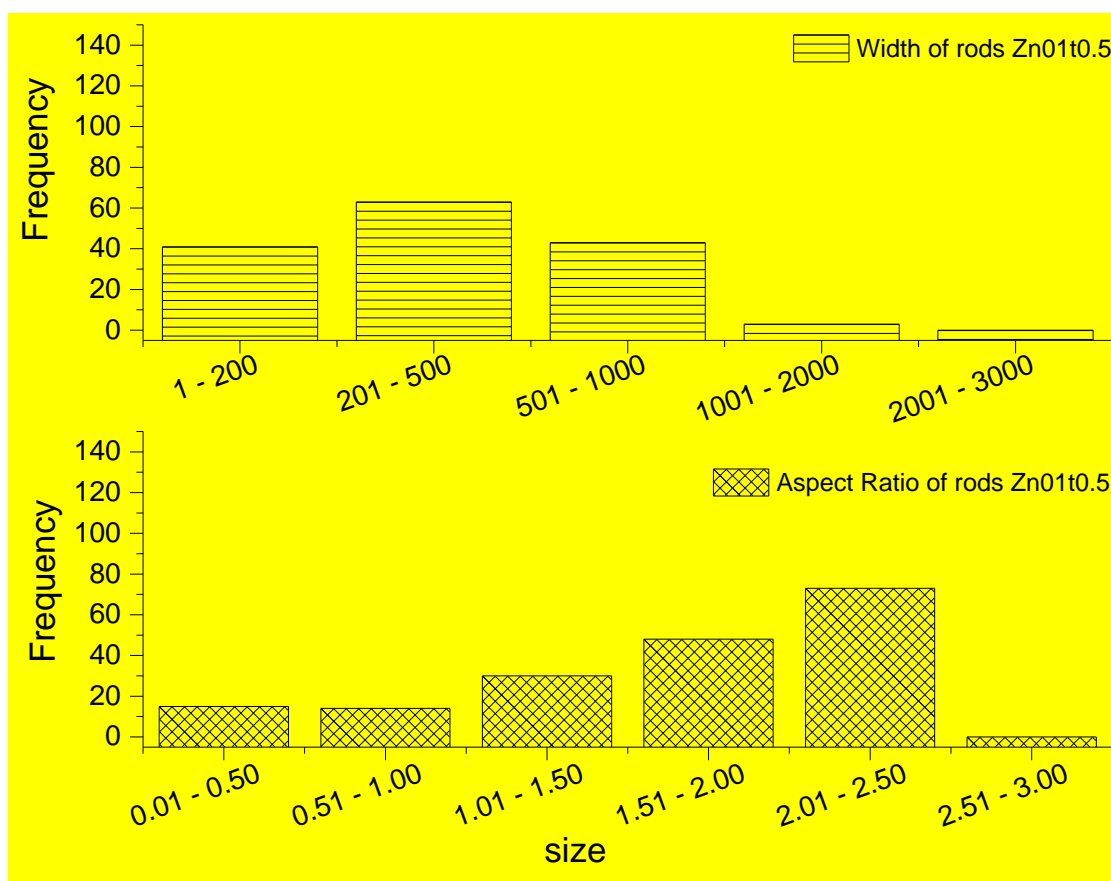


Figure 4.11: Histogram showing particle size distribution and aspect ratios in sample *Zn01t0.5*.

A comparison of particle sizes from all the samples (widths and aspect ratios) analysing the effects of hydrothermal treatment durations on particle sizes is presented in section 4.3.9 (Figures 4.34 and 4.35).

Further examination of the rod-like particles on the TEM (Figure 4.12), showed that the substructure observed on the basal sections of the rod-like particles seen in Figure 4.10 consisted of approximately 20 nm primary nanoparticles. High resolution TEM (HRTEM) lattice imaging showed these nanoparticles were collectively aligned within 20° of common $\langle 0001 \rangle$ growth direction of the bulk microrods (Figure 4.13b). Evidence of the polycrystalline nature was further confirmed through SAED analysis (Figure 4.13c), which produced a diffraction pattern with visible smearing of the spots indicative of slight misalignment among these primary particle (< 20 nm nanoparticles).

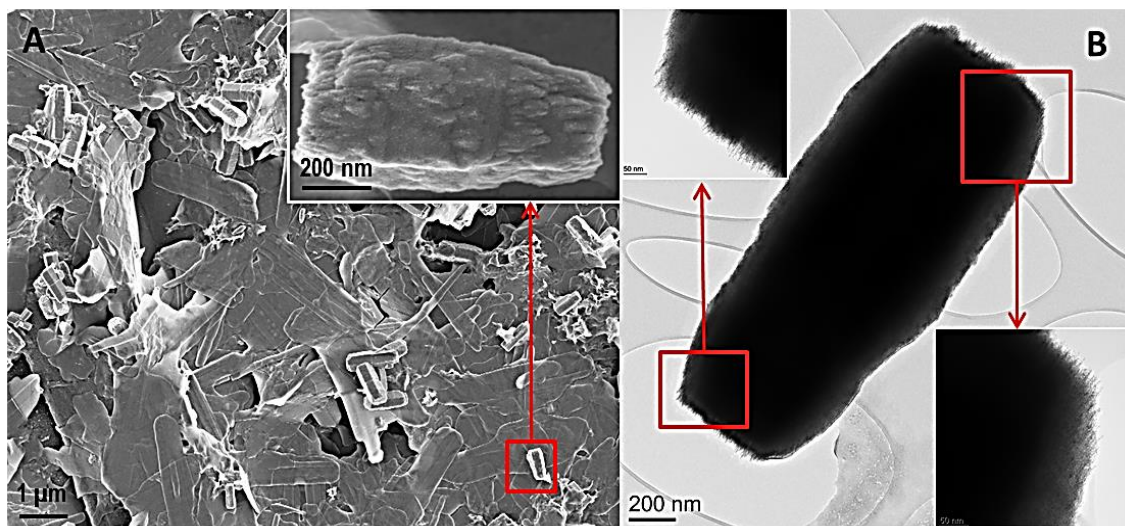


Figure 4.12: (a) SEM of sample $Zn_{01}t_{0.5}$, where a particle similar to the one examined in the TEM is highlighted; (b) TEM, insets are HRTEM images showing substructure on ends and sides of the particle.

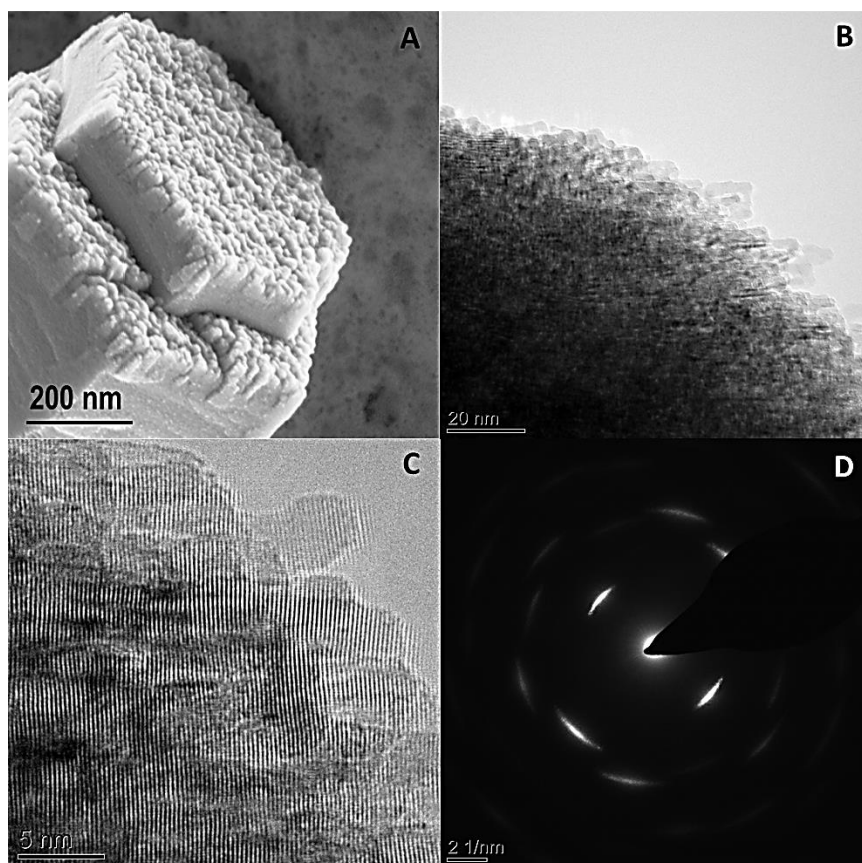


Figure 4.13: (a) SEM and (b) HRTEM images of rod from sample $Zn_{01}t_{0.5}$ showing crystalline nature of substructure on basal planes, (c) lattice imaging, (d) TEM SAED pattern of showing smearing of diffraction spots.

4.2.3 One Hour (1 h) Hydrothermal Treatment Products

X-ray diffraction analysis of sample *Zn01t1* (Figure 4.14) obtained after a fresh supply of sample *Zn01t0* had undergone hydrothermal treatment for a dwell time of 1 h indicated that the composition of the sample was pure monophasic wurtzite zinc oxide (ICDD reference file 04-013-6607). A plot of the X-ray diffraction pattern obtained and ICDD reference pattern is shown in Figure 4.14.

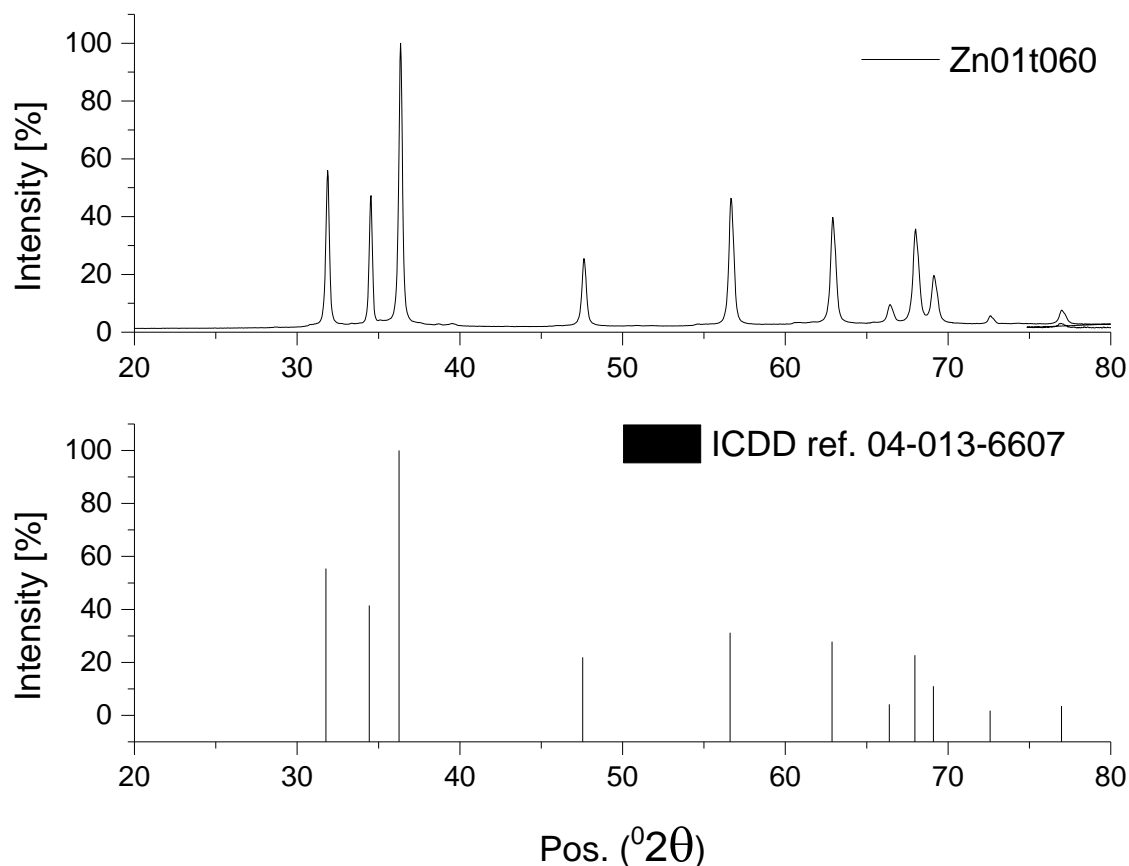


Figure 4.14: X-ray diffraction pattern of sample *Zn01t1* showing phase composition to be zinc oxide.

From SEM analysis of sample *Zn01t1* (Figure 4.15) it was observed that there was a lower prevalence of the sheet / flake-like morphology that was dominant in samples *Zn01t0* and *Zn01t0.5*. sample *Zn01t1* contained mainly (~75%) rod-like particles. However, many had largely uneven surfaces similar to the 0.5 h rods with evidence of stepped longitudinal and lateral growth albeit with the noticeable absence of the < 20 nm granular nanocrystallites observed on the basal ends of the rods as shown in Figure 4.16a. In addition it also appeared

that the rods were visibly larger in size than the ones observed in sample $Zn01t0.5$ (Figure 4.16).

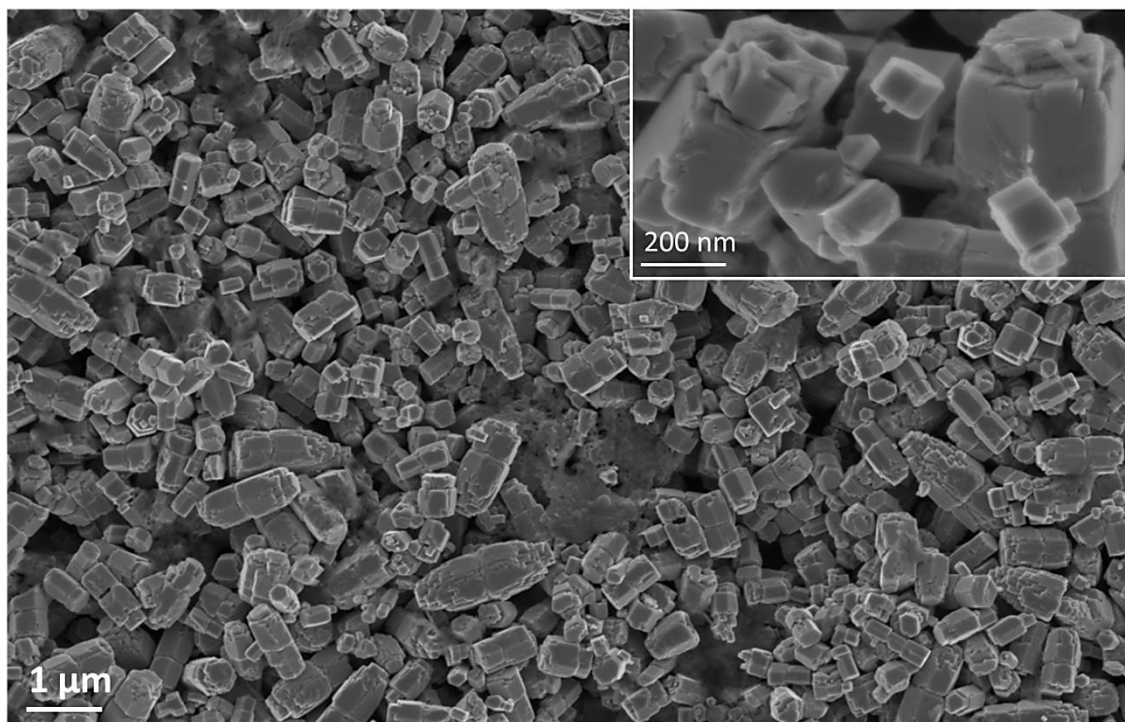


Figure 4.15: SEM micrographs of sample $Zn01t1$ particles showing double rod morphology (inset) higher magnification to highlight uneven surfaces.

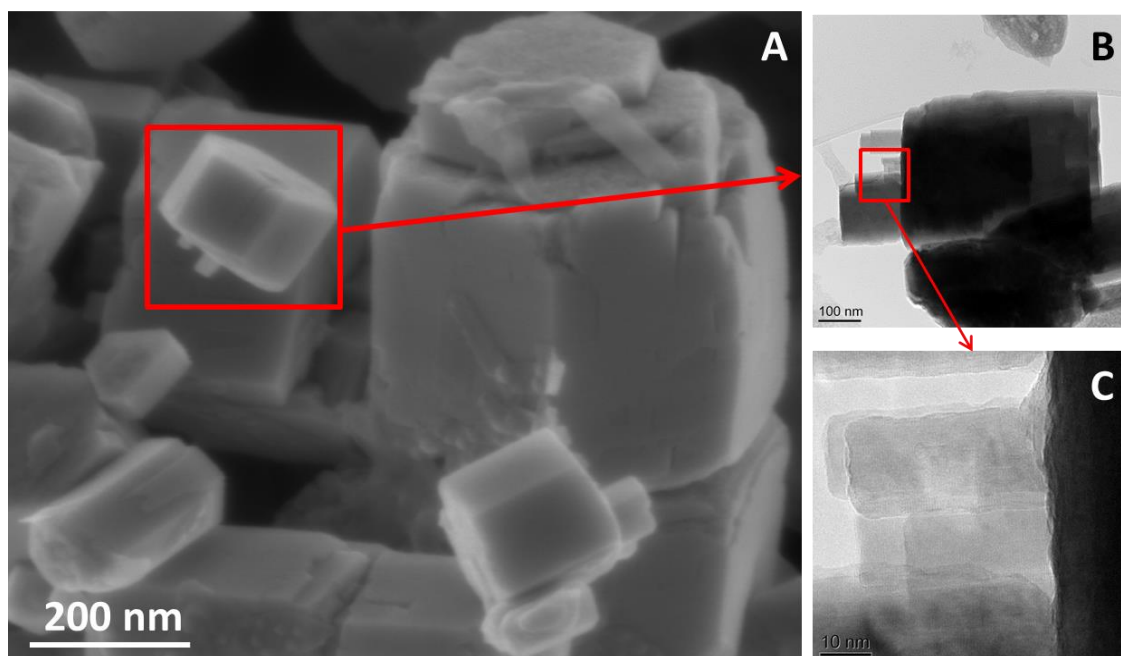


Figure 4.16: SEM and TEM micrographs of $Zn01t1$ particles showing details of nanostructured particle growth.

Analysis of TEM images revealed that the previously polycrystalline substructure growing off the basal planes of pre-existing rods (Figure 4.13) may have recrystallized into single crystal particles. This inference is based on the observation of lattice planes running coherently in the [0001] direction as shown by the HRTEM lattice image in Figure 4.16c.

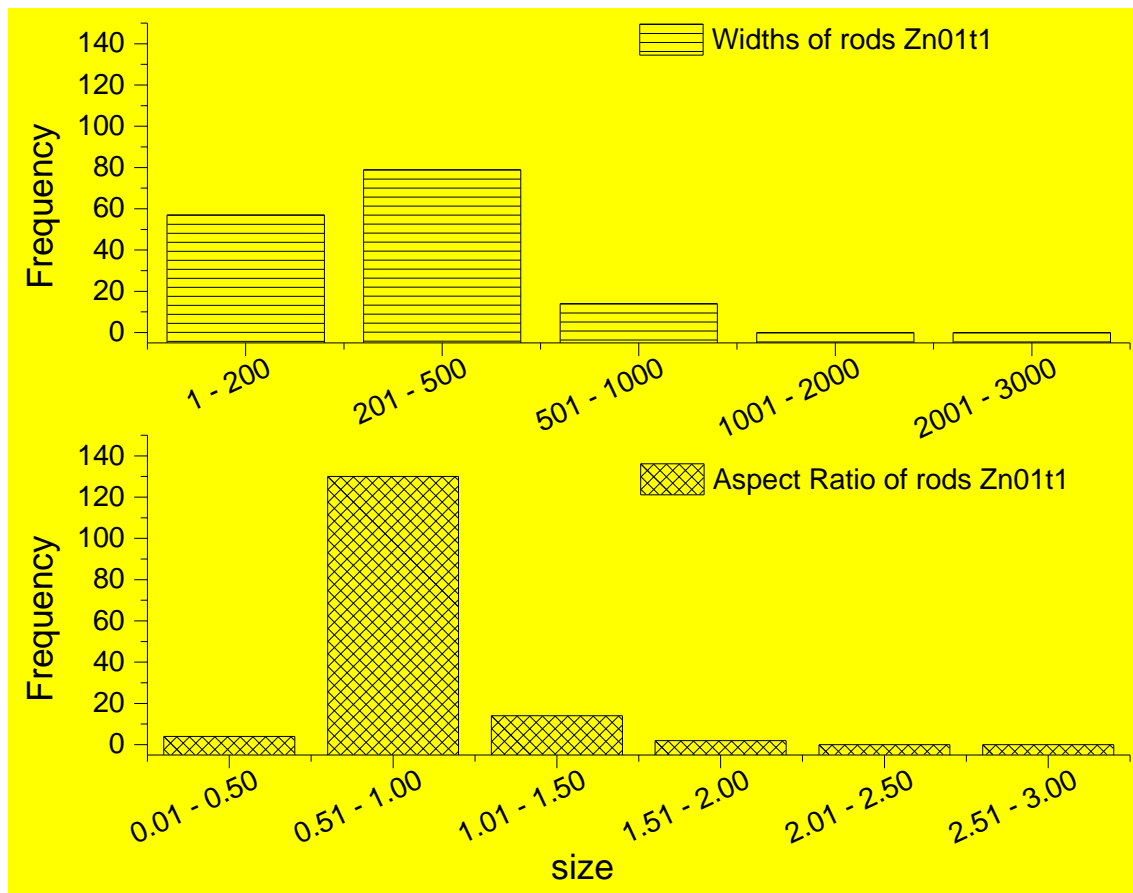


Figure 4.17: Histogram showing distribution of width of particles and aspect ratios in sample *Zn01t1*.

4.2.4 Three Hour (3 h) Hydrothermal Treatment Products

X-ray diffraction analysis of sample *Zn01t3*, 3 h hydrothermal treatment, showed that the phase composition of the sample was wurtzite zinc oxide (ICDD reference file number 04-013-6607). No other phases or impurities were detected by the XRD analysis. The resulting powder diffraction pattern is presented in Figure 4.18.

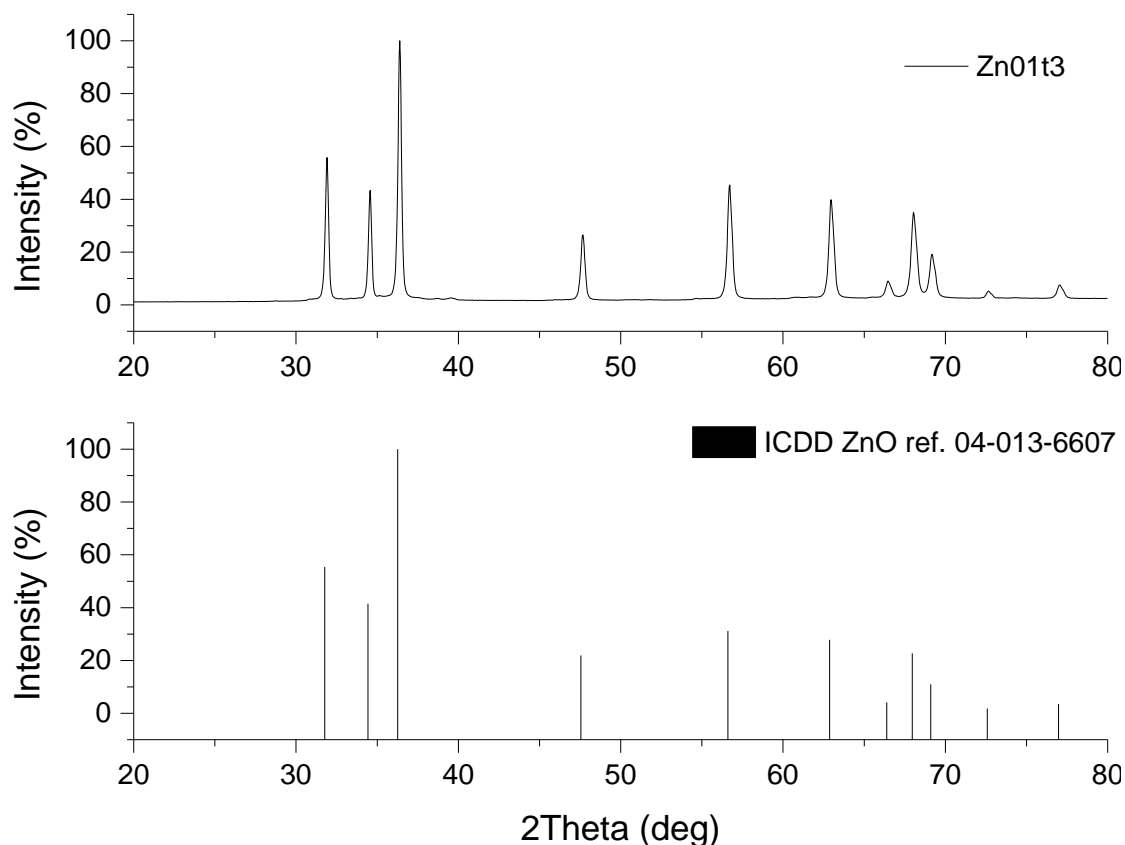


Figure 4.18: X-ray diffraction pattern of sample *Zn01t3*.

Analysis of SEM micrographs of sample *Zn01t3* (Figure 4.19) showed the particles bore a strong similarity to the particles observed after 1 h of hydrothermal treatment (sample *Zn01t1*), with many of the rods still showing the lateral and longitudinal stepped growth observed in sample *Zn01t0.5*. Also, it was observed that the particles in this sample appeared to have larger dimensions relative to the 1 h hydrothermal products. Figure 4.18 contains SEM micrographs showing the particles observed in sample *Zn01t3*.

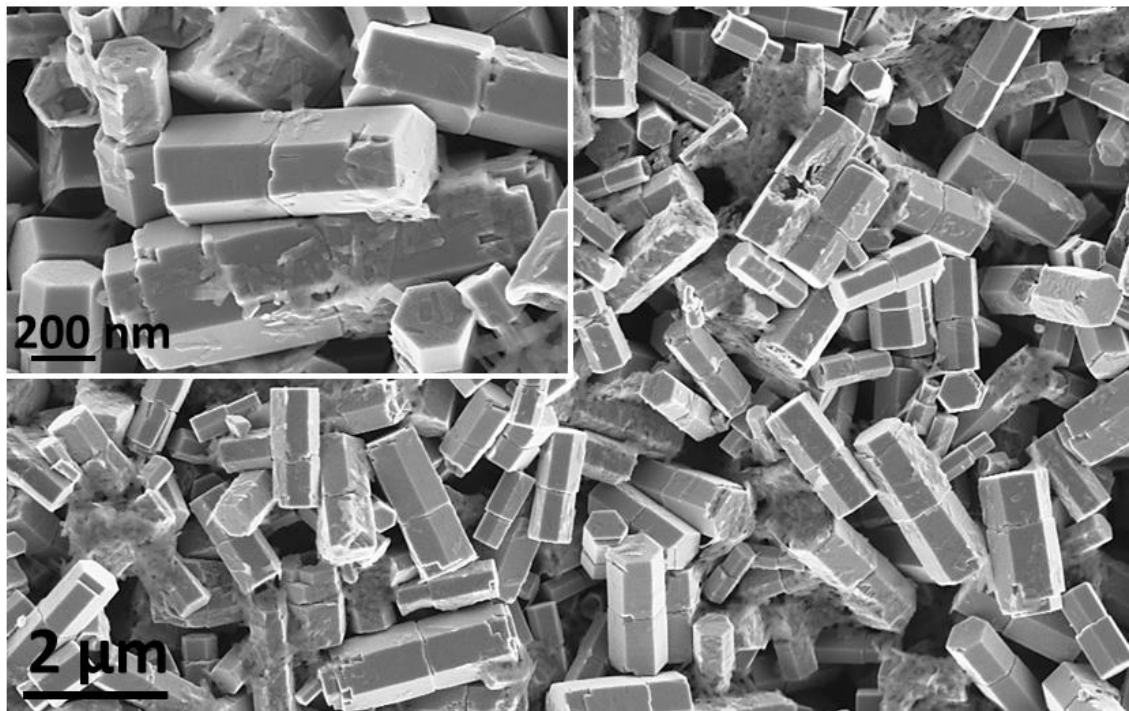


Figure 4.19: SEM micrographs of sample *Zn01t3*.

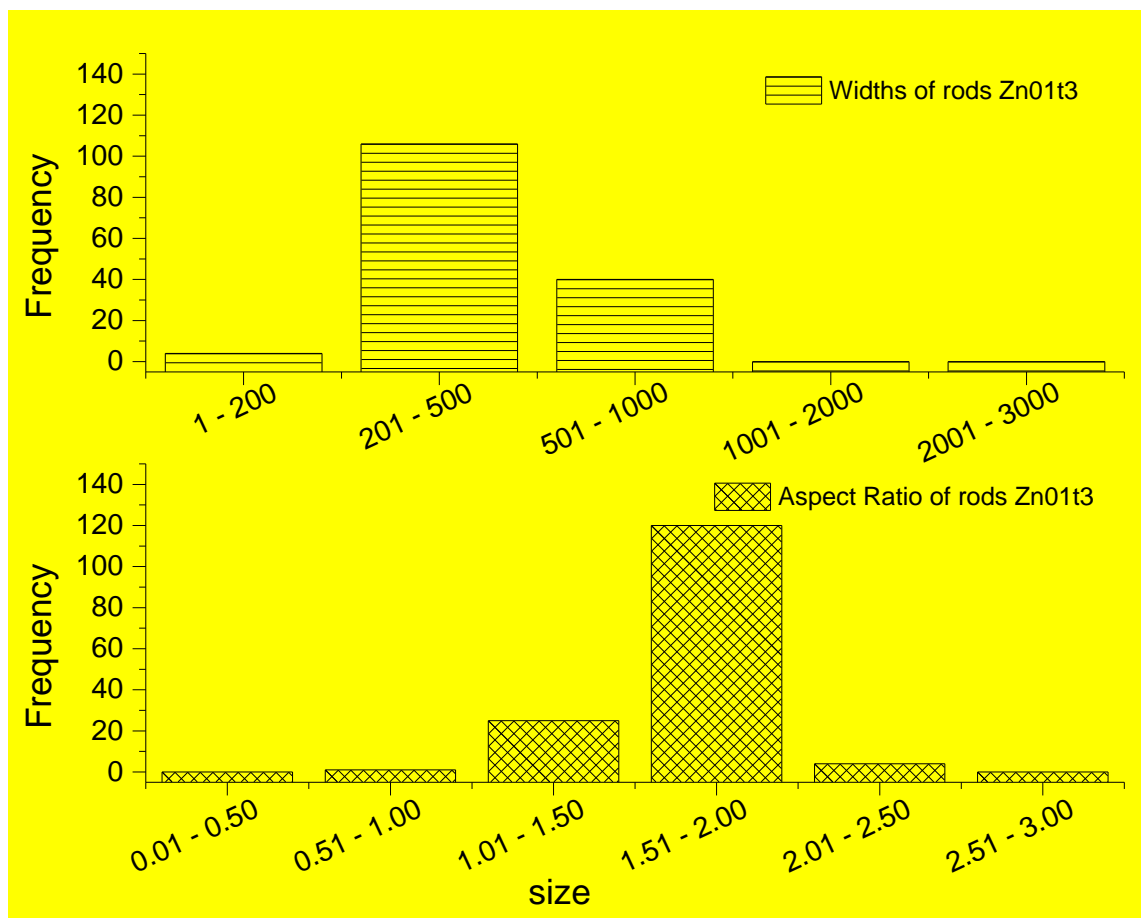


Figure 4.20: Distribution of particle widths and aspect ratios in sample *Zn01t3*.

4.2.5 Six Hour (6 h) Hydrothermal Treatment Products

X-ray powder pattern obtained from analysis of sample *Zn01t6* revealed the phase composition of the sample to be pure single-phase wurtzite zinc oxide as indexed by ICDD reference pattern number 04-013-6607 as presented in Figure 4.21.

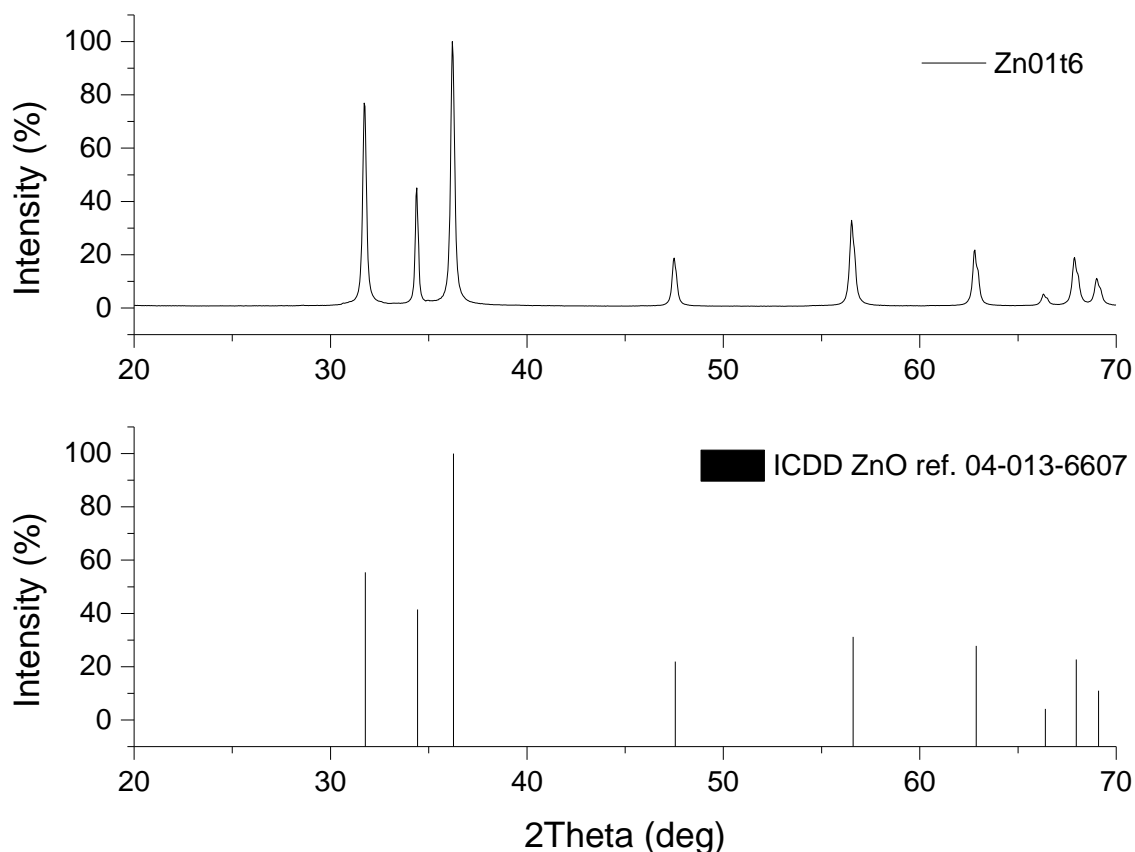


Figure 4.21: X-ray diffraction pattern of sample *Zn01t6*.

SEM showed the presence of particles with mainly well-defined hexagonal double rod morphology (Figure 4.22). The occasional presence of some irregular shaped particles was also observed. These irregular shaped particles (sometimes resembling lozenges) were distinctly different from the sheet or flake-like particles previously observed in samples *Zn01t0*, *Zn01t0.5* and *Zn01t1*. It is thought that they first emerged in sample *Zn01t3* however; it was difficult to differentiate them from the sheet like particles in that sample.

Analysis of particle size distribution from 150 randomly measured particles using SEM images, showed that the double rod particles had widths ranging between 50 nm and 1 μm , while lengths were on the average 500 nm for a single rod and 1 μm for double rods as presented in Figure 4.23.

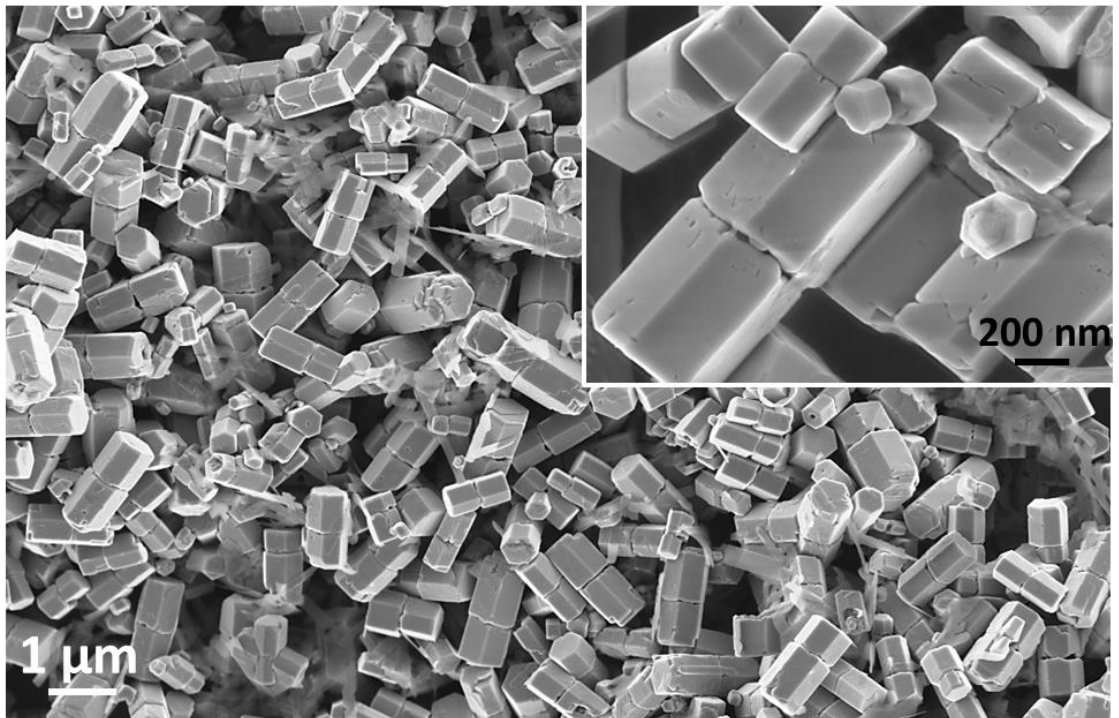


Figure 4.22: SEM micrographs of sample *Zn01t6*.

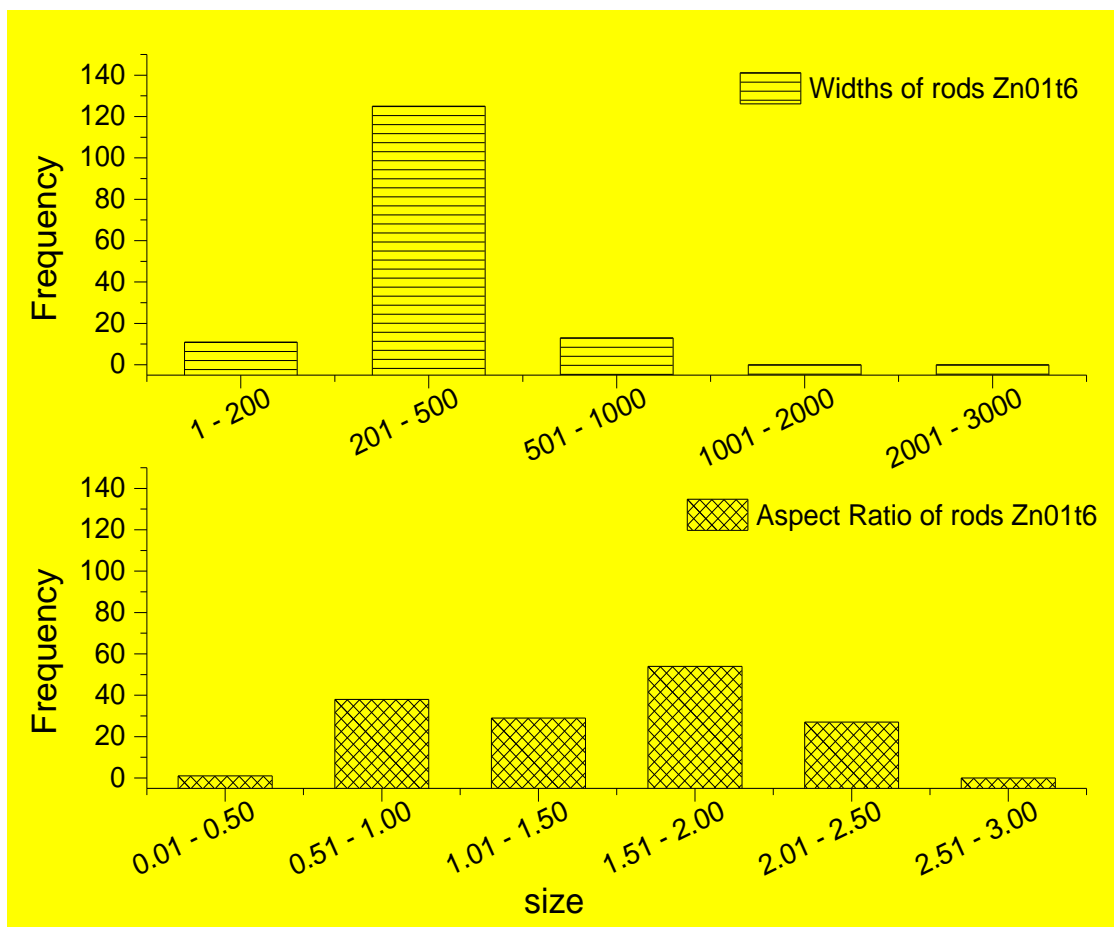


Figure 4.23: Distribution of particle widths and aspect ratios in sample *Zn01t6*.

4.2.6 Twelve Hour (12 h) Hydrothermal Treatment Products

X-ray powder diffraction analysis of sample *Zn01t12*, confirmed that they were phase-pure zinc oxide with the hexagonal wurtzite crystal structure (ICDD ref. 04-013-6607) as presented in Figure 4.24.

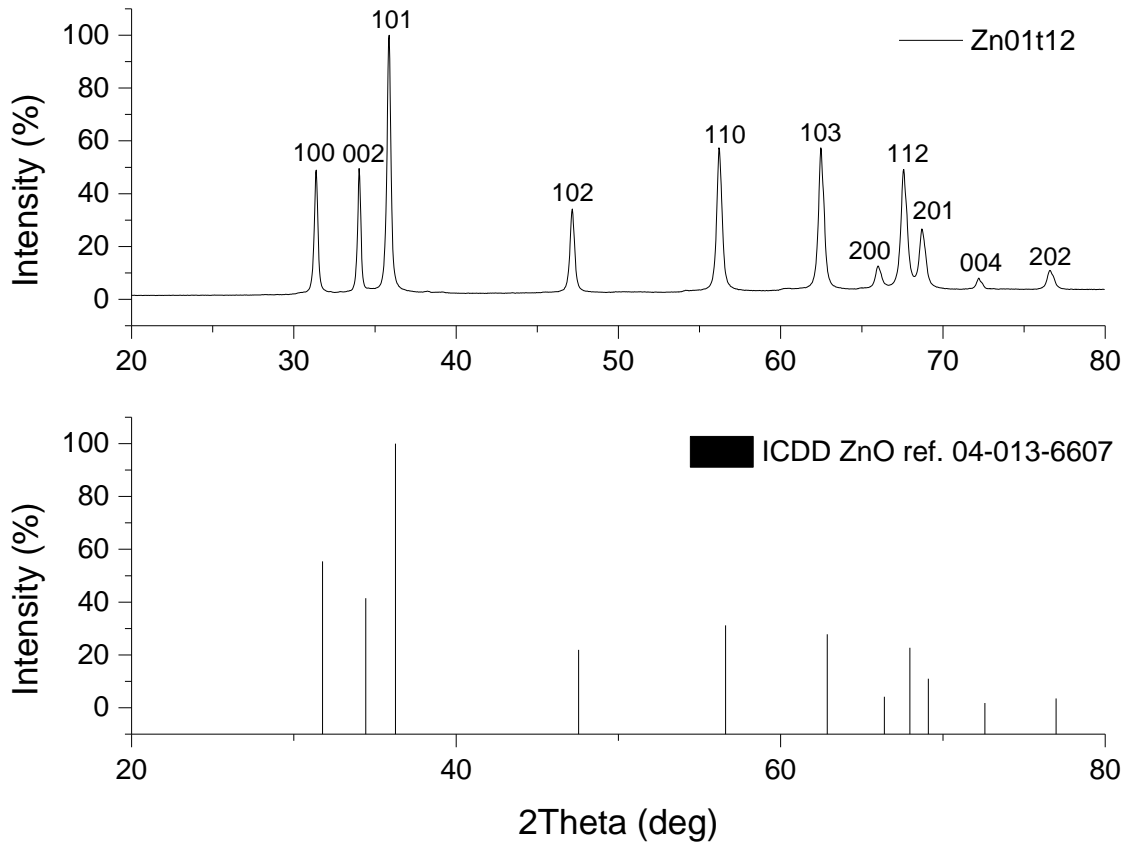


Figure 4.24: X-ray diffraction pattern of sample *Zn01t12*.

Results of SEM analysis sample *Zn01t12* showed the presence of a relatively broad distribution of particle sizes and more than one type of particle morphology (Figure 4.25) which included single rods, double rods and some irregular particle morphologies. The continued presence of the very thin and flat nanoparticles shaped like lozenges was also noted.

From measurement of double rods (~150) in the sample, it was observed that rod widths ranged from about 50 nm to about 1 μ m, while lengths varied from between 100 nm and a maximum of around 1.8 μ m (Figure 4.26). A Histogram of particle size distribution and aspect ratios is presented in Figure 4.26.

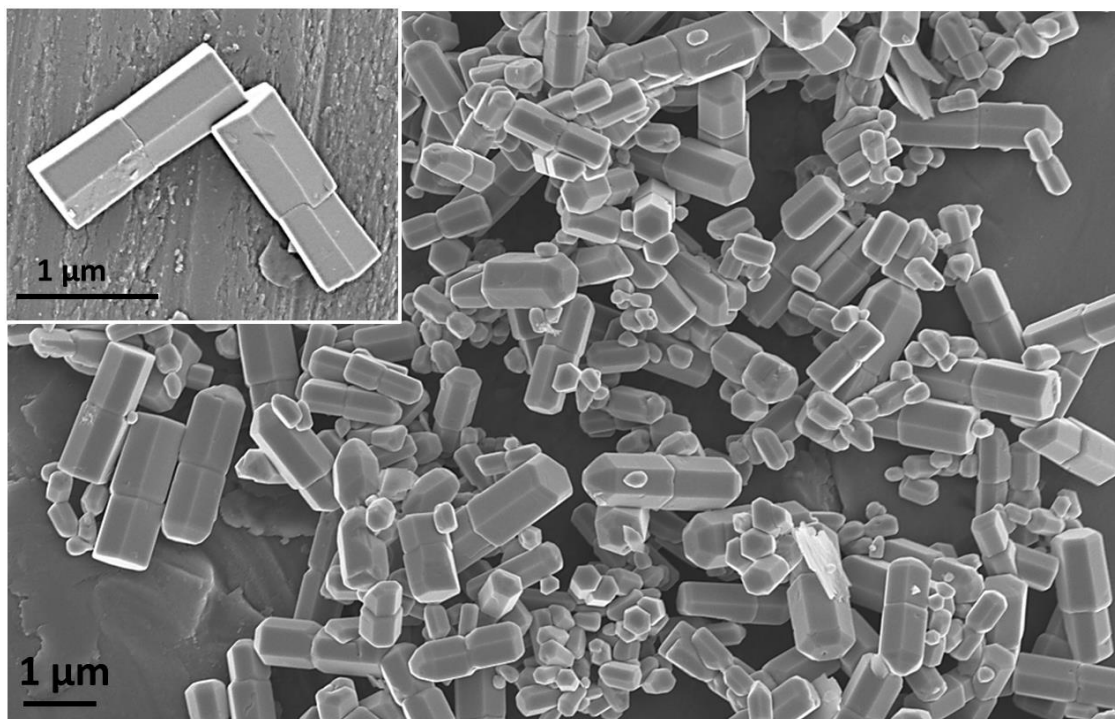


Figure 4.25: SEM of sample *Zn01t12* showing double rods and other particles.

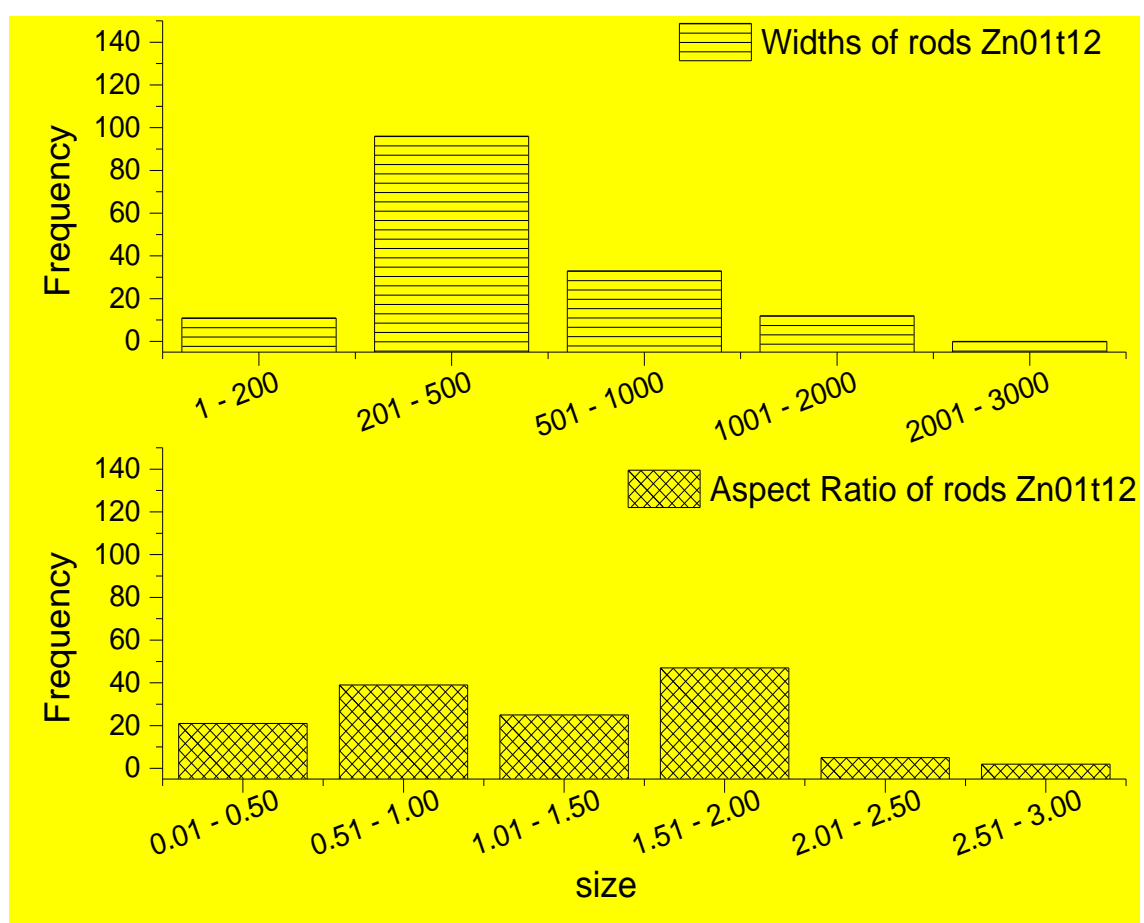


Figure 4.26: Distribution of particle width and aspect ratios in sample *Zn01t12*.

4.2.7 Twenty Four Hour (24 h) Hydrothermal Treatment Products

X-ray diffraction analysis of bulk powder of sample *Zn01t2* also confirmed that they were phase-pure zinc oxide (Figure 4.27).

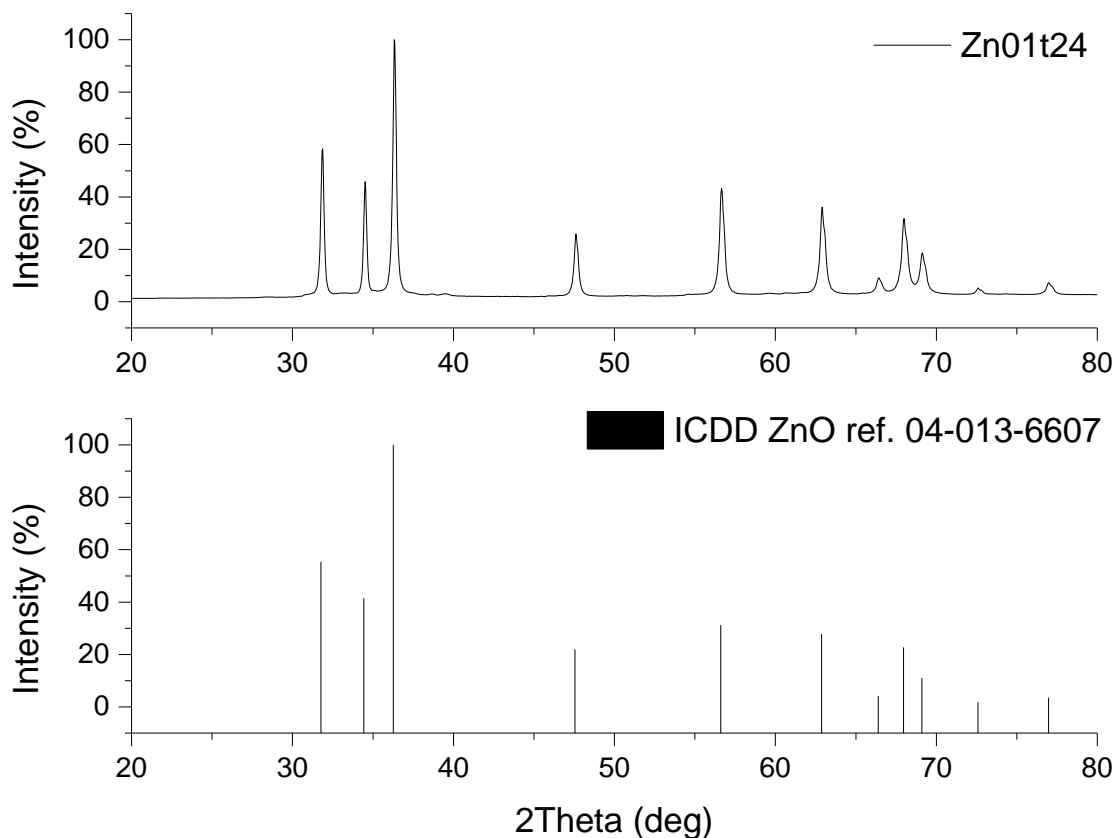


Figure 4.27: X-ray diffraction pattern of sample *Zn01t24*.

Results of examination of sample *Zn01t24* on the SEM (Figure 4.28) showed an increase in average particle size relative to sample *Zn01t12*. There also appeared to be a notable absence of the irregular shaped 'lozenges' that had been observed in preceding samples. Rod lengths reaching up to about 30 μm . particles with widths in excess of 3 μm were also recorded (Figure 4.29).

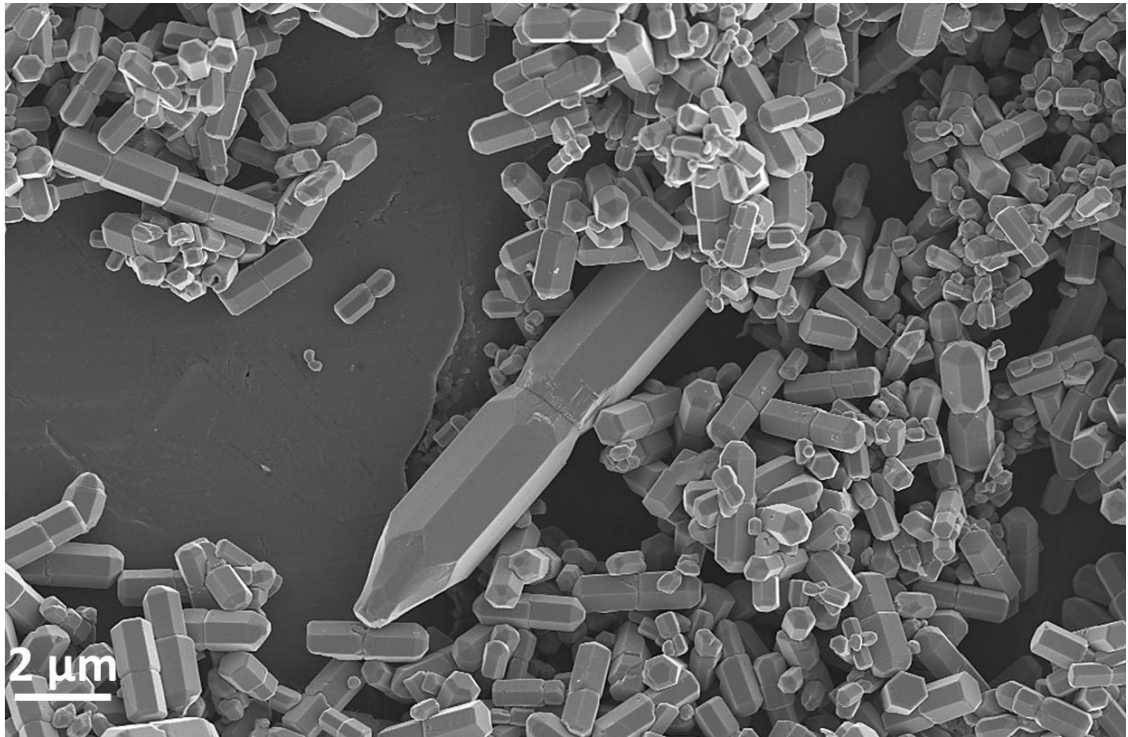


Figure 4.28: SEM image of particles from sample *Zn01t24*.

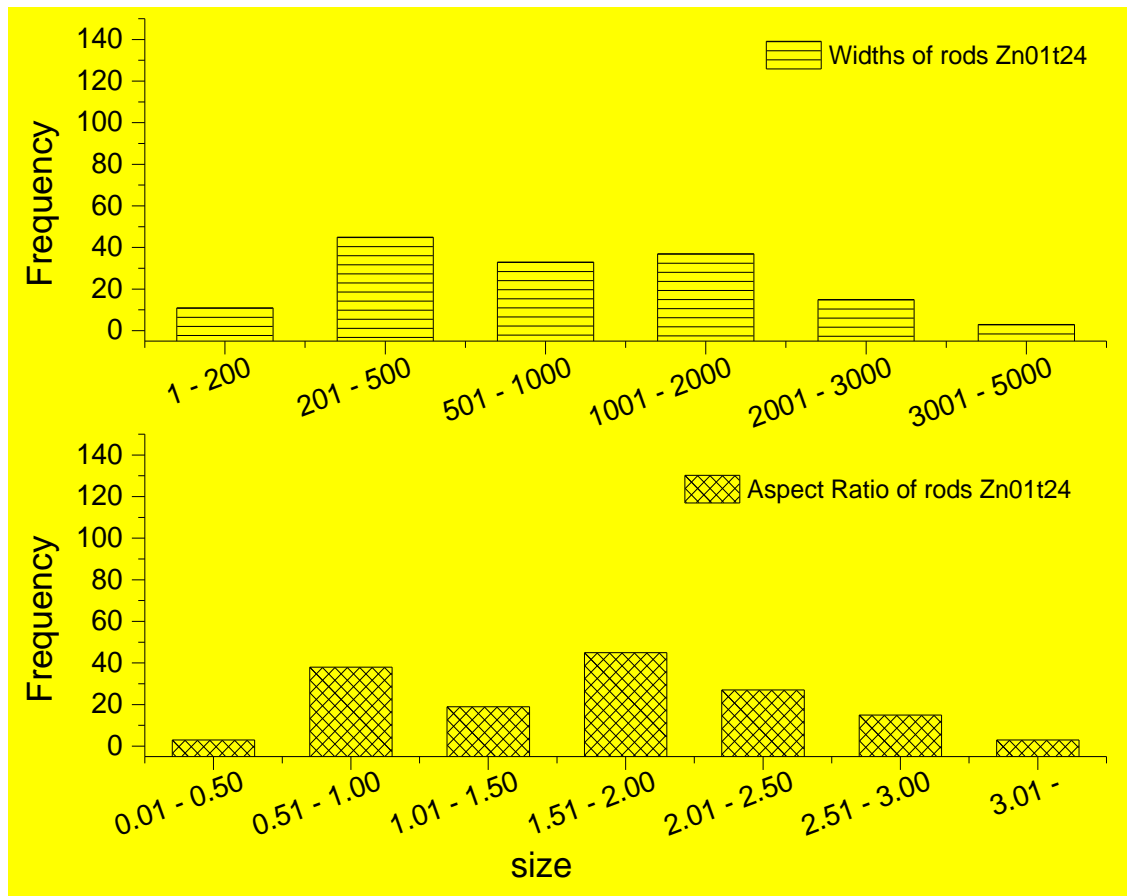


Figure 4.29: Distribution of particle width and aspect ratios in sample *Zn01t24*.

4.2.8 Further Characterisation of 12 h Hydrothermal Treatment Products

In addition to TEM, other characterisation studies were conducted on sample *Zn01t12* to serve as a benchmark for reporting the properties of zinc oxide double rods synthesised hydrothermally from zinc acetate dihydrate and sodium hydroxide.

Gas adsorption porosimetry and Brunauer–Emmett–Teller (BET) surface area measurements were conducted on sample *Zn01t12*. Levels of mesoporosity (5–50 nm) in the bulk powders were investigated using gas adsorption porosimetry. Result obtained indicated about 5.7 vol. % mesoporosity. The cumulative volume of mesopores was approximately $9.9 \times 10^{-3} \text{ cm}^3 \text{ g}^{-1}$ with an associated surface area of $\sim 2.8 \text{ m}^2 \text{ g}^{-1}$. Multipoint BET surface area measurements indicated a surface area of $10.36 \text{ m}^2 \text{ g}^{-1}$. Figure 4.30 presents the BJH adsorption plot.

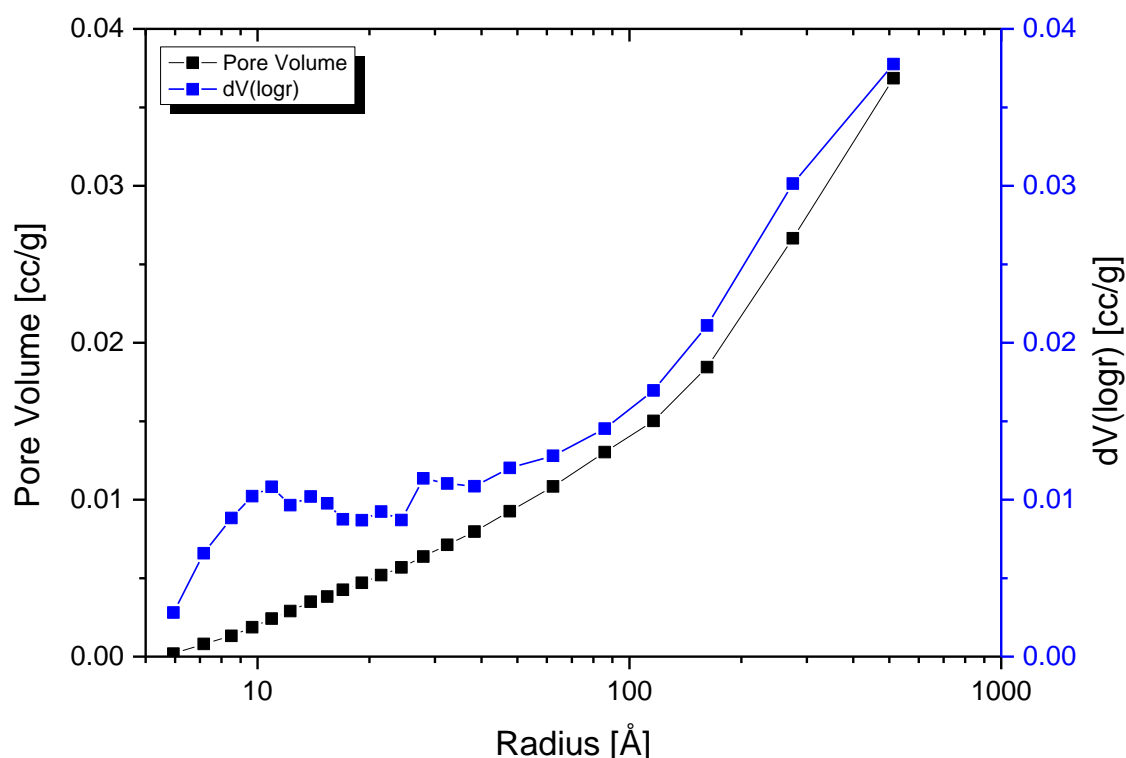


Figure 4.30: BJH adsorption plot of sample *Zn01t12*.

Fourier Transform Infrared (FTIR) Spectroscopic analysis of sample *Zn01t12* conducted on a Thermo Scientific Nicolet iS10 mid-range FT-IR Spectrometer fitted with a diamond crystal resulted in a spectrum with broad peak (hump)

between 3500 cm^{-1} and 3000 cm^{-1} attributed to (O–H) bond stretching from water adsorbed onto the particle surface; multiple peaks were also observed between 2400 cm^{-1} and 1950 cm^{-1} which was traced to ambient CO_2 or instrumental background, While the peak observed around 600 cm^{-1} is characteristic of Zn-O bond vibrations which is noted to occur between 400 cm^{-1} and 700 cm^{-1} depending on conditions of analysis (NIST, 2011). Figure 4.31 shows the FTIR spectrum of sample *Zn01t12*.

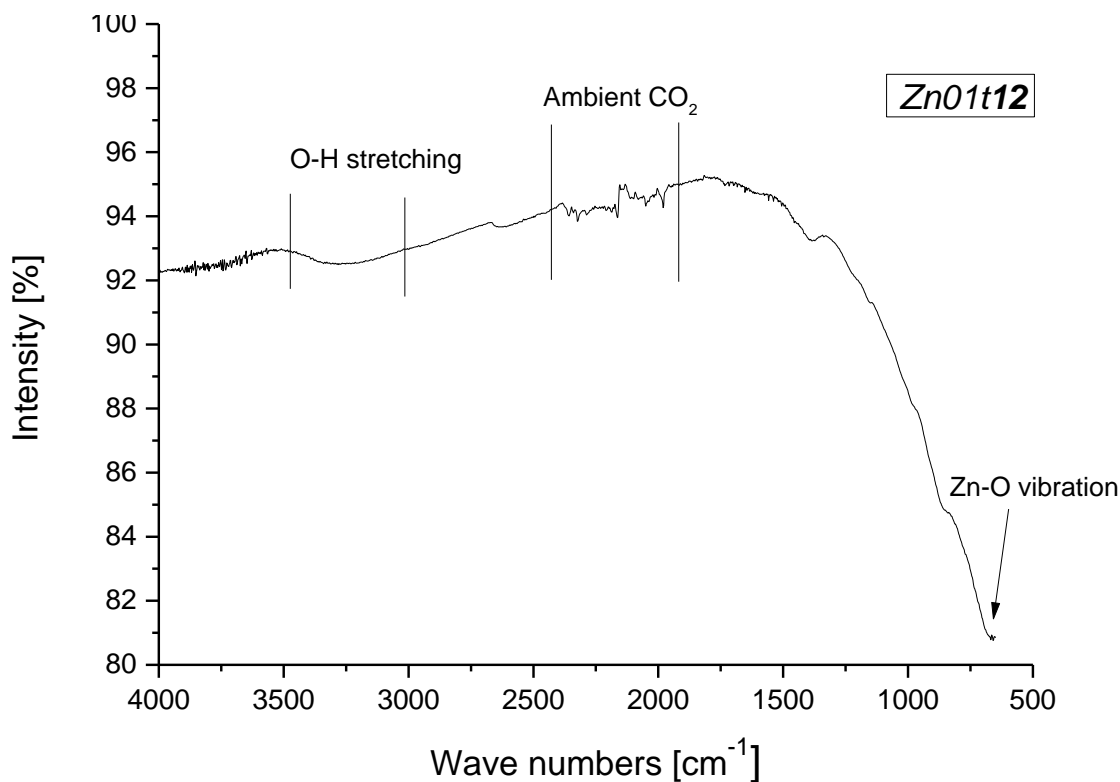


Figure 4.31: FTIR spectrum of sample *Zn01t12*.

4.2.9 Comparative Analysis of the Effect of Hydrothermal Treatment Durations (Dwell Times) on Growth Process of Zinc Oxide Hexagonal Double Rods

X-ray Diffraction

A comparison of peaks from X-ray diffraction analysis of the samples showed slight variations in relative peak intensities with respect to hydrothermal treatment durations (Figure 4.32) with peak intensity attenuation observed in some of the samples (Table 4.6), and it is thought that responsibility for its occurrence could be attached to one or more of the following:

To begin with, the variation in relative peak intensities may have resulted from sample preparation process and X-ray diffraction process. Intensity of peaks could be influenced by the smoothness or otherwise of the powder bed on the sample holder. Also two different types of powder sample holders were used.

Secondly, variation in relative intensities of powder X-ray diffraction patterns could be as a result of particle size, shape and orientation effects (see section 3.2.1.4).

A comparison of particle widths and aspect ratios as a function of hydrothermal treatment times is presented in Figure 4.34 and 4.35, while Figure 4.32 is a plot comparing the X-ray diffraction patterns of the zinc oxide particles as a function of hydrothermal treatment duration

Table 4.6: Comparison of relative peak intensities of X-ray diffraction patterns showing slight variations in peak intensities.

N. B. for purposes of easy comparison and annotation, Table 4.6 has been relocated to the next page and formatted differently from previous tables.

0 h			0.5 h			1 h			3 h			6 h			12 h			ZnO Reference			h k i l			
d	2 Θ	I	d	2 Θ	I	h	k	i	l															
[Å]	[°]	[%]	[Å]	[°]	[%]																			
2.820	31.7	83	2.816	31.8	100	2.807	31.9	55	2.805	31.9	55	2.820	31.7	78	2.851	31.4	48	2.814	31.8	55	1	0	-1	0
2.722	32.9	16	2.698	34.2	5	2.687	34.4	1	2.685	34.4	1													
2.652	34.8	15																						
2.608	34.4	61	2.605	34.4	32	2.598	34.5	47	2.595	34.6	43	2.608	34.4	45	2.634	34.0	48	2.603	34.4	42	0	0	0	2
									2.553	35.1	2													
2.481	36.2	100	2.477	36.3	91	2.471	36.4	100	2.469	36.4	100	2.481	36.2	100	2.504	35.9	100	2.476	36.3	100	1	0	-1	1
						2.326	38.7	1	2.325	38.7	1				2.353	38.2	1							
2.232	40.4	1				2.281	39.5	1	2.281	39.5	1				2.304	39.1	1							
2.002	45.3	2																						
1.915	47.5	23	1.914	47.5	12	1.910	47.6	24	1.908	47.7	25	1.915	47.5	18	1.928	47.1	32	1.911	47.5	22	1	0	-1	2
1.878	48.5	5																						
1.662	55.3	1										1.627	56.5	32	1.694	54.1	0							
1.629	56.5	36	1.627	56.6	33	1.625	56.7	44	1.624	56.7	44	1.626	56.7	20	1.637	56.2	55	1.625	56.6	31	1	1	-2	0
1.563	59.1	6	1.556	59.4	1	1.528	60.6	1							1.538	60.2	1							
1.481	62.7	22	1.480	62.8	13	1.476	62.9	37	1.475	62.9	38	1.479	62.8	21	1.485	62.5	54	1.477	62.9	28	1	0	-1	3
						1.476	64.1	23	1.475	64.1	22	1.478	64.0	13	1.485	62.7	33							
1.411	66.2	4	1.409	66.3	5	1.406	66.4	7	1.406	66.5	7	1.409	66.3	4	1.415	66.0	9	1.407	66.4	4	2	0	-2	0
									1.406	66.7	4	1.380	67.9	18	1.385	67.6	46							
1.382	67.8	16	1.381	67.9	13	1.378	68.0	33	1.377	68.0	33	1.380	68.1	11	1.385	67.8	29	1.378	68.0	23	1	1	-2	2
						1.377	68.2	22	1.377	68.2	20	1.360	69.0	10	1.365	68.7	23							
1.362	69.0	10	1.361	69.0	10	1.358	69.1	17	1.357	69.2	17	1.360	69.2	6	1.365	68.9	15	1.358	69.1	11	2	0	-2	1
						1.358	69.3	11	1.357	69.4	10													

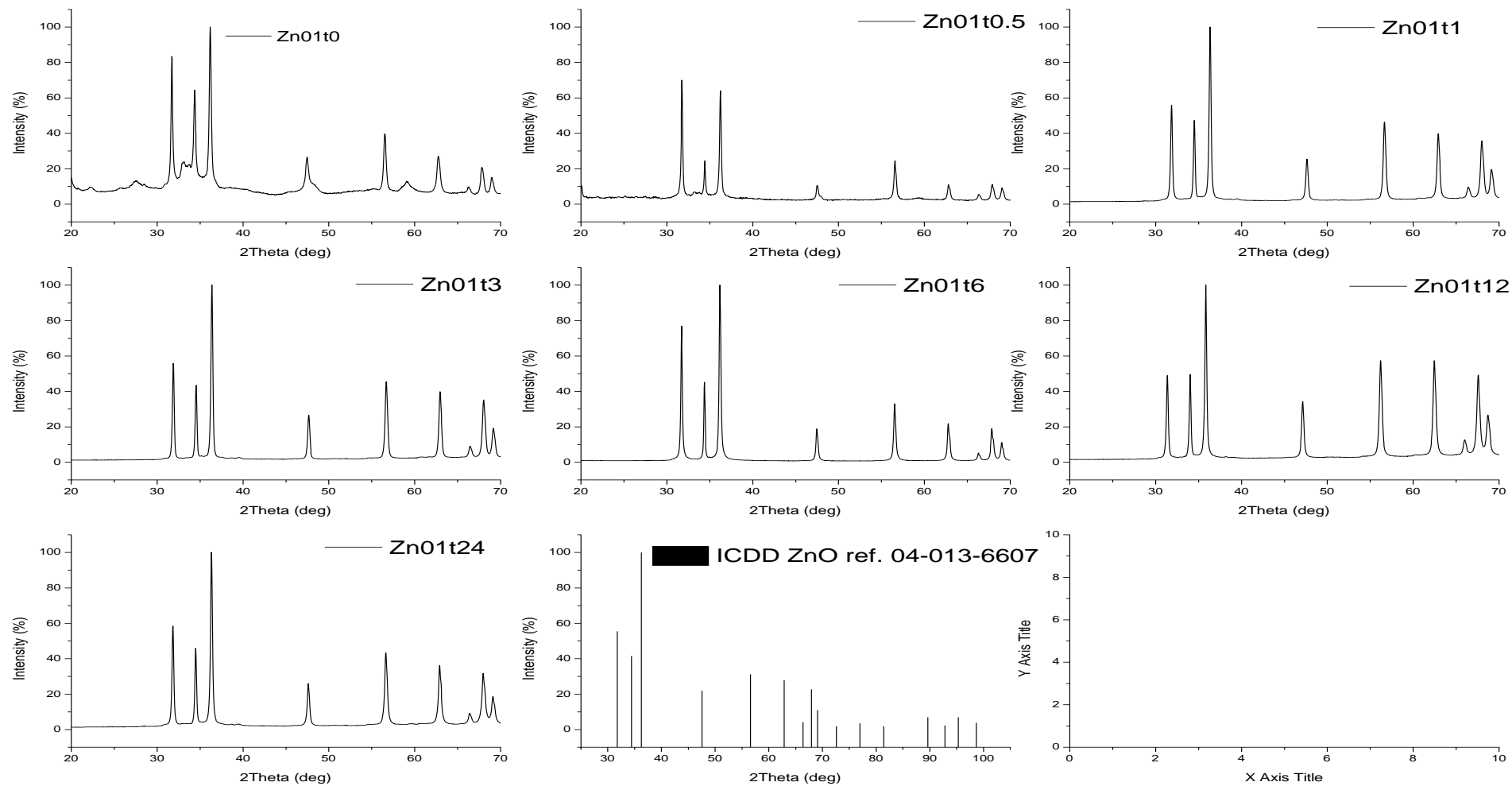


Figure 4.32: Compilation of X-ray diffraction patterns showing slight changes as a function of hydrothermal treatment time.

Particle Shape

Based on results obtained from SEM analysis of samples Zn01t0 to Zn01t24 (Figure 4.34), it was observed, that each of the samples contained one or more distinct particle morphologies (Table 4.7). In providing a descriptive labelling of the morphologies observed they were tagged as sheet like (or flake like) particles, equiaxed nanoparticles, irregular shaped particles, lozenge shaped nanoparticles, hexagonal single rods, double rods, hollow double rods, nanoflakes, and nanoclusters.

The observation of multiple particle shapes in each of the samples was most likely due to the fact that usually, particle growth under hydrothermal conditions is inhomogeneous in nature with crystal nucleation and growth processes occurring continuously all through the course of the hydrothermal process and termination of the process at any point should capture particle representative of different particle growth stages. Although majority of the particles captured during sampling would reflect the general picture of state of things at that stage of development, there are bound to be particles which would show a higher developmental stage relative to the bulk (because they nucleated earlier) or a lower developmental stage relative to the bulk (because they nucleated much later). To obtain a sample comprising entirely of the final stage of particle growth, one would have to extend the length of the hydrothermal treatment until complete (100 %) conversion of all the feed material in the reaction medium has been achieved and all reactive processes exhausted (if possible). However, an advantage of the foregoing phenomenon is that it provides the opportunity of being able to track the evolution particle growth with each sample providing clues to preceding and future stages of the current bulk particles

pH of the Reaction Medium

The pH values of the post hydrothermal treatment contents of the reactor were monitored and changes in pH values as a function of length of hydrothermal treatment was monitored.

On the overall, a gradual decline in pH values was observed with increasing hydrothermal dwell times (Figure 4.33).

Starting with the untreated precursor suspension (i.e. sample *Zn01t0*) which had a pH ~9, a steep drop in pH values was noticed after 0.5 h of hydrothermal treatment (by measuring the pH value of sample *Zn01t0.5*), with pH values dropping from ~ 9 in sample *Zn01t0* to pH ~ 7.2 in sample *Zn01t0.5*. It was observed that this event coincided with the emergence of hexagonal rods in 0.5 h hydrothermal products.

Further decreases in pH values occurred with increasing reaction times up to a final pH of approximately 6.5 as observed in sample *Zn01t12* after which no further significant decrease in pH was observed.

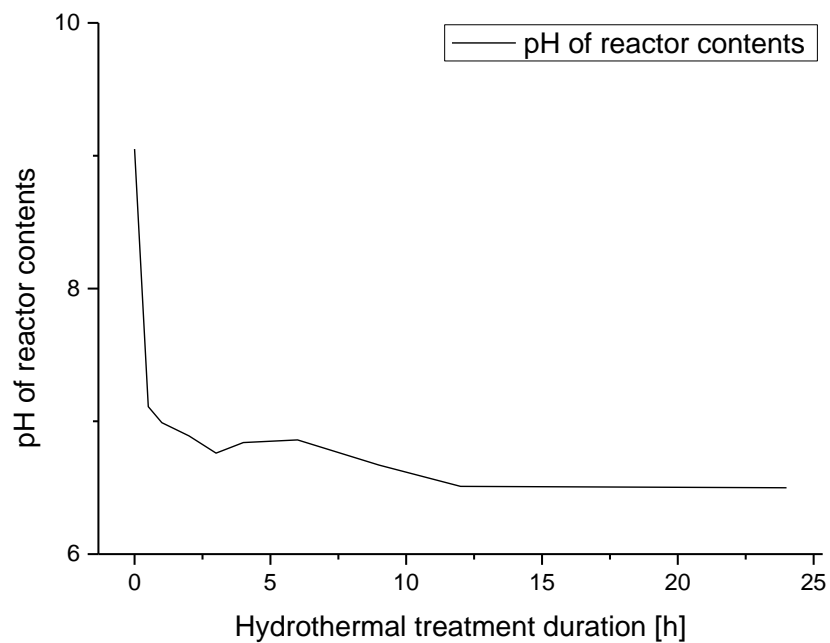


Figure 4.33: pH profile as a function of hydrothermal treatment duration.

Observations of reduction in pH value as a function of length of hydrothermal treatment could be as a result of rapid crystallisation of ZnO rod-like particles from the precursor suspension especially during the early stages of hydrothermal treatment as described in 4.2.10. Also, reduction in pH of final products may not have exceeded the value of 6.5 largely because that is roughly the pH value of a zinc oxide-in-water suspension.

Table 4.7: Description of particle morphologies in different samples as observed through scanning electron microscopy.

Sample	Particle shapes observed
Zn01t0	irregular shaped particles, sheet-like particles, equiaxed nanoparticles
Zn01t0.5	Hexagonal double rods, Hexagonal single rods, irregular shaped particles, sheet-like particles, equiaxed nanoparticles
Zn01t1	Hexagonal double rods, Hexagonal single rods, irregular shaped particles, lozenge shaped particles
Zn01t3	Hexagonal double rods, Hexagonal single rods, irregular shaped particles, lozenge shaped particles
Zn01t6	Hexagonal double rods, Hexagonal single rods, irregular shaped particles, lozenge shaped particles
Zn01t12	Hexagonal double rods, Hexagonal single rods, lozenge shaped particles
Zn01t24	Hexagonal double rods, Hexagonal single rods

Particle Size

Observations regarding changes to particle sizes with respect to hydrothermal treatment times was made by analysing a minimum of 150 particles from a collection of SEM micrographs of each sample. Although it was difficult to correlate changes in particles sizes as a function of hydrothermal treatment time largely because of the variation in percentage content of single rod and double rod particles. Double rod particles indicated higher aspect ratios in comparison to single rod particles. However, on the overall, there was a shift in particle width ranges with the trend indicating a general increase in aspect ratios with increasing hydrothermal treatment times.

Figure 4.35 shows a comparison of particle widths as a function of increasing hydrothermal dwell times, while Figure 4.36 is a plot of aspect ratios showing progressive increase in particle anisotropy as hydrothermal treatment durations increased. Data for the plots in Figures 4.35 and 4.36 were obtained by measuring a minimum of 150 particles from each sample.

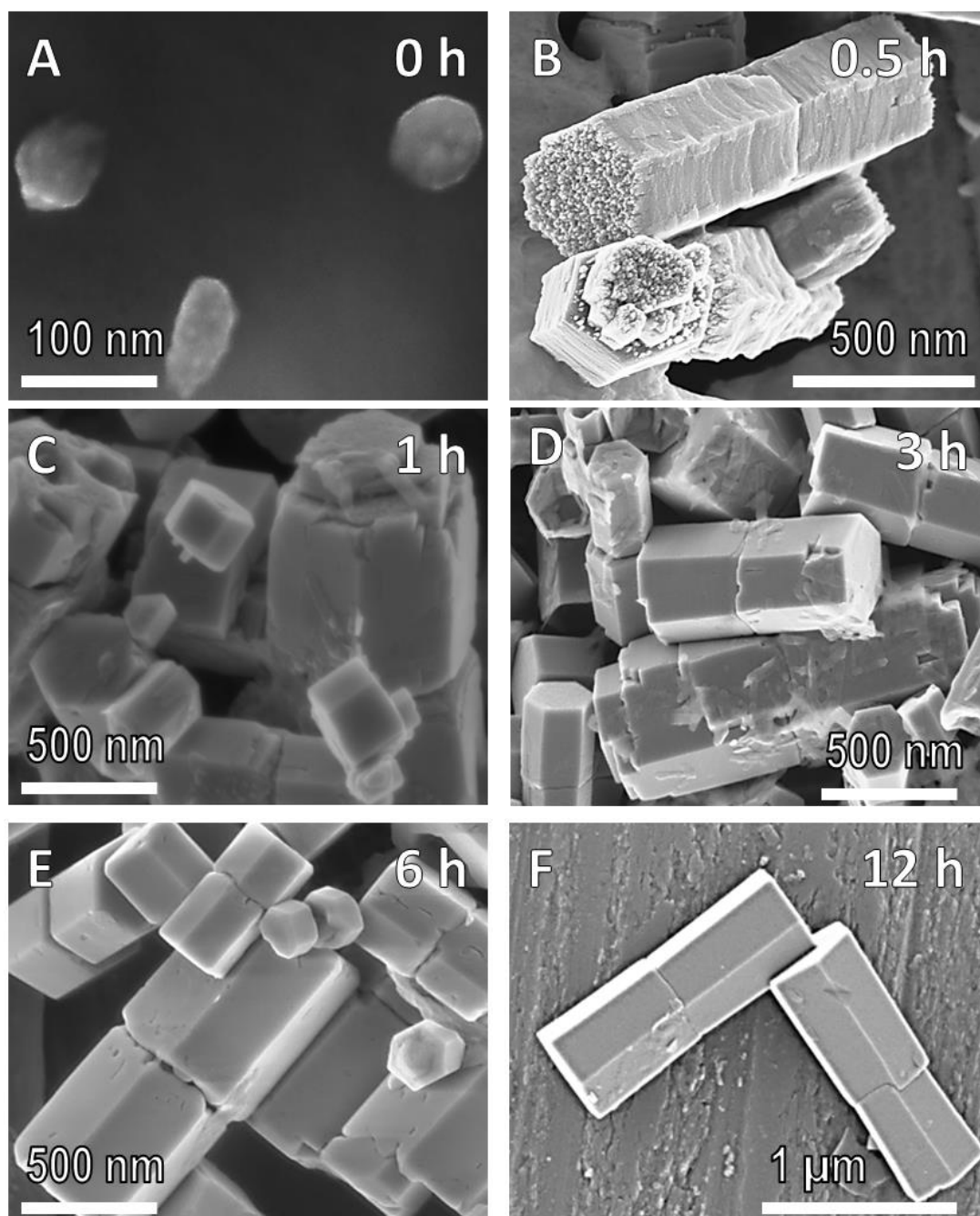


Figure 4.34: Collage of SEM images highlighting changes in particle shape and size with respect to hydrothermal treatment time (A) 0 h, (B) 0.5 h, (C) 1 h, (D) 3 h, (E) 6 h, (F) 12 h.

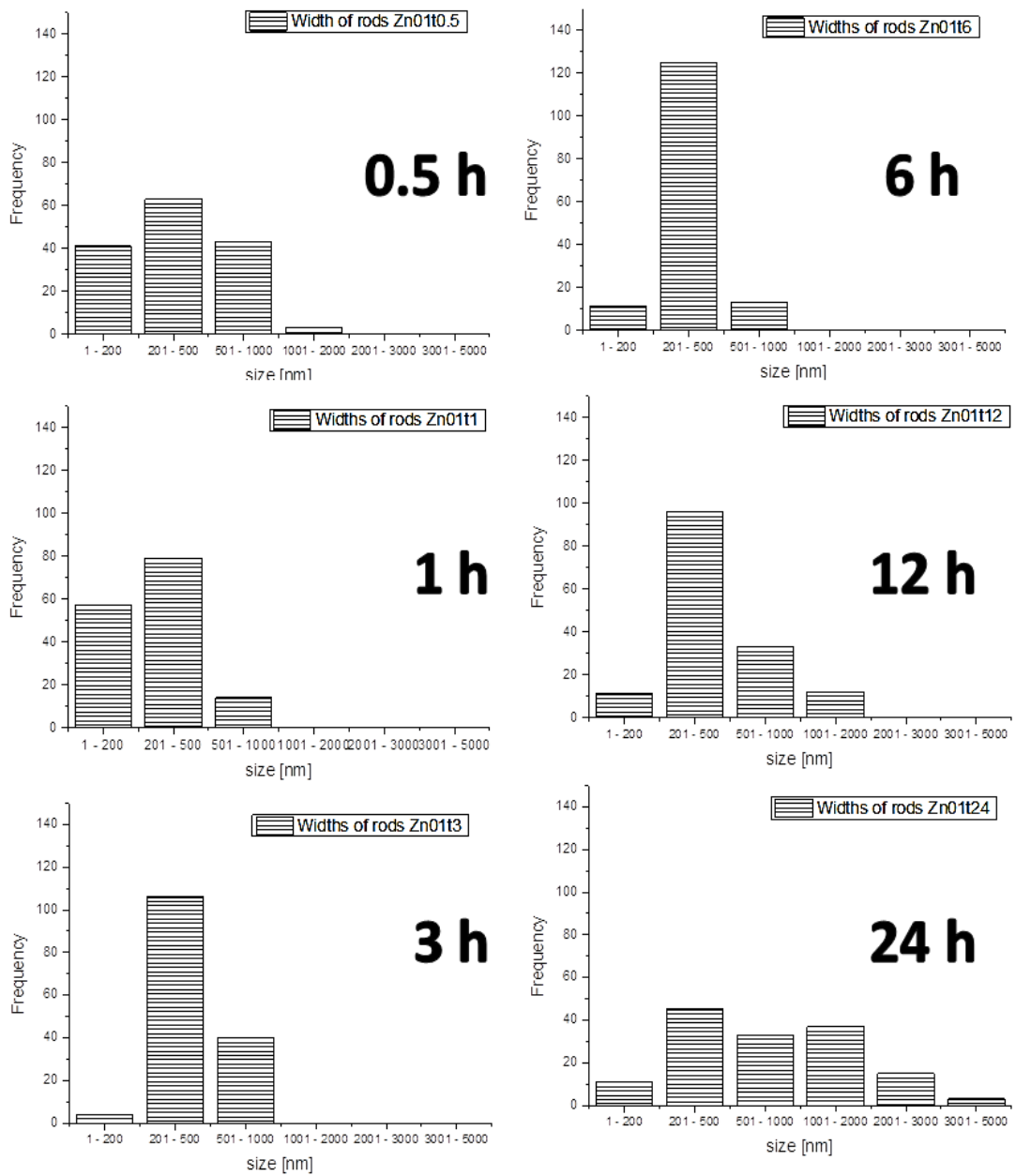


Figure 4.35: Comparison of particle widths as a function of hydrothermal treatment times showing gradual increase in particle widths as hydrothermal treatment duration (dwell times) increased.

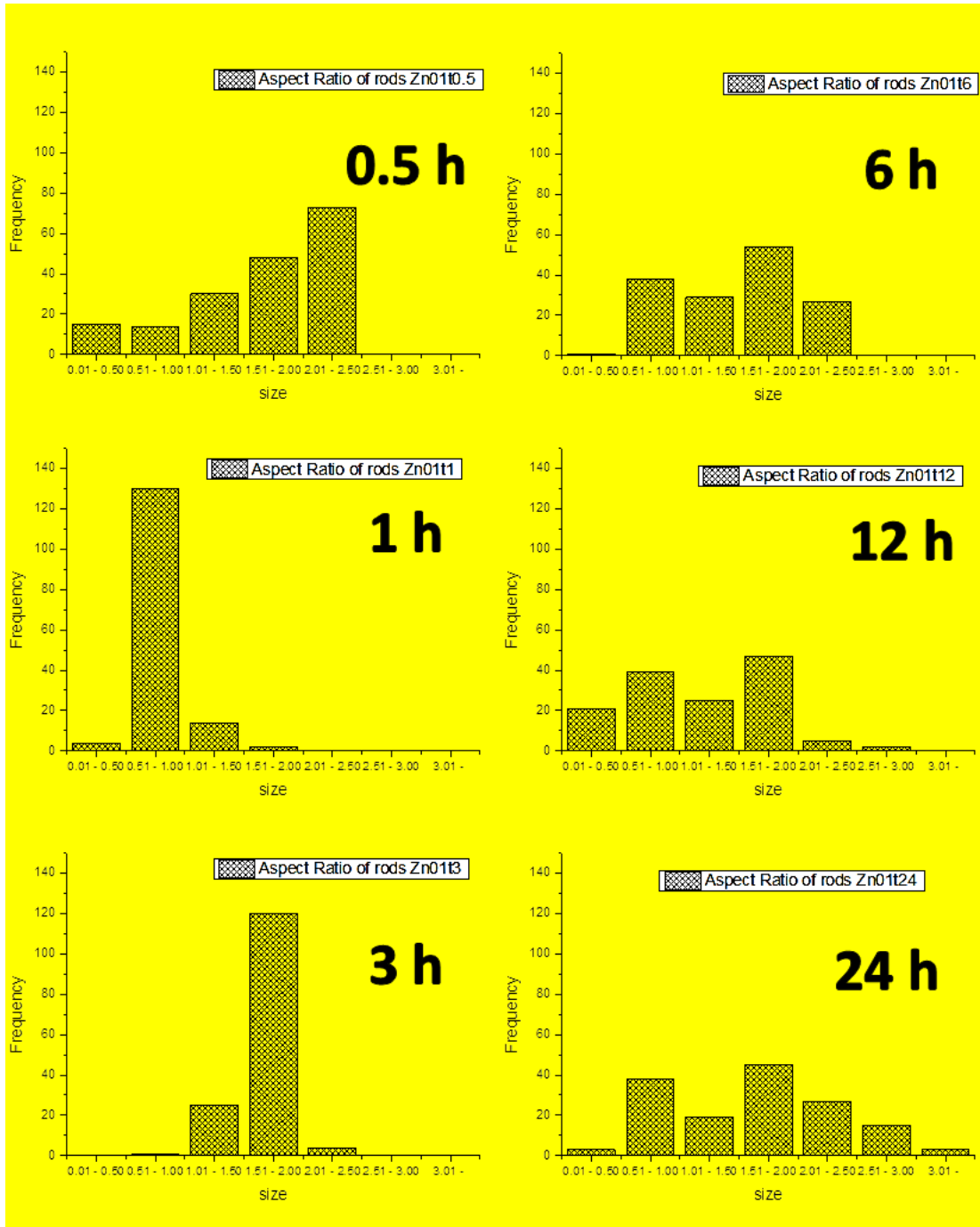


Figure 4.36: Comparison of aspect ratios of particles as a function of hydrothermal treatment time showing increase in particle anisotropy with increasing hydrothermal treatment times.

4.2.10 Chemistry, Crystal Structure, Synthesis Conditions, Particle Morphology Relationships and Zinc Oxide Double Rod growth Mechanisms

To set the stage for discussions on the growth process of the hexagonal double rods, it is necessary to briefly examine existing knowledge on the growth of this type of zinc oxide particle focussing on the relationships between the chemistry of the synthesis process, zinc oxide's crystallographic properties, conditions of synthesis and the morphology of the particles.

Chemistry

The chemistry of the synthesis of zinc oxide double rods from a solution of zinc acetate and sodium hydroxide follows a complex chemical pathway which is difficult to model in its entirety due to the many intermediate reactions and side reactions that contribute to the emergence of the final product. Nevertheless, the foregoing is an attempt to provide some level of insight into the chemistry of the process.

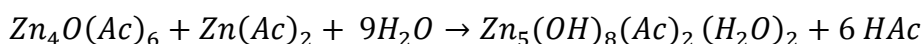
The dissociation of zinc acetate and sodium hydroxide in water to generate sodium, zinc ions as well as hydroxide and acetate radicals could be described by the following equations:



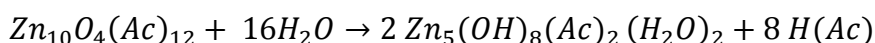
Where: $Ac = CH_3COO$



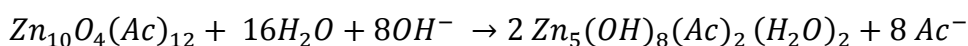
The formation of Layered basic zinc acetate (LBZA) has been noted to occur via H₂O-induced reorganization of tetrahedral (ZnO₄⁶⁻) species formed during initial nucleation process as shown below (Baruah and Dutta, 2009):



Equation 4.3



Equation 4.4

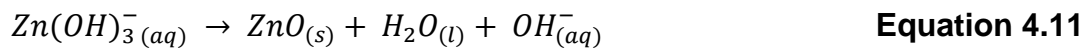
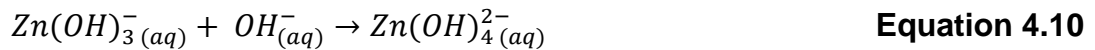
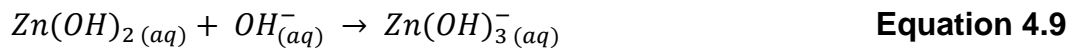


Equation 4.5

The precipitation of metastable zinc hydroxide (ϵ -Zn(OH)₂) from the reaction mixture was not observed at any time during the course of particle growth, hence it is thought, that the reactions described by Equations 4.6 & 4.7 were either suppressed, or its kinetics was too fast to have been observed.



Equations 4.8 to 4.12 attempt to chronicle the chemical processes that lead to the precipitation of zinc oxide from solution. It is widely acknowledged that the chemistry of nucleation and growth of the particles is relatively complex involving the interplay of a varied number of factors (Baruah and Dutta, 2009; Moezzi et al, 2011).



Crystal Structure and Growth Mechanism

Growth of wurtzite zinc oxide generally occurs in three directions viz: <0001> (comprising [0001] and [000 $\bar{1}$] directions), <2 $\bar{1}$ 10> (comprising \pm [2 $\bar{1}$ 10], \pm [$\bar{1}$ 2 $\bar{1}$ 0], \pm [$\bar{1}$ 120] directions) and <0110> (comprising \pm [01 $\bar{1}$ 0], \pm [10 $\bar{1}$ 0], \pm [1 $\bar{1}$ 00] directions) with the relative rate of growth in each direction determining the final shape of the crystal (Baruah and Dutta, 2009). The polar {0001} facets have a higher surface energy than the nonpolar {01 $\bar{1}$ 0} or {2 $\bar{1}$ 10} facets, and hexagonal rods are formed when growth rate in the <0001> direction is faster than other growth directions (referred to as c-axis directed growth), resulting in larger {01 $\bar{1}$ 0} or {2 $\bar{1}$ 10} faces (Figure 4.37) (Wang, 2004; Baruah and Dutta, 2009).

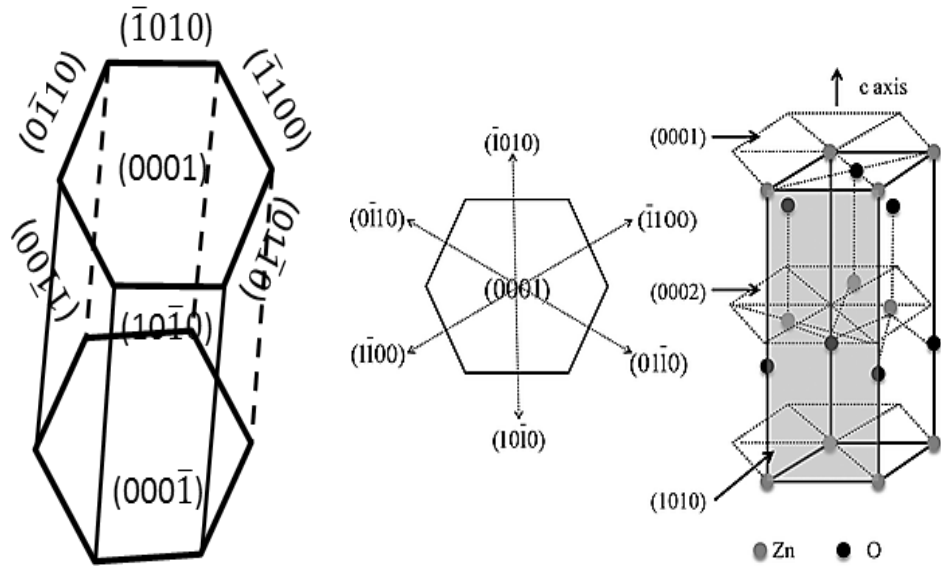


Figure 4.37: Schematic showing crystal planes in a wurtzite zinc oxide hexagonal rod (Amin, 2012).

There is some degree of uncertainty surrounding the mechanisms responsible for the emergence of hexagonal zinc oxide double rods (Baruah and Dutta, 2009; Wang et al., 1998; Hu et al., 2004; Bitenc et al., 2010).

It has been suggested that bi-pyramidal shaped zinc oxide double rods resulted from the occurrence of a crystal twinning process in which tetrahedral ZnO_4^{6-} (from $\text{Zn}(\text{OH})_2$) linked up at the basal planes and nucleated to create an interfacial junction. Crystal growth then proceeded via incorporation of ZnO_4^{6-} growth units on either side, along the $\langle 0001 \rangle$ directions leading to the emergence of double rods (Figure 4.38a) (Wang et al., 1998).

It was also proposed that the growth of dumbbell shaped hexagonal zinc oxide rods followed a similar process to that of the bipyramidal shape described above with the major difference being that in the case of the dumbbell shaped double rods, the tetrahedral ZnO_4^{6-} growth units that were involved in the creation of the interparticle junction were not directly linked together (as was the case earlier) but rather were connected by cations of the base specie used in synthesis e.g. K^+ or Na^+ as shown in Figure 4.38b.

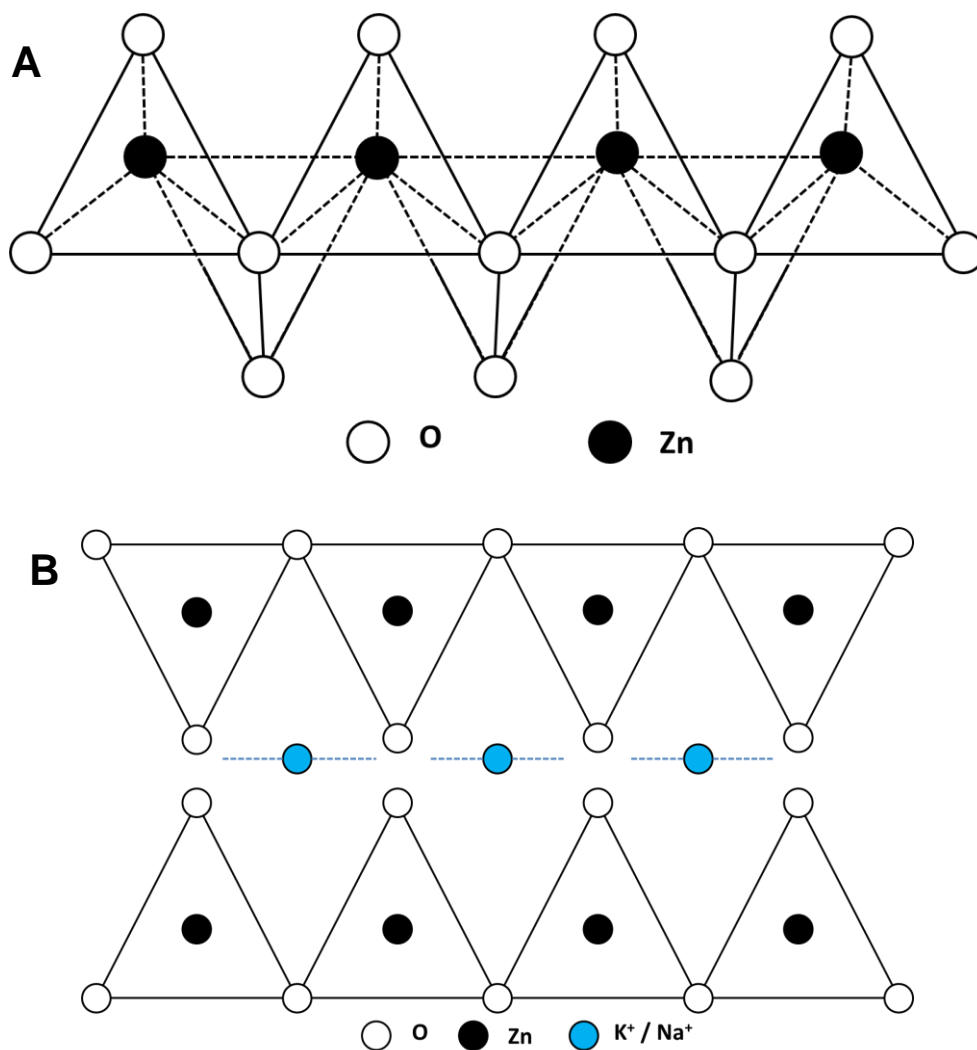


Figure 4.38: Illustration of particle growth via crystal twinning leading to emergence of (A) bi-pyramidal shaped (B) dumbbell shaped zinc oxide hexagonal double rods (Wang et al., 1998).

Another mechanism that was proposed for the formation of hexagonal double rods involved the linkage of two single rods. Here, zinc oxide crystallites first nucleate out of solution and then grow into individual hexagonal rods. These individual single rods then become attached at their {0001} faces leading to the formation of double rods (Figure 4.39). The development foregoing process was hinged on the exhibition of crystallographic polarity within the wurzite structure of zinc oxide. Zinc oxide rods are known to have terminals with opposing polarity occasioned by the alternating arrangement of planes of Zn and O atoms along the c-axis (Hu et al., 2004). The formation of star shaped multipod particles through this

process has also been reported, showing that the linkage process could involve more than just two rod-like particles (Hu et al., 2004).

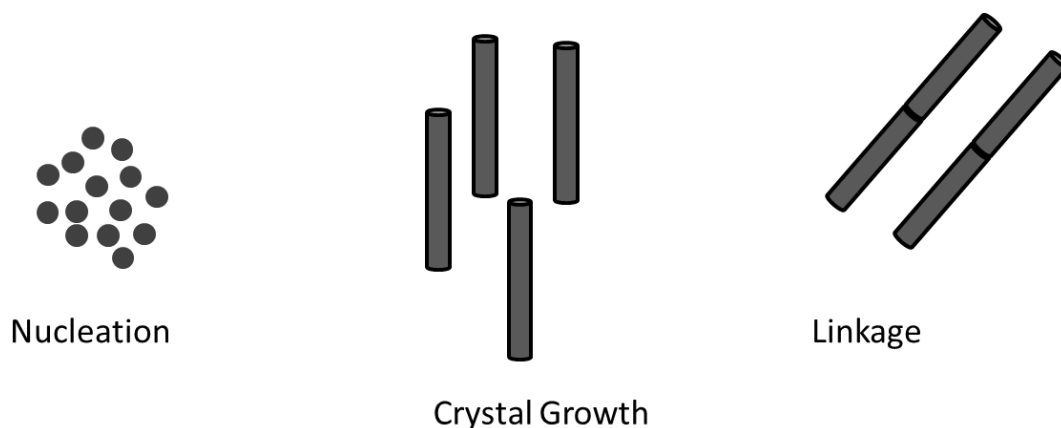


Figure 4.39: Illustration of linkage mechanism leading to formation of zinc oxide hexagonal double rods (Hu et al., 2004).

It has been observed, that rod attachment could also involve the prismatic sides, i.e. $\{10\bar{1}0\}$ facets, of the hexagonal rods (i.e. side to side attachment) as shown in Figure 4.41 (Liu and Zheng, 2003).

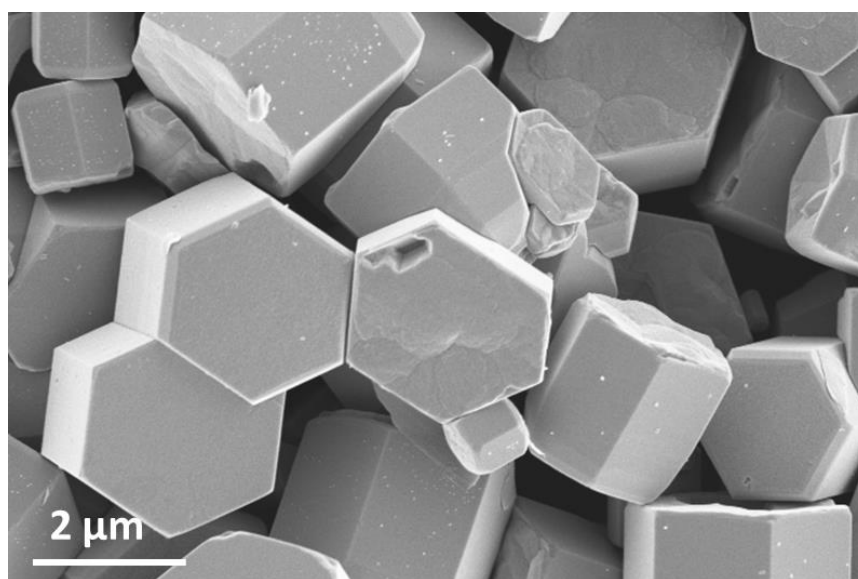


Figure 4.40: SEM image showing side to side attachment of ZnO rods.

It has been reported, that the presence of dopants or impurities, could act as triggers for the nucleation and growth of hexagonal double rods. Using energy dispersive X-ray spectroscopy (EDXS), Bitenc et al., (2010) performed an analysis of the interfacial junction within a zinc oxide double

rod particle synthesised from the reaction of zinc nitrate hexahydrate and urea in an open reactor. The analysis revealed the presence of silicon (~ 1 atomic layer thick) at the interfacial junction (Figure 4.41).

Based on findings from their EDXS analysis, [Bitenc and co-workers \(2010\)](#) suggested that the silicon layer may have played a role in the formation of the double rod morphology, by serving as nucleation base for [0001] directed rod growth on both sides of the silicon layer. It was reported however, that silicon was not intentionally introduced into the reaction mixture, and also that the reactants were found to have had insignificant silicon content ($< 0.1\text{mg L}^{-1}$). Hence the authors were of the opinion that the silicon impurity originated from the glassware that was used for the synthesis process.

The authors were also of the opinion that after silicon-aided formation of interfacial junction, c-axis directed rod growth proceeded simultaneously through attachment of zinc oxide nanoparticles, as well as through the incorporation of ions on the surface of the particles with the end products having hexagonal double rod morphology ([Bitenc, et al., 2010](#)).

Figure 4.41 shows the interfacial junction of a double rod particle and EDXS analysis of spots on the particle ([Bitenc, et al., 2010](#)).

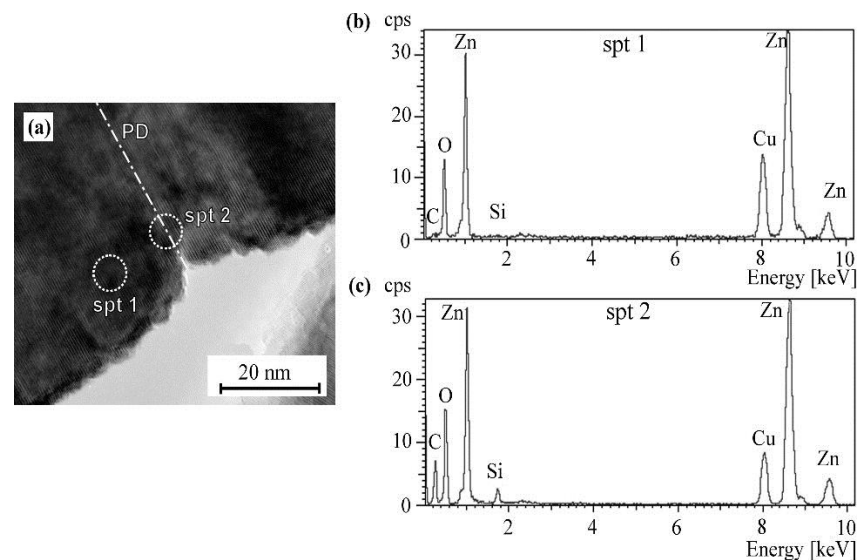


Figure 4.41: (a) TEM micrograph of the interfacial junction of a double rod particle (b) Result of EDXS analysis of area labelled as 'spt1' (c) Results of EDXS analysis of area labelled as 'spt2' ([Bitenc et al., 2010](#)).

4.2.11 Hierarchical Growth Process of Zinc Oxide Hexagonal Double Rod Particles

Based on observations of from scanning and transmission electron microscopic analysis of the samples *Zn01t0* to *Zn01t24*, deductions were made regarding the pathway through which particle morphology evolution and growth process of the zinc oxide double rod particles progressed. It is important to note that some of the stages mentioned were observed to have occurred simultaneously or were captured within the same time frame, but have been separated to provide clarity of presentation.

A hierarchical process of growth is proposed comprising the following key stages of growth:

Stage 1: Growth of the hexagonal double rods, is thought to have started with the emergence of equiaxed zinc oxide crystallites having sizes of less than 20 nm from large amorphous and sometimes polycrystalline sheet-like zinc oxide material within the first hour of hydrothermal treatment.

Stage 2: The equiaxed crystallites then aggregated together to form thin lozenge shaped polycrystalline particles after which they appeared to have fused together and recrystallised to produce 50 nm thick nanoplates which stack up in a stepwise manner along the c-axis [0001] direction to yield rod like particles with layered (stepped) (0001) faces.

Stage 3: The rod-like particles made up essentially of stacks of 50 nm zinc oxide plates underwent a further stage of recrystallization to produce single rod particles with relatively smooth terminal ends.

Stage 4a: A stage of heterogenous particle growth then ensued with the equiaxed nanocrystallites described in stage 1 being deposited on the basal planes of single rod particles from stage 3 of particle growth.

Stage 4b: In a parallel and concurrent process, two or more single rod-like particles from stage 3 become attached to create a double rod particle. The attachment preferentially occurs at the (0001) basal faces (i.e. end to end

attachment) Although sideways attachment of single particles have also been observed (Figure 4.40).

Stage 5a: double hexagonal rods were then formed on completion of stage 4a through the growth of a second rod via deposition of nanocrystallites and repetition of stages 1 to 3 on the terminal (0001) face of a pre-existing single rod particle. With the pre-existing rod acting more or less as a substrate or seed crystal for the growth of the second rod. Rods formed through this way appear not to have any gaps at the interfacial junction separating the two component rods. Also usually one of the rods (the base rod) also appears to have slightly larger dimensions than its partner rod.

Stage 5b: double hexagonal rods were formed on completion of stage 4b through the attachment of two single rod particles. The single rod particles developed independent of one another and then become attached via their (0001) faces leading to the creation of a double rod particle. Particles formed via this process appeared to have noticeable gaps at the point of attachment (interfacial junction) probably due to incomplete sealing of the seam created when the two rods became fused.

Presented in Figure 4.42 is a schematic description of the different stages involved in the development of the hexagonal double rods highlighting mechanisms for double rod formation via secondary growth of existing rod and end to end attachment of individual rods.

Figure 4.43 is a schematic diagram produced from SEM images obtained from samples to illustrate the key stages involved in the hierarchical growth of zinc oxide microrods from zinc acetate and sodium hydroxide under hydrothermal conditions. The arrow going straight from stage 3 to stage 5 implies formation of hexagonal double rods through end to end attachment of single rods as described in stage 5b

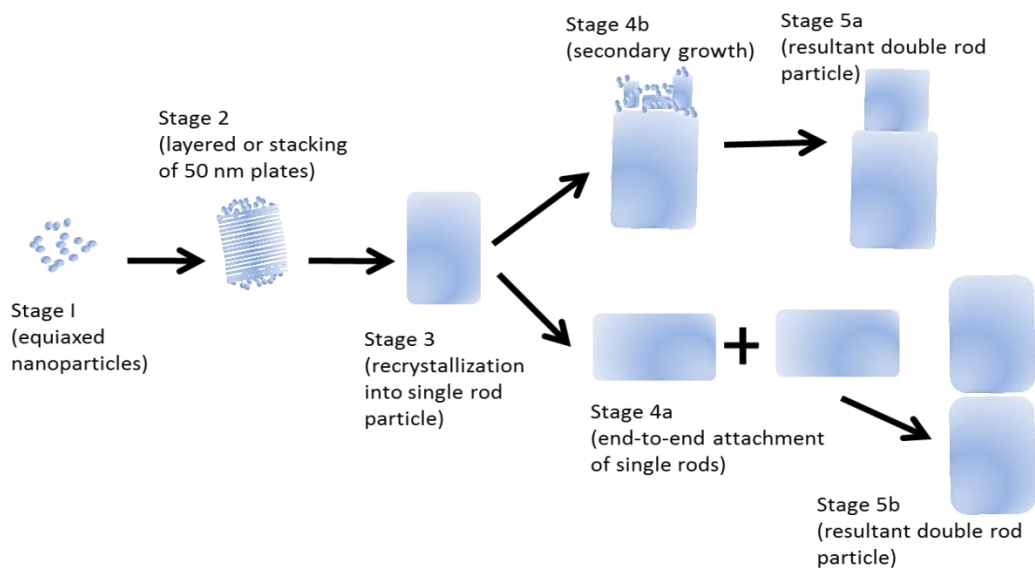


Figure 4.42: Schematic describing key growth stages leading to formation of zinc oxide hexagonal double rods (*not drawn to scale*).

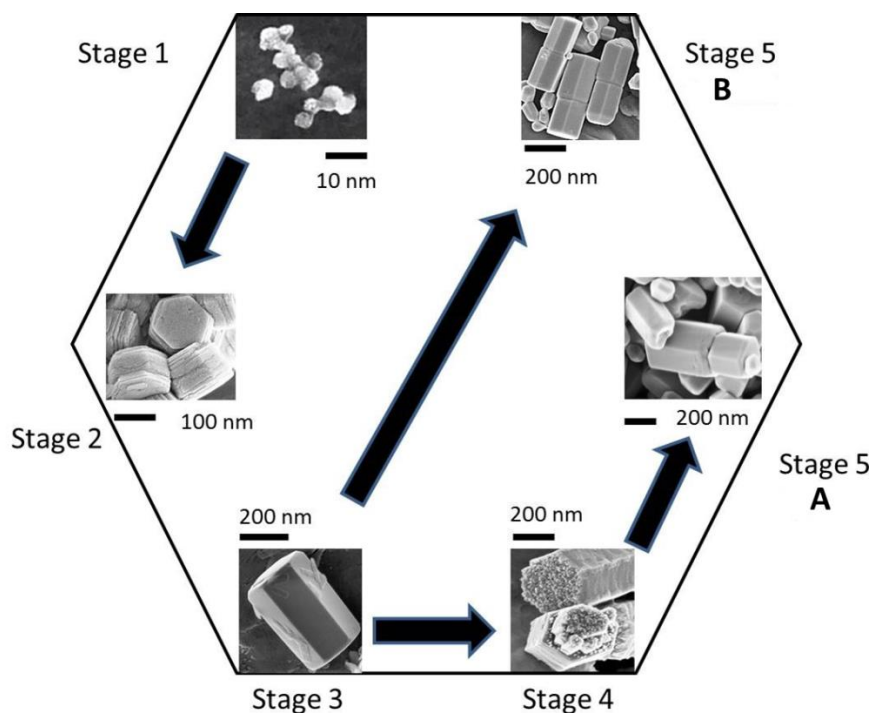


Figure 4.43: Schematic describing particle growth stages using SEMs of ZnO particles from zinc acetate and sodium hydroxide. Image in stage 1 shows equiaxed nanoparticles; Image in stage 2 shows striated particle showing evidence of stacking of nanoplates while SEM in stage 3 is a single rod particle and SEMs in Stages 4 5a & 5b show double rod growth via secondary growth and end to end attachment of rods.

Figure 5.44 is a collection of SEM images of particles from samples $ZnO_{1t0.5}$ and ZnO_{1t12} arranged to highlight particle growth involving deposition of crystallites on an existing rod-like particle as described in stage 5a

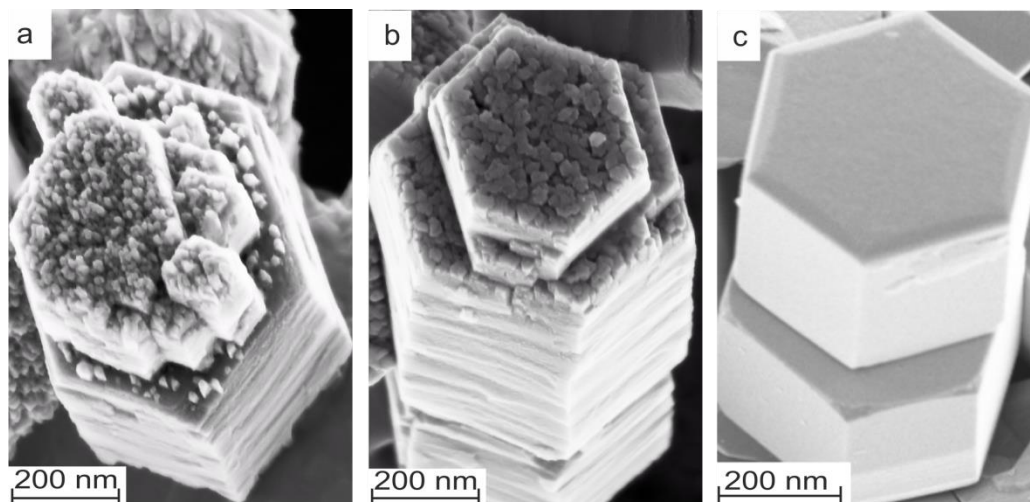


Figure 4.44: SEM collection illustrating (a) particle deposition on an existing rod-like particle and (b) subsequent stages of recrystallizing to produce (c) a well-defined hexagonal double rod.

The development of the particle growth mechanism described above has been based solely on observations made from electron microscopy and X-ray diffraction analysis. However, one cannot discount the possibility of other particle growth mechanisms such as crystal twinning, being involved in the formation of the double rods., from results obtained from particle characterisation, growth process as described appears to be the most probable.

4.3 Investigation via FIB-SEM and TEM, of Particle Formation Process and Interfacial Junctions in Zinc Oxide Hexagonal Double Rods

It was observed that there appeared to be two different types of the hexagonal double rod present in sample *Zn01t12*. Although observations of differences between the two types of particles were visible in the SEM, transmission electron microscopy provided a clearer visualisation of the differences between stage 5a and stage 5b double rod particles.

TEM images of the first set of double rod particles (Figure. 4.45) showed the rods had a compact interface with little or no gaps observed at the interfacial junction within the double rod particle. For purposes of identification these set of particles are labelled stage 5a particles.

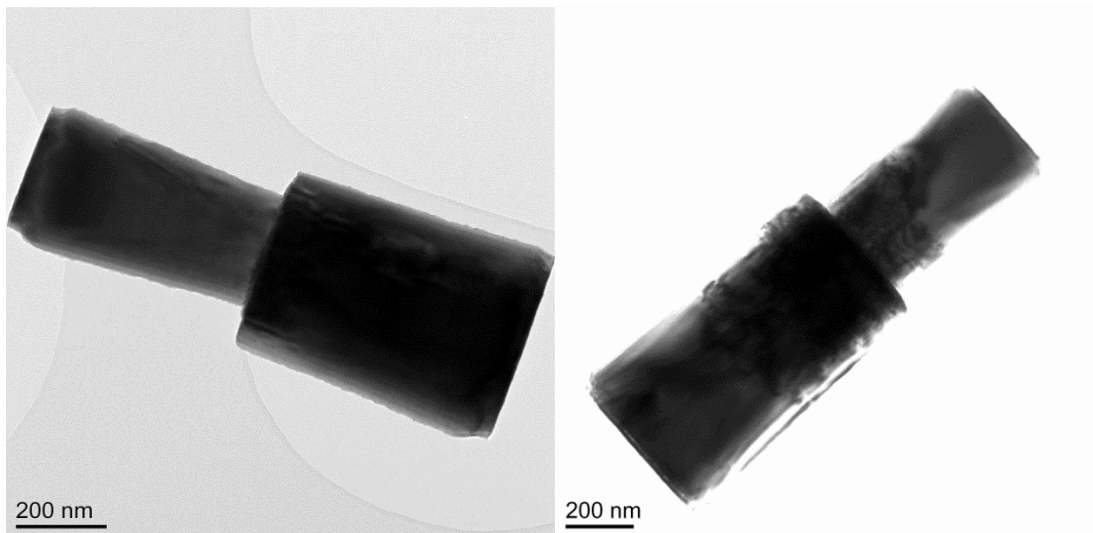


Figure 4.45: TEM micrograph of a stage 5a double rod (b) TEM of same particle with contrast modified to highlight the absence of hollow cavities and gaps at the interface between the components of the double rod.

Closer examination via HRTEM of the interfacial junction within the double rod particle (Figure 4.46) revealed the (0002) lattice planes of the crystal ran coherently across the interfacial junction within the rod along the [0001] growth direction of the bulk double rod particle. Figure 4.46 is a combination of low magnification, high resolution TEM and lattice images showing the coherence of (0002) lattice planes across the interfacial junction.

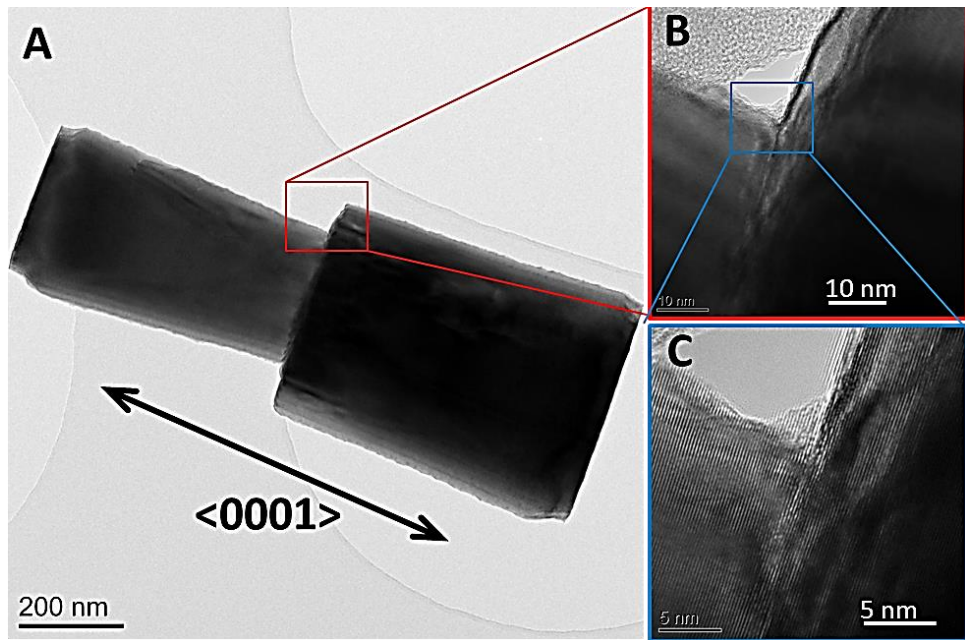


Figure 4.46: (a) low magnification, (b) high resolution TEM, and (c) lattice imaging showing no discontinuity between component rods and (0002) lattice planes running coherently across the interfacial junction.

The second type of hexagonal double rod particles appeared to possess disjointed seams with visible dislocations and gaps on one or both sides of the interfacial junction within the double rod particle (Figure 4.47). For purposes of identification these set of particles are referred to as stage 5b particles.

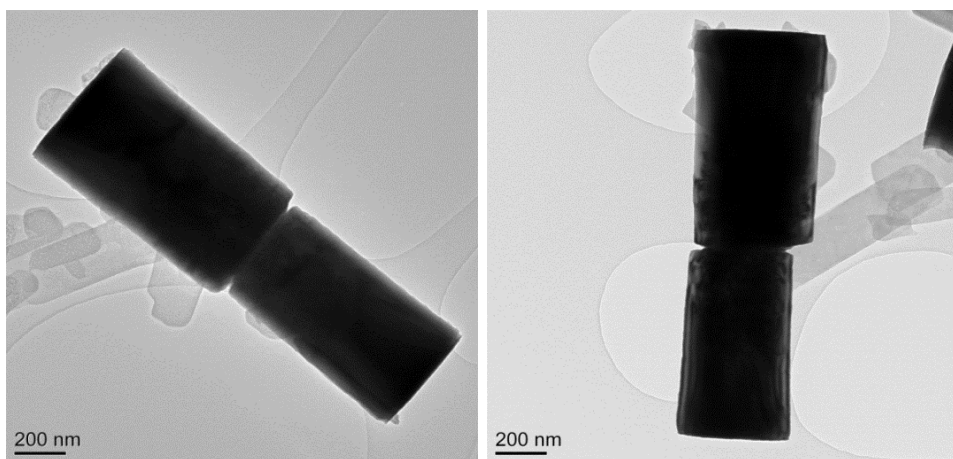


Figure 4.47: TEM micrograph of a stage 5b double rods showing (a) gaps at interfacial junction (b) disjointed interface between components of the double rod particle.

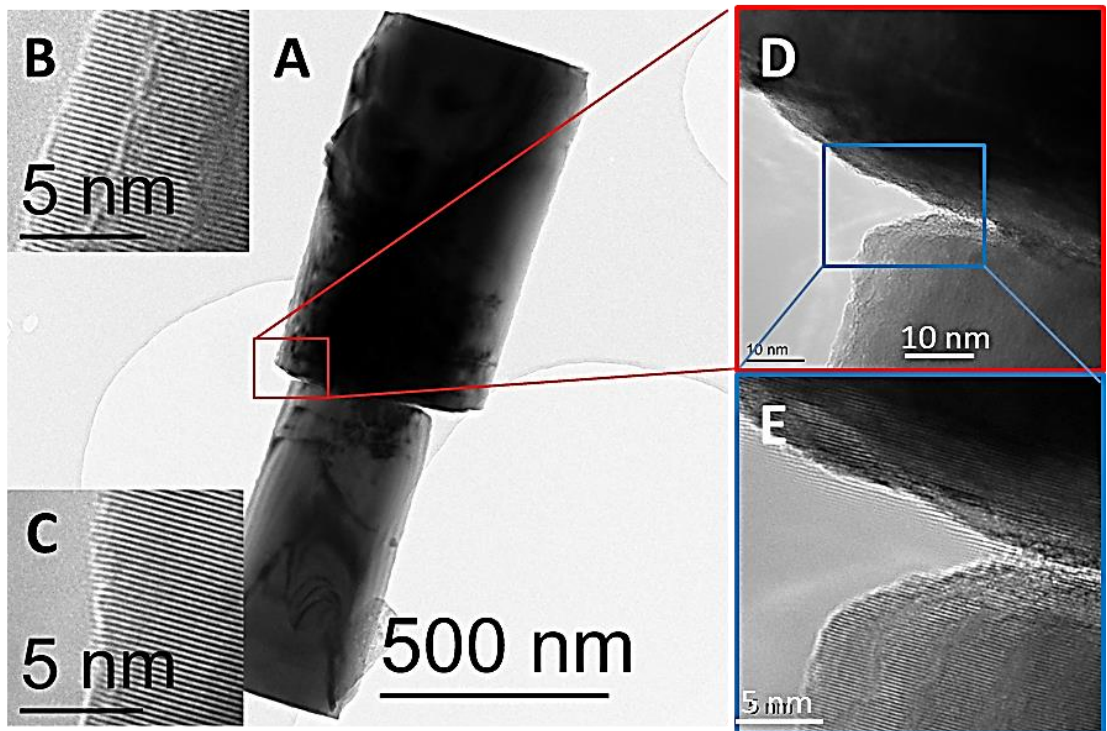


Figure 4.48: (a) low magnification showing disjointed interface (b – c) lattice imaging showing (0002) planes of individual component rods (d) HRTEM of interface and (e) lattice imaging showing (0002) lattice planes at the interfacial junction with gaps.

4.3.1 Energy Dispersive Spectroscopy on the TEM (TEM- EDX line scan)

Due to previously reported observations of a silicon rich region at the interfacial junction of the double rod particles which was introduced unwittingly into the system (Bitenc et al., 2010), an attempt was made to investigate the possibility of the occurrence of such phenomena in our double rods produced by performing a scanning transmission electron microscopy (STEM) line scan across the interfacial junction of one of the stage 5a double rod particles (which were deemed to have been formed via deposition of particles of the base of an existing rod) as shown in Figure 4.49.

The detection of the presence of silicon layer(s) at the interfacial junction of our rods would have indicated that the phenomena of impurity induced crystal twinning as described by Bitenc and coworkers (2010) may have played a significant role in the emergence of the double rods, hence building a case for the development of a third mechanism in addition to the previously articulated processes to explain the emergence of hexagonal double rods under hydrothermal conditions.

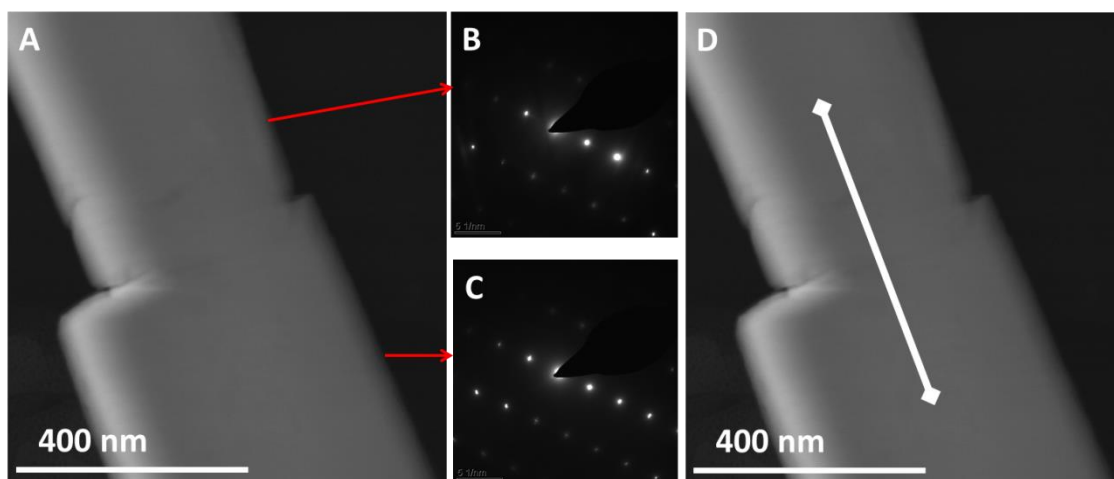


Figure 4.49: (a) STEM micrograph of interfacial junction within stage 5b type of particle (b-c) TEM-SAED patterns from top and bottom sections of double rod particle showing diffraction as a single crystal (d) line indicating the area analysed by TEM- EDX line scan.

Contrary to the findings of [Bitenc and co-workers \(2010\)](#), results of the TEM-EDX line scan (Figure 4.50), showed that there was no significant and localized spike in silicon signal as the scan progressed across the interfacial junction within the double rods which may have been tell-tale signs of the presence of a silicon-rich impurity region at interfacial junction. A comparative scan performed across the copper specimen grid covering the same distance as the EDX line scan on the particle, confirmed observations of the absence of significant difference between the silicon signals from the background and the particle.

Furthermore, it can be noted that because a Si (Li) detector or a silicon drift detector (SDD) is used to capture the EDX signals for most types of TEM-EDX analysis, silicon is commonly detected by TEM-EDX irrespective of the specimen composition, and is generally considered to originate from instrumental factors.

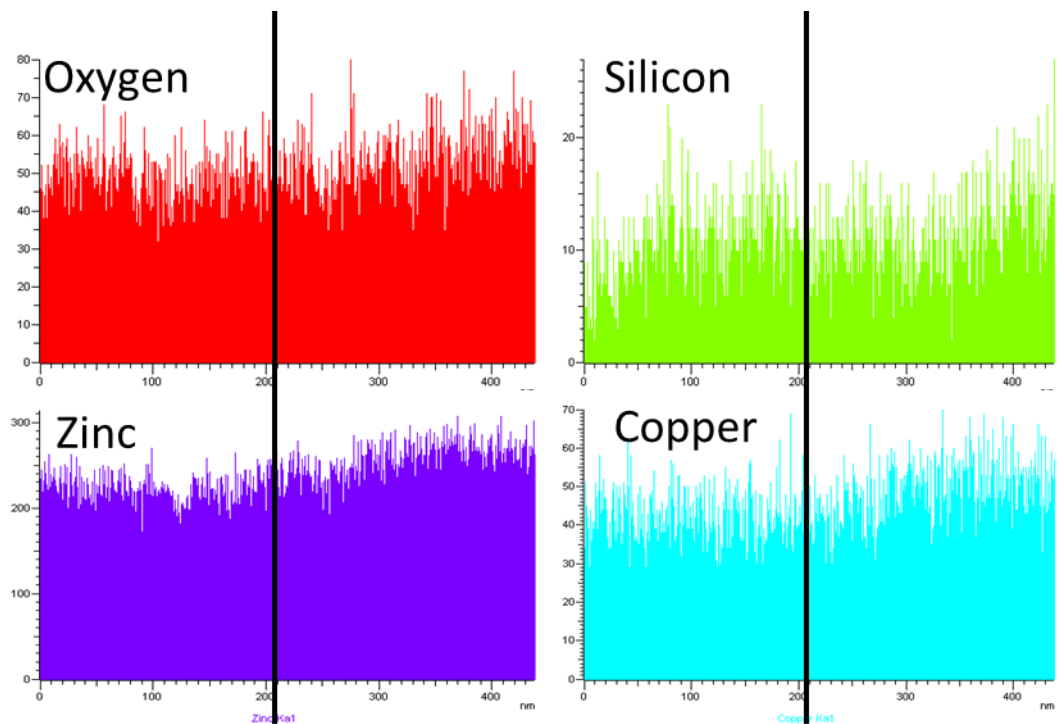


Figure 4.50: Results of TEM-EDX line scan across the interfacial junction between top and bottom components of a double rod particle showing no sudden rise in silicon signal across the interface relative to zinc, oxygen and copper signal from the specimen grid. Thick black line indicates interfacial junction between component rods.

4.3.2 Focused Ion Beam Milling

To acquire further insight into the structural details of the hexagonal double rod particles, the focused ion beam (FIB) milling technique was used in combination with transmission electron microscopy (TEM) to study the internal structure of the stage 5a hexagonal double rod particles. Longitudinal sections were milled out of selected double rod particle (Figure 4.51) for analysis on the TEM. Figure 4.50 shows rod selected prior to milling and the product cross-section in a TEM lamella after FIB milling.

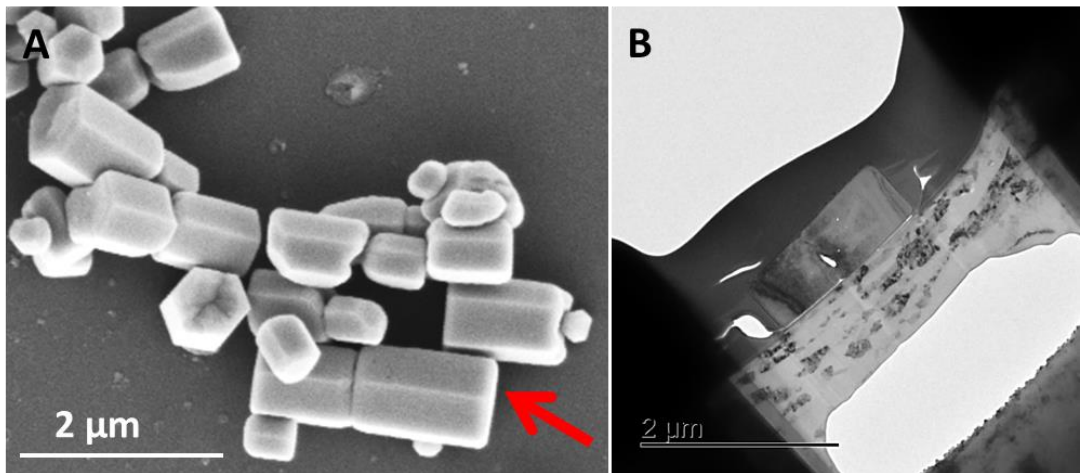


Figure 4.51: SEM of double rod and TEM of the longitudinal cross section.

Analysis of the milled longitudinal section showed the presence of a well-defined cavity at the interface between the top and bottom sections of the double rod (Figure 4.52).

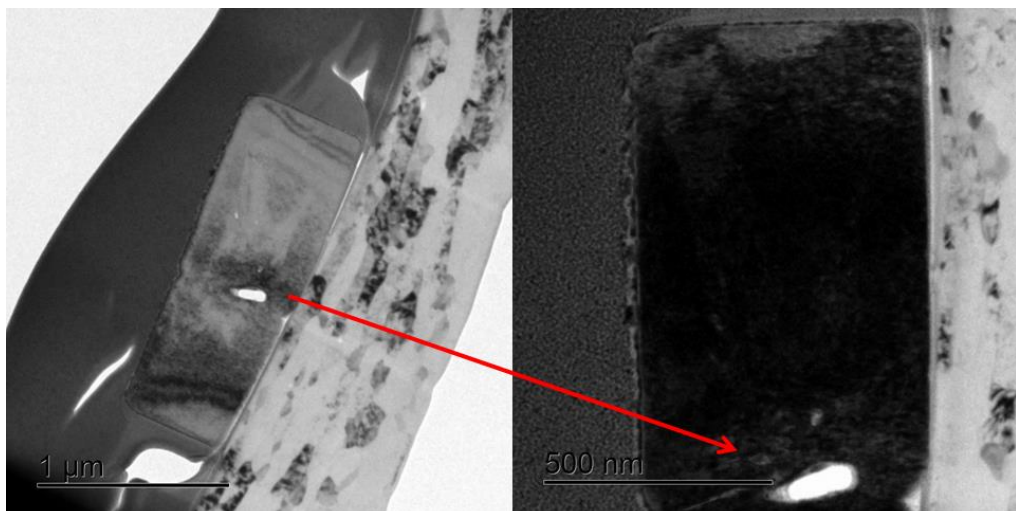


Figure 4.52: TEM showing cavity at interfacial junction inside double rod.

TEM-SAED of at the edge and middle portions of the top and bottom sections on either side of the cavity at the interfacial junction in the double rod section revealed the monocrystalline nature of the double (Figure 4.53).

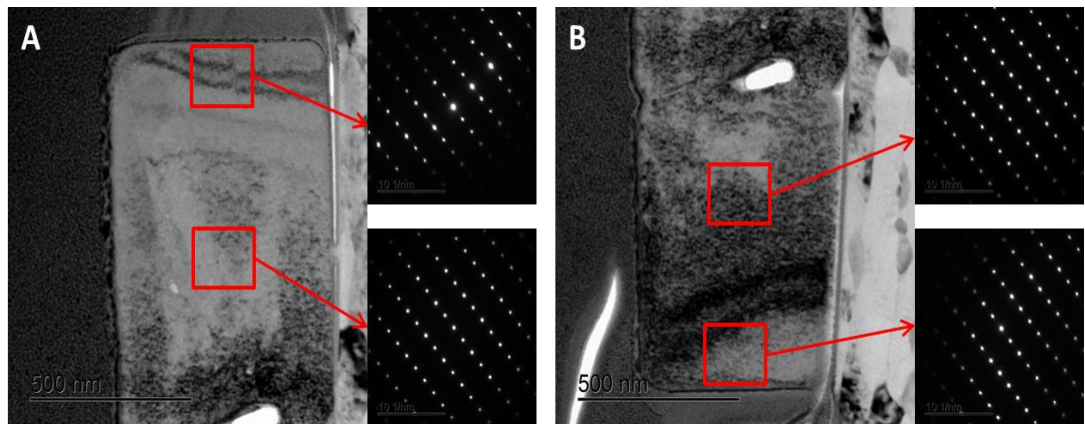


Figure 4.53: TEM-SAED diffraction pattern from edge mid-portions of the top and bottom component of a double rod particle.

In addition, HRTEM showed the presence of a seam at the interfacial junction with (002) lattice planes running across the seam (Figure 4.54).

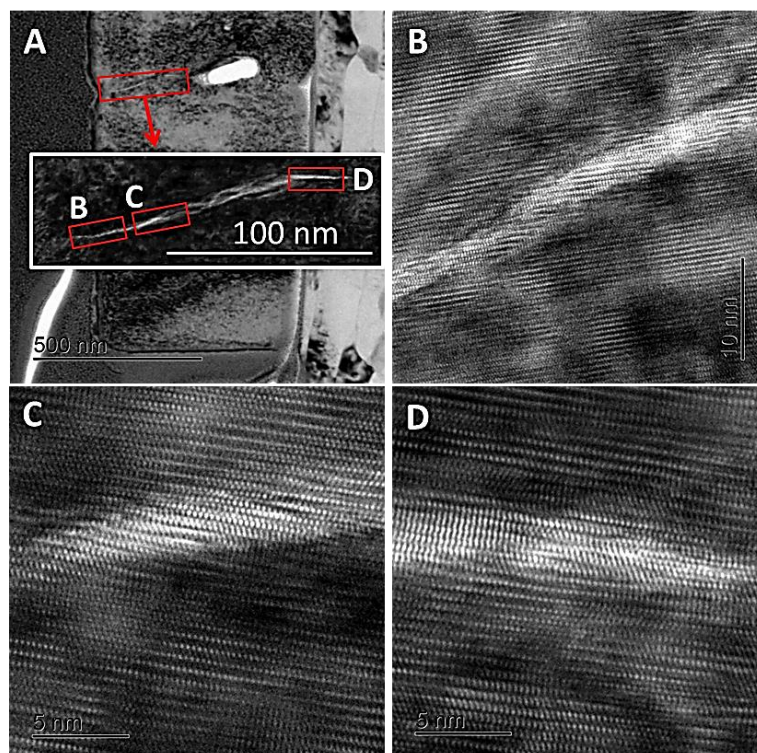


Figure 4.54: TEM image showing the presence of a seam at the interfacial junction of component rods.

The observation of internal cavities at the interfacial junction runs contrary to the hypothesis that growth of the hexagonal double rods was initiated at the interfacial junction (i.e. it is inconsistent with crystal twinning process). It would be difficult to explain the presence of the internal cavities if crystal twinning were to have been responsible for the double rod formation. Therefore, it is thought that what rather may have happened was that the hexagonal double rod particles were formed by end to end attachment of two separate rod particles. The internal cavity could have resulted from the alignment of the (0001) faces of the top and bottom sections that were not perfectly flat at the time the rods became attached. SEM images show, that the many of the basal faces of single rod particles which coexisted with double rod particles had a pitted, concave profile. The occurrence of pitted surfaces in the hexagonal rods may have been due to the dissolution of zinc hydroxide from the core of the particle into solution. This explanation could also be the reason hollow rods were also observed (Figure 4.55). Furthermore, it has been noted that 1D zinc oxide particles terminate in ends with opposing polarities (Coleman and Jagadish, 2006; Wang, 2004). This phenomenon could have aided the end to end attachment process of the single rod particles.

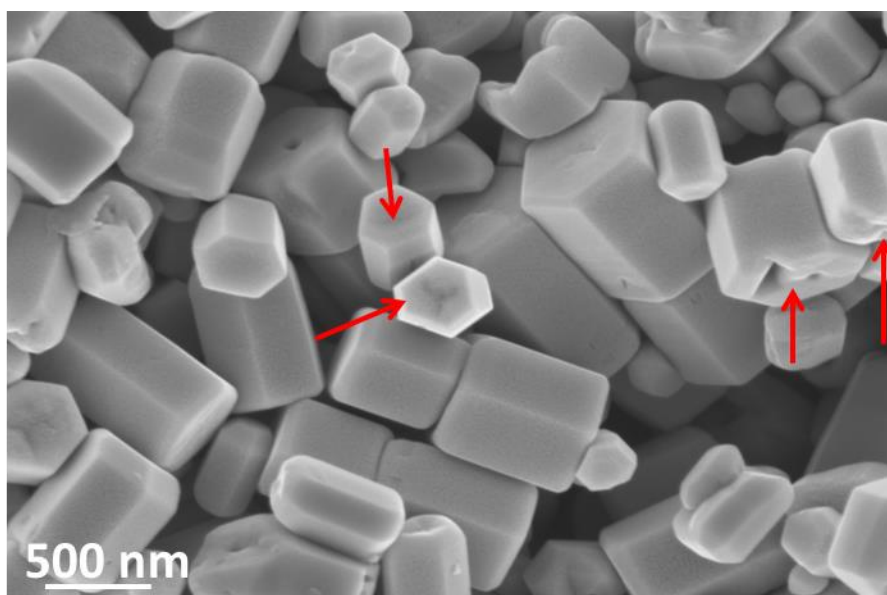


Figure 4.55: SEM image of sample *Zn01t12* showing single rod particles with pitted surfaces in coexistence with double rod particles.

4.4 Effect of pH on Particle Growth Process

Moving away from discussions focused on the growth process of zinc oxide hexagonal double rods, we now examine the effect changes in the pH value of the precursor suspension prior to hydrothermal treatment had on particle morphology of the product particles.

Precursor suspensions were prepared from sodium hydroxide and zinc acetate dihydrate following steps described in section 2.1.1.1, and the pH values of the suspension were adjusted to approximately 7, 11 and 13 before hydrothermal treatment for a dwell time of 12 h.

The resultant samples have been labelled samples *Zn01p7*, *Zn01p11*, *Zn01p9* and *Zn01p13* to indicate pH values of 7, 9, 11 and 13 respectively.

4.4.1 pH 7 Precursor Suspension

Diffraction pattern obtained from X-ray diffraction analysis of sample *Zn01p7* was identified as wurtzite zinc oxide using ICDD reference file number 04-013-6607 (Figure 4.56a). SEM imaging showed the presence of mainly three types of particle morphologies (Figure 4.56b). The first were nanobelts very similar to lozenge shaped particles observed in sample *Zn01t12*. In addition there were relatively large hexagonal single and double rod particles with sizes similar to sample *Zn01t24* particles.

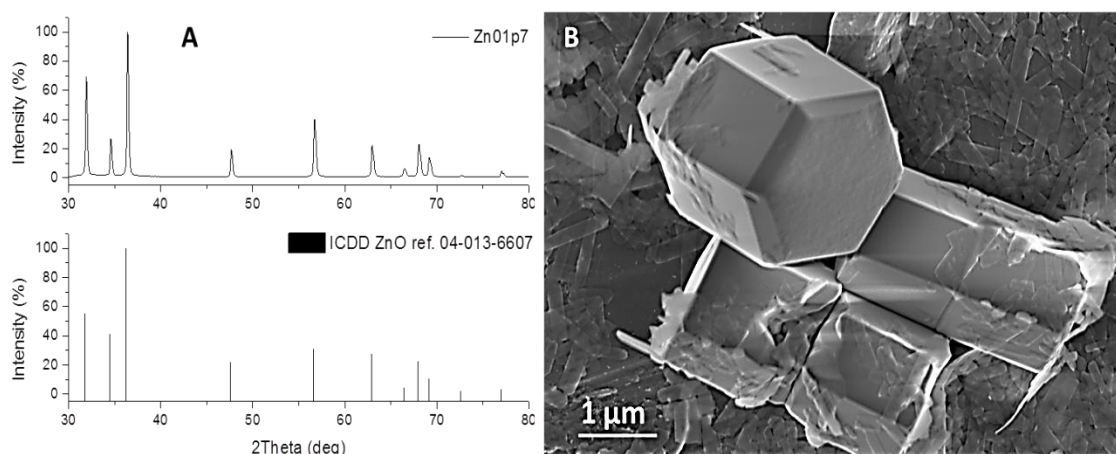


Figure 4.56: (a) XRD pattern of sample *Zn01p7* compared with ICDD reference pattern for zinc oxide (b) SEM image of sample *Zn01p7* showing three different types of particle shapes.

4.4.2 pH 9 Precursor Suspension

A precursor suspension with pH 9 was used to produce the double rod particles presented in section 4.2.6, therefore sample *Zn01p9*, is the same as sample *Zn01t12*. Therefore, for details of characterisation of particles produced from a pH 9 precursor suspension refer to the aforementioned section (i.e. see Section 4.2.6 for further details).

4.4.3 pH 11 Precursor Suspension

X-ray diffraction pattern obtained for sample *Zn01p11* also showed that phase composition was wurtzite zinc oxide (Figure 4.57a). SEM revealed the presence of particles with nanoflake morphology throughout the sample. The thickness of the nanoflake particles ranged from ~ 5 nm to 50 nm (Figure 4.57b).

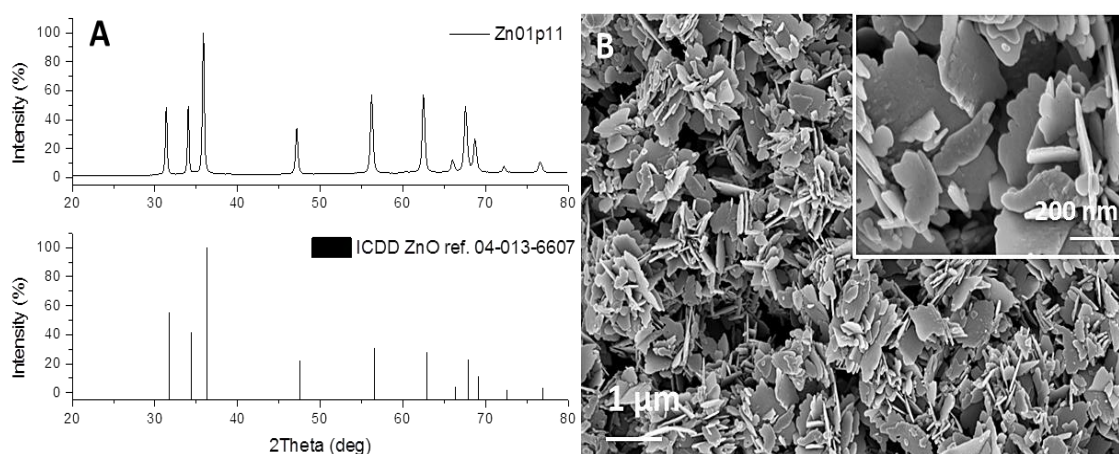


Figure 4.57: (a) XRD pattern of sample *Zn01p11* compared with ICDD reference pattern for zinc oxide (b) SEM image showing nanoflakes.

4.4.4 pH 13 Precursor Suspension

SEM analysis of products of hydrothermal reaction of pH 13 precursor suspensions for 12 h dwell time showed that they were mainly made up of flower-like nanoparticle clusters (Figure 5.58b). Particles with this type of structure, have been previously reported (Xie, et al., 2009; Li, et al., 2011). While XRD confirmed bulk powder composition to be wurtzite zinc oxide.

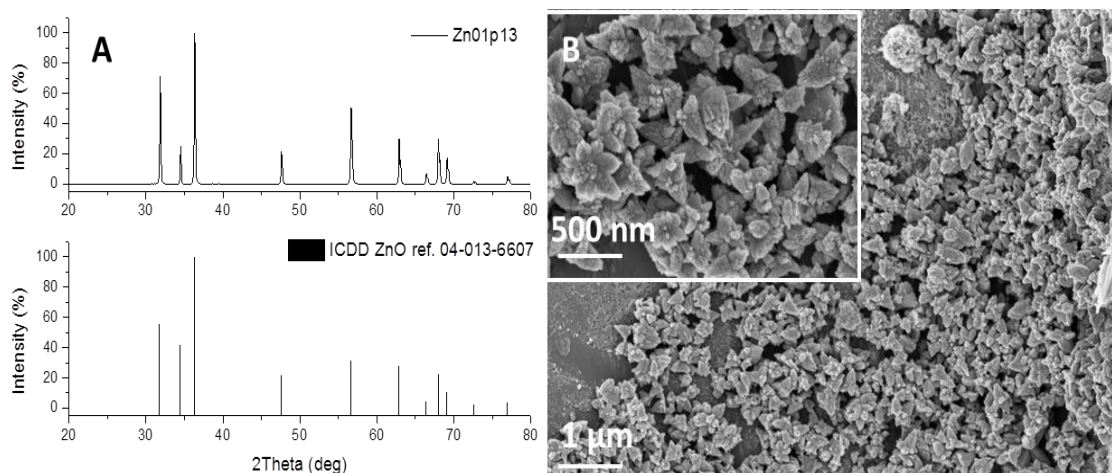


Figure 4.58: (a) XRD of sample *Zn01p13* compared with ICDD reference pattern for zinc oxide (b) SEM image showing flower-like nanoclusters.

4.4.5 Comparative Analysis of the Effect of pH on Particle Growth

SEM images of the product particles showed that changes in pH of the precursor suspension had a significant effect on the shape and size of the product particles (Table 4.8).

Evidence from SEM showed that particle growth became increasingly inhibited as the pH of the precursor suspension increased, as average particle sizes dropped as pH values rose. Table 4.8 contains details of particle sizes as a function of pH of precursor suspension.

Table 4.8: Changes in particle shape and size as a function of precursor pH.

Sample	pH	Particle Shapes	Avg. Particle Sizes
<i>Zn01p7</i>	7	lozenge shaped particles Hexagonal double rods, Hexagonal single rods,	2 μm x 4.5 μm (rods) 0.2 μm x 1.0 μm (lozenges)
<i>Zn01p9</i> (a.k.a. <i>Zn01t12</i>)	9	Hexagonal double rods, Hexagonal single rods, equiaxed nanoparticles, lozenge shaped particles	2 μm x 4.5 μm (rods) μm x 0.8 μm (lozenges) 0.05 μm (equiaxed)
<i>Zn01p11</i>	11	nanoflake shaped particles,	0.03 μm x 0.3 μm
<i>Zn01p13</i>	13	Flower-like nanoparticle clusters	0.05 μm x 0.2 μm

Chapter 5

Results and Discussion II

Synthesis and Characterisation of High Aspect Ratio Zinc Oxide Hexagonal Microrods from Zinc acetate and Ammonium Hydroxide

5.1 Introduction

This chapter provides details of the results of experimental investigation into the hydrothermal growth of high aspect ratio zinc oxide rods using ammonium hydroxide and zinc acetate dihydrate ($\text{CH}_3(\text{COO})_2 \cdot 2\text{H}_2\text{O}$) as starting reagents as described in section 2.1.1.1

X-ray powder diffraction analysis was employed to acquire information on phase composition of bulk powder, while scanning electron microscopy was used to observe changes in particle size and morphology in relation to variations in synthesis conditions. Histograms of particle size distribution were produced by measuring a minimum of 150 random particles from multiple SEM micrographs.

Section 5.2 of this chapter presents results highlighting the effect of variation in length of hydrothermal dwell times on particle characteristics.

Discussion of results in section 5.3, are centered on observations related to phase transformation from orthorhombic zinc hydroxide to wurtzite zinc oxide phase during the early stages of hydrothermal growth. A number of mechanisms that could possibly describe the transformation process are examined.

Section 5.4 dwells on the role of ammonia (and ammonium ions) in the synthesis process, considering its influence on the pH of reaction medium.

While section 5.5 examines hydrothermal growth of zinc oxide comparing and contrasting results presented in chapters 4 and 5.

5.1.1 Samples

Samples were prepared by subjecting precursor suspensions to varying durations of hydrothermal treatment and then recovering product particles at the end of each of the processes. Starting with a sample collected just after the completion of precursor preparation steps (sample *Zn02t0*), samples were collected after various hydrothermal dwell times up to a maximum of 24 h dwell time. Table 5.1 provides a listing of the samples prepared and some of the conditions of synthesis. Other details of synthesis conditions and experimental parameters have been discussed in section 2.1.1.2.

Table 5.1: Listing of samples and a selection of experiment conditions.

s/n	Sample	Approximate pH (post reaction)	Temperature [°C]	Reaction Volume [mL]	Hydrothermal dwell time [h]
1	<i>Zn02t0</i>	9.0	120	100	0
2	<i>Zn02t1</i>	9.0	120	100	1
3	<i>Zn02t2</i>	8.9	120	100	2
4	<i>Zn02t3</i>	8.8	120	100	3
5	<i>Zn02t6</i>	8.7	120	100	6
6	<i>Zn02t12</i>	8.7	120	100	12
7	<i>Zn02t24</i>	8.7	120	100	24

5.2 Effect of Hydrothermal Treatment Duration on Particle Characteristics

5.2.1 Freshly Prepared Precipitate, No Hydrothermal Treatment

Powder X-ray diffraction analysis of the dried as-prepared '0' h precursor suspension (sample *Zn02t0*) showed that the sample was crystalline in nature. The main peaks in the resulting diffraction pattern were identified as wulfingite (ϵ -Zn(OH)₂) with an orthorhombic crystal structure according to reference pattern number 04-012-2300 in the ICDD database (Figure 5.1). Table 5.2 provides details of the phase indexing process.

In addition to the wulfingite peaks, other peaks were also observed in sample *Zn02t0*'s diffraction pattern which had no corresponding match in ICDD reference pattern for zinc hydroxide. Further comparisons of these peaks were made against ICDD reference patterns for zinc oxide (No. 04-005-5072), zinc acetate (No. 00-052-0080), zinc acetate hydrate (ICDD reference No. 00-033-1464) without any success in obtaining reasonable matches. A survey of literature however showed, that peaks with similar characteristics have been previously observed and are thought to be due to the presence of unconverted layered basic zinc acetate (LBZA) as described in section 4.2.1 (Ku et al., 2008; Tarat, et al., 2014; Tang, et al., 2012; Honoso et al., 2004).

An examination of sample *Zn02t0* on the SEM showed the presence of micron sized octahedral shaped particles (Figure 5.2) with particle size ranging between 300 nm and 6 μ m (Figure 5.3). Similar crystal morphology has been reported by other researchers for crystalline zinc hydroxide (Wang, et al. 2013; Kusaba, et al., 2010; Qian, et al., 2005; McBride et al., 2003).

Figure 5.1 is a plot of the diffraction pattern of sample *Zn02t0* along with the ICDD reference pattern file number 04-012-2300 for wulfingite (ϵ -Zn(OH)₂) that was used in phase identification; corresponding hkl planes have been labelled. Figure 5.2 contains a SEM micrograph of sample *Zn02t0* showing the presence of octahedral shaped particles. Alongside the SEM image, is a schematic diagram identifying the {111} facets of the octahedral particle.

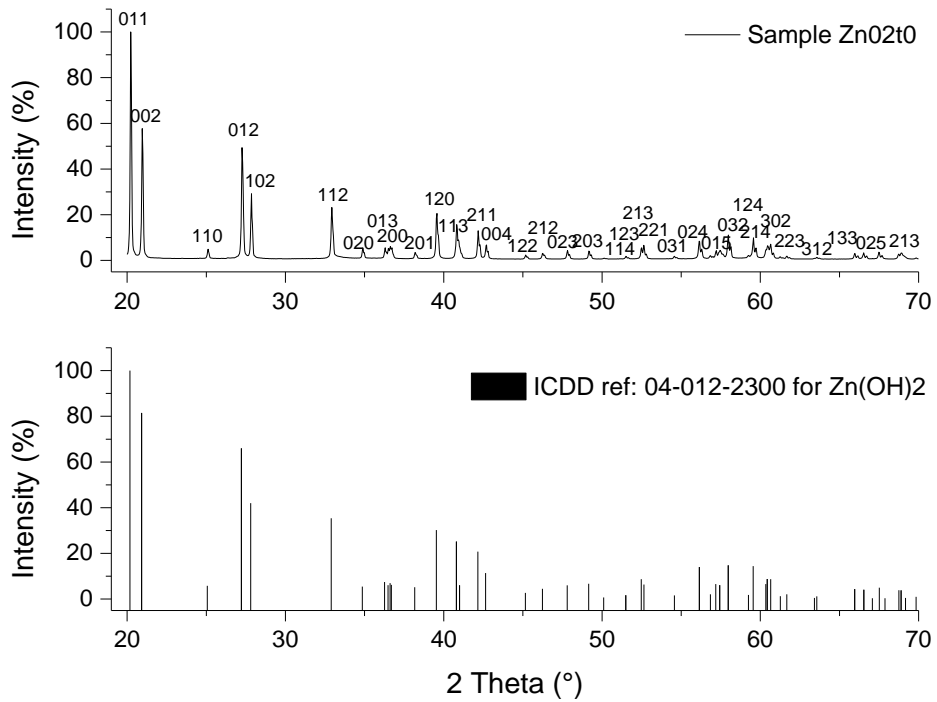


Figure 5.1: X-ray diffraction pattern of sample $Zn02t0$, showing peaks indexed to wulfgite [ϵ - $Zn(OH)_2$] and ICDD ($Zn(OH)_2$) reference pattern.

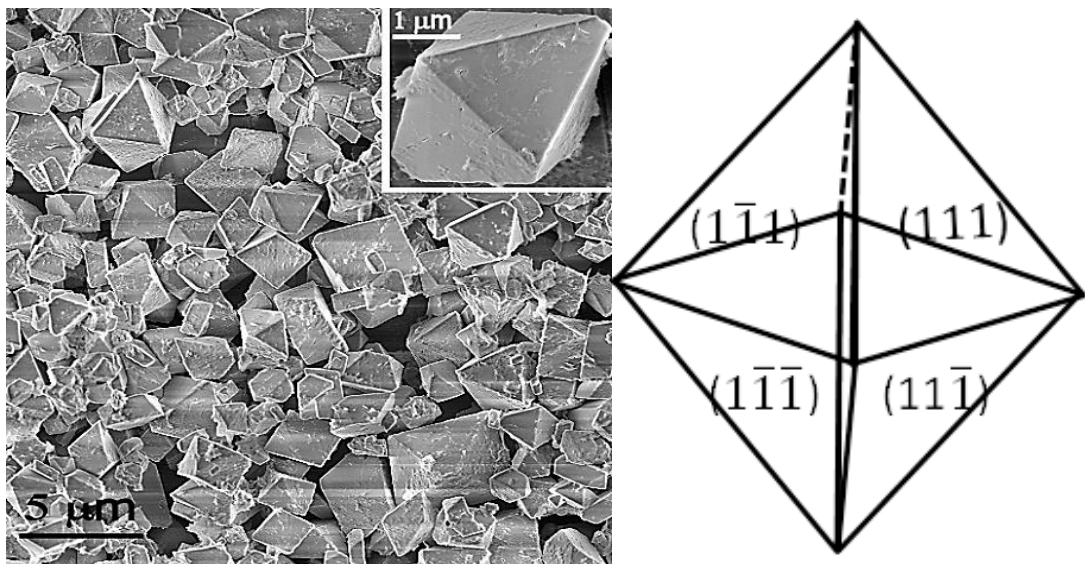


Figure 5.2: (left) SEM image showing octahedral shaped particles (inset) higher resolution image of a single particle (right) a schematic of an octahedral crystal structure showing the $\{111\}$ planes.

Figure 5.3 is a histogram of particle size distribution of sample *ZnO₂t0* obtained by measuring one side of more than 150 individual octahedral particles from multiple SEM images.

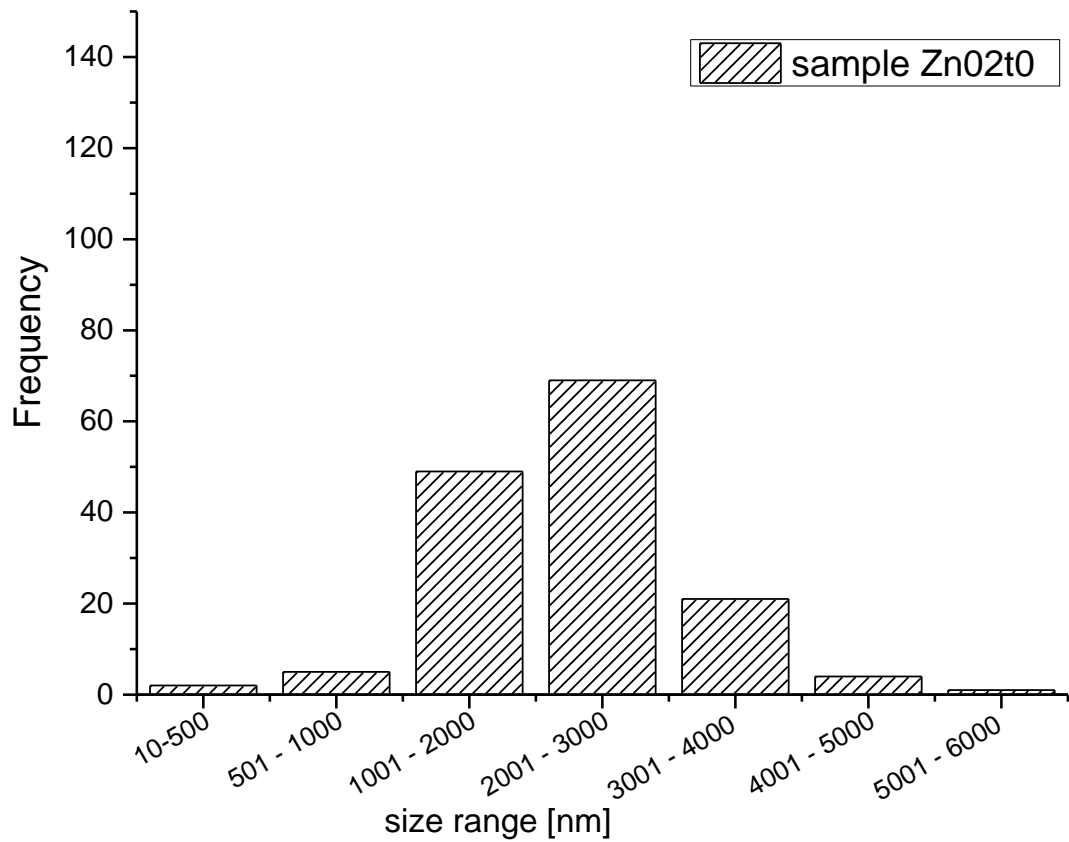


Figure 5.3: Histogram of particle size distribution in sample *ZnO₂t0*.

Table 5.2 shows a comparison of peak positions ($^{\circ}2\theta$) and d-spacings (\AA) of freshly prepared precursor powder (sample *ZnO₂t0*) and ICDD reference pattern for wulfingite (number 04-012-2300).

Table 5.2: Indexing of peaks from sample *ZnO* to ICDD reference pattern for 04-012-2300 for wulffingite.

Sample <i>ZnO</i>			ICDD Wulffingite ref. (04-012-2300)						
2θ	d [Å]	I [%]	2θ	d [Å]	I [%]	<i>h</i>	<i>k</i>	<i>l</i>	<i>l</i>
20.2	4.387	100.0	20.2	4.397	100	0	1	-1	1
21.0	4.237	57.2	20.9	4.245	81.5	0	0	0	2
			20.9	4.245	81.5	1	0	-1	1
25.1	3.545	4.1	25.1	3.550	5.8	1	1	-2	0
26.3	3.382	0.3							
27.3	3.269	45.7	27.2	3.274	66	0	1	-1	2
			27.2	3.274	66	1	1	-2	1
27.9	3.202	27.7	27.8	3.206	42	1	0	-1	2
32.9	2.719	22.5	32.9	2.721	35.4	1	1	-2	2
34.9	2.571	4.4	34.9	2.572	5.5	0	2	-2	0
36.3	2.475	4.8	36.3	2.476	7.5	0	1	-1	3
			36.5	2.461	6.1	0	2	-2	1
36.6	2.456	3.6	36.6	2.453	7	2	0	-2	0
36.7	2.450	4.2	36.7	2.448	6.2	1	0	-1	3
38.2	2.356	2.9	38.2	2.356	5.2	2	0	-2	1
39.6	2.279	19.8	39.5	2.278	30.2	1	2	-3	0
40.8	2.211	14.8	40.8	2.210	25.2	1	1	-2	3
			40.8	2.210	25.2	2	1	-3	0
			41.0	2.199	6	0	2	-2	2
			41.0	2.199	6	1	2	-3	1
42.2	2.143	12.1	42.2	2.142	20.8	2	1	-3	1
42.7	2.119	6.1	42.7	2.118	11.4	0	0	0	4
45.2	2.007	1.7	45.2	2.006	2.7	1	2	-3	2
46.2	1.963	2.5	46.2	1.962	4.5	2	1	-3	2
47.8	1.903	3.7	47.8	1.901	6	0	2	-2	3
49.2	1.851	3.5	49.2	1.852	6.7	2	0	-2	3
49.3	1.850	1.7							
50.1	1.819	0.4	50.1	1.819	0.7	1	1	-2	4

Sample Zn02t0			ICDD Wulfingite ref. (04-012-2300)						
2θ	d [Å]	I [%]	2θ	d [Å]	I [%]	h	k	i	l
51.5	1.773	1.2	51.5	1.773	1.7	1	2	-3	3
			51.5	1.773	1.7	2	2	-4	0
52.5	1.742	4.6	52.5	1.742	8.7	2	1	-3	3
52.6	1.737	6.1	52.6	1.737	6.4	2	2	-4	1
54.6	1.681	1.2	54.6	1.680	1.6	0	3	-3	1
56.1	1.637	7.9	56.1	1.637	14	0	2	-2	4
			56.1	1.637	14	2	2	-4	2
56.8	1.619	1.5	56.8	1.618	2.1	1	3	-4	0
57.2	1.609	3.6	57.2	1.610	6.6	0	1	-1	5
			57.4	1.603	6.1	1	0	-1	5
57.5	1.602	3.8	57.4	1.603	6.1	2	0	-2	4
58.0	1.590	10.0	58.0	1.590	14.8	0	3	-3	2
58.1	1.589	5.4	58.0	1.590	14.8	1	3	-4	1
59.2	1.559	1.6	59.3	1.558	1.8	3	1	-4	0
59.6	1.551	9.2	59.6	1.551	14.4	1	2	-3	4
59.7	1.551	4.7							
			60.4	1.533	6.6	3	1	-4	1
			60.4	1.531	8.8	1	1	-2	5
60.5	1.530	6.0	60.4	1.531	8.8	2	1	-3	4
60.7	1.529	6.6	60.7	1.525	8.7	3	0	-3	2
60.8	1.521	2.4							
61.3	1.512	1.0	61.3	1.512	1.3	1	3	-4	2
61.7	1.503	1.3	61.7	1.503	2.1	2	2	-4	3
			63.4	1.466	0.5	0	3	-3	3
63.6	1.462	0.7	63.6	1.462	1.2	3	1	-4	2
66.0	1.415	2.4	66.0	1.415	4.4	0	2	-2	5
			66.0	1.415	4.4	3	0	-3	3
66.2	1.415	1.5							
66.5	1.405	2.7	66.5	1.404	4.1	1	3	-4	3
66.7	1.404	1.4	66.5	1.404	4.1	2	3	-5	0

5.2.2 One Hour (1 h) Hydrothermal Treatment Products

X-ray diffraction analysis of products obtained after 1 h of hydrothermal treatment showed that phase composition was also wulfingite (Figure 5.4).

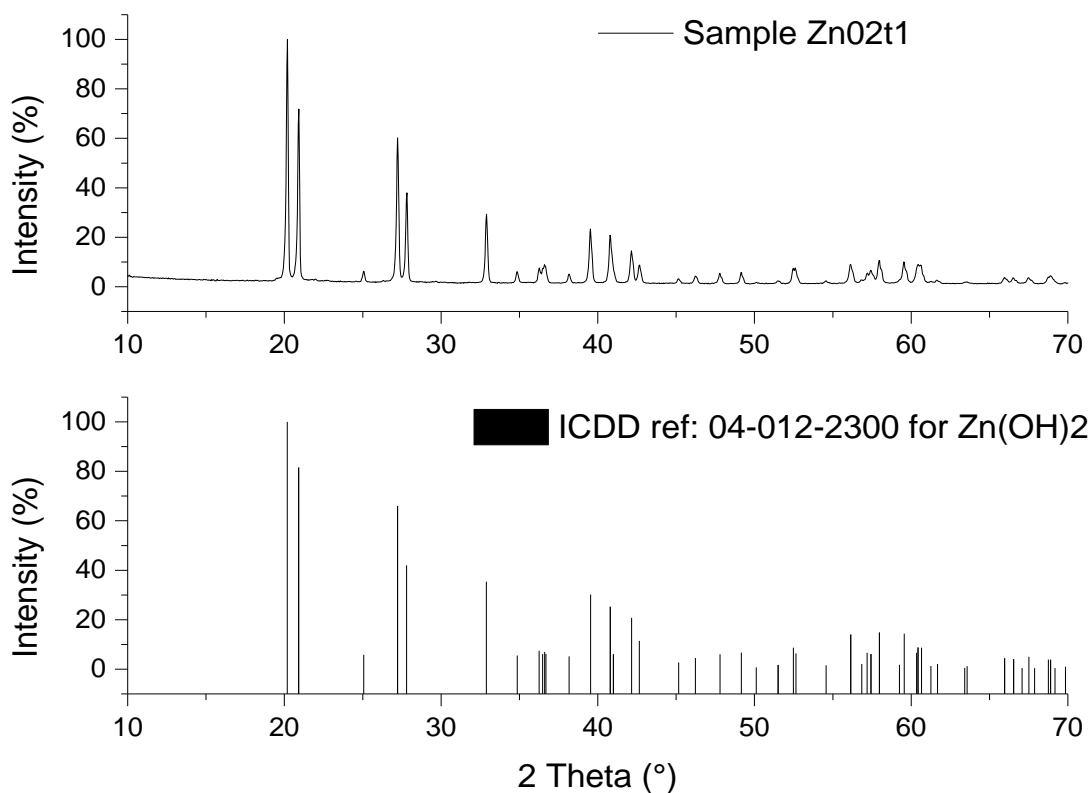


Figure 5.4: X-ray diffraction pattern of sample *Zn02t1* and ICDD reference pattern number 04-012-2300 for wulfingite.

SEM micrographs of sample *Zn02t1* showed the presence of multifaceted particles. Although the particles bore some form of similarity to particles in sample *Zn02t0*, there was an apparent lack of uniformity/regularity in particle dimensions. In addition, the presence of a few rod-like particles was observed (highlighted by red arrows in Figure 5.5).

An analysis of about 150 random particles from SEM micrographs indicated that there was a 95 % abundance of the multifaceted 'zinc hydroxide' particles. It appeared, that the average sizes of particles in sample *Zn02t1*, was slightly lower than those in sample *Zn02t0* (Figure 5.6). Sizes of the particles were obtained by measuring the shorter side of the particles to obtain a 'width' measurement and the longer side to calculate 'aspect ratios'.

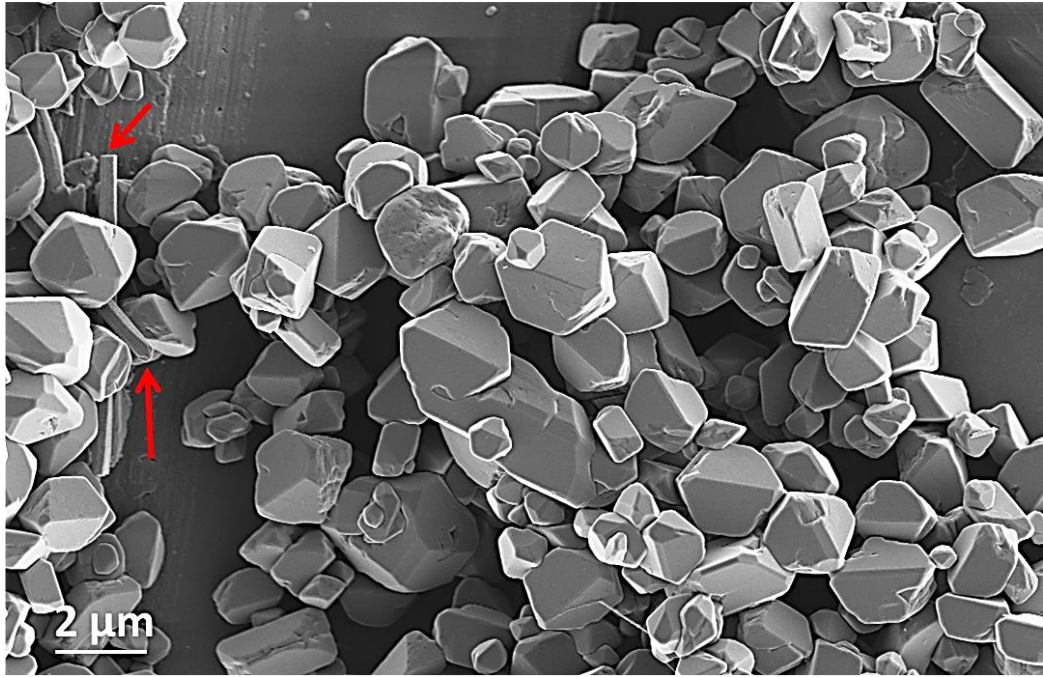


Figure 5.5: SEM micrograph of sample *Zn02t1* showing rod like particles (red arrow) surrounded by multifaceted particles.

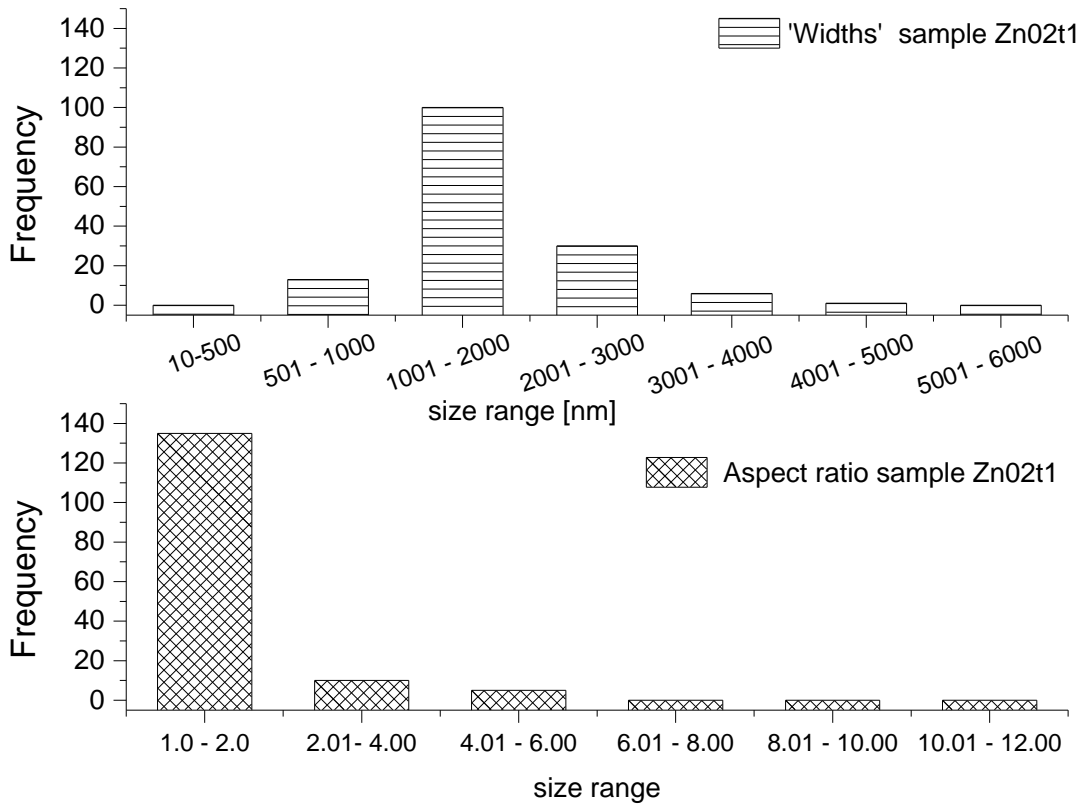


Figure 5.6: Histogram showing particle size distribution in sample *Zn02t1*.

Although SEM images showed the presence of some elongated particles which could be an indicator of c-axis directed particle growth by zinc oxide, there was no significant match between the peaks in the X-ray powder diffraction pattern of sample *Zn02t1* and that of the reference pattern for wurtzite zinc oxide (ICDD ref 04-013-6607) as shown in Figure 5.7.

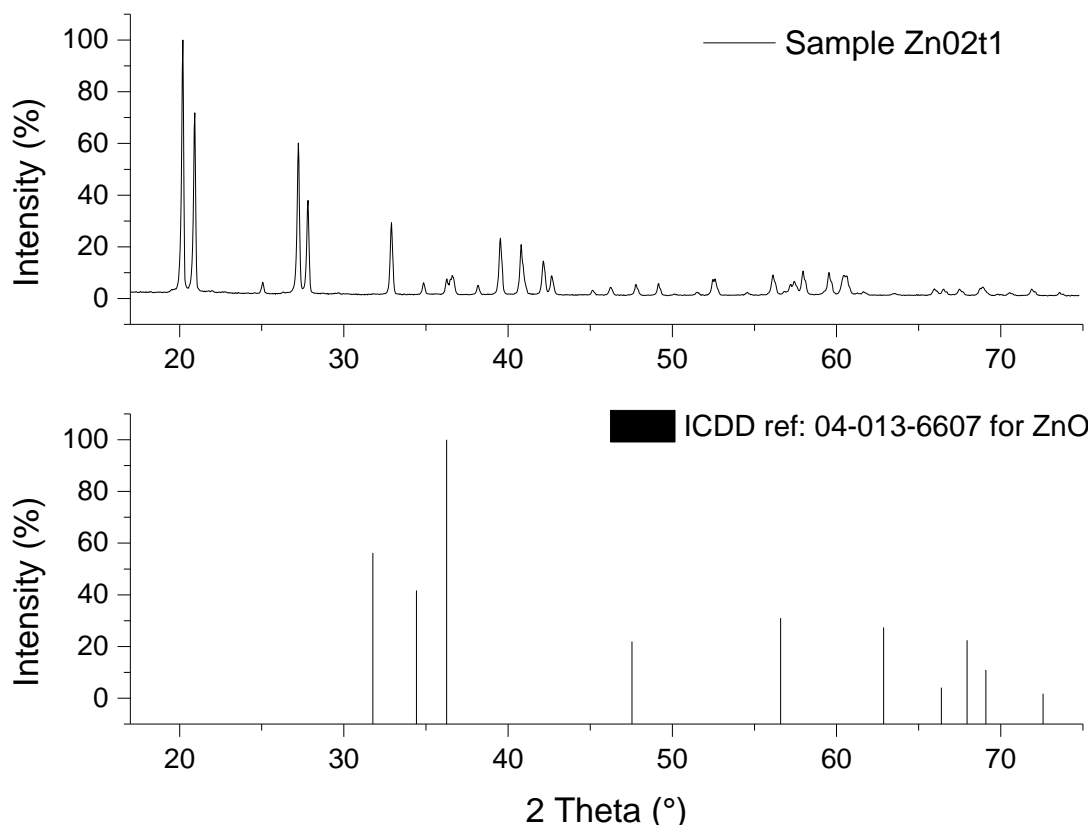


Figure 5.7: Comparison between X-ray diffraction pattern of sample *Zn02t1* and ICDD reference pattern 04-013-6607 for zinc oxide.

It was not possible to further investigate if the rod-like particles were ZnO or Zn(OH)₂ through energy dispersive X-ray spectroscopy (EDXS). It was not also possible to image the lattice planes of the particles on the transmission electron microscope due to the challenge of transferring representative particles onto a holey carbon TEM grid, as the particles were too large in size. Furthermore, the particles that did get transferred onto the grid were not electron transparent enough to be suitable for imaging in the TEM.

5.2.3 Two Hour (2 h) Hydrothermal Treatment Products

Evidence of Zn(OH)_2 to ZnO phase transformation was first observed in the analysis of X-ray diffraction data for sample *Zn02t2* (Figure 5.8). The sample's XRD pattern, had peaks from both wurtzite zinc oxide (ICDD ref. 04-013-6607) and orthorhombic ϵ - Zn(OH)_2 (ICDD ref. 04-012-2300), indicating multiple phase composition. The predominant phase was wurtzite zinc oxide. This sample (sample *Zn02t2*) provided the first instance in which wurtzite zinc oxide phase was identified in any of the hydrothermal products obtained via this synthesis process.

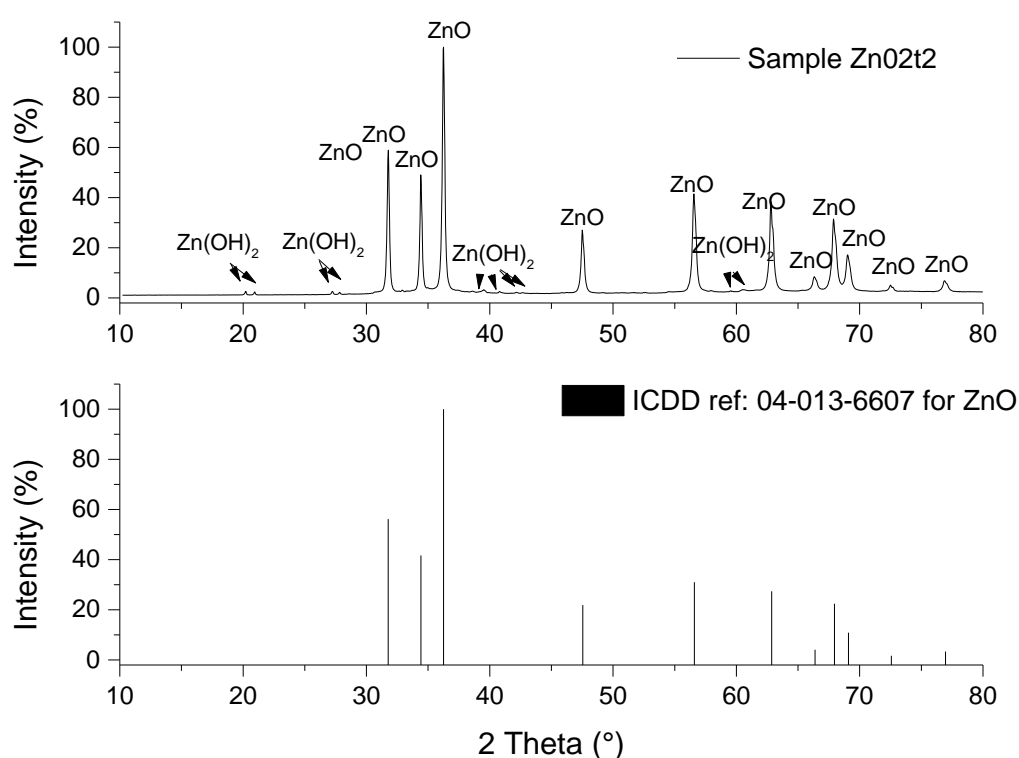


Figure 5.8: XRD pattern of sample *Zn02t2* compared with ICDD reference for ZnO . Peaks from phases indexed to ZnO and Zn(OH)_2 are highlighted.

SEM analysis of sample *Zn02t2* showed an increased presence of high aspect ratio hexagonal rods in coexistence with boulder-like particles (Figure 5.9). The average sizes of the boulder-like particles were similar to those observed in the 1 h sample, but the particles were less faceted. The boulder-like particles appeared to have previously been octahedral shaped particles, but now in a transition / transformation cum dissolution process.

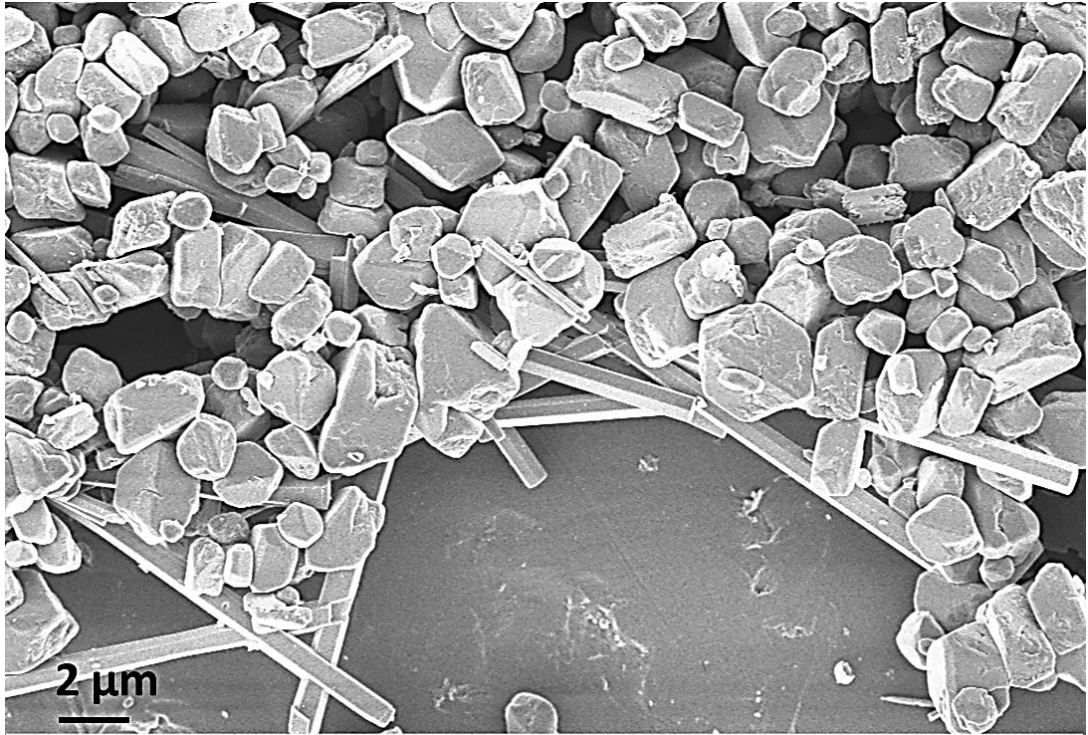


Figure 5.9: SEM showing the co-existence of octahedral shaped multifaceted and hexagonal rod-like particles in sample *ZnO₂t₂*.

Due to the nature of particle shapes, size measurements were separated into short side (denoted widths) and long side (denoted as lengths) as presented in Figure 5.10. This was done to account for both types of particle shapes without having to measure them separately (as there would not have been enough particles to generate a statistically significant data).

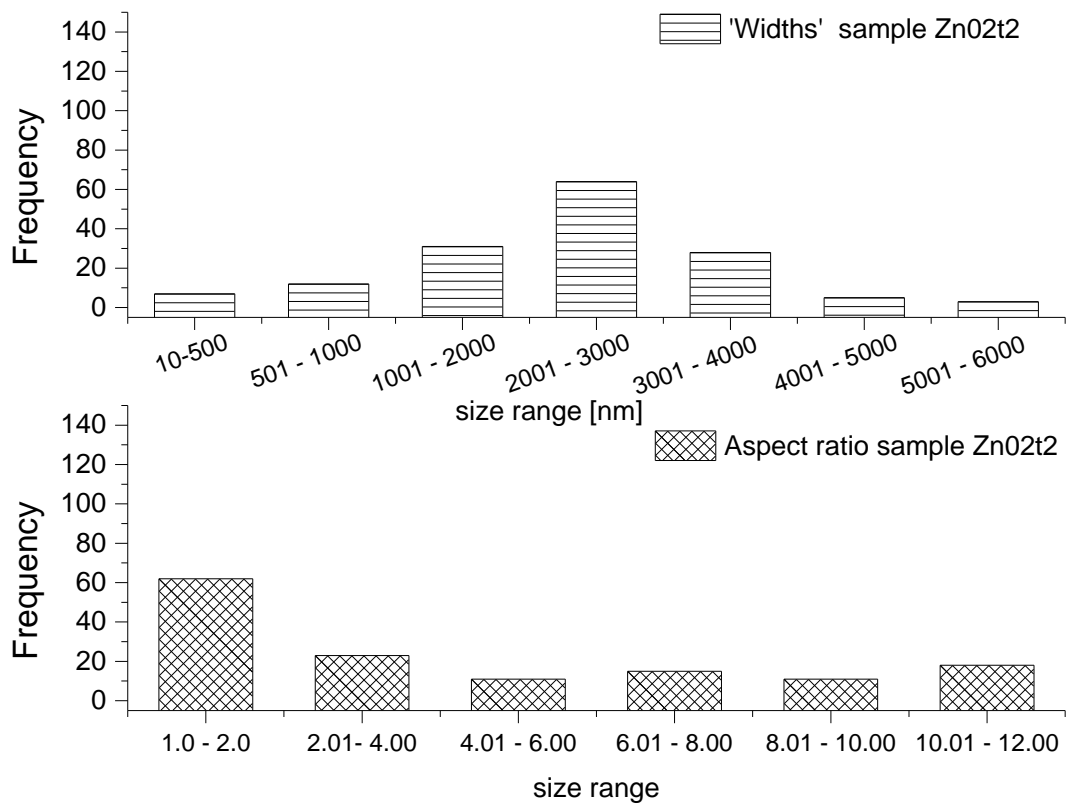


Figure 5.10: Histogram showing particle size distribution and distribution of particle aspect ratios in sample *ZnO₂t₂*.

5.2.4 Three Hour (3 h) Hydrothermal Treatment Products

X-ray diffraction analysis sample *ZnO2t3* indicated extensive conversion of wulffite to monophasic hexagonal wurtzite zinc oxide (Figure 5.11). All the main peaks in sample *ZnO2t3*'s diffraction pattern were indexed to hexagonal wurtzite zinc oxide (ICDD ref. 04-013-6607).

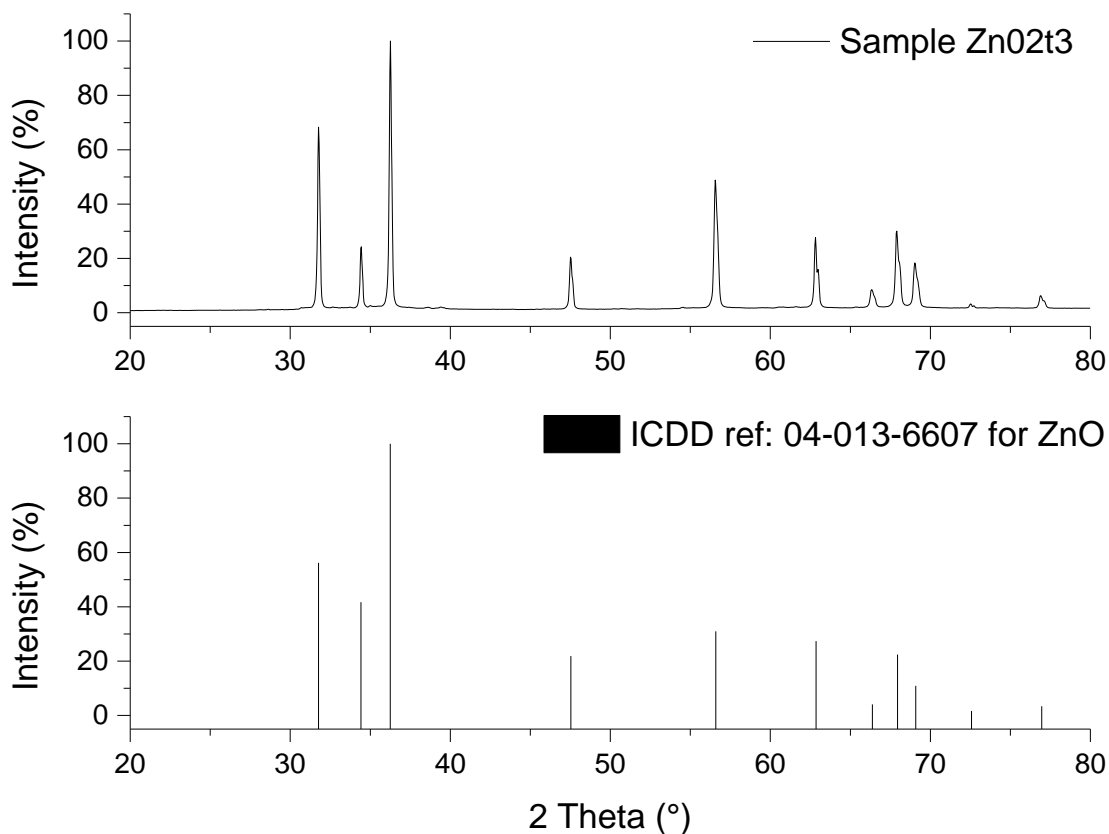


Figure 5.11: X-ray diffraction pattern of sample *ZnO2t3* and ICDD reference pattern for zinc oxide.

SEM images of sample *ZnO2t3* showed that majority of the particles in the sample were rod-like with hexagonal cross sections. The occasional presence of multifaceted particles was however observed (as highlighted in figure 5.12), but the sample was essentially made up of hexagonal faceted rod-like particles many which had sharp pencil-like tips. Analysis of particle size distribution showed that the hexagonal rod particles had aspect ratios ranging between 4: 1 and 12: 1 (Figure 5.13).

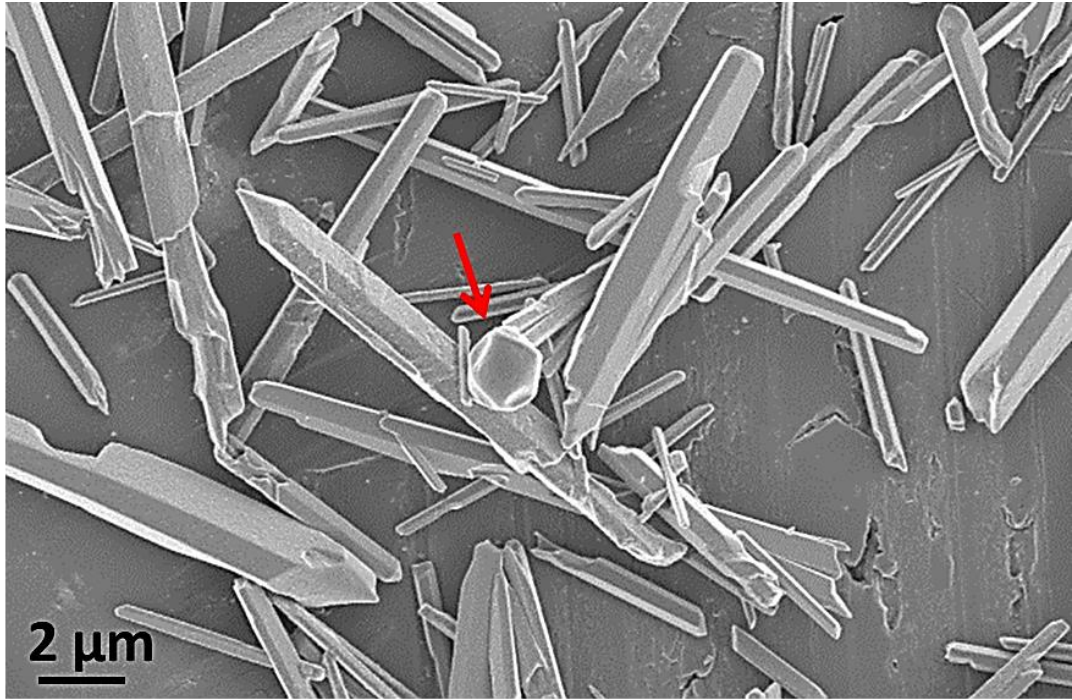


Figure 5.12: SEM micrograph of sample *Zn02t3* with arrow highlighting a multifaceted particle.

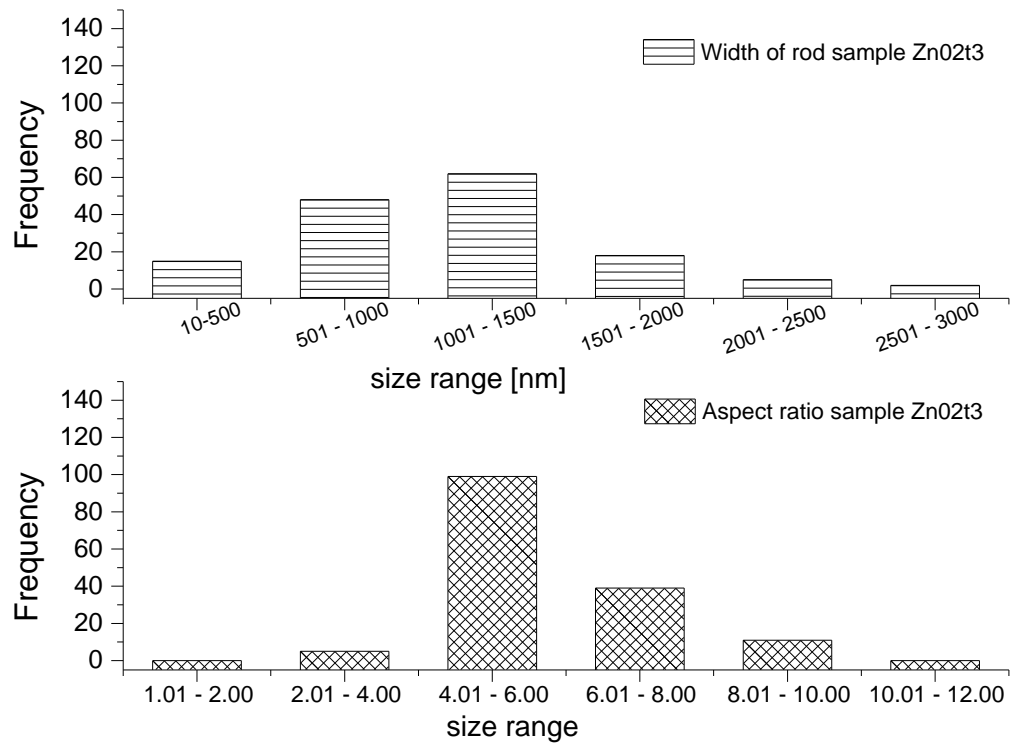


Figure 5.13: Histogram showing particle size distribution and aspect ratio in sample *Zn02t3*.

5.2.5 Six Hour (6 h) Hydrothermal Treatment Products

The X-ray powder pattern obtained from analysis of sample *ZnO2t6* revealed phase composition of the sample to be pure phase wurtzite zinc oxide as indexed by ICDD reference pattern number 04-013-6607 (Figure 5.14).

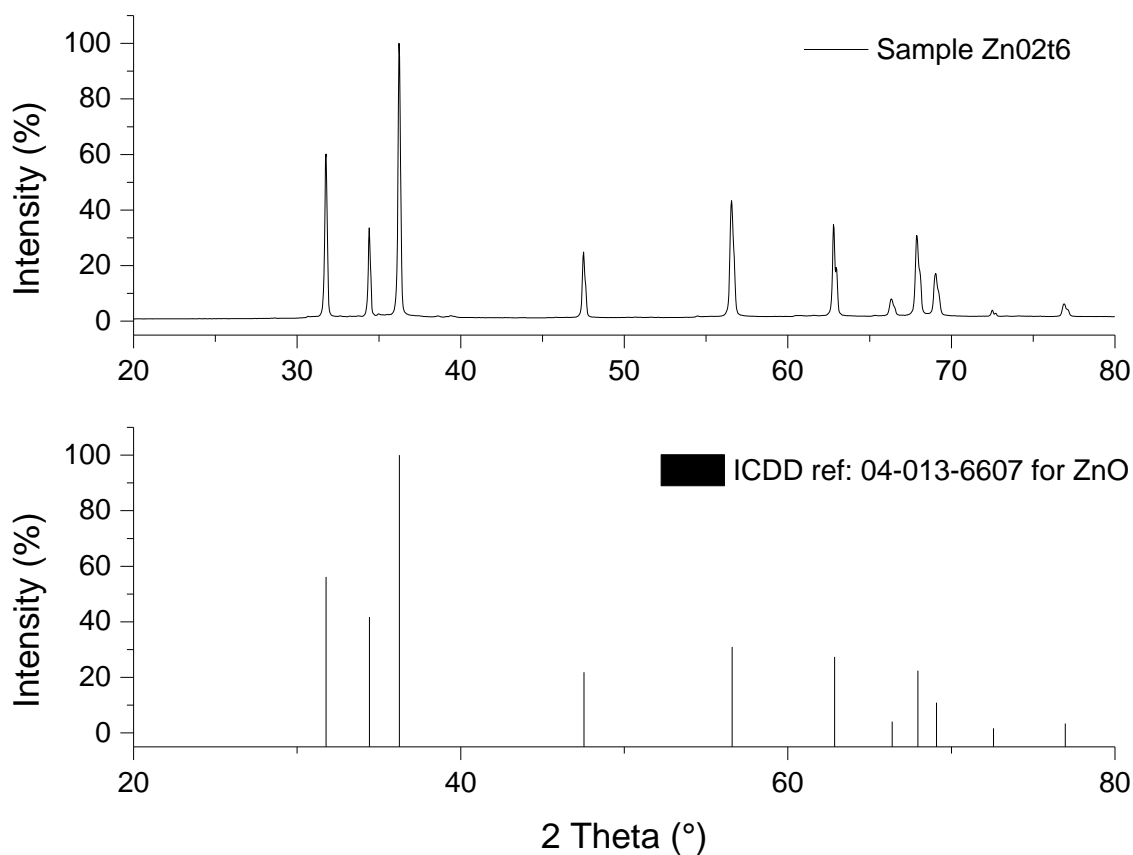


Figure 5.14: X-ray diffraction pattern of sample *ZnO2t6* and ICDD reference pattern 04-013-6607 for zinc oxide.

SEM analysis of sample *ZnO2t6* showed the presence of elongated rod-like particles throughout the sample (Figure 5.15). The particles in sample *ZnO2t6* appeared to have slightly higher aspect ratios in comparison to the dimensions of particles in sample *ZnO2t3* largely as a result of increased particle lengths although a slight reduction in the width of rods relative to the 3 h sample was observed (Figure 5.16).

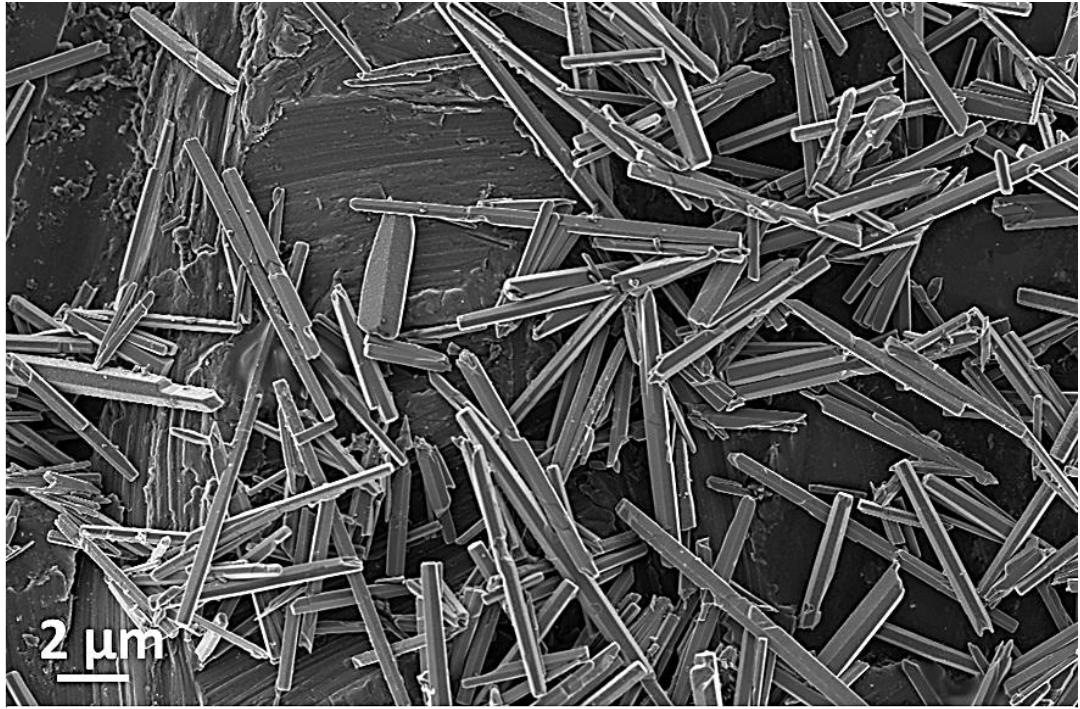


Figure 5.15: SEM micrograph of sample Zn02t6.

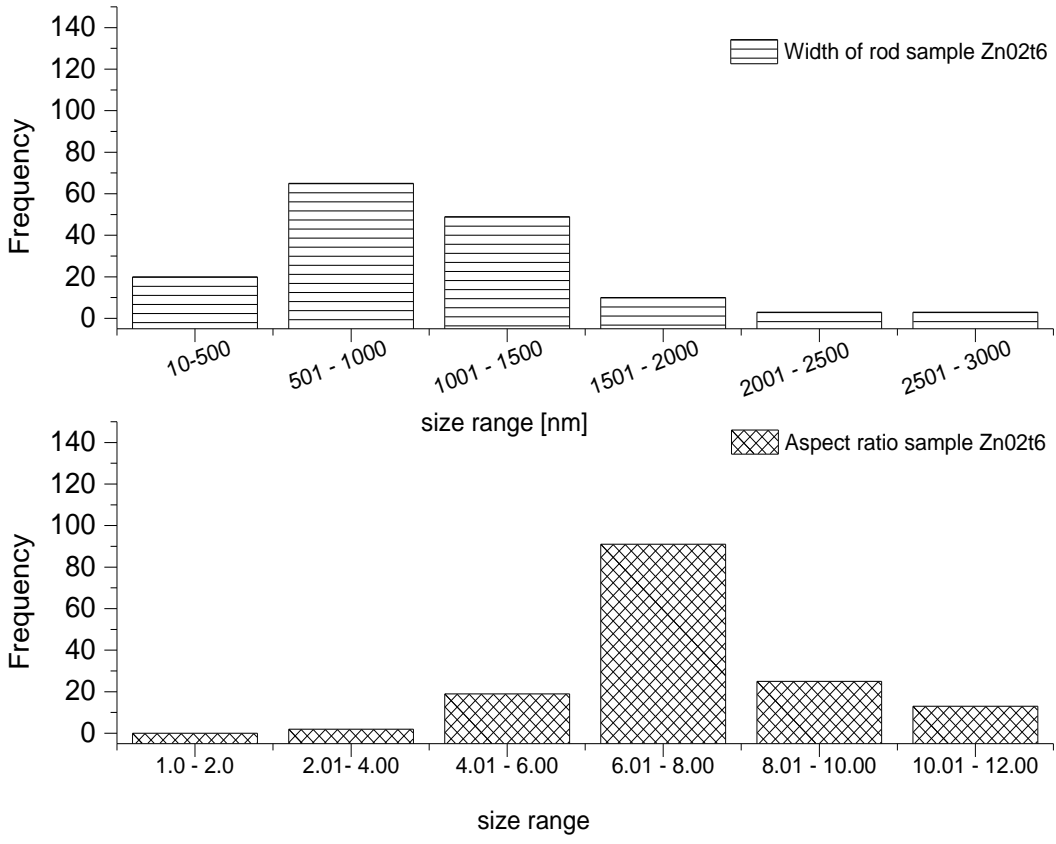


Figure 5.16: Histogram showing particle size distribution in sample Zn02t6.

5.2.6 Twelve Hour (12 h) Hydrothermal Treatment Products

X-ray powder diffraction analysis of sample *Zn02t12*, confirmed that they were phase-pure zinc oxide with the hexagonal wurtzite crystal structure (ICDD ref. 04-013-6607) as presented in Figure 5.17.

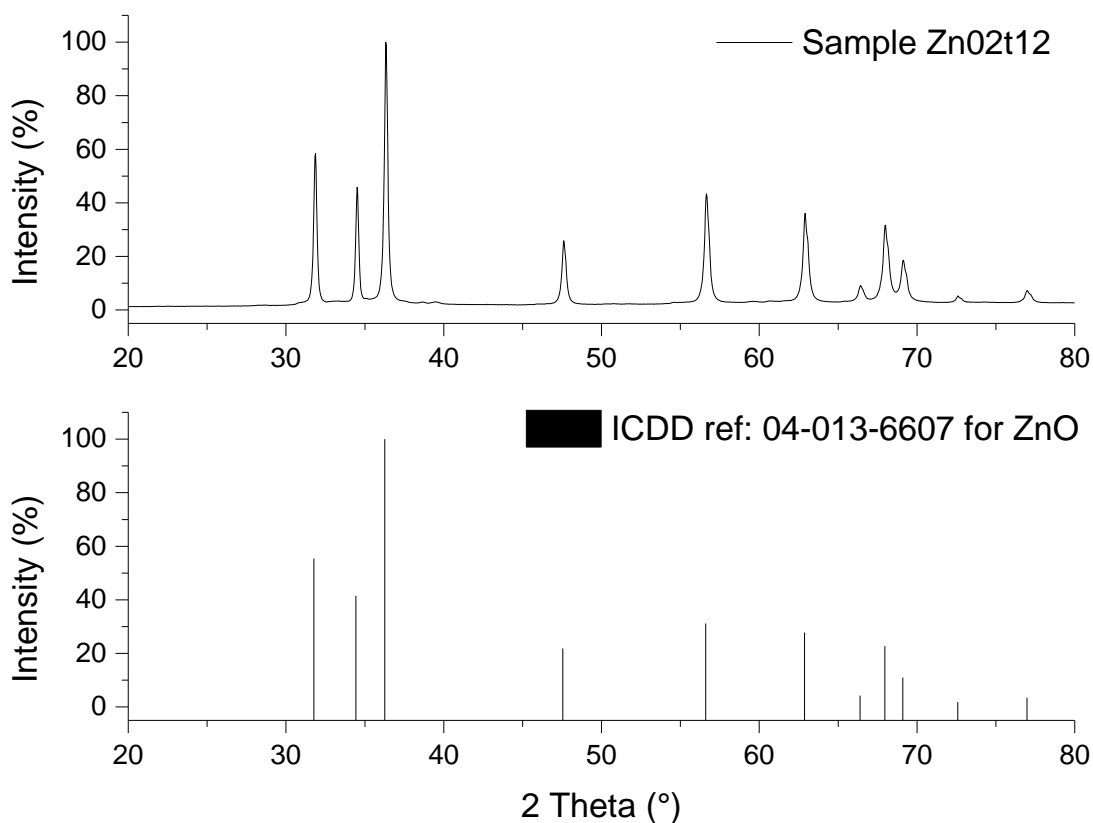


Figure 5.17: X-ray diffraction pattern of sample *Zn02t12* and ICDD reference pattern 04-013-6607 for zinc oxide.

Scanning electron microscopy showed the presence of a broad size distribution of well-defined and high aspect ratio hexagonal microrods (figure 5.18a). Thus the hexagonal basal section of the rods coincides with the $\{0001\}$ planes, whilst the sides of the hexagonal prisms denote the $\{10\bar{1}0\}$ planes (figure 5.18b).

Rod lengths ranged between 1 and 20 μm , while widths of between 100 nm and 2 μm were obtained from measurements of more than 150 particles in SEM micrographs (Figure 5.19).

5.2.7 Twenty Four Hour (24 h) Hydrothermal Treatment Products

X-ray diffraction analysis of the 24 h hydrothermal treatment products (sample *Zn02t24*) revealed the presence of monophasic wurtzite zinc oxide as indicated by ICDD ZnO reference pattern 04-013-6607 (Figure 5.20).

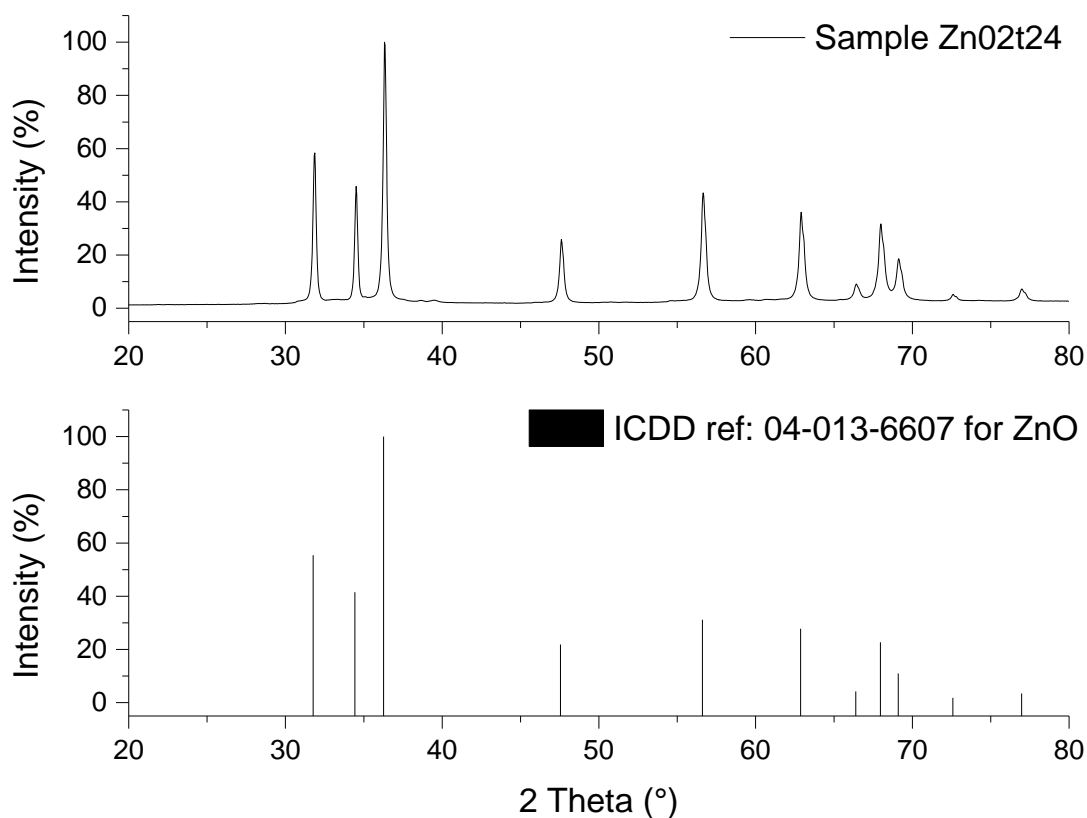


Figure 5.20: X-ray diffraction pattern of sample *Zn02t24*.

SEM of sample *Zn02t24* showed no significant changes in particle shape or size in comparison to observations made in sample *Zn02t12* other than that there appeared to be an increased presence of pitted rods (Figure 5.21), which may have been as a result of re-dissolution of the zinc oxide rods into the reaction medium.

pH measurements of the post-hydrothermal contents of the hydrothermal reactor recorded a pH value of ~8.7. Since zinc oxide is amphoteric in nature and as such would readily dissolve under acidic or basic conditions, prolonged exposure of the zinc oxide rods to mildly basic conditions under elevated pressure and temperature (hydrothermal conditions) could have triggered particle re-dissolution, hence the occurrence of pitted surfaces.

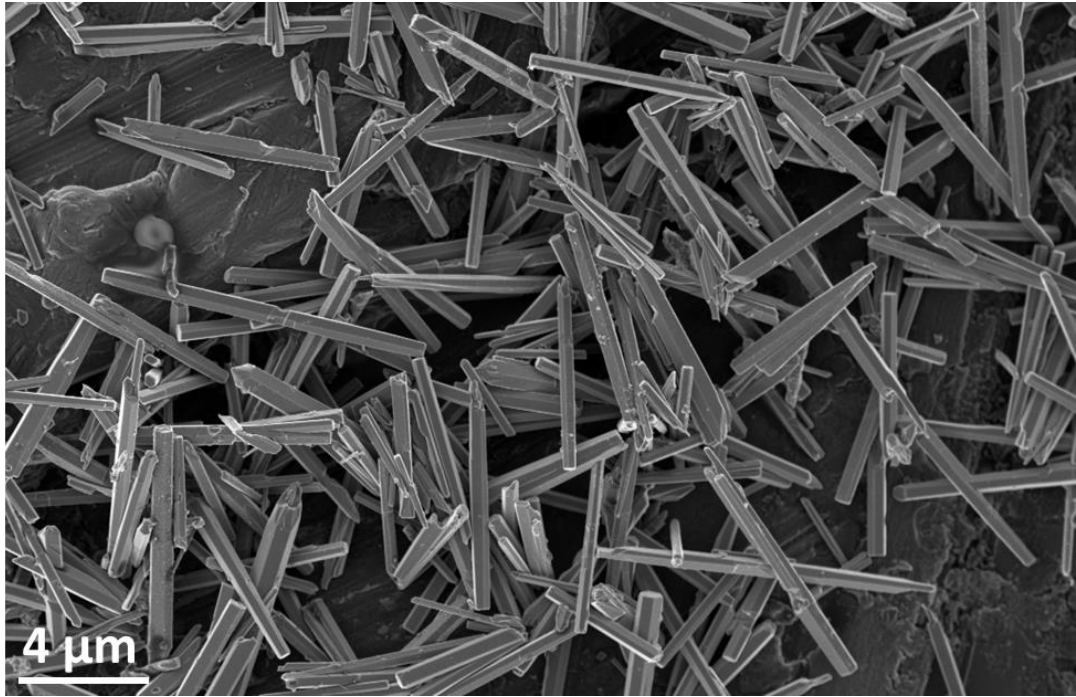


Figure 5.21: SEM micrograph of particles from sample Zn02t24.

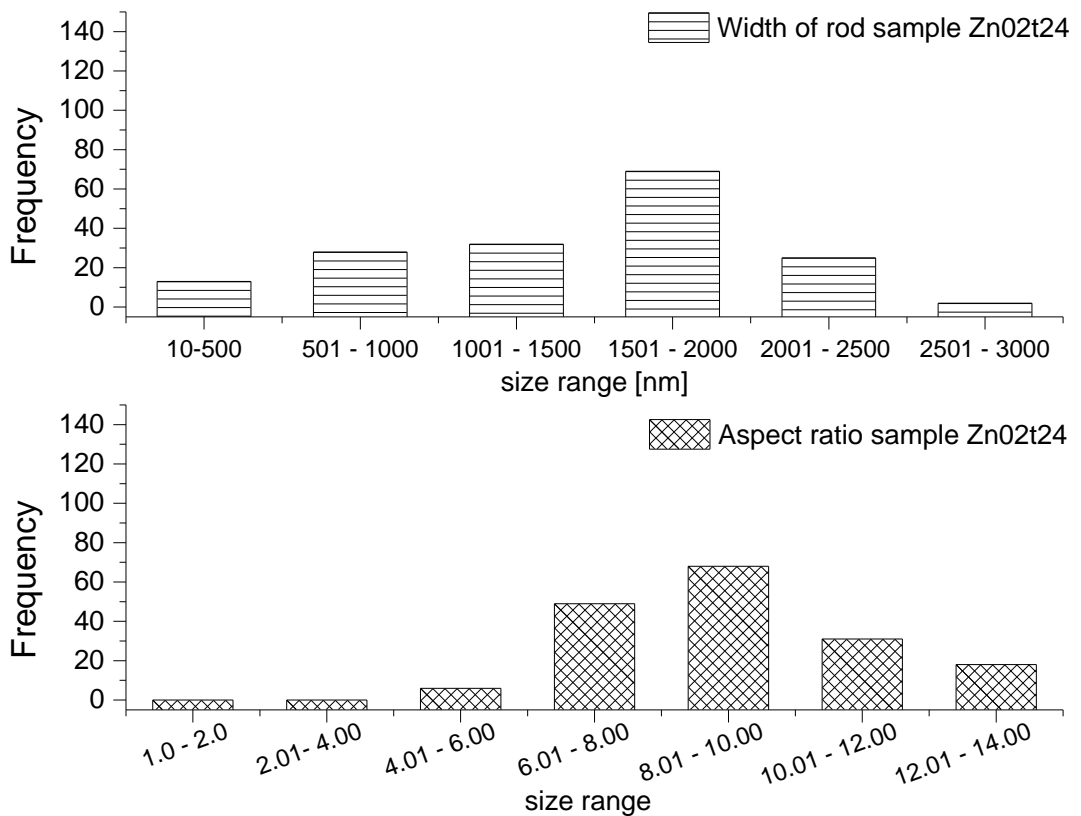


Figure 5.22: Histogram showing distribution of particle size and aspect ratios in sample Zn02t24.

5.3 Phase Transition from Zinc Hydroxide (wulfingite) to Zinc Oxide (wurtzite)

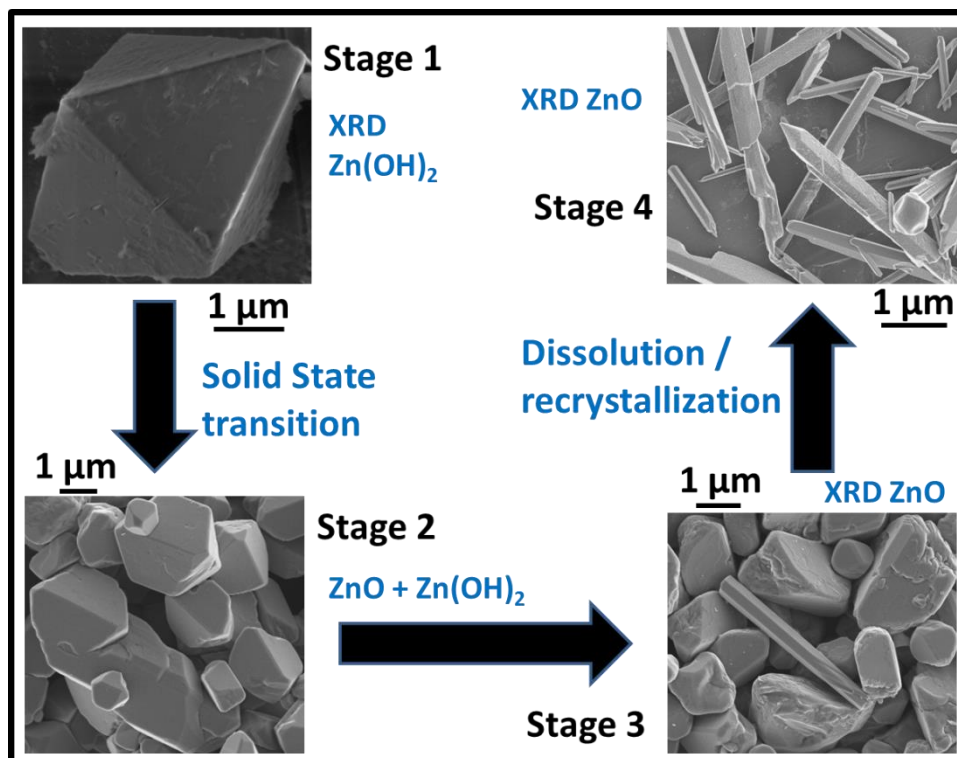


Figure 5.23: Schematic representation of the major particle growth stages for the high aspect ratio hexagonal zinc oxide rods using SEM images.

Figure 5.23 above illustrates a summary of the discussions presented in this section by showing SEM images highlighting the key morphological changes that were observed in the course of the phase/shape transformation. Analysis of information gathered through X-ray diffraction analysis (Figure 5.24) and scanning electron microscopy (Figure 5.25), showed that a progressive phase transformation / transition from crystalline orthorhombic wulfingite zinc hydroxide ($\text{Zn}(\text{OH})_2$) to crystalline hexagonal wurtzite zinc oxide (ZnO) occurred, accompanied by changes in particle morphology as a function of hydrothermal dwell times, starting from zinc hydroxide in sample *Zn02t0* which had an octahedral particle shape (Stage 1), and ending with wurtzite zinc oxide in sample *Zn02t3* with a hexagonal rod-like particle morphology (stage 4). This section provides insights into a number of mechanisms that could possibly explain the phenomena behind observations recorded via electron microscopy and powder X-ray diffraction.

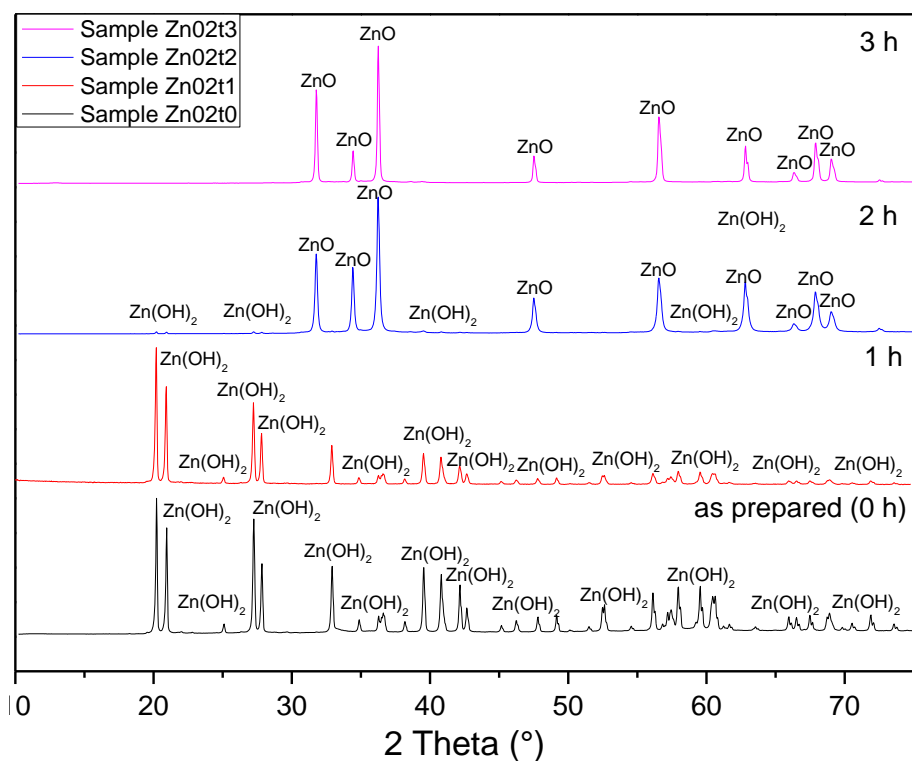


Figure 5.24: A comparison of X-ray diffraction patterns showing graduation phase transition as a function of hydrothermal dwell time.

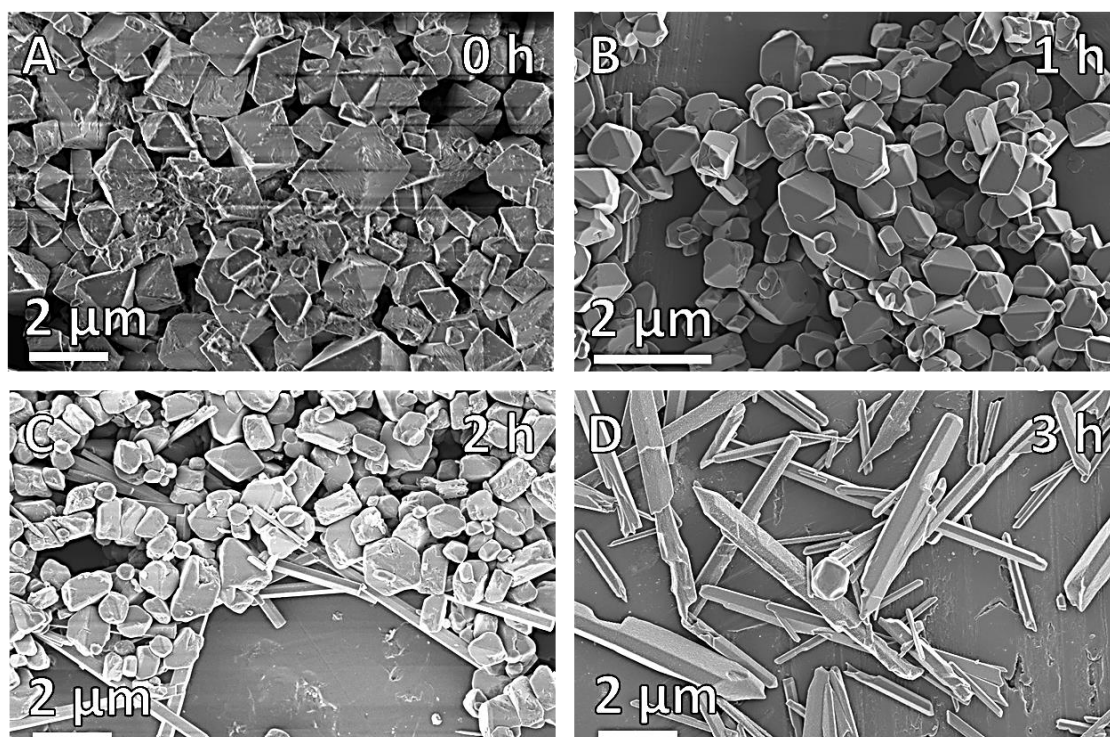


Figure 5.25: A comparison of SEMs showing changes in particle morphology as a function of hydrothermal dwell times.

The particle evolution process and phase transformation that was observed in the hydrothermal growth of zinc oxide from zinc acetate and ammonium hydroxide follows a rather complex path involving the interplay of a number of phenomena, many of which have been documented in literature, and are explored below.

Site Specific Deposition

It has been suggested that the $\text{Zn}(\text{OH})_2$ to ZnO phase transformation process could involve site-specific deposition of zinc oxide crystallites from the reaction medium on faces of the octahedral zinc hydroxide particles leading to a gradual build-up of zinc oxide around a zinc hydroxide core (Qu and Jia, 2009).

High magnification SEM micrographs of samples ZnO₂t₂, showed the presence of nanocrystallites coexisting with hexagonal rods and multifaceted particles (Figure 5.29), which could lend support to the foregoing theory. However, there is not much further evidence from characterisation results to suggest that the site-specific deposition mechanism, was a major player in the $\text{Zn}(\text{OH})_2$ to ZnO phase transformation process. Furthermore, the occurrence of the foregoing phenomena would lead to the expectation, that a significant number of hollow hexagonal rods would be observed in later stage samples caused by the selective dissolution of zinc hydroxide core of the $\text{Zn}(\text{OH})_2/\text{ZnO}$ composite particles (Kołodziejczak-Radzimska and Jesionowski, 2014; Baruah and Dutta, 2009). However such was not the case. Therefore, it is thought that the likelihood of site-specific deposition of ZnO crystallites onto $\epsilon\text{-Zn}(\text{OH})_2$ particles being significantly or solely responsible for the emergence of hexagonal rods of wurtzite zinc oxide from octahedral wulffingite particles may be low.

Pressure Induced Structural Transformation

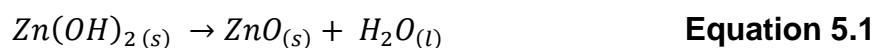
Exploring another phenomena, pressure induced structural transformations have been observed to occur in wulffingite $\epsilon\text{-Zn}(\text{OH})_2$ crystals (Kusaba et al., 2010). Phase transitions were observed in single phase wulffingite resulting in a transition from an orthorhombic crystal structure at room temperature and atmospheric pressure to a hexagonal one at increased pressure (2.1x

10⁶ KPa) and temperature. Also, the synthesis of metastable octahedral ZnO through the ultrasonic reaction of Zn(NO₃)₂ · 6H₂O and C₆H₁₂N₄ has been reported (Pholnak, et al., 2011).

One can note however that although there was a change in crystal structure, the chemical composition of both the start and end products in Kusaba et al., (2010) remained Zn(OH)₂, whereas in our own experiments, phase transition from orthorhombic zinc hydroxide to hexagonal zinc oxide was observed (Figure 5.24). Furthermore, the autogenous pressure and temperature conditions of the hydrothermal system under which the particles (high aspect ratio hexagonal zinc oxide rods) were formed were not as severe as those documented by Kusaba and co-workers; pressure values in our system rarely exceeded 250 KPa in the 125 mL acid digestion vessel used (model 4748, Parr Instruments, Illinois, USA).

Solid State Decomposition of Zn(OH)₂ to ZnO

Nicholas et al., (2012) documented temperature based Zn(OH)₂ to ZnO phase transformation using a combination of X-ray diffraction, X-ray photoelectron spectrometry (XPS) and secondary ion mass spectroscopy (SIMS). They observed that surface exchange of oxygen (O) atoms coupled with dehydration could result in the direct solid state decomposition of Zn(OH)₂ particles to ZnO particles. The feasibility of this conversion process was anchored on the endothermic nature and small free energy difference that characterises the thermodynamics of the decomposition at room temperature as described in equation 5.1 (Ramamurthy and Secco, 1968; Nicholas et al., 2012).



$$[\Delta H = +48.53 \text{ kJmol}^{-1} ; \Delta G_{298}^{\circ} = -1.1 \text{ kJmol}^{-1}]$$

Therefore, minute increases in ambient temperature and pressure conditions such as would occur during hydrothermal synthesis runs could easily drive the transition process (Moezzi, et al., 2011).

Analysis of SEM micrographs of early stage hydrothermal products (1 h to 3 h), appear to provide evidence supporting the foregoing phenomena. Analysis of XRD pattern of sample *Zn02t2* (Figure 5.24), indicated presence of ZnO and Zn(OH)₂ phases, while predominantly boulder-like particles were observed in SEM micrographs (Figure 25). This could mean that although many of the boulder-like particles bore physical resemblance to multifaceted ϵ -Zn(OH)₂ particles they may have had a different phase composition (i.e. ZnO), showing direct transition from solid ϵ -Zn(OH)₂ to solid ZnO.

Attempts at describing particle morphology transition from octahedral to hexagonal morphology via solid state transition mechanism suggested the opening up the octahedral particles (broadening of the tips) resulting in the appearance of new crystal facets which would then form the {01 $\bar{1}$ 0} and {0001} crystal planes of the hexagonal crystal structure (Wang, 2009).

Although there appears to be evidence signalling the occurrence of solid state decomposition of zinc hydroxide to form zinc oxide, this mechanism may not be able to sufficiently provide an all-inclusive description of the phase transition from ϵ -Zn(OH)₂ to ZnO under hydrothermal conditions in this thesis. This hypothesis, does not seem to take into cognisance, the solution based chemical interactions that characterise the synthesis of zinc oxide from NH₄OH and zinc acetate dihydrate among other observations. For instance, it does not provide an explanation for the role other species of zinc hydroxide could have played in the development of zinc oxide particles. It is known that multiple forms of zinc hydroxide and zinc hydroxo-complexes are involved in the solution synthesis of zinc oxide of which wulfingite is the most stable form (Reichle et al., 1975; Moezzi et al., 2011). Therefore, other mechanisms could also be involved in the complex nature of the hydrothermal synthesis of ZnO from zinc acetate and ammonium hydroxide.

Dissolution Recrystallization

Another hypothesis that could potentially describe the phase transition and morphology changes observed with respect to phase transition of wulfingite ϵ -Zn(OH)₂ to wurtzite ZnO under hydrothermal conditions, is the gradual

dissolution of wulffite octahedral shaped particles, followed by recrystallization as wurtzite zinc oxide hexagonal rods. It is known, that both zinc oxide and zinc hydroxide are amphoteric compounds, and that solubility plays a key role in the dynamics of particle formation (Schindler et al., 1964). Zinc hydroxide could undergo multiple pH-induced hydroxo-complex transformations (ZnOH^+ , Zn(OH)_2 , Zn(OH)_3^- , Zn(OH)_4^{2-} and polynuclear $\text{Zn}_2\text{OH}^{3+}$, $\text{Zn}_2(\text{OH})_6^{2-}$, $\text{Zn}_4(\text{OH})_4^{4+}$), which would affect its solubility characteristics as shown in figure 5.26 (Zhang and Muhammed, 2001). As such, the pH of the reaction medium could significantly influence the type of zinc hydroxo-complex existing in the medium and this in turn could influence the characteristics of the eventual product particles (Reichle et al., 1975).

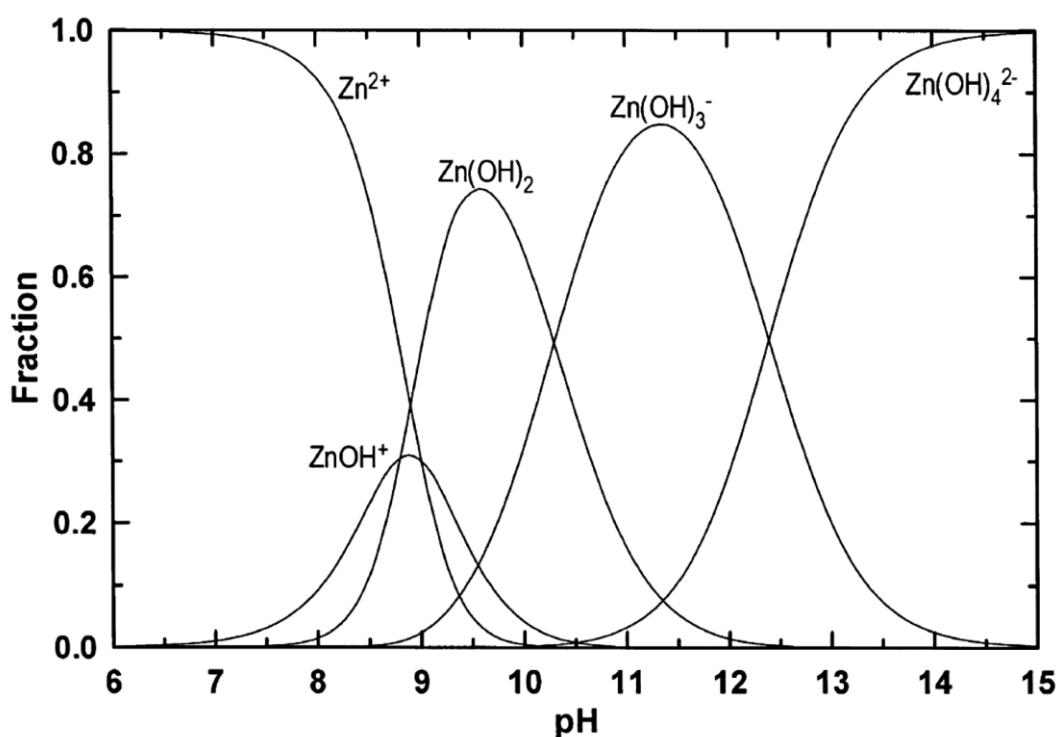
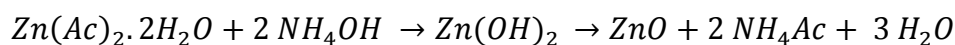


Figure 5.26: Distribution of Zn(II) hydroxo-complexes in equilibrium with crystalline zinc oxide at infinite dilution at 298 K (Zhang and Mohammed, 2001).

The overall ZnO formation from the reaction of zinc acetate dihydrate and ammonium hydroxide could be written as:



Equation 5.2

Zinc acetate dissolves in water and dissociates to release zinc ions and acetate radical as shown below:

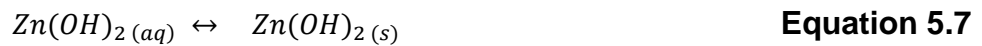
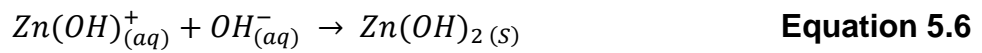


Where: $Ac = CH_3COO$

Ammonium hydroxide being a weak base, partially dissociates to liberate ammonium (NH_4^+) and hydroxide (OH^-) ions as shown in Equation 5.3

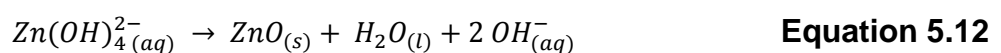
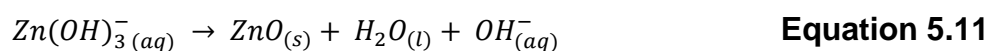
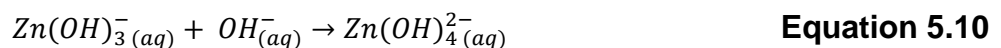
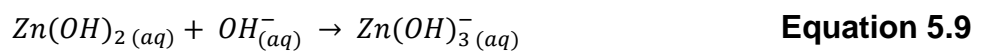


The formation, and precipitation of zinc hydroxide can be described by the following chemical equations (Moezzi, et al., 2011):



Ammonium ions (NH_4^+) and hydroxide (OH^-) ions could combine with zinc ions (Zn^{2+}) to form aqueous hydroxo–zinc, ammine–hydroxo zinc and zinc hydroxide salt complexes such as: hexaaquazinc ($[Zn(NH_3)_4(H_2O)_2]^{2+}$ or $[Zn(NH_3)_4]^{2+}$) (Zhang and Muhammed, 2001; Moezzi, et al., 2011; Park, et al., 2014).

An increase in reaction temperature and consequently hydrothermal pressure could have resulted in the dissolution of the $Zn(OH)_2$ crystals and subsequent recrystallization of ZnO which then developed into hexagonal wurtzite rods. Equations 5.8 to 5.12 provide a description of the dissolution process of wulfingite ε - $Zn(OH)_2$ particles into the reaction system before subsequent recrystallization of wurtzite ZnO (Moezzi, et al., 2011); chemical equations involving the acetate radical have not been included.



In other set of experiments where base species were switched, by replacing ammonium hydroxide with sodium hydroxide (described in Chapter 3), there was no observation of the precipitation of wulffingite ϵ -Zn(OH)₂ or any other form of zinc hydroxide particles prior to the emergence of zinc oxide particles. What was rather observed was the presence of zinc oxide particles in the freshly prepared '0 h' precipitate at room temperature.

Furthermore, evidence obtained from SEM analysis of sample *Zn02t2* as shown in figure 5.28, where a hexagonal rod is seen evolving from an irregular shaped multifaceted crystal sample supports the theory that hexagonal wurtzite zinc oxide rods of crystallized from dissolved metastable Zn(OH)₂ octahedral particles; although one is not sure if the rods may have grown independently of the multifaceted boulder-like particles.

Also, high magnification SEMs in Figure 5.29 show hexagonal rods coexisting with irregular shaped boulder-like particles and nanocrystallites. The shape of the boulder-like particles is suggestive of particles losing faceted edges due to dissolution, while the nanocrystallites could be zinc oxide particles recrystallizing from solution. Figure 5.27 is a schematic showing a hypothetical pathway through which zinc oxide could have been produced from zinc acetate dihydrate and ammonium hydroxide.

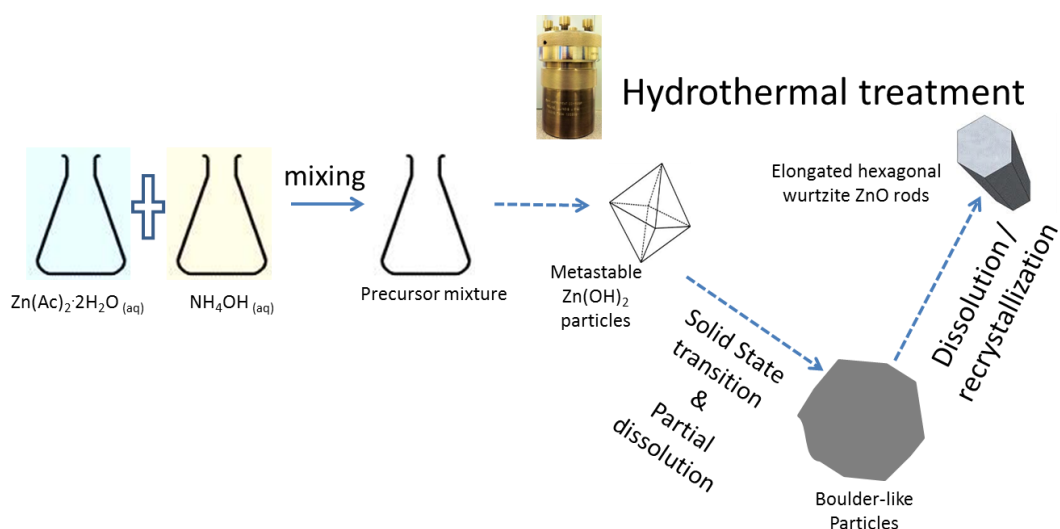


Figure 5.27: Schematic illustrating hypothetical pathway for formation of zinc oxide from zinc acetate and ammonium hydroxide (*not to scale*).

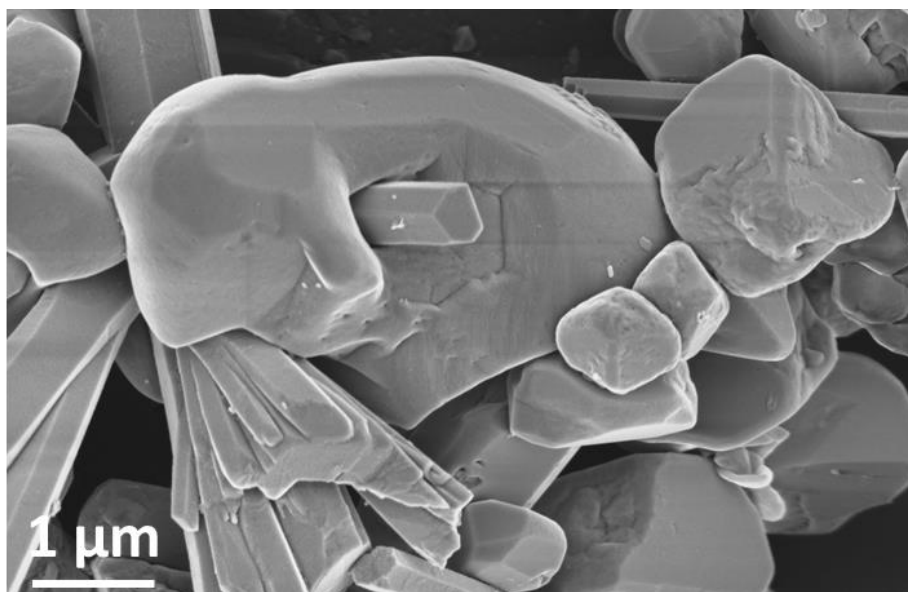


Figure 5.28: SEM showing a hexagonal rod-like particle evolving from a Zn(OH)_2 boulder-like particle, surrounded by both particle types.

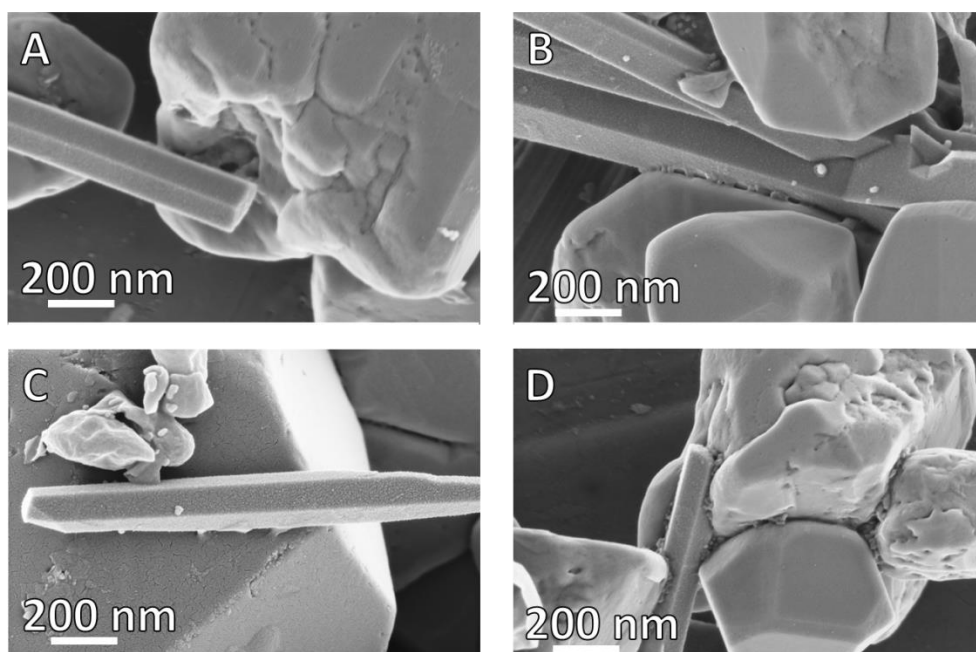


Figure 5.29: SEM micrographs showing multifaceted or boulder like particles coexisting with a hexagonal rod particle and crystallites.

In summary, it is thought, that phase transition from wulffingite $\epsilon\text{-Zn(OH)}_2$ to wurtzite ZnO under hydrothermal conditions involved a combination of mechanisms of which solid state decomposition of Zn(OH)_2 to ZnO and dissolution / recrystallization process were key actors.

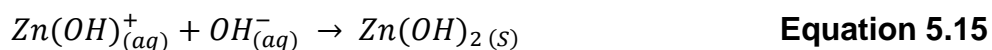
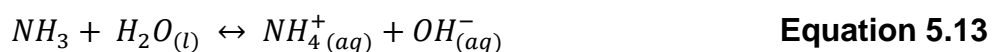
5.4 Investigating the Role of Ammonia in Buffering the pH of Reaction Medium and Particle Growth

There is a strong likelihood that ammonia and ammonium ions played an important role in ZnO particle formation process. Considering the combinative action of the following:

- pH-based $\text{Zn}(\text{OH})_2$ solubility,
- The formation of aqueous ammine–hydroxo zinc complexes, by ammonium and zinc ions coupled with
- The knowledge that NH_4OH was present in stoichiometrically excess quantities in the reaction system (only about 0.07 moles of NH_4OH would have been needed to achieve stoichiometric balance, while ~ 0.47 moles of NH_4OH was introduced into the reaction system), and
- Values recorded from pH measurements.

To be able to appropriately incorporate the foregoing analysis into the $\text{Zn}(\text{OH})_2$ to ZnO phase transformation process that was observed to occur in the context of solution based synthesis, there is the need for a particle formation mechanism that would involve initial precipitation of zinc hydroxide followed by dissolution of the zinc hydroxide particles and then recrystallization of final zinc oxide rods (Figure 5.27). Variations in reaction temperature and associated pressure during hydrothermal processing, could also have played a supportive role in the dissolution of the $\text{Zn}(\text{OH})_2$ crystals and subsequent recrystallization as ZnO.

In further scrutiny of the role of pH in the dynamics of particle growth, it is understood that zinc hydroxide, the precursor for the hexagonal rods is pH sensitive (Zhang and Mohammed (2001)). At a prevalent pH of ~ 9 inside the Teflon lined hydrothermal vessel, the reaction medium should contain mainly $\text{Zn}(\text{OH})_2$ (Figure 5.25) which should then precipitate out as the octahedral wulffite particles observed via scanning electron microscopy and X-ray diffraction analysis samples *Zn02t0* to sample *Zn02t2*.



From the foregoing chemical equations, one can note that the consumption of OH⁻ ions in the system by the process of crystallisation of octahedral wulfingite particles in equations 5.14 and 5.15, would force equation 5.13 to the right according to Le Chatelier's principle resulting in the introduction of more OH⁻ ions into the reaction system, hence the relative stabilisation of pH over the course of hydrothermal treatment as observed in these set of experiments (figure 5.30).

Figure 5.30 shows a pH profile obtained by measuring the pH of the contents of the hydrothermal reactor at the end of each hydrothermal treatment for the dwell time indicated. pH variations occurring during the course of the hydrothermal reaction process could not be monitored.

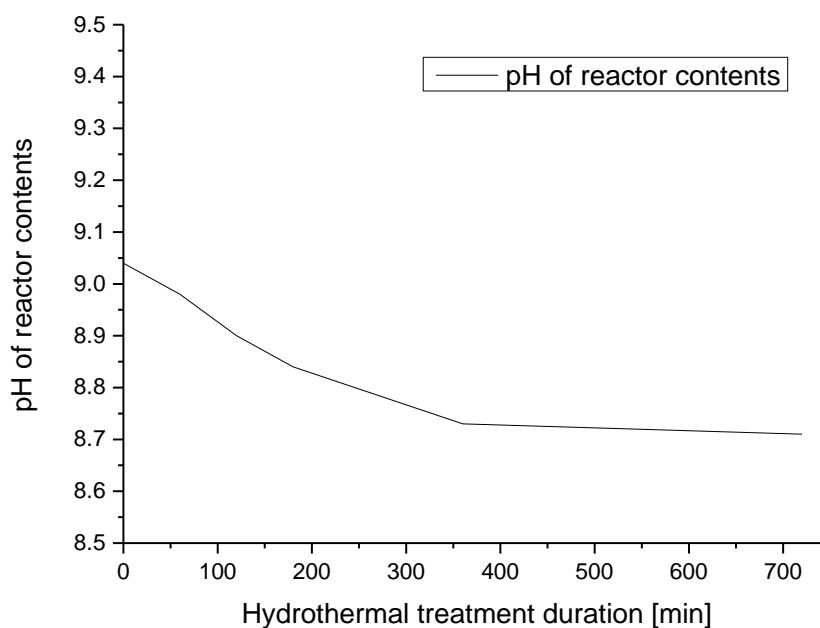


Figure 5.30: pH profile of reactor contents as a function of dwell time.

5.5 Hierarchical Growth of Zinc Oxide Hexagonal Double Rods (Chapter 4) and High Aspect Ratio rods (Chapter 5)

One of zinc oxide's strengths as a semiconductor material is its ability to crystallize into several shapes. It is also widely understood that ZnO has a preference for growth along the c-axis under hydrothermal conditions (Baruah and Dutta, 2009). Many researchers have documented growth via self-assembly in ZnO usually driven by its intrinsic crystallographic polarity (Wang, 2004; Bamiduro, et al., 2014). ZnO's multi-shape capabilities make it difficult to pin its growth process to a single particle formation mechanism. This is further compounded by the inherent challenges in observing particle growth under hydrothermal conditions. Thus despite recent advances in the studies of particulate growth at the nano-level, there is little consensus on the single or multiple growth mechanisms which could be responsible for the formation of elongated particulate structures of zinc oxide.

In chapter 4 the hydrothermal growth of zinc oxide hexagonal double rods from zinc acetate and sodium hydroxide was discussed, while this chapter provides details of hydrothermal growth of high aspect ratio zinc oxide hexagonal rods from zinc acetate and ammonium hydroxide. Although, particle growth and reaction pathways for experiments reported in chapter 4 and 5 are different, both involved the development of intermediate particle morphologies before the emergence of the hexagonal wurtzite rods. Also, the growth of hexagonal ZnO rods, in both sets of experiments was observed to be hierarchical, epitaxial in nature and c-axis directed.

A comparison of results presented in both chapters showed that the type of base employed to moderate the pH of the starting solution has a strong bearing on the characteristics of the final ZnO product resulting from differences in growth mechanisms.

Changes in relative surface energy of lattice planes and hence preferred growth habit due to differences in adsorption characteristics of and variation in concentration of Na^+ , NH_4^+ and OH^- ions during nucleation and primary growth is one explanation for these results. The differing size and electronegativity of the NH_4^+ and Na^+ cations could lead to differences in

cation adsorption characteristics on the surfaces of growing ZnO clusters (or intermediates species). Given that crystal habit reflects planes of lowest surface energy and slowest growth rate, the Na⁺ ions would appear to minimise the differences in energies between the {01 $\bar{1}$ 0} and {0001} planes relative to other planes such that rod-like growth along <0001> is suppressed. With the NH₄OH rods, the differences in growth rate between the {01 $\bar{1}$ 0} and {0001} planes relative to other planes appeared to be quite large, hence the emergence of high aspect ratio rods.

A secondary re-crystallisation (coarsening) mechanism is inferred by the bimodal sizes evident especially in SEM images of the NaOH sample. Through TEM, it was observed that particle assembly in the polar <0001> direction was a factor in the formation of the hexagonal rods in both NaOH and NH₄OH based rod growth. Evidence of the former is shown in the SEM micrographs presented in Figure 5.31b and 5.31c. The ammonium hydroxide high aspect ratio hexagonal microrods were difficult to study structurally using TEM because of their lack of electron transparency (due to particle thickness), except at particle extremities. However high magnification SEM, showed evidence that some rods were segmented in a manner indicative of step wise growth and a recrystallization of assembled sub units (Figure 5.32).

In conclusion, a comparison of chapters 4 and 5 show that substantial changes to the shape and size of ZnO particles during hydrothermal processing can be produced by switching base species demonstrated in this thesis by the use of NH₄OH and NaOH to moderate the starting pH of a zinc acetate solution. Also hydrothermal growth of zinc oxide particles, can be explained in terms of a multi-stage secondary growth process involving sequential nucleation and growth mechanisms coupled with epitaxial alignment along the polar [0001] direction of wurtzite ZnO.

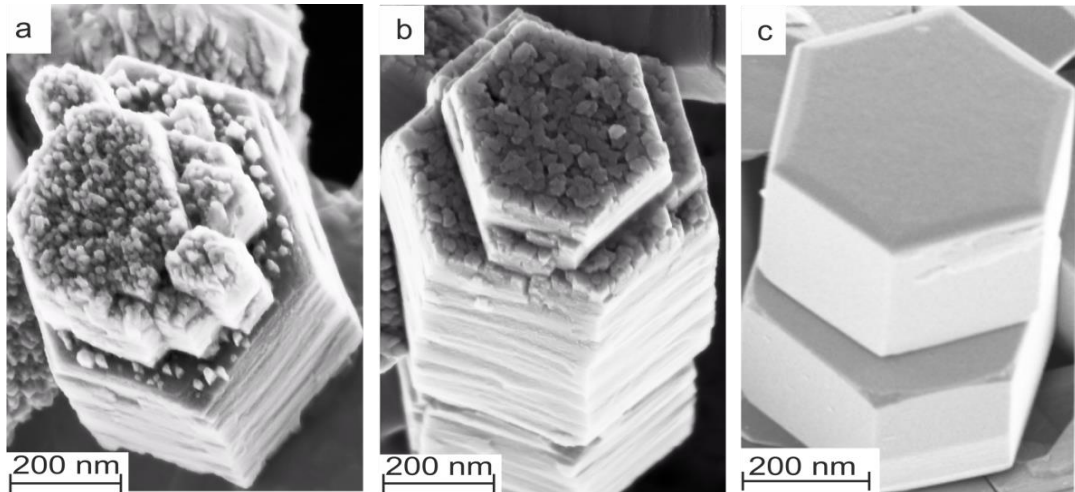


Figure 5.31: Combination of high magnification SEM micrographs illustrating particle growth sequence of zinc oxide hexagonal double rods; (a) particle from sample *Zn01t0.5* showing deposition of nanoparticles on the basal sections of an existing rod-like particle and (b) subsequent stages of recrystallizing to produce (c) a well-defined hexagonal double rod from sample *Zn01t12*.

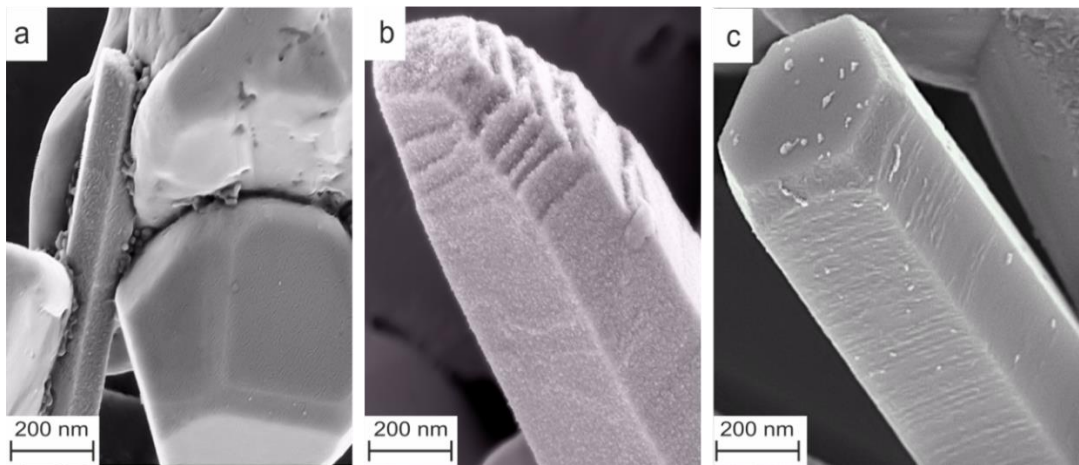


Figure 5.32: Combination of high magnification SEM micrographs illustrating ZnO particle growth sequence of high aspect ratio hexagonal rods (a) particle from sample *Zn02t2* showing co-existence of hexagonal rod-like with multifaceted octahedral shaped and boulder-like particles (b) another particle from sample *Zn02t2* showing stepwise growth of the basal planes (c) particle from sample *Zn02t12* showing a fully recrystallized rod with well-defined hexagonal basal terminal.

Chapter 6

Results and Discussion III

Synthesis and Characterisation Sodium Zirconate from Zirconium Acetate and Sodium Acetate

6.1 Introduction

The last two chapters have been focused on the presentation and discussion of results from the synthesis and characterisation of hydrothermally prepared zinc oxide.

In this chapter, results from the synthesis and characterisation of another metal oxide are presented. Simple evaporation of precursor suspension to powder and the use of spray drying were employed as alternative methods of particle synthesis instead of hydrothermal synthesis in a bid to explore synthesis routes with potentially lower carbon footprints (energy requirements) relative to the hydrothermal process.

As a result of better kinetics of CO₂ absorption at relatively low CO₂ partial pressures and high temperatures relative to other alternatives (Li₂ZrO₃ and K₂ZrO₃) as well as having better sorbent regeneration potentials (Pfeiffer et al., 2007; Cortés-Palacios et al., 2012), sodium zirconate (Na₂ZrO₃) is considered to be a strong candidate for post-combustion capture (PCC) of CO₂ from fossil fuel fired power plants and other single-point industrial emitters as well as for sorption enhanced steam reformation (SESR), where absorption of CO₂ at elevated temperatures is desired to shift chemical equilibrium in favour of greater product (H₂) yields and purity (López-Ortiz et al., 2005; Ochoa-Fernández et al., 2005); hence the motivation for including

results of investigation into its synthesis and characterisation as a chapter in this thesis.

Sodium acetate and zirconium acetate in nitric acid were used for particle synthesis. Spray drying involved pneumatic atomisation (using a two-fluid atomizer) of both acetate solutions to generate an aerosol which was then sprayed through a drying chamber after which the dried precursor precipitate was collected (Gretzinger and Marshall, 1961). Further details of synthesis process are provided in section 3.1.2.

The focus of discussions in this chapter follows a similar trend to previous chapters i.e. examination of the effect of changes to synthesis conditions on the properties of the product materials. As was the case in chapters 4 and 5, X-ray powder diffraction analysis (XRD) was used to determine the phase content of the powders, while scanning and transmission electron microscopy (SEM and TEM) were employed to observe microstructural details of the sodium zirconate particles. In addition, this chapter introduces the use of thermogravimetric analysis (TGA) to probe the CO₂ capture characteristics of the product powders.

In terms of layout of the chapter, section 6.2 dwells on communicating the results of sample characterisation, which mainly involves presentation of the X-ray diffraction patterns and SEM images of samples obtained after calcination, carbonation for 1 h and multicycle TGA analysis. Discussions consider possible chemical pathways to describe the synthesis process.

Section 6.3 compares the CO₂ capture performance of the samples prepared via the two synthesis routes in addition to a commercially sourced sample. Analysis of percentage CO₂ conversion, durability over multiple TGA cycles and the influence of microstructure on performance of the samples is examined.

6.2 Effect of Synthesis Route on Characteristics (Phase Content and Morphology) of Sodium Zirconate Powders

6.2.1 Samples

Analytical experiments on the TGA were performed to investigate the influence of powder preparation method on the characteristics of powders produced via evaporation drying and spray drying routes. Table 6.1 provides details of some of the samples generated.

Table 6.1: List of samples and selected experiment conditions.

S/N	Sample	Precursor Route	Calcination conditions	Number of Carbonation-decarbonation cycles
1	<i>NZ01</i>	Evaporation dried	None	0
2	<i>NZ01c0</i>	ditto	900 °C, 2 h	0
3	<i>NZ01c1</i>	ditto	900 °C, 2 h	0.5 (carbonation only)
4	<i>NZ01c10</i>	ditto	900 °C, 2 h	10
5	<i>NZ01c20</i>	ditto	900 °C, 2 h	20
6	<i>NZ01c30</i>	ditto	900 °C, 2 h	30
7	<i>NZ01c50</i>	ditto	900 °C, 2 h	50
8	<i>MELSORB</i>	n/a	None	20
9	<i>NZ02</i>	Spray dried	None	0
10	<i>NZ02c0</i>	ditto	900 °C, 2 h	0
11	<i>NZ02c1</i>	ditto	900 °C, 2 h	0.5 (carbonation only)
12	<i>NZ02c10</i>	ditto	900 °C, 2 h	10
13	<i>NZ02c20</i>	ditto	900 °C, 2 h	20
14	<i>NZ02c30</i>	ditto	900 °C, 2 h	30
15	<i>NZ02c50</i>	ditto	900 °C, 2 h	50

6.2.2 Precursor Powders

X-ray diffraction analysis of powders obtained after completion of evaporation drying and spray drying synthesis processes (Figure 6.1), showed that powders from both processes contained a mixture of sodium carbonate, monoclinic zirconium oxide and sodium zirconate (Figure 6.2). However, the spray dried powder appeared to have a higher monoclinic zirconium oxide content in addition to traces of reactants (sodium acetate and zirconium acetate). The powder XRD patterns were compared with ICDD reference patterns file numbers 01-071-1833, 00-035-0770, 01-083-0944, for sodium carbonate (Na_2CO_3), sodium zirconate (Na_2ZrO_3), and monoclinic zirconium oxide (m-ZrO_2) respectively. Figure 6.1 is the x-ray diffraction patterns of precursor powders obtained from evaporation drying and spray drying methods while Figure 6.2 shows a comparison of both experimental diffraction patterns with ICDD reference patterns for sodium zirconate and sodium carbonate and monoclinic zirconium oxide.

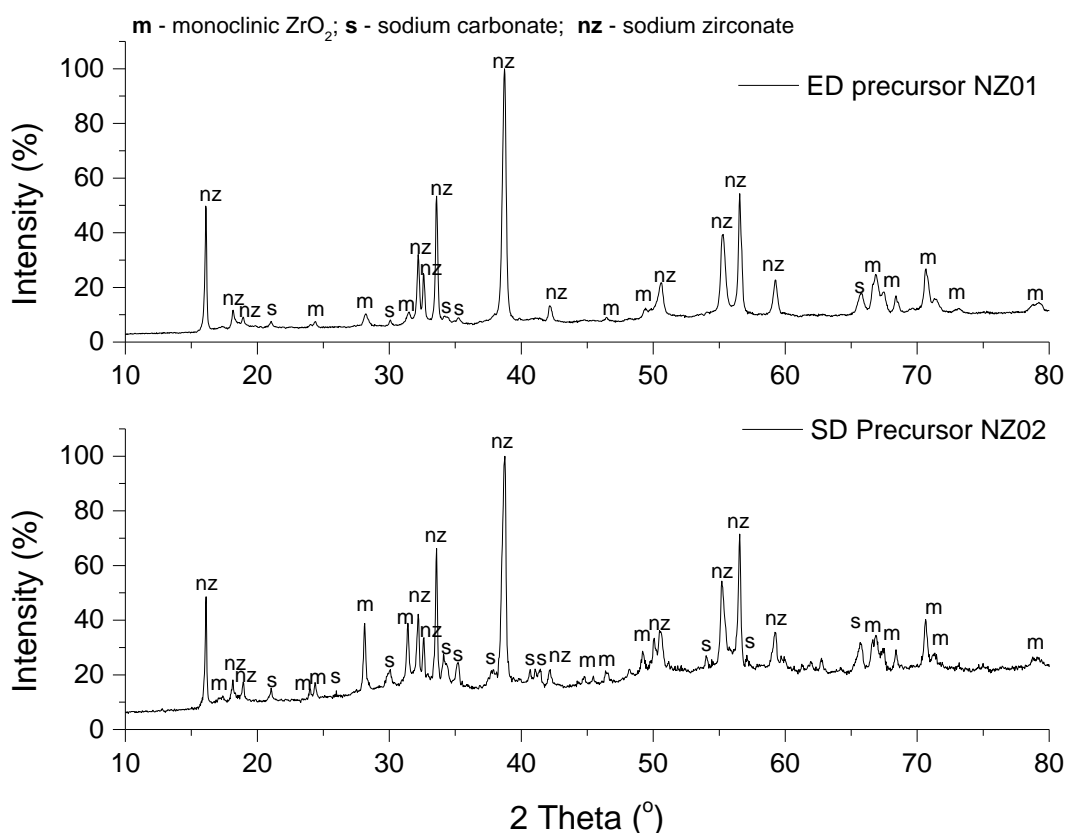


Figure 6.1: XRD plot of as prepared precursor powders obtained from evaporation drying (ED) and spray drying (SD) synthesis routes.

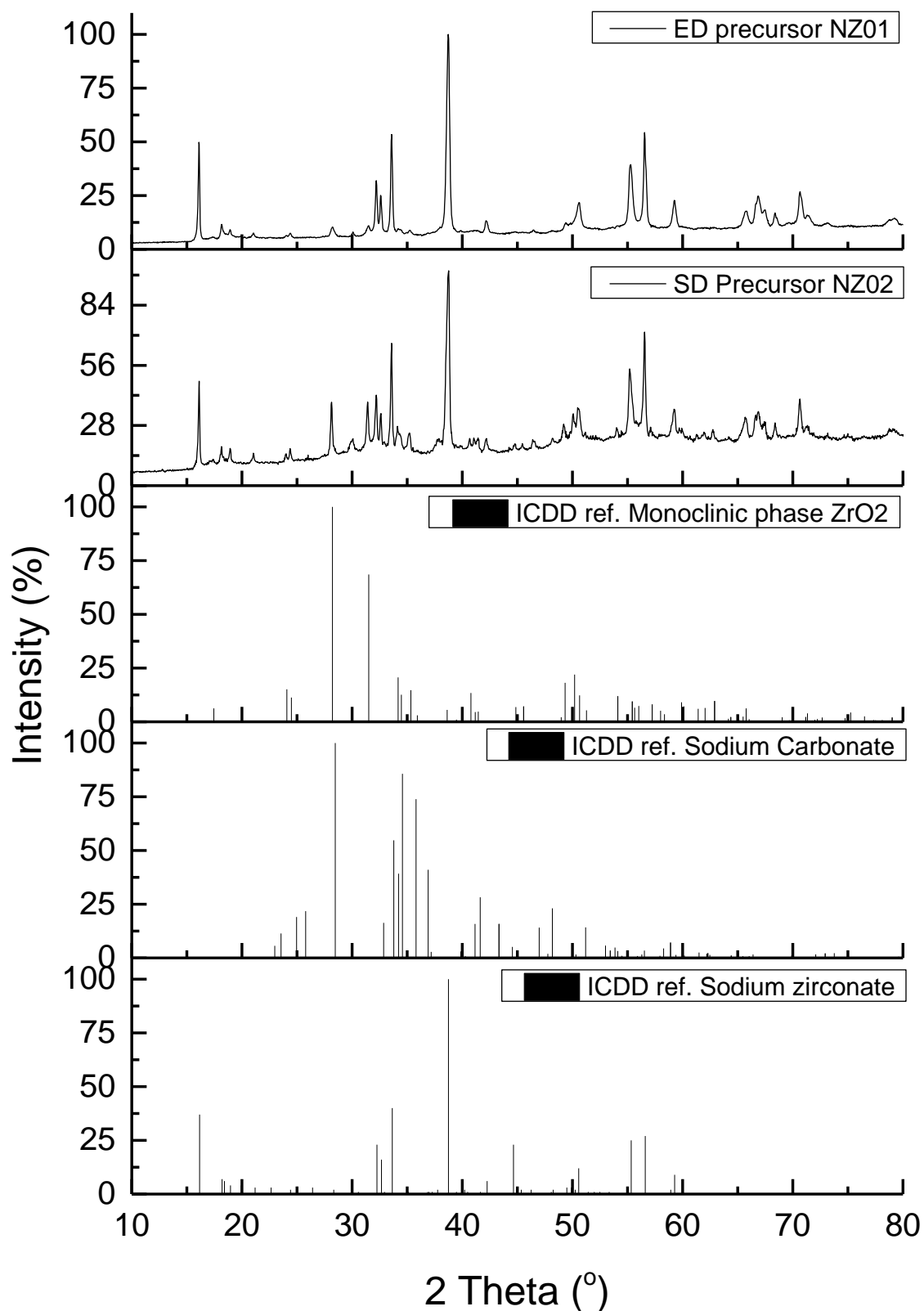


Figure 6.2: Comparison of XRD patterns of precursor powders from evaporation dried and spray dried routes with ICDD reference patterns for sodium carbonate, sodium zirconate and monoclinic zirconia.

6.2.3 Freshly Calcined Powders

Precursor powders from both synthesis routes (i.e. evaporation drying and spray drying) were calcined in a Carbolite chamber furnace for 2 h at 900 °C.

Evaporation Dried (ED) Sample NZ01c0

X-ray powder diffraction analysis after calcination, revealed changes in the phase content (Figure 6.3). Sodium zirconate was identified as the main phase (ICDD reference file 00-035-0770) coexisting with a minor proportion of monoclinic zirconium dioxide (ICDD reference file 01-083-0944) and sodium carbonate, which could have originated from unconverted reagents.

Figure 6.3 is a plot of the X-ray diffraction pattern of the sample compared with ICDD reference pattern 00-035-0770 for sodium zirconate. Corresponding miller indices have been labelled ('m' and 's' indicate peaks identified as monoclinic ZrO_2 and Na_2CO_3 respectively). Table 6.1 provides details of phase indexing of sample NZ01c0 to ICDD reference 00-035-0770.

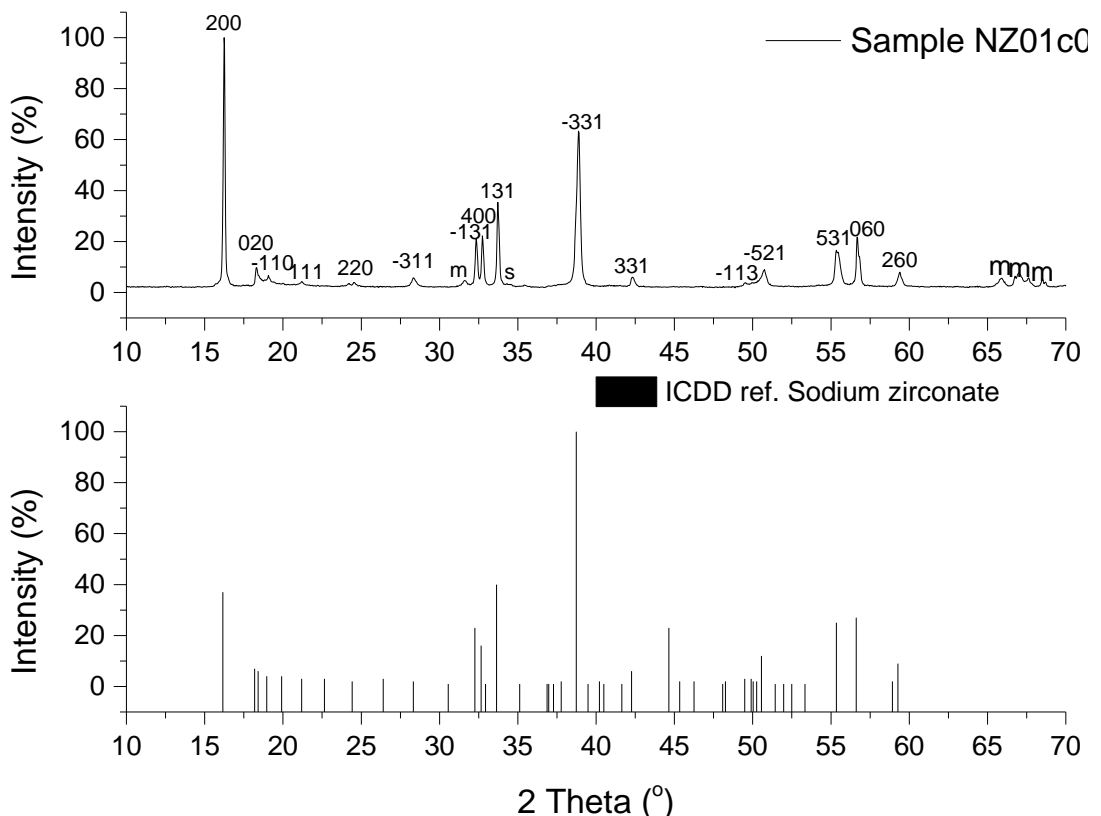


Figure 6.3: XRD plot of freshly calcined evaporation dried sample NZ01c0; peaks from sodium zirconate labelled with corresponding miller indices.

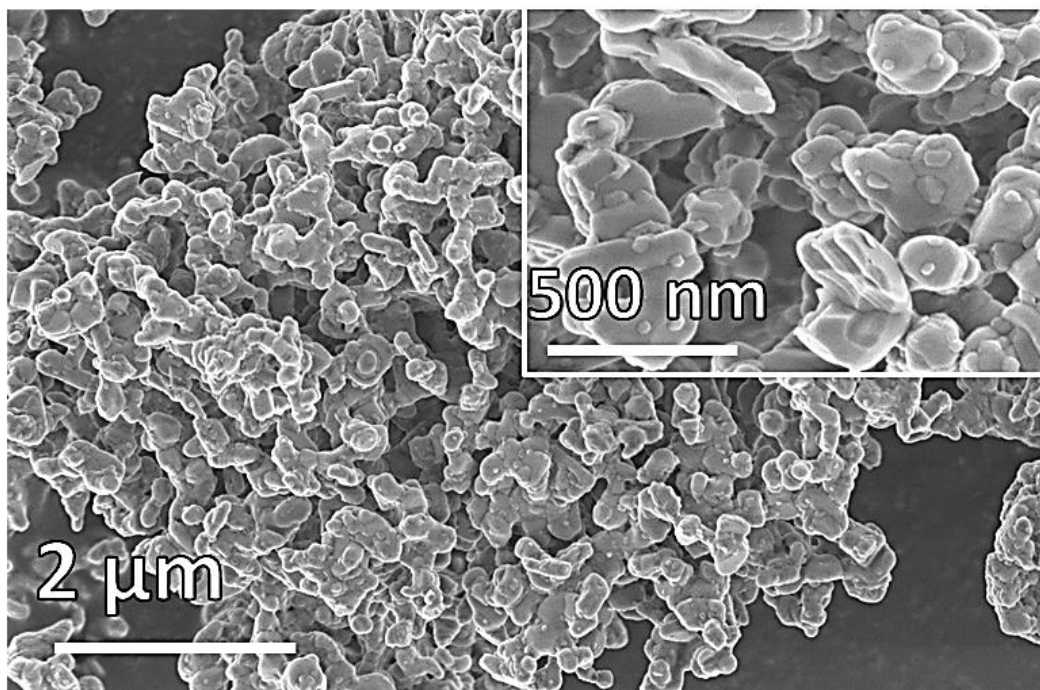


Figure 6.4: SEM of freshly calcined evaporation dried sample *NZ01c0* showing irregular shaped loose aggregates of particles.

SEM analysis showed that sample *NZ01c0* contained loosely aggregated irregular shaped particles. The agglomerates were about $\sim 10 \mu\text{m}$ in size consisting of $< 500 \text{ nm}$ primary particles as shown in Figure 6.4.

Spray Dried (SD) Sample *NZ02c0*

XRD analysis of freshly calcined spray dried powder (sample *NZ02c0*) also revealed sodium zirconate as the main phase with the presence of monoclinic zirconia and sodium carbonate detected (Figure 6.5).

SEM of sample *NZ02c0* from the spray drying route, revealed the sample was composed of hollowed out rounded particles having sizes ranging between $0.5 - 20 \mu\text{m}$. These rounded particles had a granular substructure consisting of irregular shaped nanoparticles (widths $< 100 \text{ nm}$); many of them looked deflated and some appeared to be ruptured (Figure 6.6).

Figure 6.5 is a plot of the XRD pattern of sample *NZ02c0* and ICDD reference pattern 00-035-0770 for sodium zirconate, peaks have been labelled with their corresponding miller indices while 'm' and 's' were used to denote peaks identified as monoclinic zirconia and sodium carbonate respectively.

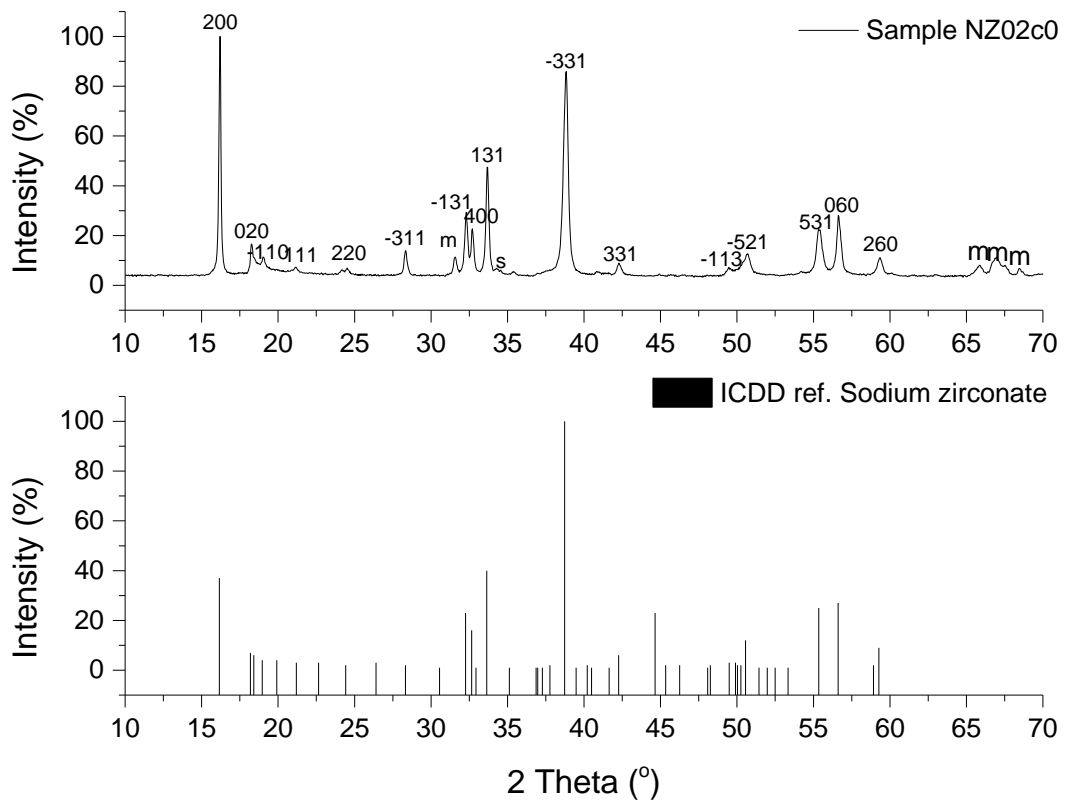


Figure 6.5: XRD plot of freshly calcined spray dried sample *NZ02c0*; peaks from sodium zirconate labelled with corresponding miller indices.

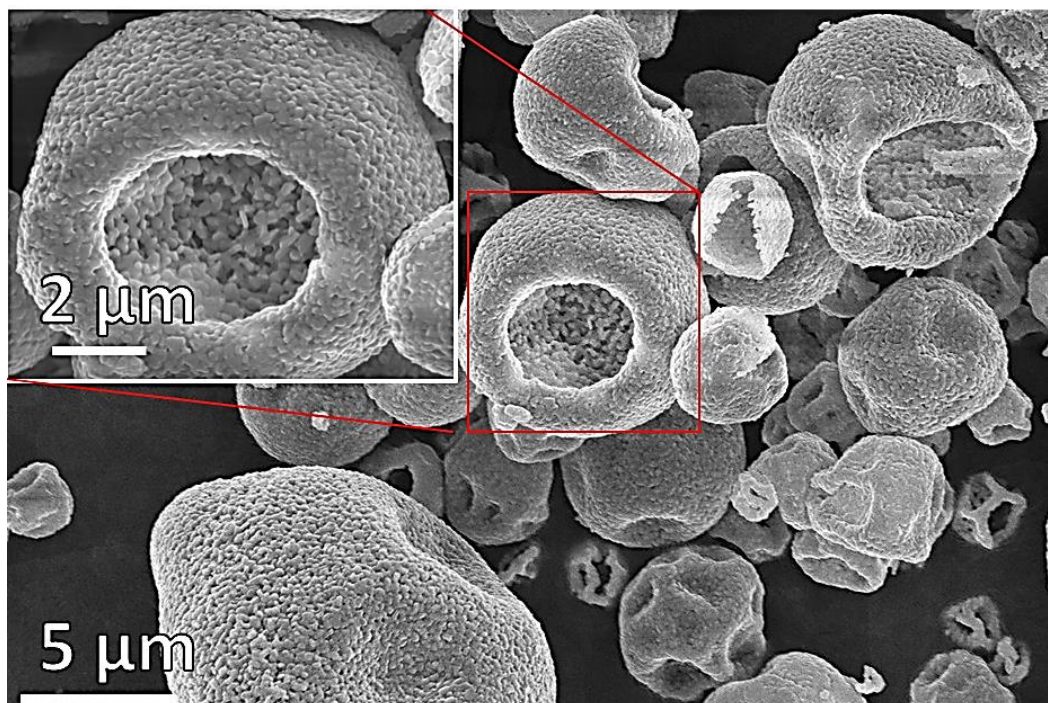


Figure 6.6: SEM of freshly calcined spray dried sample *NZ02c0* showing hollow granules of sodium zirconate with nanostructure.

Table 6.1: Indexing of peaks from samples *NZ01C0* (evaporation dried) and *NZ02C0* (spray dried) to ICDD Na_2ZrO_3 pattern 00-035-0770.

Sample NZ01C0			Sample NZ02C0			Na ₂ ZrO ₃ ICDD ref. 00-035-0770			
°2θ	d [Å]	I [%]	°2θ	d [Å]	I [%]	°2θ	d [Å]	I [%]	<i>h k l</i>
16.2	5.455	100	16.2	5.469	100	16.2	5.479	37	2 0 -2 0
18.3	4.847	8	18.2	4.857	13	18.2	4.873	7	0 2 -2 0
						18.4	4.814	6	0 1 -1 1
19.1	4.653	4	19.0	4.659	7	19.0	4.675	4	-1 1 0 1
						19.9	4.455	4	1 2 -3 0
21.2	4.192	2	21.1	4.203	2	21.2	4.190	3	1 1 -2 1
						22.7	3.922	3	-2 1 1 1
24.5	3.624	2	24.4	3.647	2	24.4	3.642	2	2 2 -4 0
						26.4	3.373	3	2 1 -3 1
28.3	3.149	4	28.3	3.150	10	28.3	3.148	2	-3 1 2 1
						30.6	2.923	1	3 2 -5 0
31.6	2.830	2	31.5	2.834	8				
32.3	2.767	21	32.3	2.771	28	32.3	2.773	23	-1 3 -2 1
32.7	2.734	24	32.7	2.737	21	32.7	2.740	16	4 0 -4 0
						32.9	2.718	1	3 1 -4 1
33.7	2.656	40	33.7	2.660	51	33.6	2.662	40	1 3 -4 1
						35.1	2.553	1	-4 1 3 1
						36.9	2.436	1	0 4 -4 0
						37.0	2.430	1	-1 2 -1 2
						37.3	2.410	1	2 3 -5 1
						37.8	2.380	2	1 4 -5 0
38.7	2.326	29							
38.9	2.314	63	38.8	2.316	81	38.7	2.323	100	-3 3 0 1
						39.5	2.281	1	1 2 -3 2

Sample NZ01C0			Sample NZ02C0			Na ₂ ZrO ₃ ICDD ref. 00-035-0770			
°2θ	d [Å]	I [%]	°2θ	d [Å]	I [%]	°2θ	d [Å]	I [%]	<i>h k l</i>
						40.2	2.241	2	4 1 -5 1
						40.5	2.226	1	2 4 -6 0
						41.6	2.167	1	-3 2 1 2
42.3	2.136	4	42.2	2.137	5	42.3	2.137	6	3 3 -6 1
						44.6	2.028	23	3 4 -7 0
						45.3	1.998	2	5 2 -7 0
						46.3	1.961	2	-4 2 2 2
						48.1	1.891	1	5 1 -6 1
						48.3	1.884	2	3 2 -5 2
49.5	1.840	2	49.4	1.843	3	49.5	1.840	3	-1 1 0 3
						49.9	1.826	3	6 0 -6 0
						50.0	1.822	2	4 4 -8 0
						50.3	1.814	2	0 1 -1 3
50.7	1.798	7	50.7	1.800	9	50.6	1.804	12	-5 3 2 1
						51.4	1.6587	25	5 3 -8 1
						52.0	1.6244	27	0 6 -6 0
						52.5	1.5661	2	3 4 -7 2
						53.3	1.5577	9	2 6 -8 0
55.3	1.659	18	55.3	1.660	21	55.3	1.659	25	5 3 -8 1
56.7	1.623	26	56.6	1.624	30	56.6	1.624	27	0 6 -6 0
						58.9	1.566	2	3 4 -7 2
59.4	1.555	6	59.3	1.556	8	59.3	1.558	9	2 6 -8 0

A comparison of SEM micrographs of evaporation dried sample *NZ01c0* and spray dried sample *NZ02c0* showed significant differences in the morphology of the particles produced from both synthesis routes (Figure 6.7). While the particles from the evaporation drying route appeared to be

loosely bound aggregates of nanoparticles with no specific shape, the particles from the spray drying route, contained largely rounded particles (0.5 μm to 20 μm) with nanoparticle substructure.

The primary particles that made up the aggregates in the evaporation dried sample were also irregularly shaped with sizes ranging from 50 - 300 nm, while the nanoparticles that made up the substructure of the rounded particles found in the spray dried sample appeared to be anisotropic in size having widths < 100 nm and lengths of between 100 – 300 nm.

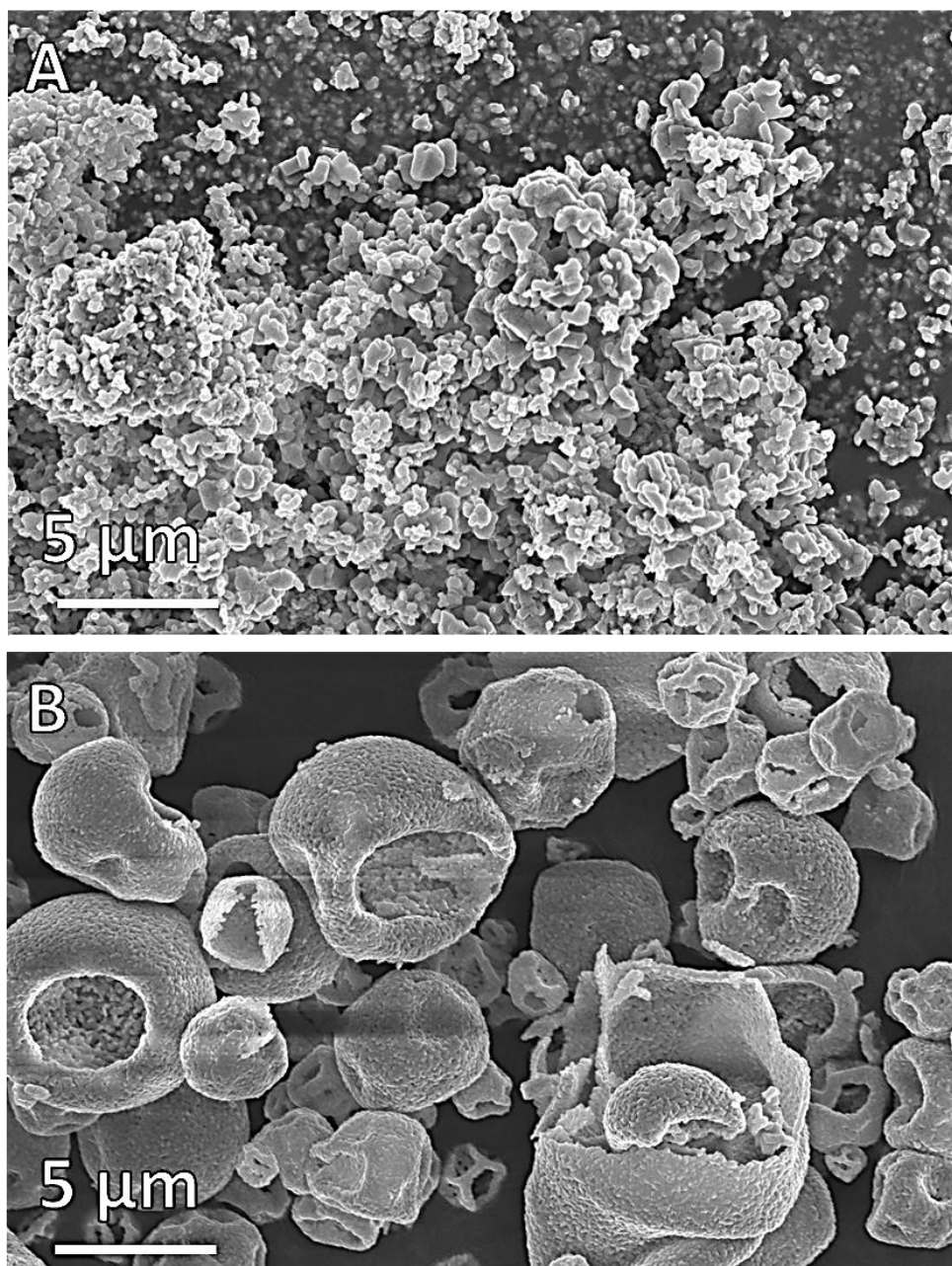


Figure 6.7: Comparison of evaporation dried sample *NZ01c0* and spray dried sample *NZ02c0* showing differences in particle morphology.

The effect of synthesis route on particle morphology can be seen in Figure 6.7. The rounded shape of particles in the spray dried powder (Figure 6.7b) can be traced to the spray drying process. During spray drying, the atomisation process mixes the reagent solutions and produces an aerosol in the form of droplets. As the aerosol droplets dry out, solvent evaporation commences from the exterior surface of the droplets, creating a situation where solution becomes trapped in the core of the aerosol droplets. As the drying process progresses, the solvent in the core of the droplets becomes vaporised and diffuses out of the solid enclosure. The rate at which this vaporisation and gas escape occurs determines the shape and structure of the final particle. If the vapour escapes gradually or gently, deflated particles are formed due to the shell of the particles partially collapsing inwards on exit of vapour. In the event of rapid exit of gases, the force of escape could rupture the droplet resulting in the emergence of ruptured particles (Gretzinger and Marshall, 1961; Nimmo et al., 2005).

Figure 6.8 is a schematic illustrating the formation of ruptured and deflated hollow rounded particles from the spray drying route.

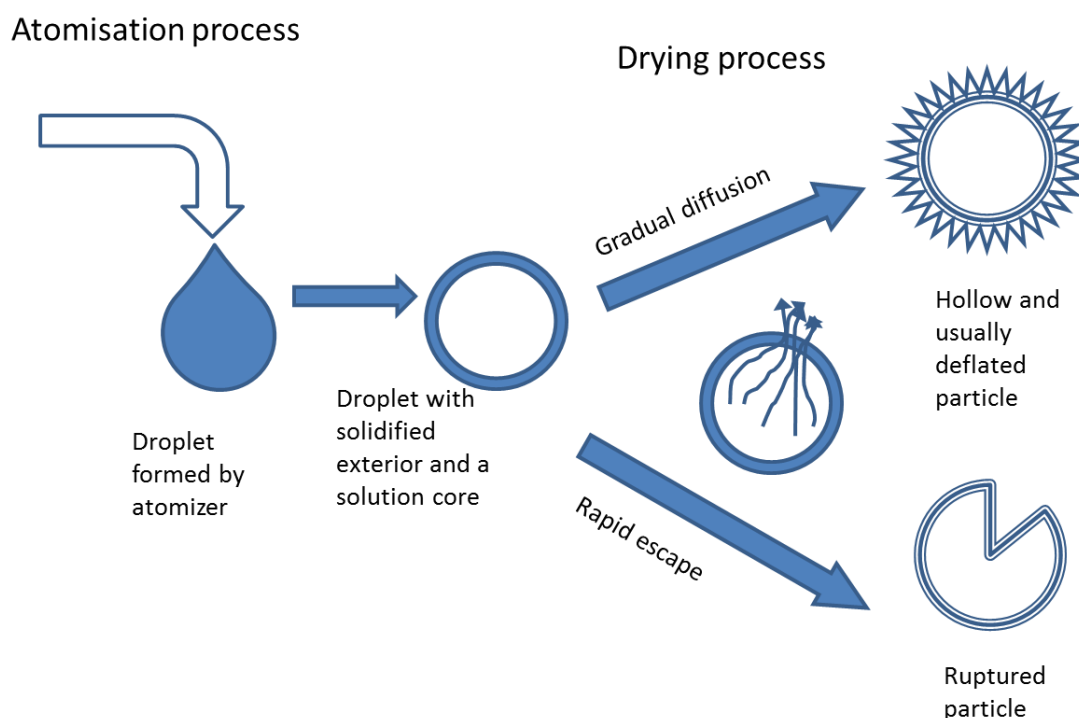
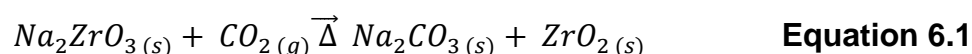


Figure 6.8: Schematic illustration of the formation of ruptured and hollow sodium zirconate precursor particles during spray drying process.

6.2.4 One Hour (1 h) Carbonation Products

In a bid to investigate the CO₂ capture properties of the powders from both synthesis routes, the freshly calcined samples were exposed to a CO₂ rich atmosphere (22% CO₂ – 78% N₂) at a temperature of 700 °C, for a duration of 1 h inside the Perkin Elmer STA 8000.

During carbonation, the sodium zirconate, absorbs and chemically binds with (i.e. captures) the CO₂ in the atmosphere leading to the formation of sodium carbonate and zirconium oxide as shown in the Equation 6.1



Evaporation Dried Sample NZ01c1

XRD analysis of the post-carbonation products revealed that evaporation dried sample *NZ01c1* had a multiphase content comprising of sodium carbonate, monoclinic and tetragonal zirconium oxide (Figure 6.7). Phase identification was achieved by comparing the experimental pattern with ICDD reference patterns 01-083-0944, 04-013-4748 and 01-071-1833 for sodium carbonate, monoclinic and tetragonal phases of zirconium oxide respectively.

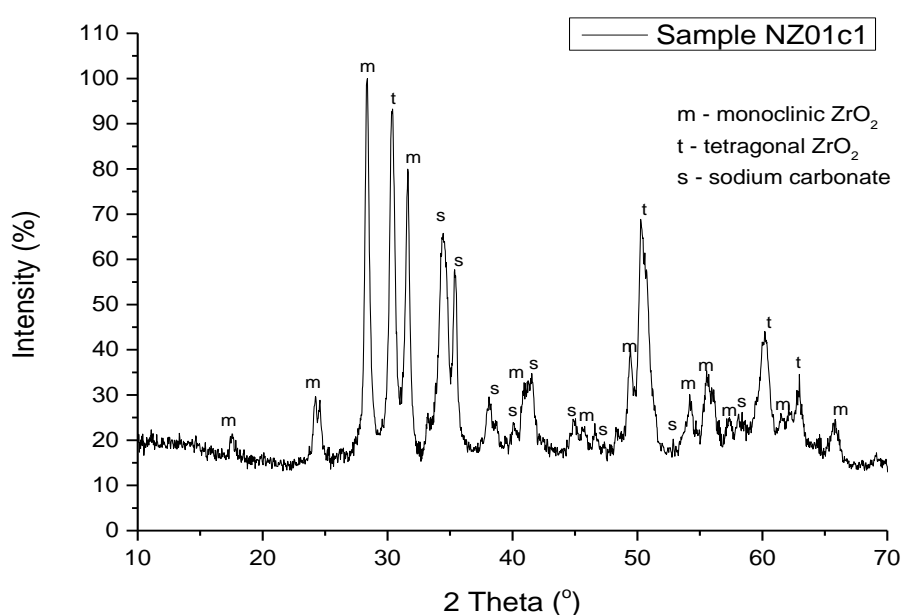


Figure 6.9: XRD pattern of evaporation dried (ED) sample *NZ01c1* after 1 h of carbonation at 700 °C in 22% CO₂.

SEM of sample *NZ01c1*, revealed the presence of large aggregates (10 – 500 μm) consisting of irregular shaped primary particles (50 - 300 nm) coated with or embedded in a smooth 'glass-like' material (Figure 6.10).

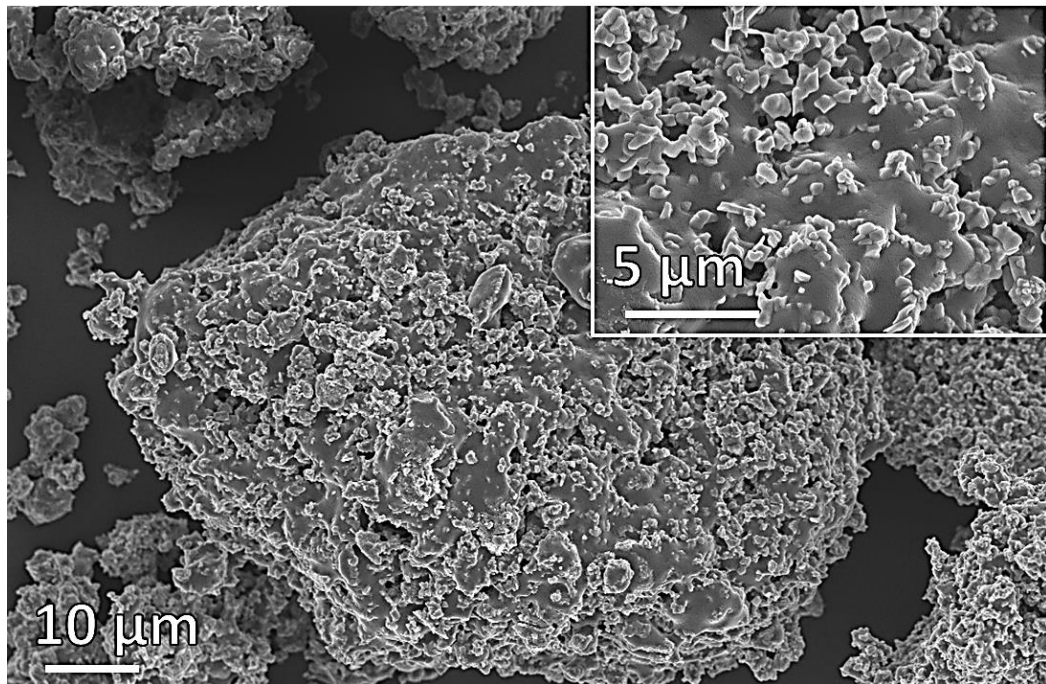


Figure 6.10: SEM of sample *NZ01c1* after carbonation for 1 h.

SEM-EDX analysis revealed that portions of the aggregates containing glass-like material gave off a sodium signal, while the nanocrystalline particles produced a zirconium rich signal (Figure 6.11). Combining information from XRD and SEM-EDX, it can be inferred, that the primary particles were zirconium oxide and the glass like material sodium carbonate.

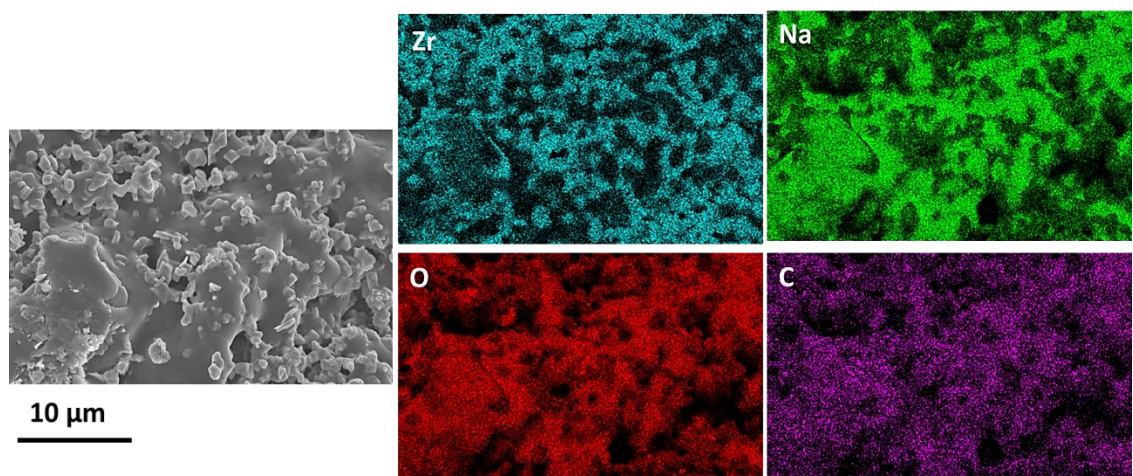


Figure 6.11: SEM-EDX of sample *NZ01c1* after 1 h carbonation.

Spray Dried Sample NZ02c1

XRD analysis of spray dried powder (sample *NZ02c1*) also revealed the sample had a multiphase composition consisting of sodium carbonate, monoclinic and tetragonal zirconium oxide (Figure 6.12). Phase identification was achieved by comparing the experimental pattern with ICDD reference patterns 01-083-0944, 04-013-4748 and 01-071-1833 for sodium carbonate, monoclinic and tetragonal phases of zirconium oxide respectively.

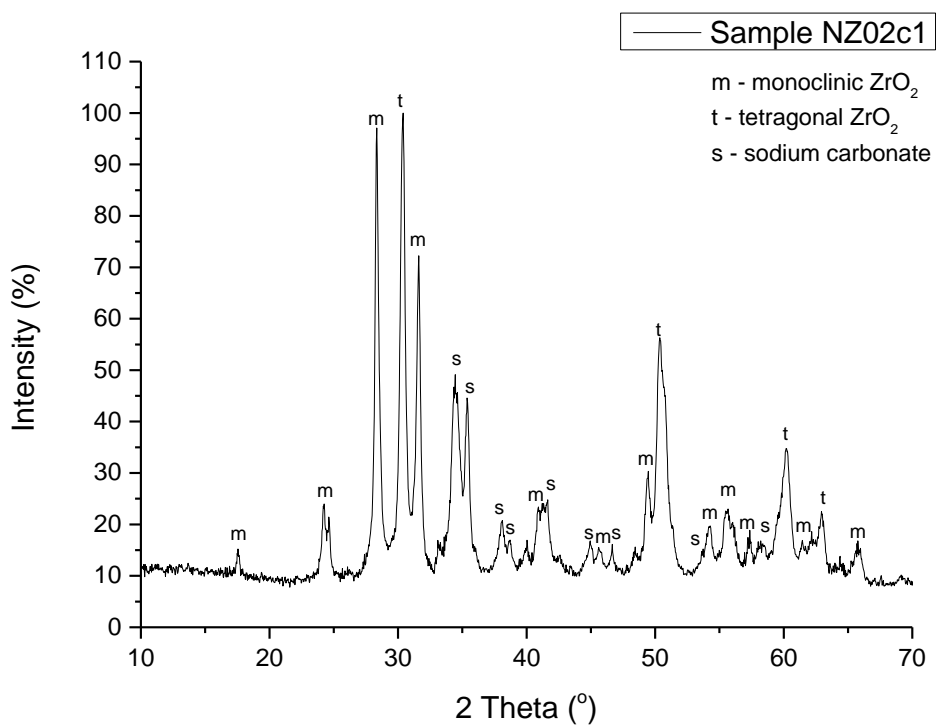


Figure 6.12: XRD pattern of spray dried (SD) sample *NZ02c1* after 1 h of carbonation at 700 °C in 22% CO₂.

Scanning electron microscopy revealed that the spray dried sample after 1 h of carbonation contained rounded particles which had a substructure comprising of irregular shaped multifaceted particles with anisotropic sizes (widths ranging between 20 – 100 nm and lengths between 100 – 500 nm). The multifaceted particles were in coexistence with smooth ‘glass-like’ (*for lack of a better description*) material that was randomly located all over the rounded particle, which could indicate the occurrence of phase separation among the carbonation products (Figure 6.13). SEM-EDX analysis yielded similar results to those obtained with respect to the evaporation dried

sample. Areas with nanoparticles produced a zirconium rich signal, while areas with the “glassy” material yielding a sodium rich signal suggesting that the chemical composition of the nanoparticles was zirconium oxide, while that of the “glassy” material was sodium carbonate which has m.p. of 851 °C.

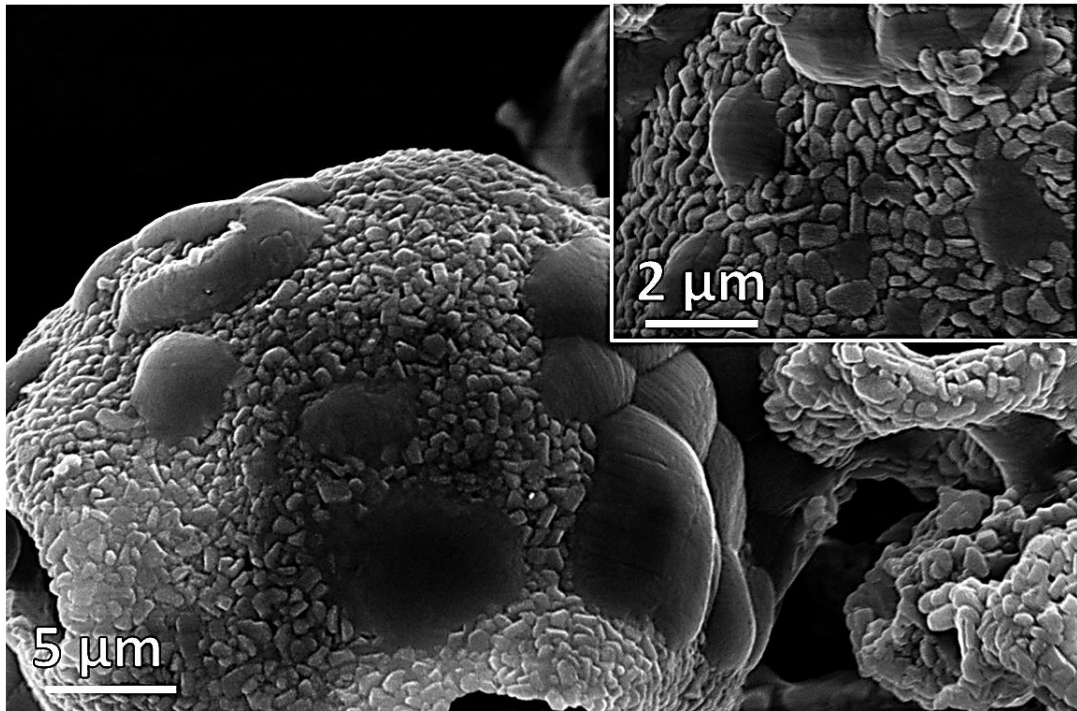


Figure 6.13: SEM of sample *NZ02c1* showing rounded agglomerate particles with substructure of nanoparticles and smooth glassy material.

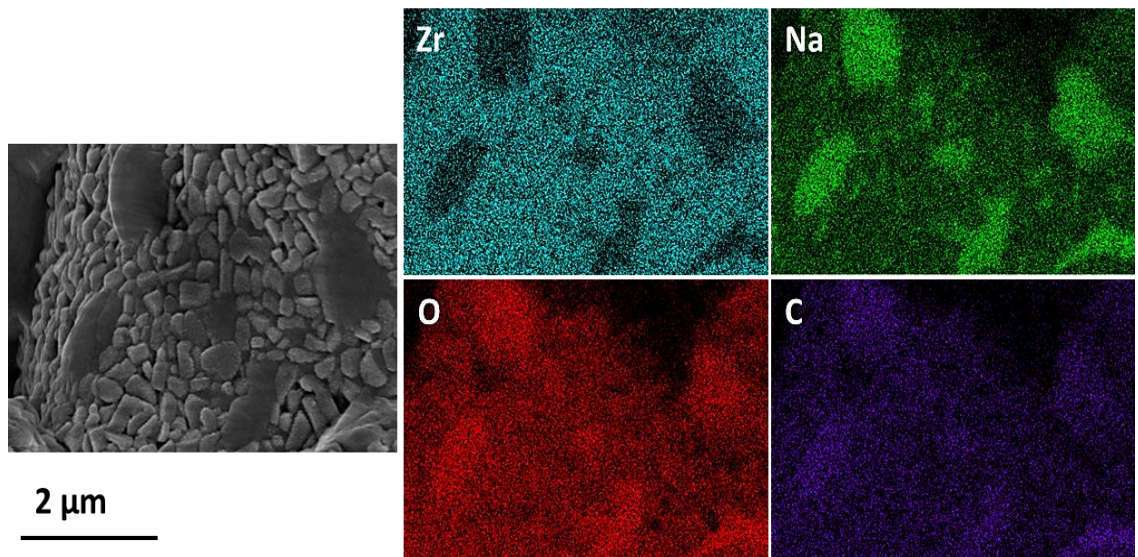
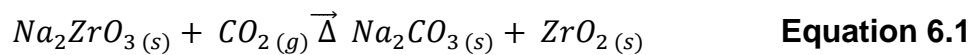


Figure 6.14: SEM-EDX of sample *NZ02c1* after 1 h carbonation showing distribution of sodium carbonate and zirconia in the sample.

6.2.5 Ten (10) Carbonation – Decarbonation Cycle Products

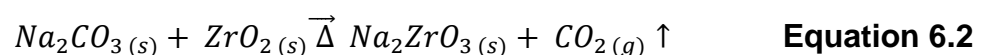
One of the major challenges faced in the development of commercially suitable sorbents for carbon capture is the progressive loss of CO₂ capture capacity with successive carbon-decarbonation cycles. For any sorbent to be deemed suitable for industrial scale CO₂ capture, it must be capable of retaining its CO₂ capture capacity to an acceptable level over continuous usage. As such, there is the need to examine how the characteristics of the sorbent material (phase content and particle morphology) change over the course of multiple carbon-decarbonation cycles.

10 complete carbonation-decarbonation cycles were conducted on the Perkin Elmer STA 8000 to achieve this. A single carbonation-decarbonation cycle starts with the exposure of freshly generated or regenerated sorbent (sodium zirconate) to a CO₂ rich atmosphere (in this case 22% CO₂ – 78% N₂) at 700 °C for 5 min which causes the sodium zirconate sorbent to absorb and react with the CO₂ present as described by Equation 6.1, this process is referred to as carbonation.



At the end of carbonation, the CO₂ captured can be extracted and the sodium zirconate sorbent regenerated by heating the products of the carbonation reaction (Equation 6.1). The use of nitrogen as purge gas during the decarbonation stage combined with temperature increase, ensures that the decomposition reaction of sodium zirconate is thermodynamically preferred to the combination reaction of sodium carbonate and zirconium oxide resulting in the regeneration of the sodium zirconate sorbent as shown by Equation 6.2 this second process is referred to as decarbonation (or calcination).

Equations 6.1 and 6.2 combined, depict a single complete TGA cycle.



Evaporation Dried Sample *NZ01c10*

Results of XRD analysis of sample *NZ01c10* showed that the sample contained multiple phases identified as Na_2ZrO_3 , Na_2CO_3 , and *m*- ZrO_2 according to ICDD reference pattern numbers 00-035-0770 01-083-0944, and 04-013-4748 respectively as shown in Figure 6.15.

Table 6.3 provides details of the phase identification process.

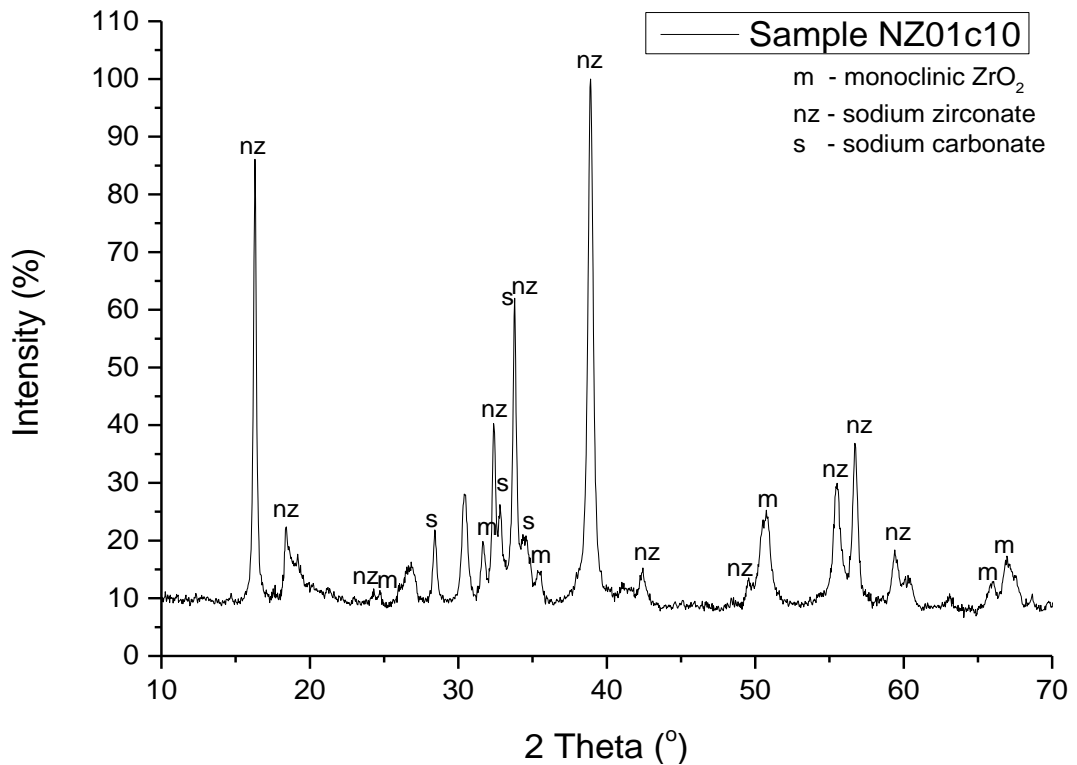


Figure 6.15: Results XRD analysis of evaporation dried (sample *NZ01c10*) after 10 TGA cycles (terminating the process on a carbonation stage).

SEM of the evaporation dried sample *NZ01c10* showed that in comparison to the freshly calcined (Figure 6.4), and 1 h carbonation products (Figure 6.10), there appeared to be a reduction in the size of the agglomerates. Average agglomerate sizes were $\sim 3 \mu\text{m}$, down from $\sim 10 \mu\text{m}$ in the freshly calcined powder (sample *NZ01c0*). However, the sizes of the primary particles remained relatively unchanged ($50 - 300 \text{ nm}$) as shown in Figure 6.16.

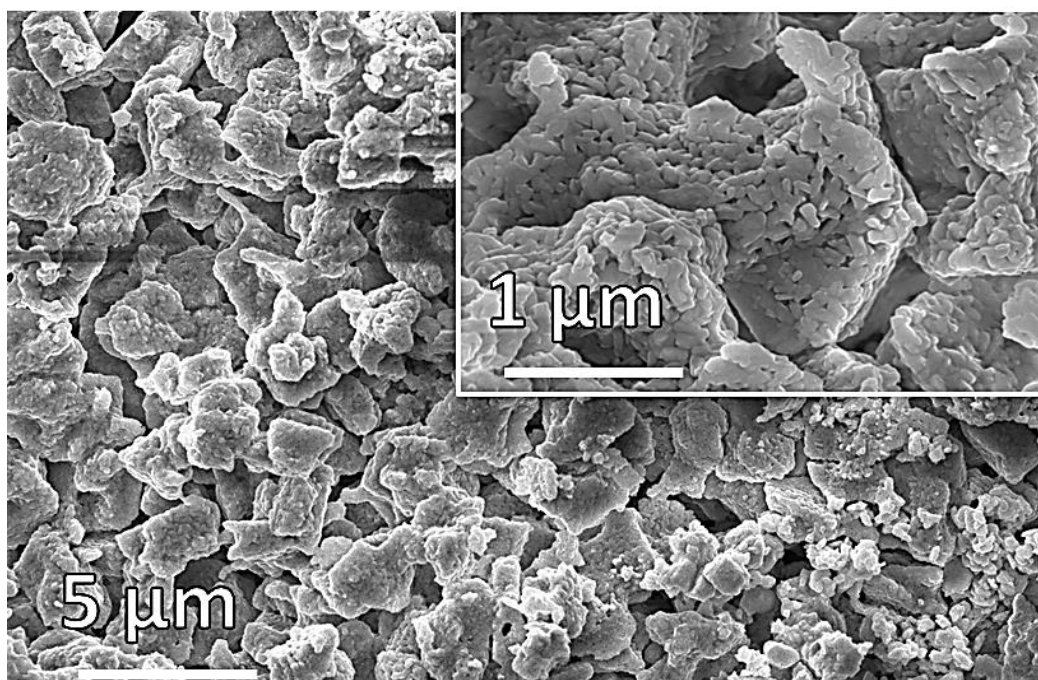


Figure 6.16: SEM of sample *NZ01c10* after 10 TGA cycles.

Spray Dried Sample *NZ02C10*

Results of X-ray analysis of sample *NZ02c10* obtained after subjecting freshly calcined spray dried sorbent to 10 TGA cycles showed the presence of multiple phases which were identified as Na_2ZrO_3 , Na_2CO_3 , and $m\text{-ZrO}_2$.

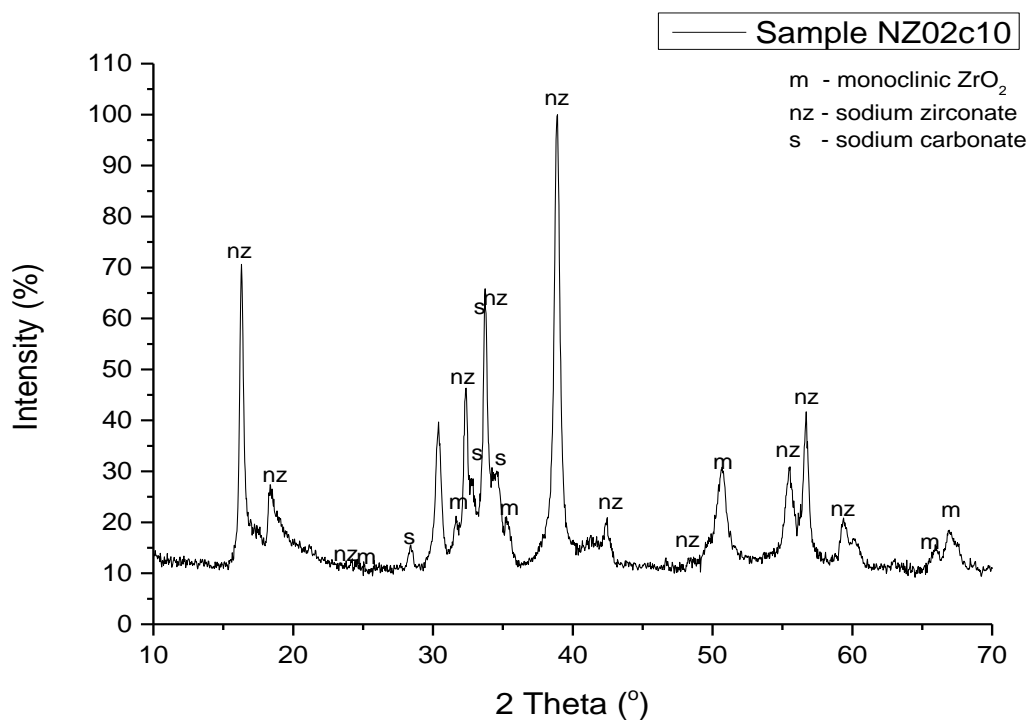


Figure 6.17: XRD of spray dried sample *NZ02c10* after 10 TGA cycles.

SEM of spray dried sample *NZ02c10* showed that the rounded agglomerate particles still retained their shapes with no significant changes in average sizes. However, changes were observed in the substructure of these agglomerates relative to freshly calcined sample *NZ02c0* (Figure 6.6) and 1 h carbonation products (Figure 6.13). The presence of some smooth “glassy” materials first seen in sample *NZ02c1* (Figure 6.13) was observed. Although in contrast to observations in Figure 6.13, the random ‘islands’ of smooth “glassy” material (which SEM-EDX showed to be sodium carbonate) were not visible on the particles of this sample. Rather, the primary nanoparticles (shown by SEM-EDX to be largely zirconium oxide) seemed to be mixed with the smooth “glassy” material, with the smooth sodium carbonate forming a sort of matrix filler within the rounded agglomerate particles.

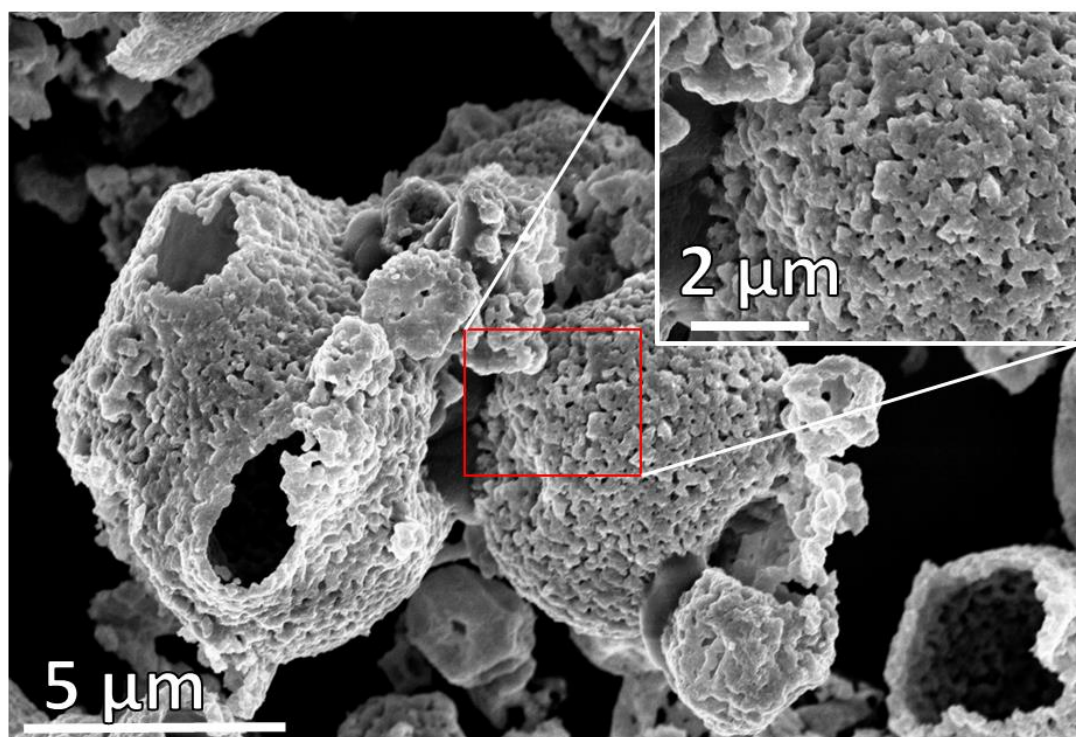


Figure 6.18: SEM of sample *NZ02c10* after carbonation for 10 TGA cycles showing a reduction in average sizes of the agglomerates relative to freshly calcined sample *NZ02c0*.

Table 6.3: identification of Phases in samples NZ01c10 and NZ02c10 using ICDD reference patterns for Sodium zirconate (00-035-0770), monoclinic zirconium oxide (01-083-0944), for 04-012-2300 for wulfingite.

Evaporation Dried NZ01c10			Spray Dried NZ02c10			ICDD ref. for Na ₂ ZrO ₃ 00-035-0770			ICDD ref. for m-ZrO ₂ 01-083-0944			ICDD ref. for Na ₂ CO ₃ 01-071-1833		
°2θ	d [Å]	I [%]	°2θ	d [Å]	I [%]	°2θ	d [Å]	I [%]	°2θ	d [Å]	I [%]	°2θ	d [Å]	I [%]
16.30	5.435	83	16.29	5.437	67	16.16	5.479	37						
18.35	4.832	13	18.32	4.840	15	18.19	4.873	7						
24.53	3.627	1				24.42	3.642	2	24.49	3.632	11			
26.94	3.307	5												
28.40	3.140	14	28.45	3.135	4							28.46	3.134	100
30.40	2.938	18	30.34	2.943	29	30.56	2.923	1						
31.64	2.826	10							31.50	2.838	69			
32.36	2.764	33	32.35	2.766	39	32.26	2.773	23						
32.78	2.729	15										32.86	2.723	16
			33.67	2.660	62	33.64	2.662	40						
33.78	2.651	59										33.79	2.651	55

Evaporation Dried NZ01C10			Spray Dried NZ02C10			ICDD ref. for Na ₂ ZrO ₃ 00-035-0770			ICDD ref. for m-ZrO ₂ 01-083-0944			ICDD ref. for Na ₂ CO ₃ 01-071-1833		
°2θ	d [Å]	I [%]	°2θ	d [Å]	I [%]	°2θ	d [Å]	I [%]	°2θ	d [Å]	I [%]	°2θ	d [Å]	I [%]
34.57	2.593	10	34.57	2.592	19							34.58	2.592	86
35.46	2.529	4							35.34	2.538	15			
38.89	2.314	100	38.87	2.315	100	38.74	2.323	100						
42.34	2.133	5	42.36	2.132	9	42.26	2.137	6						
49.50	1.840	5				49.50	1.840	3	49.33	1.846	18			
50.82	1.795	16	50.72	1.799	20				50.64	1.801	12			
55.58	1.652	19	55.44	1.656	18				55.42	1.657	10			
56.72	1.622	32	56.67	1.623	33	56.62	1.624	27	55.42	1.657	10			
59.40	1.555	11	59.20	1.560	8	59.28	1.558	9	56.02	1.640	7			
60.29	1.534	4							60.11	1.538	7			
63.03	1.474	2												
			65.86	1.417	5				65.77	1.419	6			
65.99	1.414	4							66.04	1.414	1			
66.83	1.399	9	66.83	1.399	9									
70.77	1.330	11	70.65	1.332	7									

6.2.6 Thirty (30) Carbonation – Decarbonation Cycle Products

In continuation of investigations into the effect of multiple carbonation – decarbonation cycles on phase content, particle morphology and CO₂ capture abilities of the sodium zirconate sorbent powders, the number of TGA cycles was increased to 30 using the same conditions as in previous experiments (i.e. carbonation at 700 °C for 5 min in 22 % CO₂ – 78 % N₂, followed by calcination at 900 °C in pure N₂) ending on a carbonation leg.

Evaporation Dried Sample NZ01c30

The resulting diffraction pattern from X-ray diffraction analysis of sample NZ01c30 indicated that the sample contained phases Identified as Na₂ZrO₃, Na₂CO₃, m-ZrO₂ and t-ZrO₂ according to ICDD reference files ICDD reference pattern numbers 00-035-0770 01-083-0944, 04-013-4748 and 01-071-1833 respectively.

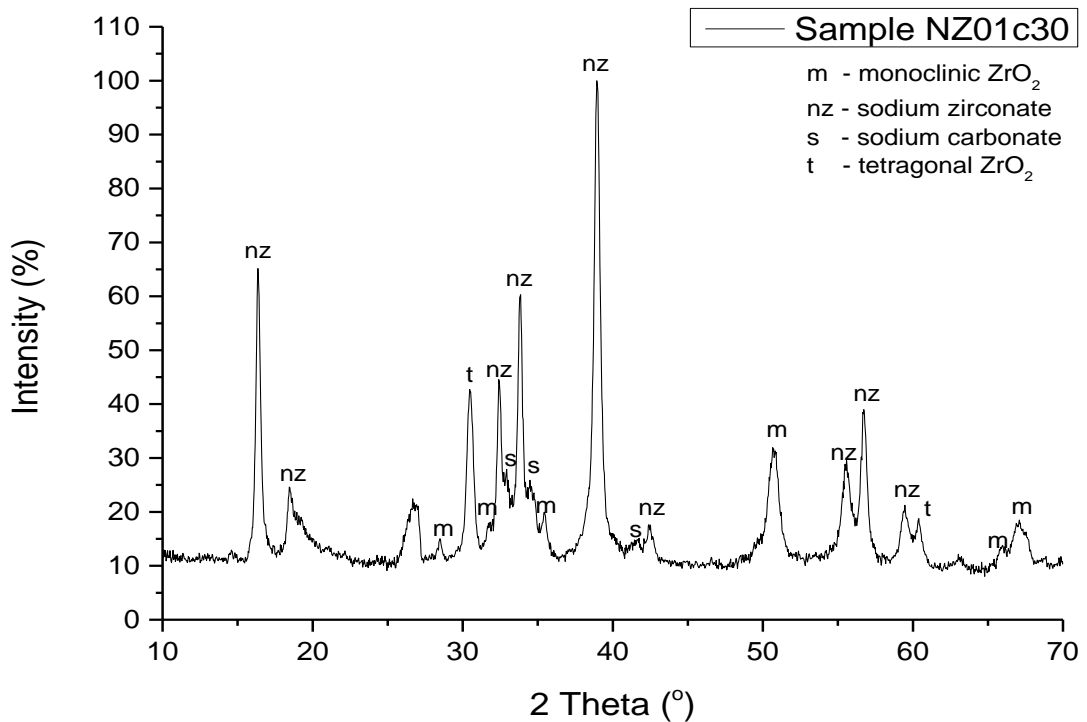


Figure 6.19: XRD pattern of sample NZ01c30.

SEM of evaporation dried sample NZ01c30 showed the presence of relatively smaller irregular shaped agglomerates with sizes varying between 1µm – 10 µm. The agglomerates consisted of smaller nanoparticles randomly meshed together and embedded in nongranular material, creating

a 'coral reef' sight when the sample on the SEM stub was viewed at low magnifications (Figure 6.20).

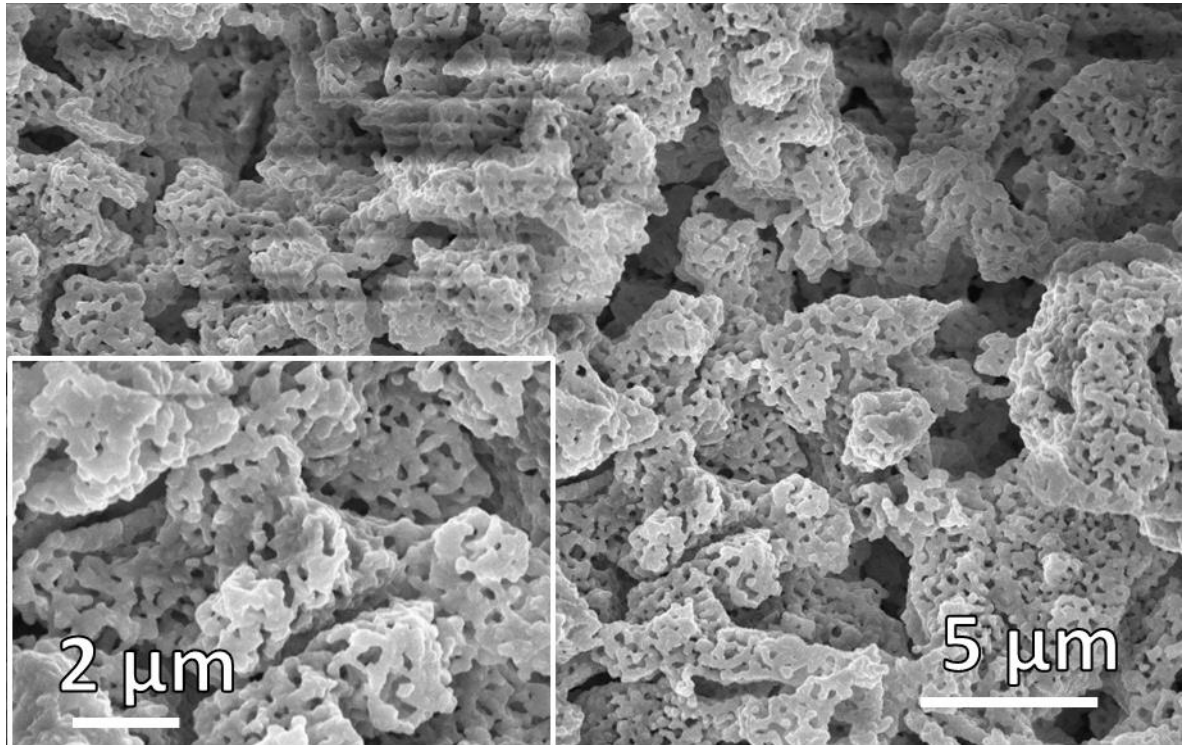


Figure 6.20: SEM of sample *NZ01c30* showing increase in nanoparticle size and porosity of agglomerates.

Spray Dried Sample *NZ02c30*

Similar to observations made with regards to evaporation dried sample *NZ01c30*, X-ray diffraction analysis of spray dried sample *NZ02c30* indicated that the sample contained phases identified as Na_2ZrO_3 , Na_2CO_3 , m- ZrO_2 and t- ZrO_2 according to ICDD reference files ICDD reference pattern numbers 00-035-0770 01-083-0944, 04-013-4748 and 01-071-1833 respectively (Figure 6.21).

SEM micrographs of sample *NZ02c30* showed the presence of largely rounded particle agglomerates, which had approximately a layer thick substructure consisting of intertwined nanoparticles. The nanoparticles appeared to be coated by non-granular material (Figure 6.22).

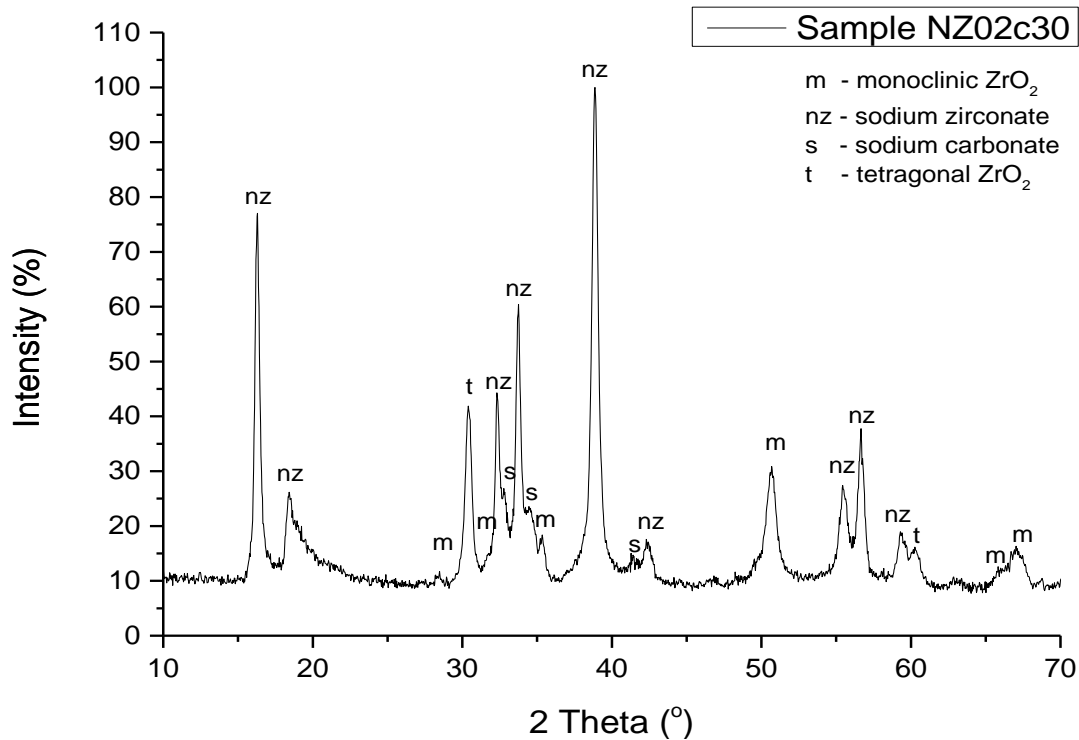


Figure 6.21: XRD pattern of sample *NZ02c30* with peaks from phases identified as sodium zirconate, sodium carbonate, monoclinic and tetragonal zirconia labelled respectively.

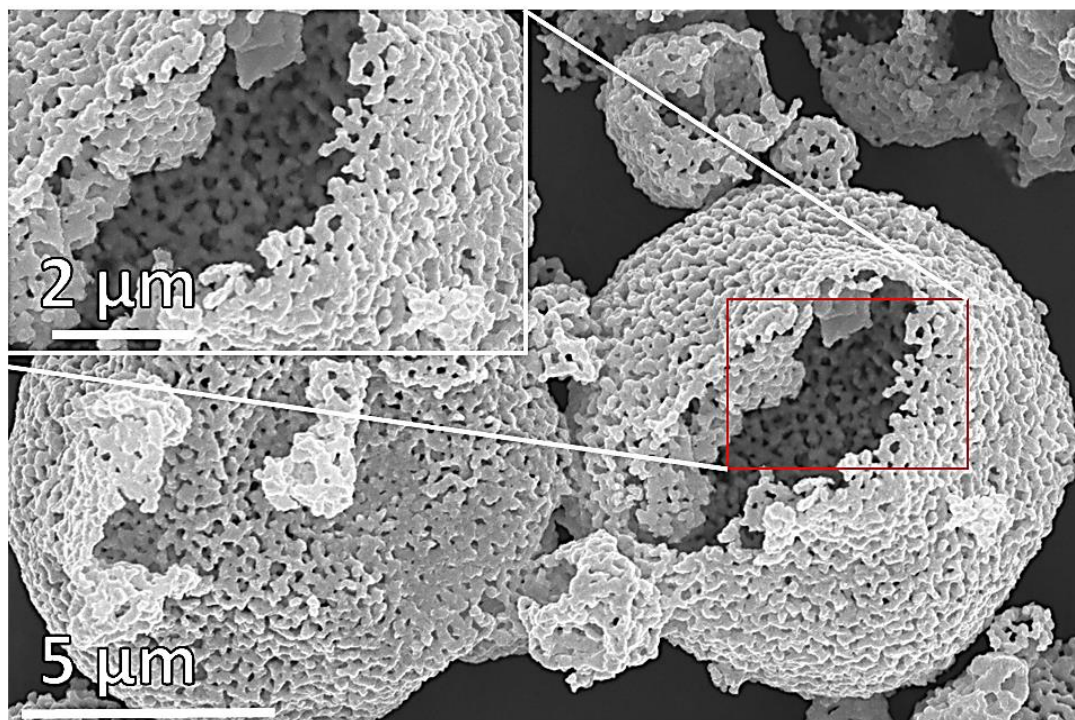


Figure 6.22: SEM of spray dried sample *NZ02c30*.

6.2.7 Comparative Analysis of Changes in Phase Content and Particle Morphology

Evaporation Dried Samples

A comparison of X-ray diffraction patterns of evaporation dried samples *NZ01*, *NZ01c0*, *NZ01c1*, *NZ01c10* and *NZ01c30* (Figure 6.23) showed evidence of changes in phase content of the sorbent powders after calcination (*NZ01c0*), carbonation (*NZ01c1*) and multiple carbonation – decarbonation cycles (*NZ01c10* and *NZ01c30*) respectively. All the samples examined, had a multiphase composition comprising of mixture of Na_2ZrO_3 , Na_2CO_3 , *m*- ZrO_2 and in some cases *t*- ZrO_2 in varying proportions. ICDD reference pattern numbers 00-035-0770 01-083-0944, 04-013-4748, and 01-071-1833 respectively were used to identify these phases. Figure 6.23 and Table 6.4 highlights differences in phase composition and percentage prevalence of the different phases (calculated from X-ray diffraction data).

Key: *m* - monoclinic ZrO_2 | *t* - tetragonal ZrO_2 | *nz* - sodium zirconate | *s* - sodium carbonate

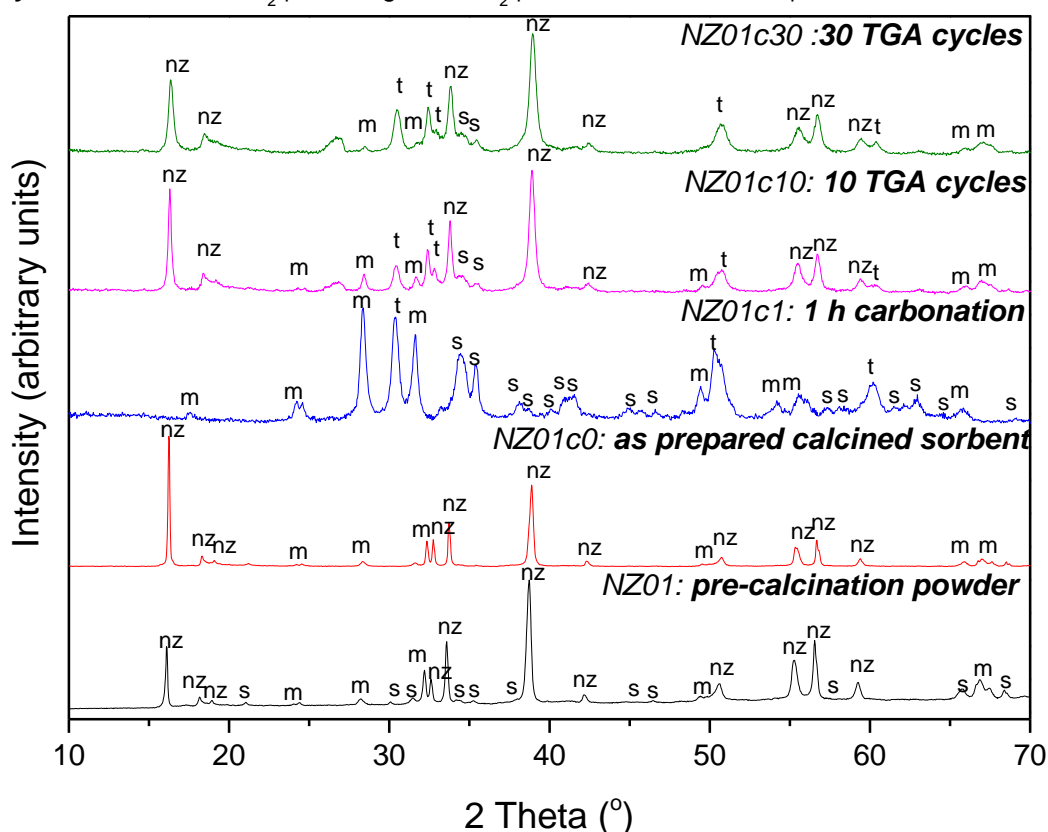


Figure 6.23: Comparison of XRD patterns of evaporation dried samples showing changes in phase content.

Table 6.4: Composition of phase content of evaporation dried samples as obtained from XRD analysis.

Sample	Conditions	Composition (wt. %)
NZ01	No calcination or carbonation	$m\text{-ZrO}_2$, Na_2CO_3 , Na_2ZrO_3
NZ01c0	Calcination (900 °C, 2 h)	Na_2ZrO_3 (~ 91 %), $m\text{-ZrO}_2$ (~ 9 %)
NZ01c1	Carbonation (700 °C, 1 h)	Na_2CO_3 (~ 59 %), $m\text{-ZrO}_2$ (~27 %), $t\text{-ZrO}_2$ (~ 14 %)
NZ01c10	10 cycles	Na_2ZrO_3 (~ 73 %), $m\text{-ZrO}_2$ (~ 9 %), $t\text{-ZrO}_2$ (~ 18 %)
NZ01c30	30 cycles	Na_2ZrO_3 (~ 74%), $m\text{-ZrO}_2$ (~ 7 %), $t\text{-ZrO}_2$ (~ 19 %)

Tetragonal zirconium oxide ($t\text{-ZrO}_2$) is a metastable polymorph of zirconium oxide which usually occurs at temperatures between ~ 1150 °C and ~ 2300 °C (Figure 6.24). However, the temperature at which this reversible $m\text{-ZrO}_2$ to $t\text{-ZrO}_2$ phase transition occurs could be influenced by particle size and pressure (Bertin and Roberts, 1999). The presence of nanoscale ZrO_2 particle sizes could lead to the phase transition occurring at relatively lower temperatures (up to room temperature).

The foregoing could be the reason for the observation of the presence of tetragonal phase of zirconium oxide in sample *NZ01c1* and subsequent samples.

However, there appears to be some level of irreversibility in the gradual conversion of $m\text{-ZrO}_2$ to $t\text{-ZrO}_2$, as the percentage content of $t\text{-ZrO}_2$ slightly increased as the number of carbonation-decarbonation cycles increased, which could have contributed to the slight, but progressive decline in CO_2 capture efficiency observed at later stages of the multicycle TGA analysis (Figure 6.28 and Figure 6.31).

	Monoclinic	↔	Tetragonal	↔	Cubic
			1167 °C		2367 °C
Density (gcm ⁻³)	5.83		6.10		6.09

Figure 6.24: Crystal polymorphs and phase transition of pure zirconium oxide (Bertin and Roberts, 1999).

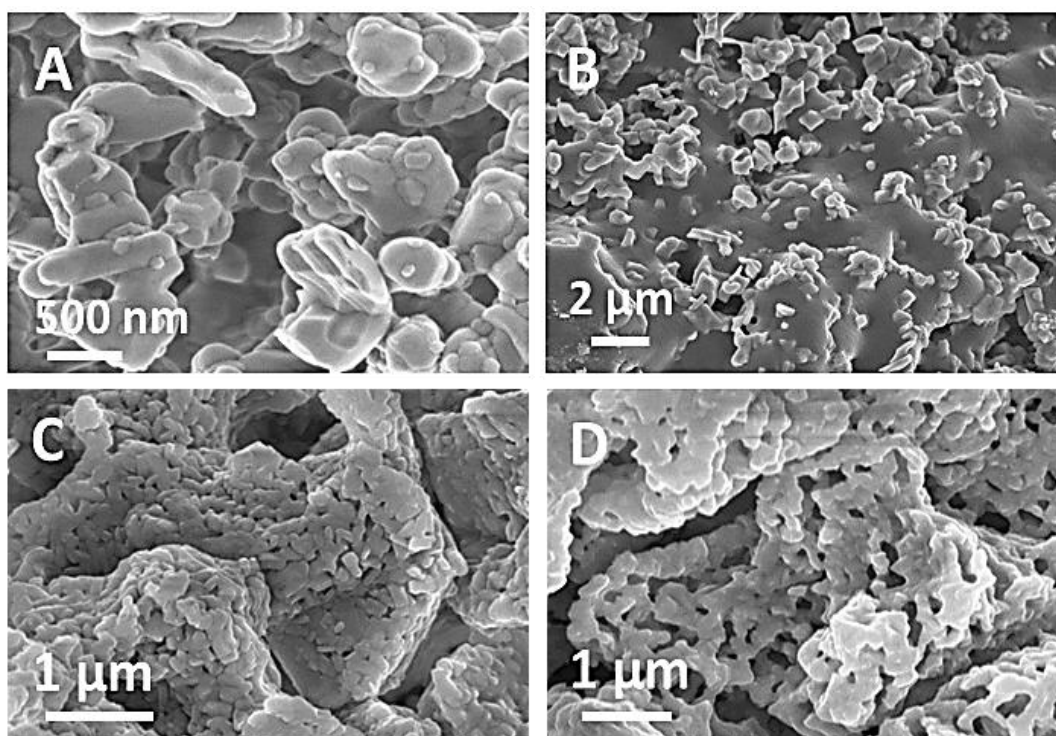


Figure 6.25: SEM of samples showing changes in substructure of sorbent agglomerate particles (a) freshly calcined sample *NZ01c0* (b) 1 h carbonation products sample *NZ01c1* (c) sample *NZ01c10* obtained after 10 TGA cycles, and (d) *NZ01c30* obtained after 30 TGA cycles.

Figure 6.25 highlights the changes observed in the microstructure of the freshly calcined evaporation dried sodium zirconate sorbent samples after carbonation, 10 TGA cycles, and 30 TGA cycles. Figure 6.25a shows the nanoparticulate substructure of the ~ 10 μm loose aggregates observed in the freshly calcined powder while the presence of smooth “glassy” material (identified as sodium carbonate) can be seen coexisting with granular

zirconia particles in Figure 6.25b resulting from the capture and reaction of sodium zirconate with CO₂ gas. As described by Equation 6.1. In Figure 6.25c the substructure of the now ~3 μm agglomerates shows densely packed zirconia particles enmeshed in sodium carbonate; suggesting some level of nanoscale mixing of the zirconia and sodium carbonate after carbonation. Figure 6.25c shows the presence of a similar substructure as observed in sample *NZ01c10*, the 10 cycle products. However, the pores within the particles appear to be relatively larger. This may be as a result of the cyclic combinative action of entry of CO₂ gas and deposition of sodium carbonate during carbonation and decomposition of sodium carbonate and escape of CO₂ gas escape during decarbonation process leaving behind a more defined framework of particles and holes over the course of 30 cycles relative to the 10 cycle products.

Spray Dried Samples

A comparison of X-ray diffraction patterns of spray dried samples *NZ02*, *NZ02c0*, *NZ02c1*, *NZ02c10* and *NZ02c30* (Figure 6.26) also revealed similar observations to those made with respect to the evaporation dried samples. All the samples had a multiphase composition comprising of Na₂ZrO₃, Na₂CO₃, *m*-ZrO₂ and *t*-ZrO₂ according to ICDD reference pattern numbers 00-035-0770 01-083-0944, 04-013-4748, and 01-071-1833 respectively. Comparing data from Tables 6.4 and 6.5, a lower percentage prevalence of monoclinic zirconium oxide (*m*-ZrO₂) and tetragonal zirconium oxide (*t*-ZrO₂) in the spray dried samples can be observed after multicycle TGA runs. This could indicate better interaction between the sodium zirconate sorbent and the CO₂ in the atmosphere which would explain the relatively higher CO₂ uptake observed with respect to the spray dried samples (Figure 6.32). Table 6.5 highlights the phases observed in each sample, and the differences in percentage composition of the phases observed in the spray dried samples.

Key: m - monoclinic ZrO₂ | t - tetragonal ZrO₂ | nz - sodium zirconate | s - sodium carbonate

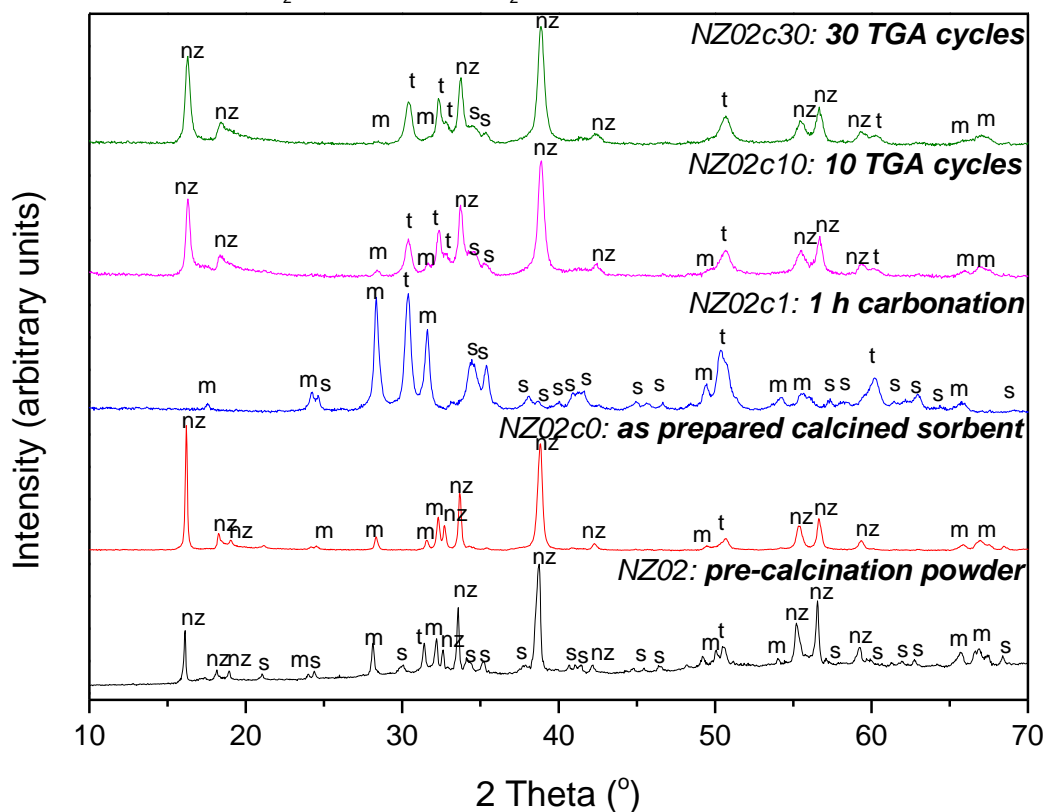


Figure 6.26: Comparison of XRD patterns of spray dried samples showing changes in phase content.

Table 6.5: Composition of spray dried samples from XRD analysis data.

Sample	Conditions	Composition (Wt. %)
NZ02	No calcination or carbonation	m-ZrO ₂ , Na ₂ CO ₃ , Na ₂ ZrO ₃
NZ02c0	Calcination (900 °C, 2 h)	Na ₂ ZrO ₃ (~ 91%), m-ZrO ₂ (~ 9 %)
NZ02c1	Carbonation (700 °C, 1 h)	Na ₂ CO ₃ (~ 53 %), m-ZrO ₂ (~29 %), t-ZrO ₂ (~ 18 %)
NZ02c10	10 cycles	Na ₂ ZrO ₃ (~ 81 %), m-ZrO ₂ (~ 6 %), t-ZrO ₂ (~ 13 %)
NZ02c30	30 cycles	Na ₂ ZrO ₃ (~ 84%), m-ZrO ₂ (~ 2 %), t-ZrO ₂ (~ 15 %)

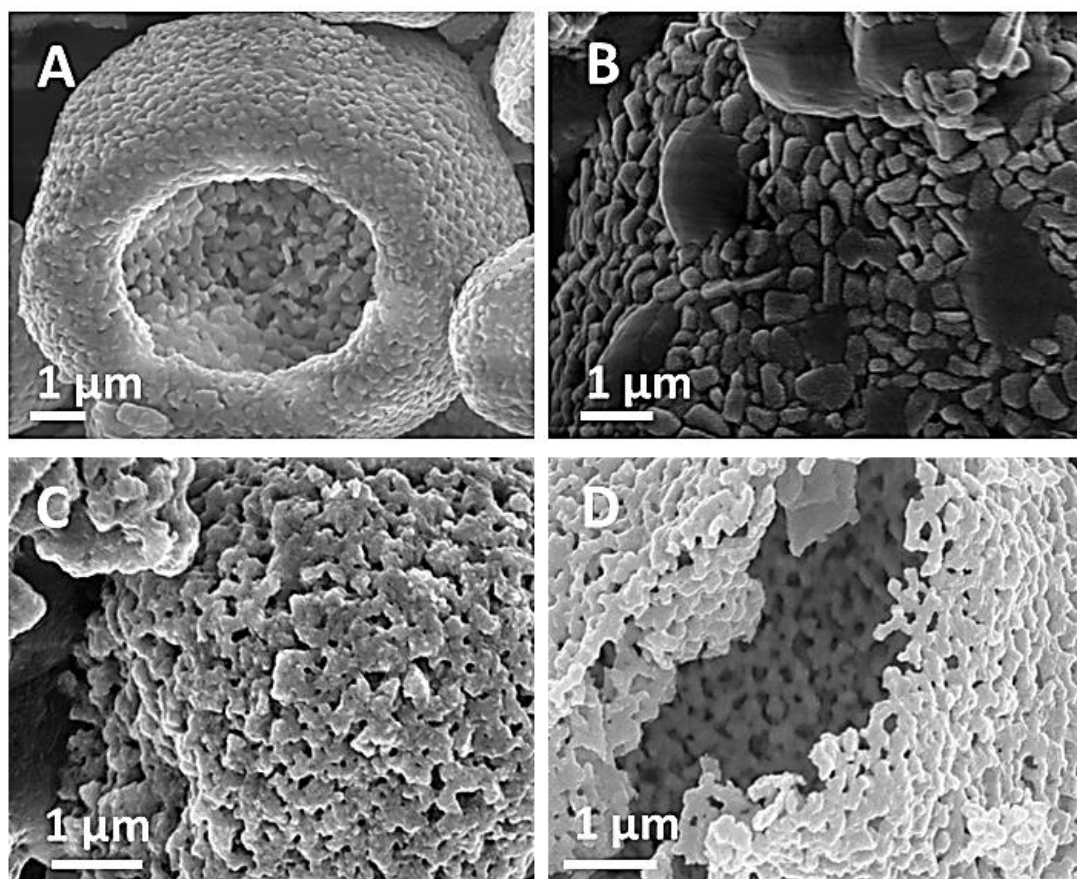


Figure 6.27: SEM of spray dried samples showing changes in substructure of rounded agglomerates (a) freshly calcined sample *NZ02c0* (b) 1 h carbonation products sample *NZ02c1* (c) sample *NZ02c10* obtained after 10 TGA cycles, and (d) *NZ02c30* obtained after 30 TGA cycles.

Figure 6.27 above shows changes in the substructure of spray dried samples. The rounded nature of the agglomerates with sizes ranging between 0.5 μm and 20 μm , results from droplet formation during atomization stage of spray drying (Figure 6.8). The freshly calcined sample (Figure 6.27a) shows the walls of the hollow particles to be about one layer of primary particle thick, and the nanosized primary particles appeared to be densely packed together. After 1 h of carbonation, the emergence of randomly located 'islands' of smooth glassy material can be observed (Figure 6.27b). It was confirmed via SEM-EDX, that this material was sodium carbonate which has a melting point of 851°C. Figure 6.27c shows the substructure of agglomerate particles after undergoing 10 TGA cycles. The zirconia particles appear mixed and matted with sodium carbonate. While the 30 TGA cycle products appear to have larger pores in between nanoparticles relative to the 10 TGA cycle sample.

6.3 Comparison of CO₂ Uptake Performance of Evaporation Dried, Spray Dried and Commercial Sodium Zirconate Powders over Multiple TGA Cycles

As previously mentioned, the commercial viability of any CO₂ sorbent material greatly depends on its durability over prolonged usage, and the amount of CO₂ the sorbent can capture per cycle, usually measured as % conversion or gram CO₂ / gram sorbent. Poor durability implies that there would be the need for frequent sorbent replacement, while low % conversion means that relatively large quantities of sorbent material would be needed to capture sufficient volumes of CO₂ for transportation and storage. Both of the foregoing scenarios are highly undesired in a commercial scenario.

A study of the CO₂ uptake performance of both evaporation and spray dried sodium zirconate sorbents was undertaken and compared with that of commercially sourced sodium zirconate sample MELSORB 2390 (MEL chemicals, Manchester, UK). The three samples (*NZ01c0*, *NZ02c0* and *MELSORB 2390*) were subjected to multiple TGA cycles in the Perkin Elmer STA 8000 for 11 h (660 min) to compare their CO₂ uptake performances.

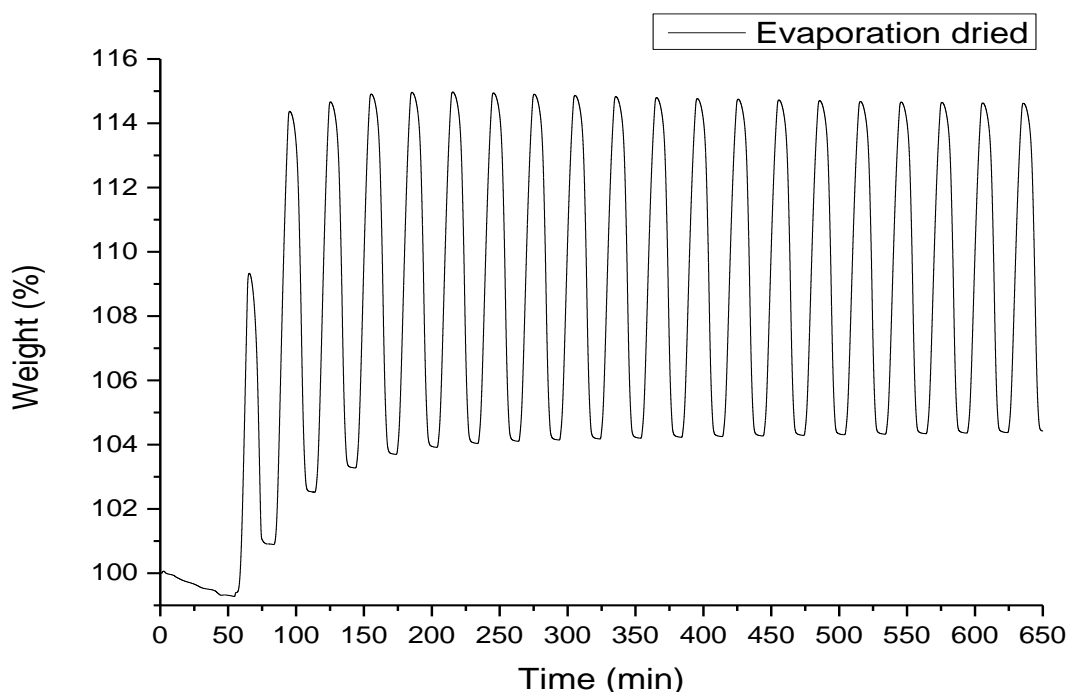


Figure 6.28: Multicycle TGA of evaporation dried sample *NZ01c0* showing percentage weight gains and losses per cycle.

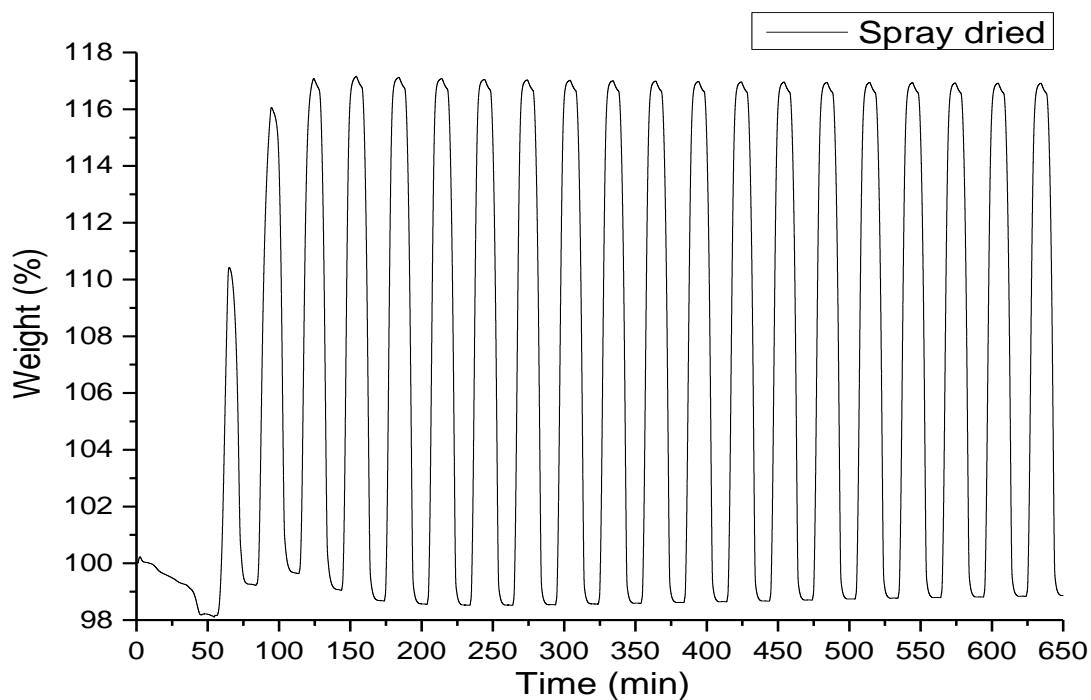


Figure 6.29: Multicycle TGA of sample *NZ02c0* showing percentage weight gains and losses per cycle over 20 cycles.

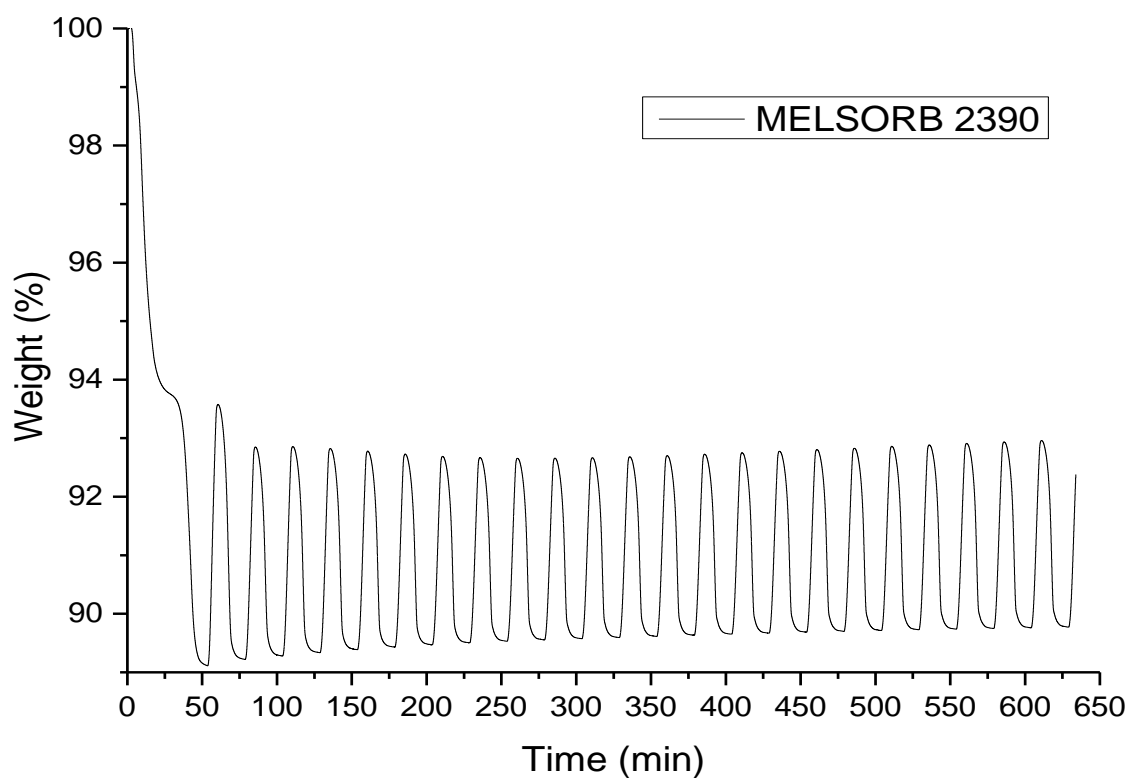


Figure 6.30: Multicycle TGA of sample *MELSORB 2390*, showing percentage weight gains and losses per cycle for 20 cycles.

Multicycle TGA plots in Figures 6.28 and 6.29, show an initially low CO₂ uptake in the first cycle which then increases over the next 2 to 3 cycles before becoming relatively stable over the course of final ~ 15 cycles. The low initial CO₂ uptake might be due to low levels of penetration of CO₂ gas into the powders during the first cycle leading to insufficient contact points between the particle and gas molecules. In subsequent cycles, levels of gas penetration would have reached a steady state value and thus no longer influence the amount of CO₂ the sorbent was able to capture.

Observations recorded with respect to the commercially sourced sample *MELSORB 2390* (Figure 6.30), appeared to follow a different trend from the in-house samples. Multicycle TGA plot of sample *MELSORB 2390* showed an initially high CO₂ uptake in the first cycle (as seen by the higher percentage change in sample weight), but then significantly drops by the next cycle and never recovers throughout the course of the remaining cycles. Also, the relatively high amount of weight loss that occurred over the first 30 minutes of analysis when the sample was being preheated in the TGA to 900 °C in pure N₂ atmosphere suggests that the *MELSORB 2390* sample may have contained some organic content which got burnt off during the course of preheating. Although the synthesis method for the *MELSORB 2390* sample was not known, an organic additive may have been included during powder preparation to inhibit particle aggregation or sintering during storage. The decomposition of this additive during the preheating stage may have been responsible for the observations made with regards to significant weight loss and severely reduced CO₂ capture efficiency.

According to the stoichiometry of the chemical reaction between Na₂ZrO_{3(s)} and CO_{2(g)} (Equation 6.1), 1 mole of Na₂ZrO_{3(s)} should combine with 1 mole of CO_{2(g)} to produce 1 mole each of Na₂CO_{3(s)} and ZrO_{2(s)}. That means the maximum possible uptake of CO₂ gas by Na₂ZrO₃, would be 0.238 g of CO₂ gas for every 1 g of Na₂ZrO₃ sorbent material. Based on the foregoing, the CO₂ capture efficiency of the three samples over the course of 20 TGA cycles was analysed, compared and plotted as percentage conversion CO₂ in Figure 6.31.

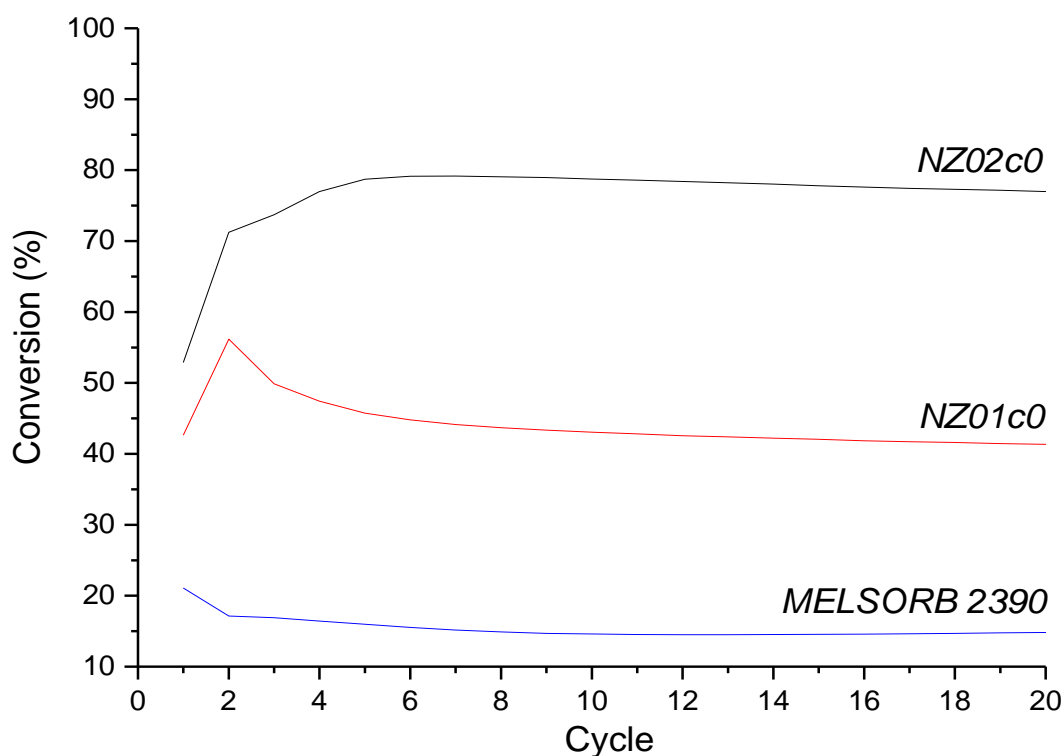


Figure 6.31: Comparison of percentage CO₂ conversion of samples *NZ01c0*, *NZ02c0* and *MELSORB 2390* over 20 TGA cycles.

The significant differences in CO₂ capture performance of the sodium zirconate samples *NZ01c0*, *NZ02c0* and *MELSORB 2390* could be traced to the differences in the microstructure and of each sample.

6.3.1 Investigation of Durability of Evaporation Dried and Spray Dried Sodium Zirconate over 50 TGA cycles

Concentrating only on samples *NZ01c0* and *NZ02c0* due to the relatively poor CO₂ uptake performance of the *MELSORB 2390* sample, the number of TGA cycles was extended to 50 cycles lasting about 26 h of continuous usage in an attempt to study the durability of the sodium zirconate powders under simulated industrial CO₂ capture conditions.

Figure 6.32 shows a multicycle TGA plot of sample *NZ02c50* superimposed on that of *NZ01c50* to highlight the difference in the performance of both samples. While both samples appeared to show a reasonable level of durability in CO₂ uptake over the course of the 50 cycles, the spray dried sample *NZ02c50* had a much improved CO₂ capture performance in comparison to the evaporation dried sample *NZ01c50*.

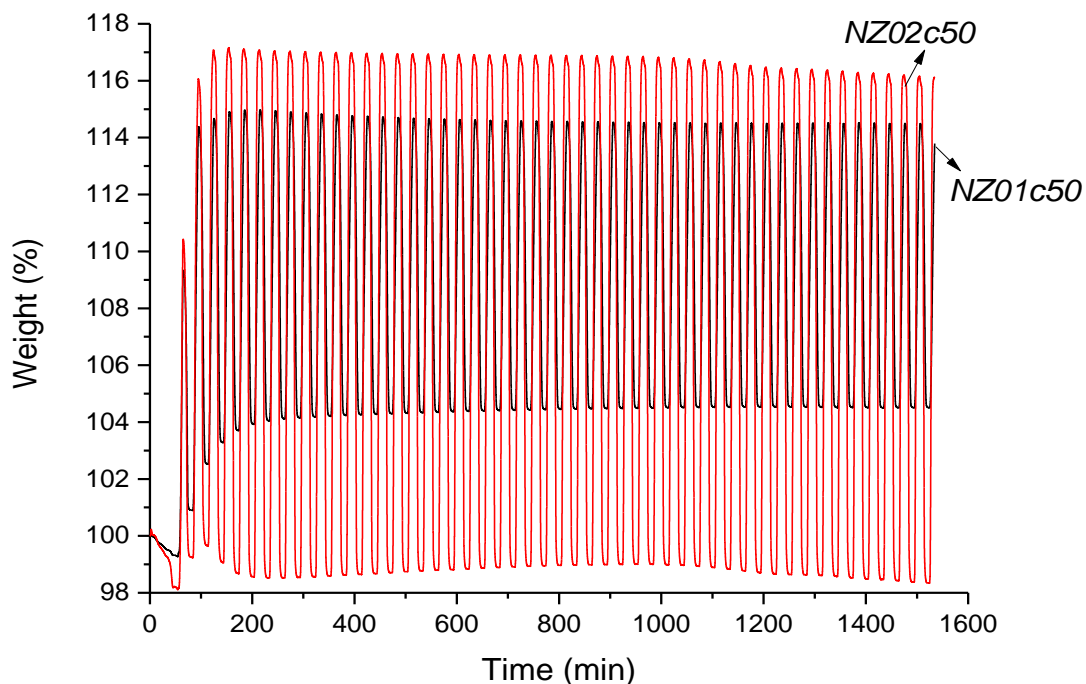


Figure 6.32: Multicycle TGA of evaporation dried sample *NZ02c50* (red) and spray dried *NZ02c50* (black) for 50 cycles.

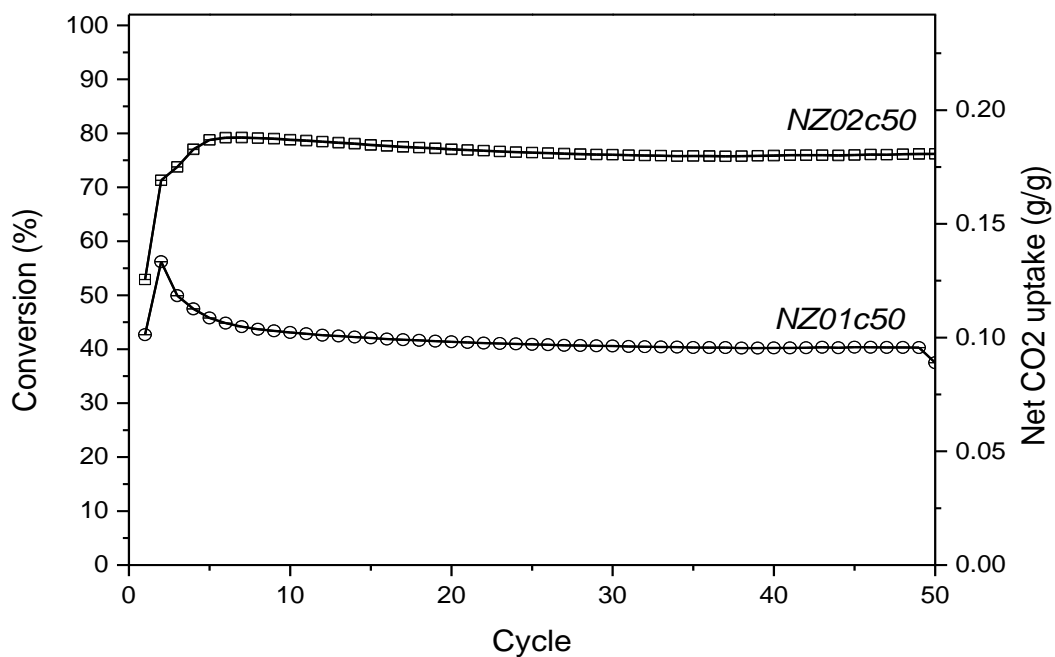


Figure 6.33: CO₂ capture efficiency over 50 TGA cycles.

From Figure 6.33, it can be seen that the CO₂ capture efficiency of the spray dried sample (*NZ02c50*) reached about 80 % of theoretical capacity and maintained roughly the same efficiency through the course of 50 cycles representing over 26 h of continuous usage.

Chapter 7

Conclusions and Recommendations

7.1 Summary of Findings and Conclusions

Details of experimental investigations into the synthesis of zinc oxide double rods and high aspect ratio rods via the hydrothermal route have been presented. Also experimental work focusing on the synthesis of sodium zirconate powders for use in CO₂ capture applications and hydrogen production via sorption-enhanced steam reforming has been included.

X-ray diffraction analysis (XRD), scanning electron microscopy (SEM), and transmission electron microscopy (TEM) were employed as key analytical techniques for sample characterisation, for both the zinc oxide and sodium zirconate particles. In addition, thermogravimetric analysis (TGA) was used extensively in the analysis of sodium zirconate samples.

7.1.1 Zinc Oxide Hexagonal Double Rods

Hexagonal double rods of zinc oxide were synthesised through hydrothermal treatment of a suspension obtained from solutions of zinc acetate dihydrate and sodium hydroxide. Findings from the synthesis and characterisation processes showed that particle growth was hierarchical in nature, with particle shape and size changing as a function of the length of hydrothermal treatment times. Evidence from XRD and SEM revealed the presence of < 20 nm equiaxed zinc oxide nanoparticles surrounded by large polycrystalline zinc oxide material in the precursor suspension prior to hydrothermal treatment (referred to as '0 h' sample), forming the first stage of the hierarchical growth process. Thus indicating that the kinetics of the reaction the two reagents to form zinc oxide was very rapid.

Other stages of the hierarchical growth process as documented by SEM and TEM, involved the aggregation of the equiaxed nanocrystallites into thin

lozenge shaped polycrystalline particles which then recrystallized and stacked up along the c-axis, [0001] direction, in the form of 50 nm nanoplates. A second recrystallization stage was then observed to have occurred which resulted in the stacked ~50 nm thick nanoplates transforming into hexagonal faceted zinc oxide rods with an average length of ~500 nm.

Based on observations from SEM and TEM, the evolutionary process of the hexagonal double rods was thought to proceed from this stage via two parallel pathways. This first pathway involved site-specific deposition of ZnO nanocrystallites on the basal surfaces of the existing single rods followed by a repetition of the previously described three stages leading to the emergence of individual rods. The overall result was that, a rod was grown on another pre-existing rod culminating in the emergence of zinc oxide hexagonal double rods. On the other parallel pathway, particle growth proceeded through end-to-end attachment of single rods that developed independently of one another resulting in two single hexagonal rods becoming a double hexagonal rod.

Although other similar theories have been proposed about the nature of the growth process that yields this relatively unique particle morphology (as discussed in 4.2.10); this is the first time, where it has been possible to provide experimental evidence (XRD, SEM, TEM) documenting the stages that served as milestones in the course of the hierarchical growth of zinc oxide hexagonal double rods.

Further investigations were carried out to study the nature of the interfacial junctions between component sections of the hexagonal double rods through a combination of focused ion beam milling (FIB-SEM) and TEM. It was observed that the growth of these double rod particles may not have been initiated at the interfacial junction as had been previously reported (see 4.3.1). Also, contrary to previous understanding of the growth of these double rods, results from this research, show that growth via secondary nucleation (deposition of nanocrystallites on pre-existing rods) and growth via end-to-end attachment of single rods were complimentary processes

which could occur simultaneously in the reaction medium under hydrothermal conditions to produce hexagonal double rods.

Finally, the sensitivity of the particle synthesis process to variations in the pH of the precursor suspension was tested. Results from pH measurements before and after hydrothermal treatment, showed that the reactive system was pH sensitive and variations in pH values by more than 1 pH value resulted in significant changes to particle morphology and size. Information acquired from the foregoing investigative process could serve to improve on existing knowledge in the field of hydrothermal synthesis of zinc oxide especially with regards the scaling up the synthesis process. Process scale up, is an activity which requires a robust understanding of the dynamics of particle growth and the effect, key process parameters such as duration of reaction and pH could have on the characteristics and properties of the product particles.

Findings made with respect to the synthesis of the double rods, have been published as an article in the Journal of the American Ceramic Society, Volume 97, Issue 5, pages 1619–1624, May 2014. Also, results of FIB-SEM analysis have also been presented in form of a conference poster. Oral presentations at conference have also been made based on both sets of results.

7.1.2 Zinc Oxide High Aspect Ratio Hexagonal Rods

High aspect ratio hexagonal rods were synthesised from the hydrothermal treatment of a precursor suspension obtained from drop-wise mixing of zinc acetate and ammonium hydroxide solutions. The particle growth process was observed to be identical to the hexagonal double rods, in that both were hierarchical in nature. However in a significant deviation from the growth process of the hexagonal double rods, the reaction / growth kinetics of the high aspect ratio rods was found to have been largely influenced by the presence of excess ammonium (NH_4^+) ions in the reaction medium.

The presence of micron-sized octahedral particles were observed via SEM in the untreated precursor suspension which XRD confirmed to be wulffingite ($\epsilon\text{-Zn(OH)}_2$). Analysis of samples obtained within the first 3 hours of

hydrothermal treatment showed a gradual transformation from wulffingite zinc hydroxide to wurtzite zinc oxide, accompanied by changes in the particle shape and size (from ~ 3 μm sized octahedral particles to ~ 1.2 μm wide hexagonal rod-like particles). This transformation process which was documented via XRD and SEM was thought to have occurred via a combination of several mechanisms including solid state phase transformation, and re-dissolution of the octahedral wulffingite particles into the reaction medium before subsequent re-crystallisation as zinc oxide with the hexagonal wurtzite crystal structure.

The occurrence of stepped particle growth of the hexagonal rods in the [0001] direction, similar to observations made with respect to secondary nucleation of double rod zinc oxide particles was also documented, in this case using SEM.

The influence of excess ammonia in the reaction system was studied via the combination of theoretical analysis and pH measurements. It was concluded, that the presence of ammonia in the reaction medium significantly influenced particle growth dynamics through the formation of aqueous ammine-hydroxo-zinc complexes and pH buffering resulting in precipitation of metastable wulffingite particles prior to emergence of hexagonal wurtzite zinc oxide rods.

A new hypothesis was therefore developed to describe the growth process of the high aspect ratio hexagonal zinc oxide rods based on findings from the research which helped provide clarity in the face of multiple propositions and hypotheses (as discussed in 5.3) about the growth process of high aspect ratio rods through this route as.

Findings made from this investigations, are in the process of been published as an article the RSC journal CrystEngComm. Other publications of results have included conference posters and oral presentations.

7.1.3 Sodium Zirconate Powders for CO₂ capture

Powders were synthesised through two methods, the first involving evaporation drying of a mixture of sodium acetate and zirconium acetate in nitric acid, while in the second method, the mixture was spray dried into powder. Particle characteristics were investigated using XRD and SEM. Findings showed that freshly calcined powders from both routes had similar chemical compositions which was a minor proportion of monoclinic ZrO₂, (~ 9 wt %), coexisting with a majority Na₂ZrO₃ phase. The ZrO₂ component was most probably unreacted ZrO₂ originating from the acetate conversion reaction. However, the morphological properties of the powders from both methods differed significantly. The evaporation dried powders contained ~10 µm sized agglomerates of < 500 nm irregular shaped particles, while the spray dried sample contained 0.5 - 20 µm sized hollow and rounded particles with nanoparticle sub-structure of < 100 nm wide irregular shaped nanoparticles. Many of them (hollow rounded particles) had apertures consistent with disruption by escaping gases during the spray drying / calcination synthesis procedure, while others were fractured or part deflated.

The stability of the CO₂ capture performance of these Na₂ZrO₃ powders were tested for up to 50 cycles under TGA conditions relevant for post combustion capture and hydrogen production via sorption-enhanced steam reforming (SESR) applications, namely carbonation at 700 °C and de-carbonation at 900 °C. It was observed that the spray dried sample had a better performance than both the evaporation dried sample and a commercially sourced sodium zirconate powder (MELSORB 2390). The spray dried powder had ~ 80 % CO₂ capture efficiency (g CO₂/g sorbent) compared to ~ 45 % and ~ 15 % efficiencies for the evaporation dried and commercial powders respectively.

The superior CO₂ capture performance of the spray dried powder relative to other samples was pinned on the microstructure of the sample. The open structure of the SD granules and the thickness of the granule walls equating to the dimension of a single primary particle easily permitted CO₂ molecules

to access a high exposed surface area. By contrast, the more dense and agglomerated ED particles had a smaller proportion of exposed surface.

The search for efficient and cost effective CO₂ capture materials is an ongoing one, and findings from our investigative process could contribute to the development of a suitable candidate for commercial applications in CO₂ capture from power stations and hydrogen production via sorption-enhanced steam reforming.

A manuscript based on the findings from the foregoing investigation is currently under preparation for publication in a suitable scientific journal.

7.2 Recommendations for Future Work

7.2.1 Scale up of Hydrothermal Synthesis of Zinc oxide Hexagonal Double Rods

With more than 7 billion people in the world, there is little possibility of bespoke production of many materials. Conventional industrial processes today are run on a continuous or semi-continuous basis with production figures in the range of hundreds of tonnes per annum. However, many reactive processes (especially crystallisation processes) are faced with a major challenge; which is being able to reproduce accurately phenomenon and results obtained during bench-scale lab experiments in the much larger process.

An investigation into the scale up of the hydrothermal synthesis of the hexagonal double rods in order to investigate the impact of process scale up on the properties of the product particles would be of significant research value to efforts at commercialising the synthesis process.

7.2.2 ZnO p-n Homojunctions

There is the need to explore the possibility of hydrothermal synthesis of ZnO p-n homojunctions through the exploitation of the secondary nucleation and end-to-end attachment processes of growth of the hexagonal double rods. This may be achieved by synthesising p-type conductivity ZnO rods followed by further growth of n-type conductivity ZnO rods on the p-type rods. Zinc

oxide particles containing p-n homojunctions could open up new applications which overcome current limitations posed by coupling zinc oxide to other materials to create p-n junctions.

7.2.3 Applications

In order to be able to fully exploit the uniqueness of the zinc double rod morphology in optoelectronic applications, there is the need for further analysis to be conducted such as electrical measurements across the double rod to investigate the influence of interfacial junction on the electrical / electronic and optical properties of the double rod particles.

7.2.4 Introduction of Spacers

Sorbent – Spacer materials could be synthesised using the sodium zirconate powders as the sorbent / matrix material, while materials such as zircon could be explored as a potential spacer materials to improve the CO₂ capture performance of the powders by mitigating the occurrence of powder sintering during the multicycle TGA analysis, which from results obtained this research work, was found to negatively impact on the CO₂ capture efficiency of the powders.

7.2.5 Further TGA Analysis

Although the powders have been tested for up to 26 h of simulated continuous usage, the analysis could be extended to 100 carbonation/decarbonation analysis cycles or more, to further investigate the effect of prolonged usage of the powders on their microstructure, and also determine how long it would take for the capture efficiency of powders to deteriorate to the point where it would be more economical to replace them.

References

- Adam, D., Explainer: Global carbon reduction targets, an article published in the Guardian newspapers, Tuesday 7 October 2008 10.11 BST (online), accessed 20 July, 2015, available at: <http://www.theguardian.com/environment/2008/jun/10/carbonemissions>
- Alammar, T., A.-V. Mudring, *Materials Letters*, 63(9–10), 2009, 732-735.
- American Zinc, *Barron's (1921-1942)*, [Boston, Mass], Dow Jones & Company Inc, 6, 22, 21-22, 1926, ISSN 10778039
- Amin, G., *White LEDs Printed on Paper—A Doctoral Thesis—Part I*, submitted to Linköping University, Department of Science and Technology, August 06, 2012, 1-3.
- Amna, T., M.S. Hassan, F.A. Sheikh, H.K. Lee, K.S. Seo, D. Yoon, I.H. Hwang, *Appl. Microbiol. Biotechnol.*, 97(4), 2013, 1725-34.
- Anderson, H., *Scanning Electron Microscope, Advantages and Disadvantages in Imaging Components and Applications*, 2010, microscope master website (online), accessed 27, February, 2015, available at: <http://www.microscopemaster.com/scanning-electron-microscope.html>
- Anthony, E.J., E.M. Bulewicz, L. Jia, *Progress in Energy and Combustion Science*, 33, 2007, 171-210.
- Arya, S.K., S. Saha, J.E. R.-V., V. Gupta, S. Bhansali, S.P. Singh, *Analytica Chimica Acta*, 737, 2012, 1– 21.
- Atteberry, J., "How Scanning Electron Microscopes Work" 21 April 2009. HowStuffWorks.com. (online), accessed 26 February 2015, available at: <http://science.howstuffworks.com/scanning-electron-microscope.htm>
- Baghbanzadeh, M., S.D. Škapin, Z.C. Orel, C.O. Kappe, *Chemistry - A European Journal*, 18(18), 2012, 5724–5731.
- Bahadur, L., M. Hamdani, J.F. Koenig, P. Chartier, *Solar Energy Materials*, 14(2), 1986, 107-120.

Ball, P., *Bright Earth: The Invention of Colour*, Random House, London, 2012, 169 – 174.

Bamiduro, F., M.B. Ward, R. Brydson, S.J. Milne, *J. Am. Ceram. Soc.*, 97(5), 2014, 1619 – 1624.

Baruah, S. and D. Joydeep, *Journal of Crystal growth*, 311, 2009, 2549 – 2554.

Batra, N., M. Tomar, V. Gupta, *J. Appl. Phys.*, 112, 2012, 114701.

Bearden, J. A., *Reviews of Modern Physics*, 39(1), 1967, 78 – 124.

Becheri, A., M. Dürr, P. Lo Nostro, P. Baglioni, *Journal of Nanoparticle Research*, 10(4), 2008, 679-689.

Beek, W. J. E., M. M. Wienk, R. A. J. Janssen, *Advanced Materials*, 16(12), 2004, 1009–1013.

Bitenc, M., G. Dražić, Z.C. Orel, *Crystal Growth & Design*, 10 (2), 2010, 830-837.

Bitenc, M., P. Podbršček, P. Dubček, S. Bernstorff, G. Dražić, B. Orel, Z.C. Orel, *CrystEngComm*, 14, 2012, 3080-3088.

Blok, L., P.L. De Bruyn, *Journal of Colloid and Interface Science*, 32(3), 1970, 518-526.

Bottom, R., *Thermogravimetric analysis*, chapter 3 in Paul Gabbott (ed) *Principles and Applications of Thermal Analysis*, Blackwell publishing, Oxford, UK, 2008, 87-97.

Brady, M.J., M. Levanoni, A. Reisinger, *Optics Communications*, 7(4), 1973, 390-393.

Brodusch, N., H. Demers, M. Trudeaub, R. Gauvina, *Surf. Interface Anal.*, 46, 2014, 1286–1290.

Brown, H. E., *New Jersey Zinc Company*, New York, 1957, 1 – 93.

Burgess, J., M. Marten, R. Taylor, *Under the Microscope: A Hidden World Revealed*, University of Cambridge Press, Cambridge, ISBN 0521399408, 11.

- Caceres, G.P., Electron Beam – Specimen Interaction, 2002, Recinto Universitario de Mayagüez, Universidad de Puerto Rico, Revised: 02/01/14.(online), accessed 26-02-2015 available at: <http://academic.uprm.edu/pcaceres/Courses/CHAMINA/HO5.pdf>
- Cadmium (Cd). 2015. Encyclopædia Britannica Online. Retrieved 02 May, 2015, available at: <http://www.britannica.com/EBchecked/topic/87955/cadmium-Cd>
- Cao, B., W. Cai, J. Phys. Chem. C, 112, 2008, 680-685.
- Cao, X., H. Zeng, M. Wang, X. Xu, M. Fang, S. Ji, L. Zhang, J. Phys. Chem. C, 112, 2008, 5267-5270.
- Carter, G., M. Ogden, C. Buckley, C. Maitland, M. Paskevicius, Powder Technology 188 (3), 2008, 222-228.
- Chan, Y.J., M.F. Chong, C.L. Law, D.G. Hassell, Chemical Engineering Journal, 155, 2009, 1–18.
- Chaúque, E.F.C., J.N. Zvimba, J.C. Ngila, N. Musee, Physics and Chemistry of the Earth, Parts A/B/C, 67–69, 2014, 140-144.
- Chen, J., J. Li, S. Qiu, Journal of Alloys and Compounds, 509, 2011, 740 – 743.
- Chen, W., D. Yu, H. Ruan, D. Li, Y. Hu, Y. Chen, Y. He, X. Fu, Y. Shao, Journal of the American Ceramic Society, 95(7), 2012, 2322–2329.
- Chen, Z., L. Gao, Journal of Crystal Growth, 293, 2006, 522–527.
- Cheng, B., E.T. Samulski, Chem. Commun., 2004, 986-987.
- Cheng, C.-L., J.-S. Lin, Y.-F. Chen, 476(1–2), 2009, 903-907.
- Cho, S., D.-S. Shim, S.-H. Jung, E. Oh, B.R. Lee, K.-H. Lee, Materials Letters, 63(9–10), 2009, 739-741.
- Cho, S., K.-H. Lee, Cryst. Growth Des., 12, 2012, 994–999.
- Choi, J.-h., X. You, C. Kim, J. Park, J.J. Pak, Journal of Electrical Engineering & Technology, 5(4), 2010, 640-645.

Cortés-Palacios, L., V.I.M Collins, A.D. Díaz, A.O. López, Chemistry and Materials Research, 2(1), 2012, 31-40

Croxall, D.F., R.C.C. Ward, C.A. Wallace, R.C. Kell, Journal of Crystal Growth, 22(2), 1974,117-124.

Cubeiro, M.L., J.L.G. Fierrob, Journal of Catalysis, 179(1), 1998, 150–162.

Cui, Q., K. Yu, N. Zhang, Z. Zhu, Applied Surface Science, 254(11), 2008, 3517-3521

Dai, Y., Y. Zhang, Q.K. Li, C.W. Nan, Chemical Physics Letters, 358(1–2), 2002, 83-86.

Damen, T. C., S. P. S. Porto, B. Tell, Phys. Rev. 142, 1966, 570.

David, H.W., Light Scattering Theory, Department of Mechanical and Aerospace Engineering, University of Florida, 1-3, (online), accessed 10-03-2015 at:
<http://plaza.ufl.edu/dwhahn/Rayleigh%20and%20Mie%20Light%20Scatterin%20g.pdf>

DDB, Vapor pressure diagrams of Water, Dortmund Data Bank Version: February 2014 (online) accessed 6 June, 2014, available at:
<http://ddbonline.ddbst.com/DDBSearch/onlineddboverview.exe?submit=Overview&systemcomplist=174&databank=MPVT>

De Liedekerke, M., Ullmann's Encyclopdia of Industrial Chemistry, 2006, Wiley-VCH, Weinheim, 56 – 60.

DEFFRA and DECCC, Department for Environment Food & Rural Affairs (DEFFRA) and Department of Energy & Climate Change, Policy paper: 2010 to 2015 government policy: greenhouse gas emissions, (online) accessed: 20 July, 2015, available at:
<https://www.gov.uk/government/publications/2010-to-2015-government-policy-greenhouse-gas-emissions/2010-to-2015-government-policy-greenhouse-gas-emissions>

Dem'yanets, L.N., L.E. Li, T.G. Uvarova, Y.M. Mininzon, Inorganic Materials, 44 (1), 2008, 40-44.

Diebold, M.P., C.R. Bettler, D.M. Mukoda, Journal of Coatings Technology July 2003, 75(942), 29-36.

Distaso, M., M. Mac'kovic', E. Spiecker, W. Peukert, Chem. Eur. J., 20, 2014, 8199 – 8209.

Dodson, E.M., J.A. Savage , Journal of Materials Science, 3(1), 1968, pp 19-25.

Duan, J., X. Huang, E. Wang, Materials Letters, 60(15), 2006, 1918-1921.

Duan, L., P. Wang, X. Yu, X. Han, Y. Chen, P. Zhao, D. Li, R. Yao, Phys. Chem. Chem. Phys., 16, 2014, 4092-4097.

Dykstra, M.J., L.E. Reuss, Biological Electron Microscopy Theory, Techniques, and Troubleshooting (2ed.), Kluwer Academic / Plenum Publishers, pp. 287.

E.M. Vogel, T.J. Nelson, Displays, 7(2), 1986, 78-80.

Elen, K., H. Van den Rul, A. Hardy, M.K. Van Bael, J. D'Haen, R. Peeters, D. Franco, J. Mullens, Nanotechnology, 20(54), 2009, 1 – 8.

EPA, Overview of Greenhouse Gases, Climate change, United States Environmental Protection Agency website, (online), Last updated on 5/7/2015, accessed 21 July, 2015, available at: <http://www.epa.gov/climatechange/ghgemissions/gases/co2.html>

Erdélyi, R., V. Halász, Z. Szabó, I.E. Lukács, J. Volk, Physica E: Low-dimensional Systems and Nanostructures, 44(6), 2012, 1050-1053.

Fahmy, A.H., E. L. Adler, IEEE Trans. Sonic., Ultrason., SU-19, 1972, 346 – 349.

Fan J.C., S.L. Chang, Z. Xie, ZnO-Based Light-Emitting Diodes, chapter 2, in Optoelectronics - Advanced Materials and Devices, S.L. Pyshkin, J.M. Ballato (eds), InTech, ISBN 978-953-51-0922-8, 2013, 25-58.

Fan Z., J.G.Lu, J. Nanosci Nanotechnol., 5(10), 2005, 1561-73.

Fan, J.C., K.M. Srekanth, Z. Xie, S.L. Chang, K.V. Rao, Progress in Materials Science, 58(6), 2013, 874-985.

Fang, X., J. Li, D. Zhao, D. Shen, B. Li, X. Wang, J Phys Chem C, 2009, 113, 21208.

Fordham, S., nature, 1940, 807.

Fretwell, A., P. Goodhew, L. Rogers, N. Fegen, Introduction to Crystallography, Indexing Directions and Planes, 'Materials Science on CD ROM' an Introduction to Crystallography, university of Liverpool, 2007, (online), accessed 07 July, 2015, available at: <http://www.materials.ac.uk/elearning/matter/crystallography/indexingdirectionsandplanes/info.html>

Fu, J.Y., P.Y. Liu, J. Cheng, A.S. Bhalla, R. Guo, Applied Physics Letters, 90, 2007, 212907.

Fujita, Y., K. Moriyama, Y. Hiragino, Y. Furubayashi, H. Hashimoto, T. Yoshida, Phys. Status Solidi C, 2014, 1–3.

Fuller, M.L., Twinning in Zinc Oxide, J. Appl. Phys. 15, 1944, 164.

Gao, X.P., Z.F. Zheng, H.Y. Zhu, G.L. Pan, J.L. Bao, F. Wu D.Y. Song Chem. Commun., 2004, 1428-1429.

Ghosh, S., D. Majumder, A. Sen, S. Roy, Materials Letters, 130(1), 2014, 215-217.

Ghule, K., A.V. Ghule, B.-J. Chen, Y.-C. Ling, Green Chem., 8, 2006, 1034-1041.

Goldburg, W.I., American Journal of Physics, 67, 1999, 1152-1160.

Gong, L., H. Jiang, F. Zhu, Materials Letters, 64, 2010, 2582–2584.

Goodhew, P., A. Callanan, L. Rogers, N. Fegen, S. Davidson, Scanning Electron Microscope (SEM), 'Materials Science on CD ROM' an Introduction to Electron Microscopes, university of Liverpool, 2007, (online), accessed 15 June, 2015, available at: <http://www.materials.ac.uk/elearning/matter/introductiontoelectronmicroscopes/sem/info.html>

Goodhew, P., D. Brook, B. Tanovic, A. Green, I. Jones, Transmission Electron Microscopy (TEM), matter website, (online), accessed 07 July, 2015, available at: <http://www.matter.org.uk/tem/>

Grattan-Bellew, P.E., American Mineralogist, 60, 1975, 1127-1129.

Gretzinger J., W.R. Marshall, Jr., AIChE journal, 7(2), 1961, 312-318

Griffin, B.J., Scanning, 33(3), 2011, 162–173.

Grimes, C.A., O.K. Varghese, S. Ranjan, Springer, US, Online ISBN 978-0-387-68238-9, 2008, 35-113.

Gringer, "Scheme TEM en" by Gringer (talk) - Commons: Scheme TEM en.png. Licensed under CC BY-SA 3.0, (online), accessed 25 June, 2015 via Wikimedia Commons -

https://commons.wikimedia.org/wiki/File:Scheme_TEM_en.svg#/media/File:Scheme_TEM_en.svg

Gunasekaran, A., Scanning Electron Microscopy, LA-SIGMA Microscopy Workshop, October 14, 2011, institute for micromanufacturing, Louisiana Tech. University, (online), accessed 27, February, 2015, available at: http://www.institute.loni.org/lasigma/document_files/workshopdocuments/SEMnotes.pdf

Guo, T.H., Y. Liu, Y.C. Zhang, M. Zhang Materials Letters, 65(4), 2011, 639-641.

Habashi, F., CIM Bull., 94, 2001, 71–76.

Hadi, W.A., M.S Shur, S.K. O'Leary, Journal of Applied Physics, 112, 2012 033720.

Haffada, S., G. Ciceroa, M. Samah, Energy Procedia, 10, 2011, 128 – 137.

Hafner, B., Scanning Electron Microscopy Primer, Characterization Facility, University of Minnesota—Twin Cities 4/16/2007, pp 1 - 29 (online) accessed 16 June, 2015, available at: http://www.charfac.umn.edu/sem_primer.pdf

Haines, P.J., Thermal Methods of Analysis: Principles, Applications and Problems, Springer Science and Business Media, Glasgow, 1995, .22-24

- Hamedani, N.F., A.R. Mahjoub, A.A. Khodadadi, Y. Mortazavi, *Sensors and Actuators B: Chemical*, 156(2), 2011, 737-742.
- Hammond, C., *The Basics of Crystallography and Diffraction*, International Union of Crystallography texts on crystallography, Oxford science publications, 3 ed., 2009
- Hanawalt, J.D., H.W. Rinn, *Powder Diffraction Journal* 1(1), 1986, 1
- Haueter, P., S. Moeller, R. Palumbo, A. Steinfeld, *Solar Energy*, 67(1–3), 1999, 161-167.
- Heiland, G., E. Mollwo, F. Stockmann, *Solid State Phys.*, 8, 1959, 193-196.
- Heiland, G., H. Ibach, *Pyroelectricity of zinc oxide*, *Solid State Communications*, 4(7), 1966, 353-356.
- Heiland, G., P. Kunstmann, *Surface Science*, 13(1), 1969, 72-8.
- Heim, J., E. Felder, M.N. Tahir, A. Kaltbeitzel, U.R. Heinrich, C. Brochhausen, V. Mailänder, W. Tremel, J. Brieger, *Nanoscale*, 7, 2015, 8931-8938.
- Helbig, R., *Journal of Crystal Growth*, 15(1), 1972, 25-31.
- Henry, D., *Electron-Sample Interactions*, *Geochemical Instrumentation and Analysis*, Henry, Louisiana State University, 29 May, 2012 (online), accessed 26-02-2015 available at: http://serc.carleton.edu/research_education/geochemsheets/electroninteractions.html
- Hofmann, D.M., A. Hofstaetter, F. Leiter, H. Zhou, F. Henecker, B.K. Meyer, S.B. Orlinskii, J. Schmidt, and P.G. Baranov, *Phys. Rev. Lett.* 88, 2002, 045504 –.
- Hosono, E., S. Fujihara, I. Honma, H. Zhou, *Adv. Materials*, 17(17), 2005, 2091–2094.
- Hosono, E., S. Fujihara, T. Kimura, H. Imai, *Journal of Colloid and Interface Science*, 272(2), 2004, 391-398.

Hu X.-L., Y.-J. Zhu, S.-W. Wang, *Materials Chemistry and Physics*, 88(2–3), 2004, 421-426

Hu, H., X. Huang, C. Deng, X. Chen, Y. Qian, *Materials Chemistry and Physics*, 106(1), 2007, 58-62.

Hutson, A. R., *Phys. Rev.*, 108, 1957, 222-230.

Illy, B., B.A. Shollock, J.L. MacManus-Driscoll, M.P. Ryan, *Nanotechnology*, 16, 2005, 320 – 324.

Ippic, Function of Zinc Oxide in Antifouling Paints, international paint and print ink council website, (online) accessed 09, April, 2015, available at: <http://www.ippic.org/site/assets/docs/Public%20AFWG/IPPIC%20Function%20of%20Zinc%20Oxide%20in%20antifouling%20paints%20final%20draft%20March%201%202012.pdf>

ISO, International Standard ISO22412:2008 Particle Size Analysis, Dynamic Light Scattering (DLS), (online), accessed 28, February, 2015, available at: <https://www.iso.org/obp/ui/#iso:std:iso:22412:ed-1:v1:en>

Iwasa, N., S. Masuda, N. Ogawa, N. Takezawa, *Applied Catalysis A: General*, 125(1), 1995, 145-157.

IZA, Zinc properties. International Zinc Association website, (online). Accessed 18 April, 2015, available at: http://www.zinc.org/basics/zinc_properties

Jaimes, R., Scanning electron microscope (SEM) ELECTRON SOURCES, CAMTEC Nanofabrication Workshop, 2013.

Jang, E.-S., J.-H. Won, Y.-W. Kim, Z. Cheng, J.-H. Choy, *CrystEngComm*, 13, 2011, 546-552.

Jezierski, G., X Ray Generation, Dept. of Chemistry & Biochemistry, University of Oklahoma website, (online), accessed 10 June, 2015, available at: <http://xrayweb.chem.ou.edu/notes/xray.html>

Ji, S., C. Ye, *J. Mater. Sci. Technol.*, Vol.24 No.4, 2008 doi: 10.3321/j.issn:1005-0302.2008.04.003

Jiaqiang, X., C. Yuping, L. Yadong, S. Jianian, Journal of Materials Science, 40(11), 2005, 2919-2921.

Jung, Y.-I., B.-Y. Noh, Y.-S. Lee, S.-H. Baek, J.H. Kim, I.-K. Park, Nanoscale Research Letters, 7(1), 2012, 43 – 48.

Jürgens, D., X-ray Diffraction, Institute of Physics Germany, 2013, (online), accessed 24-02-2015 at: http://physik2.uni-goettingen.de/research/2_hofs/methods/XRD

Kajbafvala, A., M.R. Shayegh, M. Mazloumi, S. Zanganeh, A. Lak, M.S. Mohajerani, S.K. Sadrnezhad, Journal of Alloys and Compounds, 469(1–2, 5), 2009, 293-297.

Kang, B.S., Y.W. Heo, L.C. Tien, D.P. Norton, F. Ren, B.P. Gila, S.J. Pearton, Appl. Phys. A, 80, 2005, 1029–1032.

Klingshirn, C., E. Mollwo, Zeitschrift fur Physik A, 254, 1972, 437–446.

Klingshirn, C., J. Fallert, H. Zhou, J. Sartor, C. Thiele, F. Maier-Flaig, D. Schneider, H. Kalt, Phys. Status Solidi B, 247(6), 2010, 1424–1447.

Klingshirn, C., Phys. Stat. Solidi (b), 244, 2007, 3027.

Klingshirn, C., Zeitschrift für Physik, 248(5), 1971, 433-445.

Klug, H.P., L.E. Alexander, X-ray diffraction procedures (Vol. 2). New York: Wiley, 1954, 1-.

Kołodziejczak-Radzimska A., T. Jesionowski, Materials, 7, 2014, 2833-2881.

Kopeliovich, D., Scanning Electron Microscope, substech, 31, May, 2012, (online), accessed 26, February, 2015, available at: http://www.substech.com/dokuwiki/doku.php?id=scanning_electron_microscope

Koster, L. J. A., W.J. van Strien, W.J.E. Beek and P.W. M. Blom, Advanced Functional Materials, 17(8), 2007, 1297–1302.

Kouhnavard, M., S. Ikeda, N.A. Ludin, N.B. AhmadKhairudin, B.V. Ghaffari, M.A. Mat-Teridi, M.A. Ibrahim, S. Sepeai, K. Sopian, Renewable and Sustainable Energy Reviews, 37, 2014, 397–407.

Kroger, F. A., *Physica*, 7(1), 1940, 92-100.

Krumeich F., Signals in Scanning Electron Microscopy, electron microscopy, ETH Zurich website, modified: 6 February, 2015 (online), accessed 16 June, 2015, available at: http://www.microscopy.ethz.ch/sem_detectors.htm

Ku, C.-H., H.-H. Yang, G.-R. Chen, J.-J. Wu, *Crystal Growth & Design*, 8(1), 2008, 283–290.

Kuiper, P., "Copper K Rontgen" by - Own work. Licensed under Public Domain (online) accessed 12 June, 2015 via Wikimedia Commons - https://commons.wikimedia.org/wiki/File:Copper_K_Rontgen.png#/media/File:Copper_K_Rontgen.png

Kumar, P.T., V.K. Lakshmanan, T.V. Anilkumar, C. Ramya, P. Reshmi, A.G. Unnikrishnan, S.V. Nair, R. Jayakumar, *ACS Appl Mater Interfaces*, 4(5), 2012, 2618-29.

Kuo, C.-L., T.-J. Kuo, M.H. Huang, *J. Phys. Chem. B*, 109, 20115-20121.

Kusaba, K., T. Yagi, J. Yamaura, H Gotou, T. Kikegawa, *J. Phys.: Conf. Ser.*, 2010, 215, 012001.

Larson, J. D., D. K. Winslow, L. T. Zitelli, "RF Diode Sputtered Zinc Oxide Transducers", *IEEE Trans. Sonic., Ultrason.*, SU-19, 1972, 18-22.

Laudise, R.A., A.A. Ballman, *J. Phys. Chem.*, 64 (5), 1960, 688–691.

Leclair, E.J., J.J.E. Barruel, U.S. Patent 0007351, 1850, pp. 1-4.

Lenhart, S., 2005: Scanning Electron Microscopy (online), accessed 24, January, 2014, available at: <http://www.nanoword.net/library/defgen/generate.php?termid=139>

Li, D., J. Wang, X. Wu, C. Feng, X. Li, *Ultrasonics Sonochemistry*, 20(1), 2013, 133-136.

Li, J., H. Zhuang, J. Wang, P. Xu, *Materials Letters*, 65, 2011, 1659–1662.

Li, W.-J., E.-W. Shi, M.-Y. Tian, W.-Z. Zhong, Z.-W. Yin, *Journal of Material Research*, 14(4), 1999, 1532 – 1537.

Li, W.-J., E.-W. Shia, M.-Y. Tiana, W.-Z. Zhonga, Z.-W. Yina, *Journal of Material Research*, 14(4), 1999 1532 – 1537.

Li,S., G.A. Gross, P.M. Günther, J.M. Köhler, *Chemical Engineering Journal*, 167, 2011, 681–687.

Liao, J., H. Hu, W. Fu, S. Li, Q. Chen, *Hydrometallurgy*, 121–124, 2012, 107-115.

Lim, Z.H., Z.X. Chia, M. Kevin, A.S.W. Wong, G.W. Ho, *Sensors and Actuators B*, 151, 2010, 121–126.

Lipowsky, P., M. Hirscher, R.C. Hoffmann, J. Bill, F. Aldinger, *Nanotechnology*, 18, 2007, 165603.

Liu, B., H.C. Zeng, *J. Am. Chem. Soc.*, 125, 2003, 4430 - 4431

Liu, Y., H. Lv, S. Li, G. Xi, X. Xing, *Advanced Powder Technology*, 22(6), 2011, 784-788.

Liu, Y., H. Lv, S. Li, X. Xing, G. Xi, *Dyes and Pigments*, .95(3), 2012, 443-449.

Liu, Y., K. Ai, Q.i Yuan, L. Lu, *Biomaterials*, 32(4), 2011, 1185-1192.

Look, D.C., *Superlattices and Microstructures*, 42, 2007, 284–289.

López-Ortiz, A., N.G.P. Rivera, A.R. Rojas, D.L. Gutierrez, *Separation Science and Technology*, 39, 2005, 3559-3572.

Lu J., M.N Ka, S. Yang, *Industrial & Engineering Chemistry Research*, 47 (4), 2008, 1095-1101.

Lu J.G., S. Fujita, T. Kawaharamura, H. Nishinaka, *Chemical Physics Letters*, 441(1–3), 2007, 68-71.

Lu, C.-H.; Yeh, C.-H., *Ceramics International*, 26, 2000, 351-357.

Lu, K., J. Zhao, *Chemical Engineering Journal*, 160(2), 2010, 788-793.

Lupan, O., G. Chai, L. Chow, *Microelectronic Engineering* 85, 2008, 2220–2225.

Ma, M.-G., Y.-J. Zhu, G.-F. Cheng, Y.-H. Huang, *Materials Letters*, 62(3), 2008, 507-510.

Ma, X., H. Zhang, Y. Ji, J. Xu, D. Yang, *Materials Letters*, 59(27), 2005, 3393-3397.

Mackenzie, A., D.L. Granatstein, E.J. Anthony, J.C. Abanades, *Energy & Fuels*, 21, 2007, 920-926.

Maier, C.G., G.S. Parks, C.T. Anderson, *J. Am. Chem. Soc.*, 48, 1926, 2564–2576.

Malvern, *Dynamic Light Scattering: An Introduction in 30 Minutes*, (Version 4 Technical Note), Malvern instruments website, (online), accessed 26, February, 2015, available at: <http://www.malvern.com/en/support/resource-center/technical-notes/TN101104DynamicLightScatteringIntroduction.aspx>

Malvern, *Zetasizer Nano ZS Performance, simplicity, versatility.*, Malvern Instruments, (online), accessed 24, January, 2015, available at: <http://www.malvern.com/en/products/product-range/zetasizer-range/zetasizer-nano-range/zetasizer-nano-zs/default.aspx>

Mandal, S.K., P. Dey, T.K. Nath, *Journal of Vacuum Science & Technology B*, 32, 2014, 041803.

Manovic, V., J.P. Charland, J. Blamey, P.S. Fennell, D.Y. Lu, E.J. Anthony, *Fuel*, 88, 2009, 1893-1900.

Matsui, H., H. Tabata, *Nanowires*, Paola Prete (Ed.), 2010, ISBN: 978-953-7619-79-4.

McBride, R.A., J.M. Kelly, D.E. McCormack, *J. Mater. Chem.*, 13, 2003, 1196-1201.

McK. Nobbs J., F.C. Gillespie, *Journal of Physics and Chemistry of Solids*, 31(10), 1970, 2353-2354.

Meaney, A.J., PhD Thesis submitted to the School of Physical Sciences, Dublin City University, Glasnevin, Dublin, Ireland, 2010, 6 – 11.

Messick, J. ICDD History - 70 Years of a Scientific Organization, ICDD, 2011, (online), accessed 24-02-2015 at:

<http://www.icdd.com/profile/history.htm>

Meulenkamp, A.E., Journal Physical Chemistry B, 102(29), 1998, 5566–5572.

Miller, P.H. Jr., in: Proc. Intern. Conf. on Semiconducting Materials, Reading, 1950, edited by H.K. Henisch, Butterworths Scientific Publications, London, 1951, 172.

Mitra, P., A. P. Chatterjee, H. S. Maiti, chemical deposition of ZnO films for gas sensors, journal of materials science: materials in electronics, 9 (1998) pp 441- 445

Mo, M.-S., S.H. Lim, Y.-W. Mai, R.-K. Zheng, S.P. Ringer, . Adv. Mater. 20, 2008, 339–342.

Moezzi, A., A.M. McDonagh, M.B. Cortie, Chemical Engineering Journal, 185–186, 2012, 1-22.

Moezzi, A., A.M. McDonagh, M.B. Cortie, Dalton Trans., 40, 2011, 4871-4878

Mollwo, E., H. Schreiber, Solid State Communications, 8(13), 1970, 1011-1015.

Monakhov, E.V., Journal of physics. D, Applied physics (0022-3727), 42(15), 2009, 153001.

Mondal, B., J. Dutta, C. Roychaudhury, D. Mohanta, H. Saha, Chinese Journal Of Physics, 51(5), 2013, 994 – 1005.

Moorer, W.R., J.M. Genet, Oral Surg Oral Med Oral Pathol., 53(5), 1982, 508-17.

Morioka, H., H. Tagaya, J.-I. Kadokawa, K. Chiba, Journal of Materials Science Letters, 18(12), 995-998.

Morioka, H., H. Tagaya, J.-I. Kadokawa, K. Chiba, Journal of Materials Science Letters, 18(12), 1999, 995-998.

Moulaoui, A., F. Sediri, *Ceramics International*, Volume 40(1), 2014, 943–950.

Mu, Q., C.A. David, J. Galceran, C. Rey-Castro, L. Krzemiński, R. Wallace, F. Bamiduro, S.J. Milne, N.S. Hondow, R. Brydson, G. Vizcay-Barrena, M.N. Routledge, L.J. Jeuken, A.P. Brown, *Chem Res Toxicol.*, 7(4), 2014, 558-67.

Mujeeb, R.P., K. Muraleedaran, V.M.A. Mujeeb *International Journal of Biological Macromolecules*, 77, 2015, 266–272.

NavBharat, Application, Nav Bharat Metallic Oxide Industries Pvt. Limited website, (online), accessed 09, April, 2015, available at: <http://www.navbharat.co.in/clients.htm>

Nessler, R., *Scanning Electron Microscopy*, Central Microscopy Research Facility The university of Iowa, 2015, (online) accessed 16 June, 2015, available at: <http://cmrf.research.uiowa.edu/scanning-electron-microscopy>

New Jersey Zinc Company, H.A. Nelson, technical bulletin, New York, The New Jersey zinc company, 1940, 3- 58.

Nicholas, N.J., G.V. Franks, W.A. Ducker, *CrystEngComm*, 14(4), 2012, 1232-1240.

Nimmo, W., N.J. Ali, R. Brydson, C. Calvert, S.J. Milne, *J. Am. Ceram. Soc.*, 88(4), 2005, 839–844.

NIST, Zinc oxide (French process), IR Spectrum, Condensed Phase Spectrum plot, (online) accessed: 25 May, 2015, available at: <http://webbook.nist.gov/cgi/cbook.cgi?ID=B6004648&Mask=80>

Norzinco GmbH, The process, the NORZINCO company website, 2015, (online) accessed 12 May, 2015, available at: <http://www.recylex-germany.com/en/norzinco/process.html>

NRC, *Advancing the Science of Climate Change* . Link to EPA's External Link Disclaimer National Research Council. The National Academies Press, Washington, DC, USA.

Ochoa-Fernández, E., H.K. Rusten, H.A. Jakobsen, M. Rønning, A. Holmen, D. Chen, *Catalysis Today*, 106, 2005, 41-46.

Ogura, Y., ZONESem Sample Surface Cleaning System, 2015, Hitachi High-Technologies Europe GmbH (online), accessed 26, February, 2015, available at: <http://www.hht-eu.com/cms/26970.html>

Ohashi, N., Journal of the Ceramic Society of Japan, 122(1427), 2014, 530-536.

Ohshima, E., H. Ogino, I. Niikura, K. Maedab, M. Sato, M. Ito, T. Fukuda, Journal of Crystal Growth, 260, 2004, 166–170.

Özgür, Ü., Y.I. Alivov, C. Liu, A. Teke, M.A. Reshchikov, S. Dogan, V. Avrutin, S.-J. Cho, H.A. Morkoç, Journal of Applied Physics, 98, 2005, 041301.

Öztürk, S., N. Kiliç, N. Tasaltın, Z.Z. Öztürk, . Thin Solid Films, 520(3), 2011, 932-938.

Pal, U., J. Garcia Serrano, P. Santiago, Gang Xiong, K.B. Ucer, R.T. Williams, Optical Materials, 29(1), 2006, 65-69.

Palucka, T., Overview of Electron Microscopy, history of recent science & technology, the Dibner Institute for the History of Science and Technology website, updated 10 December 2002 by Arne Hessenbruch, (online) accessed 05, May, 2015 available at: http://authors.library.caltech.edu/5456/1/hrst.mit.edu/hrs/materials/public/ElectronMicroscope/EM_HistOverview.htm

Park, S.Y., S. Kim, J. Yoo, K.-H. Lim, E. Lee, K. Kim, J. Kim, Y. Sang Kim, RSC Adv., 4, 2014, 11295.

Park, Y. S., J. R. Schneider, J. Appl. Phys. 39(7), 1968, 3049.

Pawar, R.C., J.S. Shaikh, A.A. Babar, P.M. Dhere, P.S. Patil, Solar Energy, 85, 2011, 1119–1127.

Peng, Y., A.-W. Xu, B. Deng, M. Antonietti, H. Cölfen, J. Phys. Chem. B, 110(7), 2006, 2988–2993.

Perales-Perez, O.J., M.S. Tomar, S.P. Singh, A. Watanabe, T. Arai, A. Kasuya, K. Tohji, phys. stat. sol. (c), 1(4), 2004, 803–806.

Perelshtein, I., Y. Ruderman, N. Perkas, K. Traeger, T. Tzanov, J. Beddow, E. Joyce, T.J. Mason, M. Blanes, K. Mollá, A. Gedanken, J. Mater. Chem., 2012, 22, 10736-10742.

Perkin Elmer, Frequently asked questions Thermogravimetric Analysis (TGA): A Beginner's Guide, Perkin Elmer, 2010, 3 – 5.

Pfeiffer, H., C. Vázquez, V.H. Lara, P. Bosch, Chemistry of Materials, 19, 2007, 922-926.

Pholnak C., C. Sirisathikul, D.J. Harding, Journal of Physics and Chemistry of Solids, 72, 2011, 817–823.

PhotoMterics, Thermogravimetric Analysis (TGA), PhotoMetrics website, 2012 (online) accessed 10 July, 2015 available at: <http://photometrics.net/analytical-techniques/thermogravimetric-analysis-tga>

Piekarczyk, W., S. Gazda, T. Niemyski, Journal of Crystal Growth, 12(4), 1972, 272-276.

Podbršček, P., G. Dražić, J.A. Paramo, Y.M. Strzhemechny, J. Maček and Z.C. Orel, CrystEngComm, 12, 2010,3071-3079.

Poshkus, A.C., Ind. Eng. Chem. Prod. Res. Dev., 22, 1983, 380-381

Poul, L., N. Jouini, F. Fiévet, Chem. Mater., 12 (10), 2000, 3123–3132

Pradel, K.C., W. Wu, Y. Zhou, X. Wen, Y. Ding, Z.L. Wang, Nano Letters, 13 (6), 2013, 2647-2653.

Prakash, S., R.D. Madan, Modern Inorganic Chemistry, New Delhi, S. Chand & Co. Ltd., ISBN 81-219-0074-3, 1987, 1498 – 1500.

Preston, G.D., nature, 147, 1941, 298.

Puay, N.-Q., G. Qiu, Y.-P. Ting, Journal of Cleaner Production, 8, 2014,139-145.

Pugazhenthly, L., zinc oxide, chapter 29 in Zinc Handbook: Properties, Processing, and Use In Design (Mechanical Engineering Series), 1991, CRC Press, ISBN 9780824783402, 588 – 590.

Pushpanathan, V., D.S. Kumar, J. Nanostruct Chem., 4(118), 2014, 1-7.

- Qin, Y., X. Wang, Z.L. Wang, *Nature*, 451, 2008, 809-813.
- Qu, X., D. Jia, *Journal of Crystal Growth*, 311, 2009, 1223–1228.
- Rai, P., H.-M. Song, Y.-S. Kim, M.-K. Song, P.-R. Oh, J.-M. Yoon, Y.-T. Yu, *Materials Letters*, 68, 2012, 90–93.
- Ramamurthy, P., E.A. Secco, *Canadian Journal of Chemistry*, 46(22), 1968, 3605-3606.
- Rao, V.V., What is Philosopher's wool?, *The Times of India*, Sunday Times, Feb 28, 2010, 03.53 AM IST, viewed 02, May, 2015 (online) available at: <http://timesofindia.indiatimes.com/home/sunday-times/What-is-Philosophers-wool/articleshow/5626338.cms>
- Rasmussen, J.W., E. Martinez, P. Louka, D.G. Wingett, *Expert Opinion on Drug Delivery*, 7(9), 2010, 1063-1077.
- Reed, R.B., D.A. Ladner, C.P. Higgins, P. Westerhoff, J.F. Ranville, *Environ Toxicol Chem.*, 31, 2012, 93-9.
- Reichle, R.A., K.G. Mccurdy, L.G. Hepler, *Can. J. Chem.* 53, 1975, 3841 – 3845.
- Sáaedi, A., R. Yousefi, F. Jamali-Sheini, M. Cheraghizade, A.K. Zak, N.M. Huang, *Superlattices and Microstructures*, 61, 2013, 91–96.
- Sartor, M., *Dynamic Light Scattering*, University of California, San Diego, 2003, 2–21.
- Schilling, K., B. Bradford, D. Castelli, E. Dufour, J.F. Nash, W. Pape, S. Schulte, I. Tooley, J. van den Boschi, F. Schellauf, *Photochem. Photobiol. Sci.*, 9, 2010, 495-509.
- Schindler, P., H. Althaus, W. Feitknecht, *Helv. Chim. Acta*, 47, 1964, 982–991.
- Schneck, H., R. Helbig, *Thin Solid Films*, 27(1), 1975, 101-109.
- Schulz, H., K.H. Thiemann, *Solid State Communications*, 32(9), 1979, 783–785.

Schweitzer, J., Scanning Electron Microscope, Radiological and Environmental Management webpage, Purdue University (online), accessed 07, February, 2014, available at: <http://www.purdue.edu/rem/rs/sem.htm>

Seo, B.I., U.A Shaislamov, M.H. Ha, S.-W. Kim, H.-K. Kim, B. Yang, *Physica E: Low-dimensional Systems and Nanostructures*, 37(1–2), 2007, 241-244.

Shalumon, K.T., K.H. Anulekha, S.V. Nair, S.V. Nair, K.P. Chennazhi, R. Jayakumar, *International Journal of Biological Macromolecules*, 49(3), 2011, 247-254.

Shankar, S., X. Teng, G. Li, J.-W. Rhim, *Food Hydrocolloids*, 45, 2015, 264-271.

Shin, S.-H., M.H. Lee, J.-Y. Jung, J.H. Seol, J. Nah, *J. Mater. Chem. C*, 1, 2013, 8103-8107.

Shouli, B., L. Xin, L. Dianqing, C. Song, L. Ruixian, C. Aifan, *Sensors and Actuators B*, 153, 2011, 110–116.

Shukla, P., I. Fatimah, S. Wang, H.M. Ang, M.O. Tadé, *Catalysis Today*, 157(1–4), 2010, 410-414.

Singh, A., K. Senapati, B. Satpati, M. Kumarc, P.K. Sahoo, *Phys. Chem. Chem. Phys.*, 17, 2015, 4277.

Singh, S. P., Sunil K. Arya, Pratibha Pandey, B. D. Malhotra, Shibu Saha, K. Sreenivas, Vinay Gupta, *Appl. Phys. Lett.*, 91, 2007, 063901.

Smith, K. C. A., C. W. Oatley, *Br. J. Appl. Phys.*, 6(11), 1955, 391.

Solanki, P.R., A. Kaushik, A.A. Ansari, B.D. Malhotra, *Appl. Phys. Lett.*, 94, 2009, 143901.

Song, J., J. Zhou, Z.L. Wang, *Nano Lett.*, 6(8), 2006, 1656–1662.

Soumahoro, I., S. Colis, G. Schmerber, C. Leuvrey, S. Barre, C. Ulhaq-Bouillet, D. Muller, M. Abd-lefdil, N. Hassanain, J. Petersen, A. Berrada, A. Slaoui, A. Dinia, *Thin Solid Films*, 566, 2014, 61-69.

Souza, C.R.F., I.A. Schiavetto, F.C.F. Thomazini, W. P Oliveira, *Brazilian Journal of Chemical Engineering*, 25(1), 2008, 59-69.

- Speakman, A.S., Basics of X-ray Powder Diffraction, Massachusetts Institute of Technology, Boston, 2010, 97.
- Steinfeld, A., International Journal of Hydrogen Energy, 27(6), 2002, 611-619
- Steinfeld, A., Solar Energy, 78 (5), 2005, 603-615.
- Suchanek, L.W., Journal of Crystal Growth, 312(1), 2009, 100-108.
- Suchanek, L.W., R.E. Riman, Advances in Science and Technology, 45, 2006, 184-193
- Sue, K., K. Kimura, K. Arai, Materials Letters, 58, 2004, 3229–3231.
- Sun, X.M., X. Chen, Z.X. Deng, Y.D. Li, Materials Chemistry and Physics, 78(1), 2002, 99-104.
- Sun, Y., N.G. Ndifor-Angwafor, D.J. Riley, M.N.R. Ashfold, Chemical Physics Letters, 431(4–6), 2006, 352-357.
- Suwanboon S., P. Amornpitoksuk, P. Bangrak, C. Randorn, Ceramics International, 40(1), 2014, 975-983.
- Suzuki, Y., T. Yotsuya, K. Takiguchi, M. Yoshitake, S. Ogawa, Applied Surface Science, 33–34, 1988, 1114-1119.
- Swapp, S., Scanning Electron Microscopy (SEM), Geochemical Instrumentation and Analysis, 14 December, 2013, Carleton College, Montana State University website, (online), accessed 09, March, 2015, available at:
http://serc.carleton.edu/research_education/geochemsheets/techniques/SEM.html
- Tang, C., C. Jiang, W. Lu, J. Song, Phys. Chem. Chem. Phys., 15, 2013, 8222—8227.
- Tang, L., X. Ding, X. Zhao, Z. Wang, B. Zhou, Journal of Alloys and Compounds, 544, 2012, 67-72.
- Tarat A., R. Majithia, R.A. Brown, M.W. Penny, K.E. Meissner, Surf Sci., 9, 2012, 715–721

- Tarat, A., C.J. Nettle, D.T.J. Bryant, D.R. Jones, M.W. Penny, R.A. Brown, R. Majitha, K.E. Meissner, T.G.G. Maffei, Nanoscale Research Letters, 9(11), 2014, 11.
- Tomura, K., M. Ohnishi, M. Yoshizawa, Mitsubishi Denki Giho, 46, 1972, 1147 – 1152.
- Umar, A., Y. B. Hahn, Appl. Phys. Lett., 88, 2006, 173120, 1-3.
- Ungersböck, S.-E., The Miller Index Notation, chapter 3 in: Advanced Modeling of Strained CMOS Technology, PhD dissertation, (online), submitted to the Faculty of Electrical Engineering and Information Technology, Technical University of Vienna, 2007, accessed 07 July, 2015, available at: <http://www.iue.tuwien.ac.at/phd/ungersboeck/node24.html>
- Van de Walle, C.G., Phys. Rev. Lett. 85, 2000, 1012.
- Vigneshwaran, N., S. Kumar, A.A. Kathe, P.V. Varadarajan, V. Prasad, Nanotechnology, 17, 2006, 5087–5095.
- Vogel, E.M., T.J. Nelson, Displays, 7(2), 1986, 78-80.
- Vojisavljevic, K., M. Šćepanovic, T. Sreckovic, M. Grujic-Brojcin, Z. Brankovic, G. Brankovic, J. Phys.: Condens. Matter, 20, 2008, 475202.
- Vojisavljevic, K., M. Žunic, G. Brankovic, T. Sreckovic, Science of Sintering, 38, 2006, 131-138.
- W.G., Morey, Journal of the American Ceramic Society, 36(9), 1953, 279 – 285.
- Wang, B.G., Shi, E.W., Zhong, W.Z., Cryst. Res. Technol. 1998, 33, 937–941
- Wang, C., B. Mao, E. Wang, Z. Kang, C. Tian, Solid State Communications, 141(11), 2007, 620-623.
- Wang, J. X., X. W. Sun, A. Wei, Y. Lei, X. P. Cai, C. M. Li, Z. L. Dong, Appl. Phys. Lett. 88, 2006, 233106, 1- 3.
- Wang, J., H.-f. Luo, T. Chen, Z.-h. Yuan, Nanotechnology, 21, 2010, 505603, 1-6.

Wang, J., L. Gao, *Journal of Crystal Growth*, 262(1–4), 2004, 290-294.

Wang, J.X., X.W. Sun, Y. Yang, H. Huang, Y.C. Lee, O.K. Tan, L. Vayssieres, *Nanotechnology*, 17(19), 2006, 4995–4998.

Wang, S.L., X. Jia, P. Jiang, H. Fang, W.H. Tang, *Journal of Alloys and Compounds*, 502(1), 2010, 118-122.

Wang, X., J. Song, J. Liu, Z.L. Wang, *Science*, 2007, 316(5821), 102-105.

Wang, Y.-X., J. Sun, X.Y. Fan, X. Yu, *Ceramics International*, 37(8), 2011, 3431-3436.

Wang, Z.L., *J. Phys.: Condens. Matter.*, 16, 2004, R829–R858.

Wang, Z.L., J. Song, *Science*, 312(5771), 2006, 242-246.

Wang, Z.L., *Materials Science and Engineering*, 64, 2009, 33–71.

Wang, Z.L., *Scientific American*, 298, 2008, 82-87.

Wei, A., X.W. Sun, J.X. Wang, Y. Lei, X.P. Cai, C. M. Li, Z. L. Dong, W., *Appl. Phys. Lett.*, 89, 2006, 123902 .

Willander, M., O. Nur, J.R. Sadaf, M.I. Qadir, S. Zaman, A. Zainelabdin, N. Bano, I. Hussain, *Materials*, 3, 2010, 2643-2667.

Xie, J., P. Li, Y. Li, Y. Wang, Y. Wei, *Materials Chemistry and Physics*, 114(2–3), 2009, 943-947.

Xie, J., P. Li, Y. Li, Y. Wang, Y. Wei, *Materials Letters*, 62(17–18), 2008, 2814-2816.

Xu, C., G. Xu, Y. Liu, G. Wang, *Solid State Communications*, 122(3–4), 2002, 175-179.

Xu, C.X., X.W. Sun, Z.L. Dong, M.B. Yu, *Appl. Phys. Lett.* 85, 2004, 3878 – 3880.

Xu, S., Z.L. Wang, *Nano Res.*, 3(9), 2010, 676–684.

Xu, S., Z.L. Wang, *Pure Appl. Chem.*, 83(120), 2011, 2171–2198.

Yadollahi, M., I. Gholamali, H. Namazi, M. Aghazadeh, hydrogels, *International Journal of Biological Macromolecules*, 74, 2015, 136-141.

Yan, X., Z. Li, R. Chen, W. Gao, *Crystal Growth & Design*, 8(7), 2008, 2406-2410.

Yan, Z., K. Zhu, W. Chen, *Materials Letters*, 63, 2009, 486–488.

Yang, J.H., J.H. Zheng, H.J. Zhai, L.L. Yang, Y.J. Zhang, J.H. Lang, M. Gao, *Journal of Alloys and Compounds*, 475(1–2), 2009, 741-744.

Yang, Q., Y. Ma, *International Journal of Toxicology*, 33(3), 2014, 187-203.

Yang, R., Y. Qin, L. Dai, Z.L. Wang, *Nature Nanotechnology*, 4, 2009, 34 – 39.

Yao, I.-C., P. Lin, T.-Y. Tseng, *IEEE Transactions on Nanotechnology*, 11(4), 2012, 1

Yin, M., M. Liu, S. Liu, *Sensors and Actuators B: Chemical*, 185, 2013, 735-742.

Yoshimura M., K. Bryppa, *Journal of Materials Science*, 43, 2007, 2085–2103.

Zeinali H.S., M.A. Razbani, P. Estellé, O. Mahian, *Journal of Dispersion Science and Technology*, 36(8), 2015, 1073-1079.

Zhang J., Y. Wang, B. Chen, C. Li, D. Wu, X. Wang, *Energy Conversion and Management*, 44(11), 2003, 1805-1815.

Zhang, H., B. Chen, H. Jiang, C. Wang, H. Wang, X. Wang, 32(7), 2011, 1906-1914.

Zhang, J. J., E. J. Guo, H. Y. Yue, L. P. Wang, C. Y. Zhang, J. Chang, X. Gao, *Journal of Materials Science: Materials in Electronics*, 2013, 24(9), 3435-3441.

Zhang, Y., M. Muhammed, *Hydrometallurgy*, 60, 2001, 215–236.

Zhao, M., X. Wang, L. Ning, H. He, J. Jia, L. Zhang, X. Li, *Journal of Alloys and Compounds*, 507, 2010, 97–100.

Zheng, J., Z.-Y. Jiang, Q. Kuang, Z.-X. Xie, R.-B. Huang, L.-S. Zheng, *Journal of Solid State Chemistry*, 182(1), 2009, 115-121.

Zheng, X., R. Wu, Y. Chen, *water research*, 45, 2011, 5612-562.

Zhou, J., N.S. Xu, Z.L Wang, Adv. Mater., 18, 2006, 2432–2435.

Zhu, S., X. Chen, F. Zuo, M. Jiang, Z. Zhou, D. Hui, Journal of Solid State Chemistry, 197, 2013, 69–74.

Zhuang, H., J. Li, J. Wang, P. Xu, N. An, Materials Characterization, 62(6), 2011, 593-598.

Zur Loye, H., X-Ray Diffraction, HOW IT WORKS, WHAT IT CAN AND WHAT IT CANNOT TELL US, University of South Carolina, 2013, (online), accessed 24-02-2015 at:

www.chem.sc.edu/faculty/zurloye/xrdtutorial_2013.pdf